ADDITIVE MANUFACTURING FOR ELECTRONIC SYSTEMS (AMES)

By

Mohd Ifwat Mohd Ghazali

A DISSERTATION

Submitted to
Michigan State University
in partial fulfillment of the requirements
for the degree of

Electrical Engineering — Doctor of Philosophy

ABSTRACT

ADDITIVE MANUFACTURING FOR ELECTRONIC SYSTEMS (AMES)

$\mathbf{B}\mathbf{y}$

Mohd Ifwat Mohd Ghazali

Over the last few decades, a significant interest towards the manufacturing of complex three-dimensional (3D) structures for conceptual models have led to an incredible amount of research and development. 3D structures have been an integral part of physical models or functional end-products and are widely adapted as a miniaturizing technique in manufacturing industries, and in particular, the electronics industry. Advancement in electronics technology has lead to the need for fabricating consumable electronics within a smaller lattice space. To meet the challenge of high functional density integration, Additive Manufacturing (AM) techniques by 3D printing is a promising solution for satisfying the ever-increasing demand for a higher quality product with the ability to customize based on an individual customer needs. AM techniques allows the possibility of developing low cost, multifunctional, compact, lightweight, and miniaturized electronics that can be easily integrated with conventional systems or platforms.

In this dissertation, approaches towards utilizing existing AM techniques for fabricating structures that are compatible to carry electrical functionality for RF applications is proposed. The end goal is to develop processes using AM technique as an alternate manufacturing approach to achieve a fully functional electronics system. Specifically, AM holds significant potential in realizing low-loss, high-performance, and light-weight RF components such as transmission lines, waveguides, resonators, filters, and antennas. In order to realize a complete RF system by AM, multiple processes are developed. First, to establish connection

for allowing electrical functionality, conductive traces must be patterned on the substrate. Two different metal patterning techniques for selectively patterning conductive traces on the 3D printed substrate is developed. Next, to realize a compact system, a smaller form factor is a necessity and this can be achieved by utilizing the flexibility in the third dimension (z-axis) in designing non-planar RF structures. A number of non-planar RF structures are demonstrated showcasing the advantages of AM in fabricating compact designs. Moreover, for fabricating efficient RF circuits, the losses associated with the printed plastics should be minimized. The currently available printing polymers have high dielectric loss and hence an alternative process that utilizes air as a substrate is developed by using a LEGO-like self-alignment procedure in which the structure is printed in multiple parts and snapped together face to face to integrate the complete structure. Furthermore, a number of active and passive components must be integrated into the printed plastic to achieve a RF system. For this purpose, three different solder-free embedding processes are developed to embedded active devices such as diodes into the 3D printed plastics. Finally, a combination of the above-mentioned processes is utilized to achieve a fully 3D printed electronics system and a potential application of such multi-functional system is demonstrated. Overall, this work demonstrates that 3D printing can be adopted in the fabrication of microwave and millimeter wave high functional density circuits and systems.

Copyright by MOHD IFWAT MOHD GHAZALI 2019 This dissertation is dedicated to my beloved family. . .

ACKNOWLEDGMENTS

First and foremost, I praise God, the almighty for providing me the strength and His blessing in completing this dissertation. I was able to complete this dissertation work with assistance and guidance from several individuals. I would like to take this opportunity by thanking all who had contributed in the completion of this dissertation. I would like to express my deepest gratitude to my advisor, Dr. Premjeet Chahal, for his excellent motivation, wisdom, commitment, and patience. His invaluable help with constructive comments and suggestions throughout the experimental and dissertation works have contributed to the success of this research. Secondly, I would like to thank my Ph.D guidance committee members, Dr. Edward Rothwell, Dr. Nelson Sepulveda, and Dr. Himanshu Sahasrabudhe for their advice as well as detailed review of my dissertation and providing me great feedback on my research work. I sincerely thank all my colleagues in the TESLA group, in particular Saranraj Karuppuswami, Saikat Mondal, Vincens Gjokaj and Jennifer Byford for their kindness, help, encouragement and for their valuable feedback. In addition I would like to express my deep gratitude to my senior colleagues, Dr. Park Kyoung Youl, Dr. Nophadon Wiwatcharagoses, Dr. Amanpreet Kaur, Dr. Xianbo Yang, Dr. Jose Hejase and Dr. Joshua Myers for their advice and wisdom through out my Ph.D. endeavor. Also, I would like to acknowledge all my colleagues from Electromagnetic Research Group for their help during this research work. I would like to thank Mr. Brian Wright and Mr. Greg Muller from MSU ECE shop without their assistance I would not have been able to complete this work. Also I would like to include a special warm gratitude to all those who in some way contributed to the successful completion of my dissertations work especially my friends in Malaysia and in the US.

I am grateful to the Malaysian Government and Islamic Science University of Malaysia

for providing me a generous fellowship which made it possible for me to study at MSU. Last but not least, my deepest gratitude to my parents, Mohd Ghazali Omar and Noraini Ismail, my parents-in law, Sheikh Mohd Nasir Sheikh Hassan and Hanizah Abu Hassan and my sibling Mohammad Amin Mohd Ghazali for their endless love, prayers and encouragement. Also not forgetting my beautiful wife, Raihan Farhanah Mohamad Hassan who is always there to encourage me and stand by me through good and bad times.

TABLE OF CONTENTS

| LIST OF TABLES | | |
|----------------|--|--|
| LIST (| OF FIGURES | |
| Chapte | er 1 Introduction | |
| 1.1 | Overview | |
| | 1.1.1 Additive Manufacturing Technology | |
| | 1.1.2 Applications of Additive Manufacturing Technology | |
| | 1.1.3 Additive Manufacturing Technology in Electronics Applications 14 | |
| 1.2 | Summary of Dissertation Contributions | |
| Chapte | er 2 Selective patterning process | |
| 2.1 | Introduction | |
| 2.2 | Fabrication | |
| | 2.2.1 Damascene-like Process | |
| | 2.2.2 In Situ Lift-off Process | |
| 2.3 | Process Demonstration | |
| | 2.3.1 Microstrip Transmission Line | |
| | 2.3.2 T-Line and Circular Ring Resonator | |
| | 2.3.3 Patch Antenna | |
| 2.4 | Discussion of Limitation and Possibilities | |
| 2.5 | Conclusion | |
| Chapte | er 3 3D printed non-planar components | |
| 3.1 | Introduction | |
| 3.2 | Design and Fabrication | |
| 3.3 | Simulation and Measurement Results | |
| | 3.3.1 Non-Planar Microstrip Line | |
| | 3.3.2 T-Line Resonator | |
| | 3.3.3 Elevated Patch Antenna | |
| | 3.3.4 Air Gap Patch Antenna | |
| | 3.3.5 E-Patch Antenna | |
| | 3.3.6 Monopole Based Antennas | |
| 3.4 | Discussion | |
| 3.5 | Conclusion | |
| Chapte | er 4 3D printed low loss air substrates | |
| 4.1 | Introduction | |
| 4.2 | Analysis | |
| 4.3 | Fabrication 7 | |

| 4.4 | Microstrip Line and T-Line Resonator | 74 |
|-------|--|------------|
| 4.5 | Patch Antenna | 77 |
| 4.6 | Slot Antenna | 79 |
| 4.7 | Cavity Resonator | 80 |
| 4.8 | Challenges and Limitations | |
| 4.9 | Conclusion | |
| Chapt | er 5 3D Printed Light-Weight components | 84 |
| 5.1 | Introduction | |
| 5.2 | Fabrication | |
| 5.3 | Simulation and Measurement Results | |
| 0.0 | 5.3.1 X- and K-band Rectangular Waveguides | |
| | 5.3.2 Rectangular Waveguide Iris Filter | |
| | 5.3.3 Leaky Waveguide Antenna | |
| | 5.3.4 Cavity-Backed Slotted Antenna Array | |
| 5.4 | Conclusion | |
| 5.4 | Conclusion | 91 |
| Chapt | | 98 |
| 6.1 | Introduction | 98 |
| 6.2 | Analysis | 101 |
| 6.3 | Material characterization | 103 |
| 6.4 | Fabrication Process | 105 |
| 6.5 | Measurement and Results | 109 |
| | 6.5.1 Thermal cycling | 109 |
| | 6.5.2 T-Line Resonator | 111 |
| | 6.5.3 Metamaterial-Inspired Phase Shifter | 113 |
| | 6.5.4 Tunable Patch Antenna | 116 |
| | 6.5.5 Discussions | 119 |
| 6.6 | Conclusion | |
| Chapt | er 7 3D Printed Electronic System | 199 |
| 7.1 | Introduction | |
| 7.2 | 3D Printed harmonic system | |
| 1.2 | 7.2.1 Design and Fabrication | |
| | 7.2.2 Measurement and Results | 127 |
| | 7.2.2.1 Frequency versus received power | 127 |
| | 7.2.2.2 Read range versus received power | 128 |
| | 7.2.2.3 Position versus received power | 129 |
| | - | |
| | O I | 130 131 |
| | 1 | |
| 7 9 | 7.2.3 Discussion - Harmonic Sensing System | 132 |
| 7.3 | 3D Printed Substrates for the Design of Compact RF Systems | 135 |
| | 7.3.1 Design and Fabrication | 135 |
| | 7.3.1.1 Air-Substrate based Patch Antenna | 137 140 |
| | $L.\mathfrak{d}.L.Z$ Amdimer would | 140 |

| | | 7.3.1.3 Integrated RF Module | 142 |
|--------|--------|---|-----|
| | 7.3.2 | Results | 143 |
| | 7.3.3 | Discussion- 3D Printed Substrates for the Design of Compact RF Sys- | |
| | | tems | 145 |
| 7.4 | Concl | usion | 146 |
| Chapte | er 8 | Conclusions | 147 |
| 8.1 | Future | e Work | 149 |
| | 8.1.1 | 3D Printing in Biomedical Applications: | 149 |
| | 8.1.2 | 3D Printing in Aerospace Applications: | 150 |
| | 8.1.3 | 3D Printing in Transportation Applications: | 150 |
| | 8.1.4 | 3D Printing in Smart Agriculture Applications: | 151 |
| APPE | NDIC | ES | 152 |
| APF | PENDI | X A Sputtering Process | 153 |
| APF | PENDI | X B Electroplating Process | 156 |
| BIRLI | OGR A | PHY | 158 |

LIST OF TABLES

| Table 6.1: | Tangent Loss for Different 3D Printable Polymers | 120 |
|------------|--|-----|
| Table 7.1: | Received power at the second harmonic frequency (2f ₀) for different tag | |
| | depth under the soil | 132 |

LIST OF FIGURES

| Figure 1.1: | Schematic illustration of the use of hammerstone for manufacturing 3D structure [1] | 2 |
|--------------|---|----|
| Figure 1.2: | Illustration of fabrication by subtraction process (CNC) | 6 |
| Figure 1.3: | The schematic of the injection molding process | 7 |
| Figure 1.4: | Applications of Additive Manufacturing | 9 |
| Figure 1.5: | First four wheeler made using additive manufacturing by Local Motors Strati [6] | 10 |
| Figure 1.6: | 3D printed for biomedical applications (a) Implant bearing skull. (b) Two dimensional tissue (skin) and (c) solid organs (kidney) [7-9] | 11 |
| Figure 1.7: | Illustration of photolithography process | 15 |
| Figure 1.8: | Illustration of surface micromachining process | 15 |
| Figure 1.9: | 3D printed signal conditioning circuit and Electronic circuit mechanically designed into substrate [17] | 17 |
| Figure 1.10: | Seven categories of Additive Manufacturing (Standard Terminology for Additive Manufacturing Technologies F92792-12a) | 18 |
| Figure 1.11: | The schematic of photopolymer jetting 3D printer | 19 |
| Figure 1.12: | The schematic of SLA systems | 20 |
| Figure 1.13: | Envisioned fully 3D printed RF systems | 22 |
| Figure 2.1: | Process flow diagram illustrating the fabrication of a microstrip using the damascene-like process. (a) 3D printed structure, (b) Sputter 60 nm Titanium, (c) Sputter 0.5 μ m Copper and (d) removal of the supporting material | 27 |
| Figure 2.2: | Process flow diagram illustrating the fabrication of a microstrip using in situ lift-off process. (a) 3D printed structure, (b) Sputter 60 nm Titanium, (c) Sputter 0.5 μ m Copper and (d) removal of the supporting material | 28 |

| Figure 2.3: | The cross-sectional image of a cleaned sample | 30 |
|-------------|---|----|
| Figure 2.4: | Sample structure after (a) 3D printing, (b) metallization, and (c) mechanical removal of the excess copper through the damascene-like process. | 30 |
| Figure 2.5: | In situ lift-off process is shown where a sacrificial layer is removed | 31 |
| Figure 2.6: | Microstrip T-line. (a) Final fabricated sample with dimensions and (b) Simulated and measured results | 33 |
| Figure 2.7: | T-line resonator. (a) Final fabricated sample with dimensions, and (b) Simulated and measured results | 35 |
| Figure 2.8: | Circular ring resonator. (a) Final fabricated sample with dimensions, and (b) Simulated and measured results | 37 |
| Figure 2.9: | Patch antenna. (a) Final fabricated sample with dimensions and the simulated and measured results for the antennas, (b) Radiation pattern in the E-plane (dBi) and (c) Reflection coefficient | 39 |
| Figure 3.1: | Packaging concept with 3D printed out-of-plane patch antenna | 45 |
| Figure 3.2: | Non-planar microstrip transmission line: Schematic (top and side view) and fabricated structure | 47 |
| Figure 3.3: | The simulated and measured reflection and transmission coefficient (S-parameters) of the non-planar microstrip line | 48 |
| Figure 3.4: | The simulated and measured reflection and transmission coefficient (S-parameters) of the non-planar microstrip line | 49 |
| Figure 3.5: | The simulated and measured reflection and transmission coefficient (S-parameters) of the non-planar microstrip line | 50 |
| Figure 3.6: | Horizontal mount elevated patch antenna (a) Schematic and the dimensions (b) 3D printed elevated patch antenna after metallization | 52 |
| Figure 3.7: | Simulated and measured results (a) S-parameters and (b) radiation pattern (dBi) in the E-plane of the horizontal mount elevated patch antenna. | 52 |
| Figure 3.8: | Vertical mount microstrip patch antenna (a) Schematic with dimensions, (b) image of the fabricated antenna with the SMA connector | 53 |
| Figure 3.9: | Vertical mount microstrip patch antenna, simulated and measured (a) reflection coefficient, and (b) radiation pattern | 53 |

| Figure 3.10: | Air-gap patch antenna (a) Schematic of the patch antenna with dimensions, (b) Image of the fabricated patch and (c) illustration of the integration between 3D printed substrate structure and PCB | 55 |
|--------------|---|----|
| Figure 3.11: | Air-gap patch antenna, simulated and measured (a) reflection coefficient and (b) radiation pattern | 55 |
| Figure 3.12: | Air-gap E-patch antenna (a) Design and schematic with dimensions, (b) fabricated E- patch antenna (before and after metallization) | 56 |
| Figure 3.13: | Air-gap E-patch antenna, simulated and measured (a) reflection coefficient, and (b) radiation pattern | 57 |
| Figure 3.14: | Monopole antenna (a) Design and schematic with dimensions, (b) fabricated monopole antenna, (c) simulated and measured reflection coefficient, and (d) measured radiation pattern | 59 |
| Figure 3.15: | Monopole antenna with a reflector (a) Design and schematic with dimensions, (b) fabricated vertical monopole antenna with a reflector | 59 |
| Figure 3.16: | Monopole antenna with a reflector , simulated and measured (a) reflection coefficient and (b) radiation pattern in the E-plane direction | 60 |
| Figure 3.17: | Vertical Yagi-Uda antenna (a) design and dimensions (b) image of the fabricated antenna | 62 |
| Figure 3.18: | Vertical Yagi-Uda antenna, simulated and measured (a) reflection coefficient and, (b) radiation pattern (dBi) | 62 |
| Figure 4.1: | Propagation loss of a 50 Ω transmission line as a function of loss tangent (tan δ) for substrates with different dielectric constant (ϵ_r) values | 68 |
| Figure 4.2: | Propagation loss of a 50 Ω transmission line as a function of frequency for different heights (h) and fixed $\epsilon_r = 1$ and $\tan \delta = 0$ of the air substrate. | 69 |
| Figure 4.3: | Simulation results for gain of a patch antenna as a function of substrate dielectric constant (ϵ_r) for fixed substrate height (2mm) and loss tangent $(\tan \delta = 0)$ | 70 |
| Figure 4.4: | Schematic of the cross-sectional view of proposed fabrication and LEGO-like assembly technique (a) top layer (b) bottom layer along with support pillars and (c) assembly of the two layers to achieve an air substrate | 71 |
| Figure 4.5: | Propagation loss of a 50 Ω transmission line as a function of frequency for different thickness of the 3D printed support material | 71 |

| Figure 4.6: | Damascene-like fabrication process and LEGO-like assembly for air- based substrate microwave devices using 3D printing | 73 |
|--------------|---|----|
| Figure 4.7: | Microstrip transmission line: (a) Fabricated structure before assembly with dimensions (in mm) and (b) simulated and measured S-parameters. | 74 |
| Figure 4.8: | T-line resonator: (a) Fabricated structure before assembly with dimensions (in mm) and (b) simulated and measured transmission coefficient. | 76 |
| Figure 4.9: | Patch antenna with SMA feed: (a) Dimension of patch antenna (in mm) (b) fabricated patch antenna, simulated and measured (c) reflection coefficient, and (d) radiation pattern | 78 |
| Figure 4.10: | Patch antenna with coaxial feed: (a) fabricated patch antenna with dimensions (in mm), simulated and measured (b) reflection coefficient, and (c) radiation pattern | 78 |
| Figure 4.11: | Slot antenna: (a) schematic for slot antenna with dimensions (in mm) ,(b) Image of the fabricated antenna, and the simulated and measured results (c) reflection efficient and, (d) radiation pattern | 79 |
| Figure 4.12: | Schematic for multilayer cavity resonator structure and fabricated layers before assembly (Dimensions in mm) | 81 |
| Figure 4.13: | Simulated and measured S-parameters (reflection and transmission) of cavity resonator | 81 |
| Figure 5.1: | (a) 3D printed plastic parts, (b) parts are blanket metalized, (c) the parts are snapped together, (d) shown is an example waveguide after metallization | 86 |
| Figure 5.2: | The dimension of the waveguide | 87 |
| Figure 5.3: | The pre-metallization 3D printed waveguide for K-band and X-band | 88 |
| Figure 5.4: | Simulated and measured S-parameters of the X-band waveguide (length = 100 mm) | 89 |
| Figure 5.5: | Simulated and measured S-parameters of the K-band waveguide (length = 50 mm) | 89 |
| Figure 5.6: | Schematic of an iris filter | 90 |
| Figure 5.7: | Sections of the fabricated iris filter (a) before and (b) after metal coating. | 91 |

| Figure 5.8: | Simulated and measured results of the waveguide iris filter | 91 |
|--------------|--|-----|
| Figure 5.9: | X-band leaky waveguide antenna design | 92 |
| Figure 5.10: | The simulated and measured reflection coefficient of the leaky waveguide antenna | 93 |
| Figure 5.11: | Measured and simulated radiation pattern in the H-plane of the leaky waveguide antenna at 8.8 GHz | 93 |
| Figure 5.12: | The cross-sectional view of the cavity back slotted antenna array | 94 |
| Figure 5.13: | The 3D printed structure of the cavity-backed slotted antenna (a) before and (b) after assembly, and (c) assembled after metal coating | 95 |
| Figure 5.14: | Simulated and measured \mathbf{S}_{11} of the cavity-backed slotted antenna array. | 95 |
| Figure 5.15: | Measured gain of the slotted array. The inset shows the simulated and measured radiation patterns at 7.5 GHz and 8.7 GHz, respectively | 96 |
| Figure 6.1: | Envisioned fully 3D printed RF systems | 100 |
| Figure 6.2: | The comparison of S-parameters of simulated for (a) embedded active structure using via, and (b) embedded active structure using wire bonding. | 102 |
| Figure 6.3: | Measured dielectric constant and loss tangent of the acrylic photo polymer. | 104 |
| Figure 6.4: | Schematic of the Formlabs 3D printer | 106 |
| Figure 6.5: | Fabrication steps for 3D printing of different embedding schemes: (a) Face-up (b) Face-down, and (c) Side-mount | 108 |
| Figure 6.6: | Measured I-V characteristics of the Schottky diode embedded in the cube structure | 108 |
| Figure 6.7: | Measured I-V characteristics of the Schottky diode embedded in the 3D printed package after multiple thermal cycles, the inset shows log I vs V and the optical image of vias after 20 thermal cycles (90°C) | 110 |
| Figure 6.8: | Design of the T-line resonator structure along with the dimension used, inset shows the 3D printed resonator with the embedded varactor diode. | 111 |
| Figure 6.9: | Measured results showing change in phase of the T-Line resonator under different varactor diode bias conditions | 112 |

| Figure 6.10: | Measured results showing change in resonance frequency of the T-Line resonator under different variator diode bias conditions | 112 |
|--------------|--|------|
| Figure 6.11: | Schematic of the metamaterial-inspired phase shift along with the dimension used, the inset shows the 3D printed phase shifter with embedded varactor diodes | 114 |
| Figure 6.12: | Measured results showing change in phase of phase shifter with change in biasing voltage | 114 |
| Figure 6.13: | Measured results for change in resonance frequency of phase shifter due to the change in biasing voltage | 115 |
| Figure 6.14: | Schematic and dimensions for the tunable antenna design, and the inset shows the fabricated patch antenna | 117 |
| Figure 6.15: | The comparison between simulation and measurement result for the tunable patch under different bias condition | 117 |
| Figure 6.16: | Measured results for tunable patch antenna showing change in operating frequency under different voltage bias conditions | 118 |
| Figure 6.17: | Simulated and measured radiation pattern for the tunable patch antenna at 6.4 GHz with the gain of 5.9 dBi and 5.48 dBi respectively at zero bias | .118 |
| Figure 7.1: | 3D Printed Harmonic RF System | 123 |
| Figure 7.2: | Schematic of the harmonic tag with dimensions | 124 |
| Figure 7.3: | Image of fabricated tag | 125 |
| Figure 7.4: | Geometry and dimensions of Vivaldi | 126 |
| Figure 7.5: | Schematic of the harmonic tag with dimensions | 126 |
| Figure 7.6: | Face-up solder-free embedding process of the diode using 3D printing | 126 |
| Figure 7.7: | Received power at second harmonic frequency $(2f_0)$ as a function of fundamental frequency (f_0) with a fixed Pin and read range | 128 |
| Figure 7.8: | Received power at second harmonic frequency ($2f_0 = 5.1 \text{ GHz}$) as a function of read range with a fixed input power of $+13 \text{ dBm.} \dots$. | 129 |

| Figure 7.9: | Received power, using noise floor as reference at second harmonic frequency $(2f_0)$, as a function of tag location (x, y) with a fixed Pin of $+13$ dBm and a read range of 30 cm | 130 |
|--------------|--|------|
| Figure 7.10: | Received power at the second harmonic frequency $(2f_0)$ as a function of tag angle theta with a fixed P_{in} of +13 dBm and a fixed read range of 30 cm | 131 |
| Figure 7.11: | An example of the envisioned 3D printed electronic packaging with customizable substrate for 5G applications | 136 |
| Figure 7.12: | Patterning conductive traces on 3D printed substrate using a damascene-like process | 136 |
| Figure 7.13: | An example of LEGO-like assembly process for air substrate based circuits | .137 |
| Figure 7.14: | 3D printed air substrate based patch antenna (A) Schematic with dimensions, (B) and (C) structure before and after metallization, respectively, and (D) image after LEGO-like assembly | 138 |
| Figure 7.15: | Simulated and measured results for (A) reflection coefficients (B) radiation patterns of the air substrate based patch antenna | 139 |
| Figure 7.16: | Schematic of the (A) amplifier circuit with lumped components, and (B) 3D printed configuration | 140 |
| Figure 7.17: | Simulation results for analyzing amplifier performance | 141 |
| Figure 7.18: | Image of the fabricated 3D printed amplifier | 141 |
| Figure 7.19: | 3D printed integrated RF module: schematic (A), structure before and after metallization (B) and (C), respectively, and , (D) integrated module after the assembly process | 142 |
| Figure 7.20: | Measurement setup | 143 |
| Figure 7.21: | Measured received power as a function of input frequency | 144 |
| Figure 7.22: | Measured gain as a function of bias voltage | 145 |
| Figure A.1: | Denton Vacuum Desktop Pro | 155 |
| Figure B.1: | Illustration of electroplating | 157 |

Chapter 1

Introduction

Throughout human civilization, manufacturing ingenuity has transformed drastically in terms of technology with advent of multiple economical methods for manufacturing threedimensional (3D) structures. During the primitive days, the importance of 3D structures is vital towards survival of human race for creating different tools for hunting and other day to day activities. The initial manufacturing is performed using bare hands to develop products such as knives, clothing, hunting equipment, and basic utensils. A typical example of hand made tools is a hammerstone that is used to shape different 3D structures from stones or bones as shown in Figure 1.1 [1]. The hand-made manufacturing technique involves chipping and percussion of the core material using hammerstone in which the unwanted part is subtracted off to realize the desired shape. There are a number of limitations associated with such a technique such as lower probability to reproduce in large scale and achieve precision, chipping the material is inefficient and can only be done in small pieces at a time leading to a time consuming process and it may cause danger to the person due to the flying debris. Furthermore, the finished product is dependent on the individual skill set of the craftsman and repeatability is a concern although the desired 3D structure is hand-made by the same individual as there is a higher probability for human error. As days progressed, more refined tools such as chisels are invented to replace traditional hammer stone providing more finer control on the subtractive hand-made manufacturing process called sculpturing as it allows realizing much complex 3D designs. However, this manufacturing technology is still limited in terms of scaling and mass production.

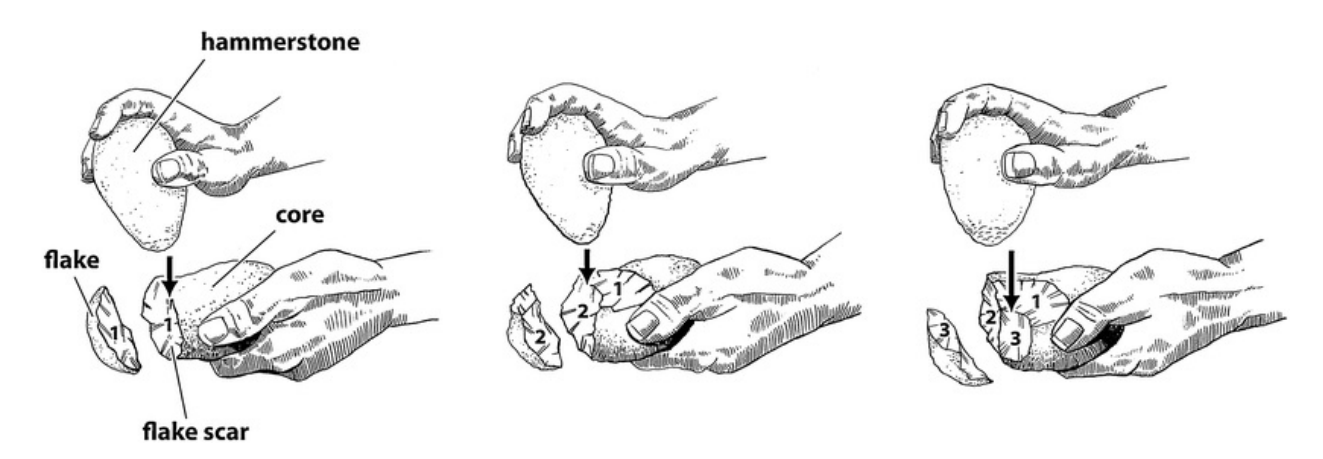


Figure 1.1: Schematic illustration of the use of hammerstone for manufacturing 3D structure [1].

The technological evolution took a huge step forward with the invention of wheels as well as the discovery of metals such as iron, and steel. The ability to transport shaped the economic landscape in which products from different areas can be transported to distant places allowing a possibility to learn and merge different manufacturing technologies. The next step in the evolution of manufacturing technique is to overcome the difficulty of hand-based manufacturing in particular to the shape metals to the desired shape. For this purpose, new techniques using animal power are developed to operate specific manufacturing machines for smelting, and metal casting [2]. The animal movement and strength acts as a power converter which provides mechanical energy to the rotational gear which then powers the casting machines. A combination of animal power based manufacturing for softening the metal and hand-based method to percussion the metal to desired shape allowed large-scale production. Furthermore, more complex structures with mixture of different materials can be realized showcasing the evolution of manufacturing techniques. In spite of the advancement, manufacturing technology in those days is largely reliant on human labor, human supervision, and requires a highly specific skill set. A reduced dependability on human and animal involvement in the manufacturing process allows increased precision, repeatability and decreases the overall time for production.

In the late eighteenth (18th) century and the early nineteenth (19th) century, a predominant shift took place from the hand-based and animal-powered manufacturing technique to a more a machine-based manufacturing technique. Instead of hand-based manufacturing of 3D structures, machines are designed to manufacture based on specific needs of the product. Invention of steam powered engines allowed replacing the animal-based power generation. Furthermore, various chemical and biological process that involves a combination of natural and formulated materials to fabricate the 3D structure came into effect triggered the Industrial Revolution around the globe. Such technological advancements allowed the manufacturer to increase the speed of production as well as the volume of the manufactured products within a shorter time frame thereby reducing the dependance on human labor except for maintaining the machines. In late 19th and early 20th century, the manufacturing became heavily dependent on machinery, and hence more advanced machines with the integration of computers and robotics system came into existence to deliver high-quality finished product.

A manufacturing industry uses conventional mass production techniques for producing a large number of products with improved repeatability and precision. However, the production is only catered to standardized products and cannot cater to individual customization. Nowadays, the demand is more towards developing manufacturing processes that allow customization according to the individual user needs and at the same time provide a multifunctional system with high-quality. To meet such demands, a shift towards 3D manufacturing approach from the conventional approach is required for catering to a plurality of applications in multiple fields. To date, most rapid prototyping designs are used to provide structural

stability, mechanical supports, initial prototype or as a packaging enclosure of the end product. Additive manufacturing (AM) is one such rapid prototyping approach to manufacture a complex 3D structure with ease.

1.1 Overview

1.1.1 Additive Manufacturing Technology

The manufacturing industry has shown significant interest in the development of new manufacturing techniques for realizing 3D structures over the past decade. A few considerations must be taken into account while designing a new 3D manufacturing process such as the availability of tools, the different fabrication procedures that allows the structure to be manufactured according to the desired design, availability and properties of process specific materials, production cost, and complexity of the geometry. There are three different methods of manufacturing 3D structure up to current date:

- (i) Subtraction process (conventional),
- (ii) Formative process (conventional), and
- (iii) Additive Manufacturing.

Subtraction process is considered the most commonly used manufacturing technique to design a 3D structure by using a computer-aided machinery that allows the material to be cut (subtracting the unwanted material) to form the desired shape. The most popular tool for subtraction method is the computer numerical control (CNC) machine [3] that uses lathes for milling, cutting, and grinding to transform a plastic-based or a metal-based material to the desired customized end-product. The CNC machine uses a cutting tool to move in X, Y and Z-axis to cut away the bulk unwanted material as shown in Figure 1.2. Usually, the structure is built in separate pieces and combined using welding to realize the end product. However, these techniques face several disadvantages such as expensive CNC machine, labor-intensive as the process requires specialty in using the machine, and the accumulation of wastes during the subtraction process.

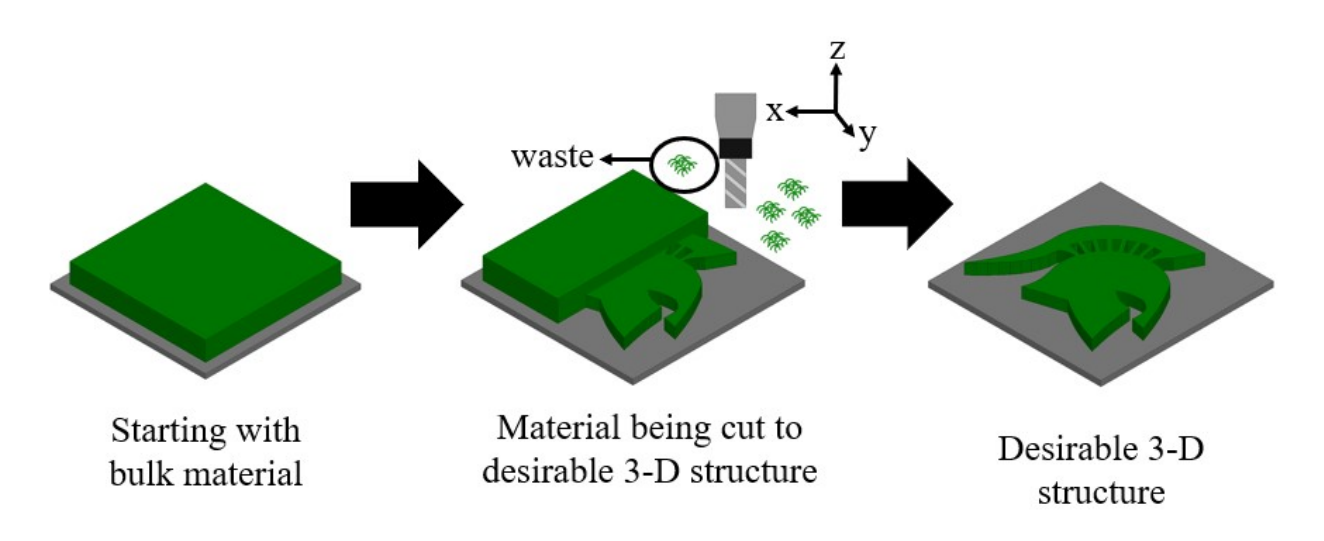


Figure 1.2: Illustration of fabrication by subtraction process (CNC).

The formative process is another conventional method for fabricating 3D structures. Usually, the formative process is related to transforming liquid-based material (e.g. metal or plastic) into the desired shape through several steps such as compression, tension, stress, and consolidation [4]. An example of a technique that uses the formative principle is the injection molding. The basic principle of injection molding is by flowing a plastic-based material which is in the glass transition state to the assigned closed mold structure to fill the void in a pressurized environment. The plastic-based material will then harden to form the desired structure. After the structure has reached certain hardness, the mold can be opened, and the final product is realized in illustration Figure 1.3. This manufacturing process requires large amount of energy due to the fact that it uses a high temperature and a high-pressure processes. Economically, the drawback of such process is that the tooling is expensive if the number of the product that needs to be manufactured is low. In addition, only a few available materials can be used to design the structures using injection molding method to produce high-quality results. This technique is also limited to realizing complex 3D structures.

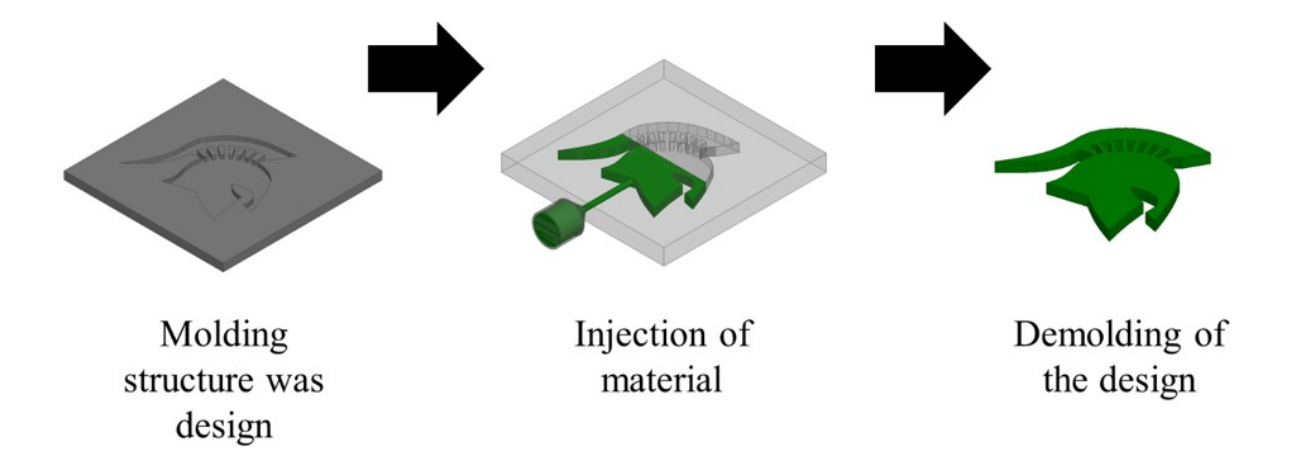


Figure 1.3: The schematic of the injection molding process.

The subtractive and formative processes are the most commonly used manufacturing processes in industries. However, further improvement in technology is necessary to reduce or eliminate the drawbacks of the conventional 3D processes. Furthermore, the competitiveness to manufacture products at a rapid speed is very important with the ever-changing need of the consumers. Such improvements allow the manufacturing to increase the productivity as well as the quality of the product to cater to individual customers.

A new paradigm shift is currently occurring in the manufacturing process where products are being manufactured at rapid speed having complex geometries as well as having multifunctional capabilities in a single packaging 3D structure. This manufacturing process is called additive manufacturing (also known as rapid prototyping, 3D printing, direct digital manufacturing, and freedom fabrication). Additive manufacturing was first introduced in the 1980s for manufacturing 3D structure as a test of concept for a fast and cost-effective prototyping of products. A formal definition by the American Society for Testing Materials (ASTM) for additive manufacturing is a process of joining materials to make objects from 3D model data, usually, layer upon layer [5]. This manufacturing process is similar to the conventional paper printer in every office desk and it allows rapid prototyping a 3D structure

with a limitless design. The process has the ability to control the design and manufacture the product depending on the individual user needs thereby providing an alternative manufacturing technique eliminating the need for excessive and expensive machinery. The next section will highlight the applications of additive manufacturing in different fields.

1.1.2 Applications of Additive Manufacturing Technology

Additive manufacturing has transformed from its humble beginning for manufacturing support materials to a well-known process to manufacture high-quality products. The initial purpose of additive manufacturing is to print a visual representation of finished products or samples. As time progressed, additive manufacturing has developed new tools and materials that are capable of manufacturing a variety of applications in different fields as shown in Figure 1.4.

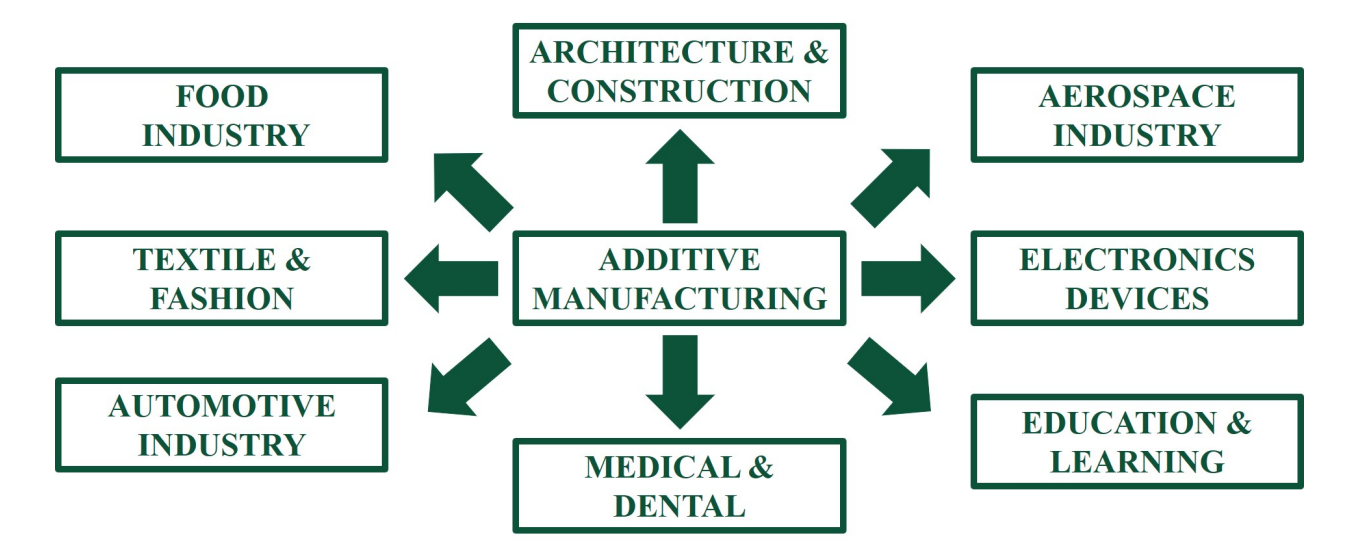


Figure 1.4: Applications of Additive Manufacturing.

One of the earliest industry to use additive manufacturing is the automotive industry. In the beginning, small parts are manufactured for prototyping purposes to do initial testing or just the overall model. Individual parts of the car are manufactured and then assembled together in the production line. As the advancement was made in additive manufacturing, the automotive industry has utilized AM to manufacture lighter weight automobile or automotive parts with complex design in a low-cost manner. These improvements lead to the upgrading the performance as well as the quality of the parts. Among those that benefits from such

improvements are the Formula One (F1) teams. For example, F1 races are organized around the world and adjustment or repair must be done on the spot. Usually, the parts are transferred from the F1 team factory but now it can be printed or manufactured where ever the races are conducted. A fully printed car has been manufactured by Local Motors which became the first ever 3D printed electric car and it took less than forty-four hours to print the entire car structure Figure 1.5 [6].



Figure 1.5: First four wheeler made using additive manufacturing by Local Motors Strati [6].

The medical fields has advanced employing additive manufacturing from printing prosthetic limbs to bones. In the preliminary stages, additive manufacturing was used to customize parts that are used on the exterior of the patients such as hearing aid or prosthetic limbs. As materials and tools for additive manufacturing advanced, the printer was used to replicate bone structures as well as tissue and organs as shown in Figure 1.6 [7,8]. However, there are still challenges to integrate the 3D structure with the body. In literature, the construction of an aortic valve is presented using additive manufacturing by using a polymer-based material called polyethylene glycol-diacrylate with hydrogel supplement with alginate. The printed structure resembles the aortic valve and functions as required similar to a real aortic valve. A number of different bio compatible materials exists that are tested for safe integrated with the cells as it is placed inside the body in [9].



Figure 1.6: 3D printed for biomedical applications (a) Implant bearing skull. (b) Two dimensional tissue (skin) and (c) solid organs (kidney) [7-9].

Aerospace and space exploration are among the other fields that utilize additive manufacturing in designing spacecrafts and satellites. As known, the cost of launching rockets or satellites requires spending a substantial amount of money. To reduce cost, AM is used at a validation stage as well as at the pre-production stage. Currently, AM has been made as an integral part of spacecraft manufacturing process due to the ability to print light weight space compatible materials. With future space exploration, additive manufacturing will become an important tool since it can be used to manufacture products or equipments real-time in space.

Manufacturing complex structures is one of the advantages of additive manufacturing. One unique example is the utilization of such advantage in fashion and textiles industry in which creative fashion designers have proposed unique and complex designs that are realized using 3D printing. For example, one of the first designers, Michael Schmidt has designed futuristic style of clothing as shown in on model Dita Von Teese. Other than clothing, accessories such as jewelry can be easily manufactured. For example, the basic structure of the jewelry is made from plastic and is coated with a metal such as silver or gold or platinum to obtain a finished product. This reduces the cost of the jewelry making but also maintains the overall look of the jewelry.

Most materials used in the earlier applications are either using polymers or a metal-based material. One of the most interesting materials used in additive manufacturing is edible food substances. The conventional method of doing 3D structure in food for example chocolate is using a casting technique similar to injection molding methods where the chocolates in the liquid form are poured into the cast and cooled to solidify. However, additive manufacturing allows the creation of 3D chocolate structure in a simpler way and unique designs can be made. In addition, the customizable structures can be realized using such processes as shown

by University of Exeter to create a face shaped chocolate structure. Other types of food that are created using 3D printing are cookies, waffles, and pizzas. This method does not just apply for food industry but also can be adapted by the aerospace industry for providing food in space.

The development of additive manufacturing has attracted significant interest from the electronic industry. An in-depth discussion on the use of additive manufacturing for different electronics applications will be presented in the next section.

1.1.3 Additive Manufacturing Technology in Electronics Applications

The main focus of this section is to show the capabilities of additive manufacturing in order to fabricate electronic components, in particular, RF-based components. 3D components in the past decades have gained significant interest in the electronics industry due to the ability to condense multifunctional components by integration into a dense structure. The current needs for electronic devices are ultra-compact, miniaturized, light-weight, and ability to perform multiple functions often integrated into a single system. The typical manufacturing process for an electronic system requires the components to be manufactured separately and assembled together after which the cast or housing is placed to enclose the systems. To fabricate such small-size devices, a technique called microfabrication technology is commonly used by the electronics industry in realizing components such as an integrated circuit, microfluidics, microsensors, and microelectromechanical (MEMs) [10–13]. This technology allows devices to be manufactured in the millimeter (mm) or sometimes in the nanometer (nm) scale. In microfabrication technology, there are several steps involved in using photolithography such as deposition of resist, patterning using a mask, and wet etching as shown in Figure 1.7. Alternate to lithography, another fabrication process usually used in MEMS is a technique called micromachining as shown in Figure 1.8 (surface micromachining). Both these techniques have a number of limitations such as the requirement of skilled labor for achieving precision and repeatability, a longer time is required to fabricate devices, and requires a cleanroom environment. In addition, these processes are not compatible to fabricate the complete product as the enclosures are often manufactured separately.

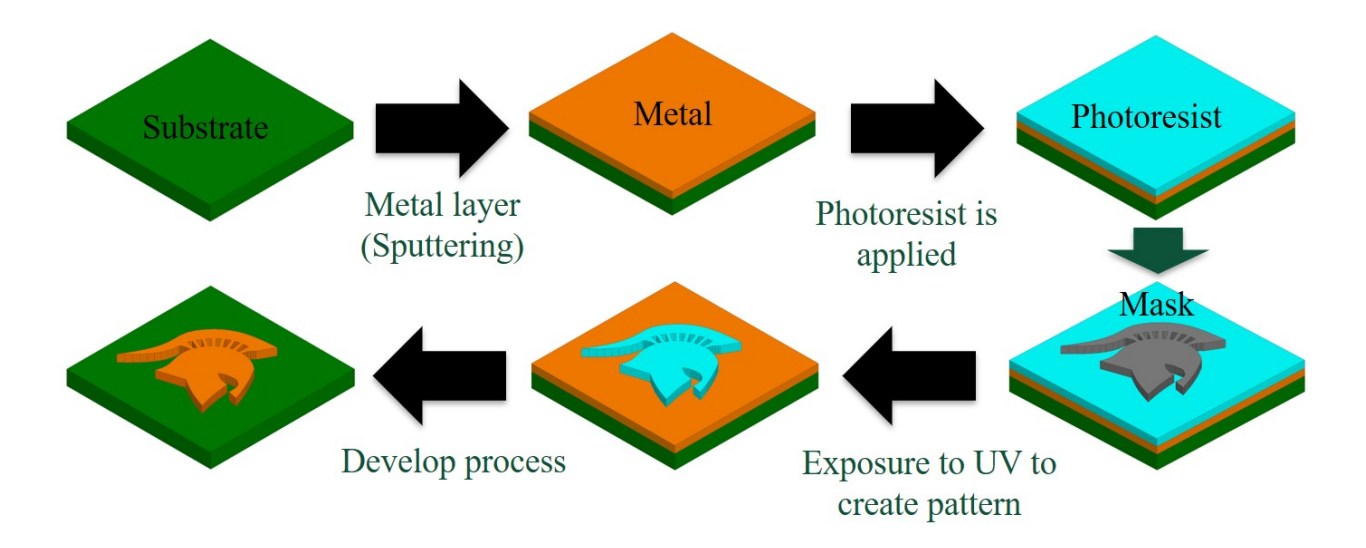


Figure 1.7: Illustration of photolithography process.

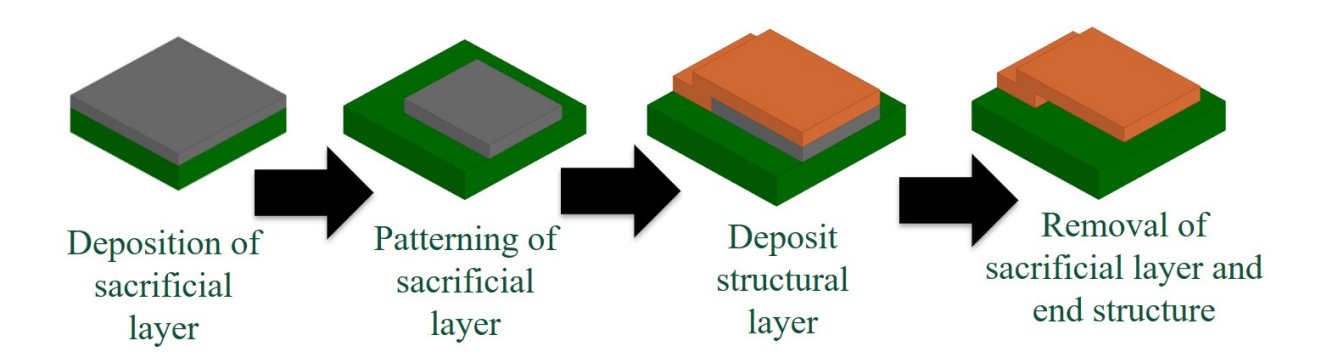


Figure 1.8: Illustration of surface micromachining process.

From the weight perspective, a number of materials have been synthesized to allow the components to achieve a lightweight feature. One of most popular material currently used in the light-weight devices is Graphene. The benefit of using graphene is due to its properties such as its strength, durability, and the lightweight aspect [14,15]. These properties allow easy integration of such material to enhance the performance and efficiency of the fabricated device. In addition to that, it can also be used as an enclosure or shielding from electromagnetic waves but a fundamental limitation of utilizing Graphene is the cost making it less affordable.

A few works exist in literature for designing multifunctional electronic devices that has the ability to incorporate multiple functionality into a single package. The conventional manufacturing technology requires the devices to be manufactured separately and assembled leading to a longer production time and consumes more space. The main goal of multifunctional devices is to provide a more affordable pricing, short manufacturing time, simplification in the manufacturing process (reduction in the number of steps), compactness, multiple functionalities, and higher efficiency. Such demand has made the electronic industry to adapt a modern technology called 3D integration.

3D integration is a process that allows layer by layer integration of active devices in a stacked manner in which the layers are connected using an interconnect [16]. 3D integration has the ability to minimize the workspace area by stacking the components using vias in the z-axis direction (vertical). Tremendous research has been carried out advancing 3D integration such as 3D packaging technology, monolithic 3D integrated circuits, and wafer to wafer circuit integration. Although this technology provides a solution for multifunctional compact devices, it is limited by the accuracy in the alignment process, the complexity in the design, as well as the overall cost of manufacturing.

As an alternative, the electronic industry has geared the manufacturing process towards AM as it simplifies the fabrication process, allows rapid prototyping, and provides the ability to print multiple materials at a lower temperature on a host substrate. It also allows printing the enclosures or shields for the different circuitry directly in various shapes and sizes depending on the needs of the consumer. Another advantage of AM is for integrating circuits designs onto packaging components such as a substrate or any form of surface that can be easily printed on. This allows additive manufacturing as an alternative method where the structure can be printed directly on the circuit board or other suitable substrates

as illustrated in Figure 1.9 [17].

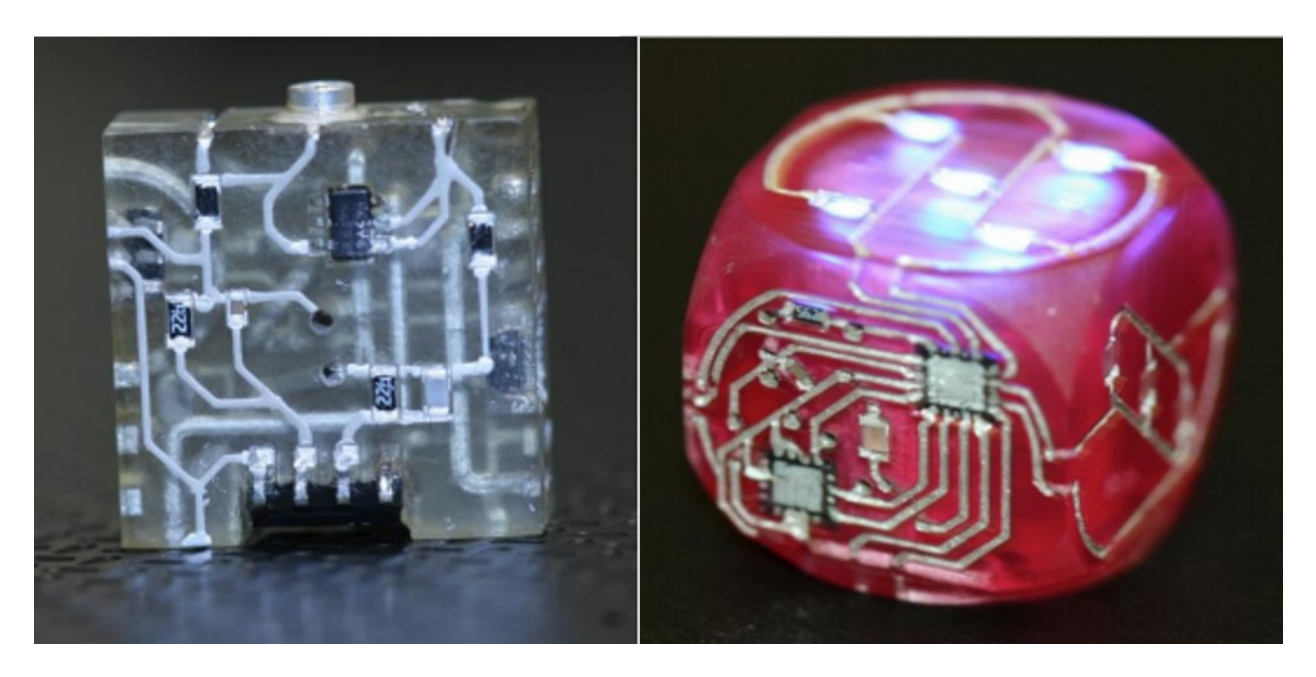


Figure 1.9: 3D printed signal conditioning circuit and Electronic circuit mechanically designed into substrate [17].

In this dissertation, AM is adopted as an alternative method to replace conventional fabrication processes (lithography and micromachining) for manufacturing RF components such as transmission lines, resonators, power dividers, waveguides, and antennas. AM have several approaches such as Vat Photopolymerization, Material Jetting, Binder Jetting, Material Extrusion, Powder Bed Fusion, Directed Energy Deposition, and Sheet Lamination [18–22] as shown in Figure 1.10. In this dissertation, the focus is on using two different AM processes, (i) Photopolymer Jetting (which fall in to the categories of Material Jetting [23], and (ii) stereolithography (SLA) which belong to the family of vat photopolymerization [24] for manufacturing different RF and microwave components.

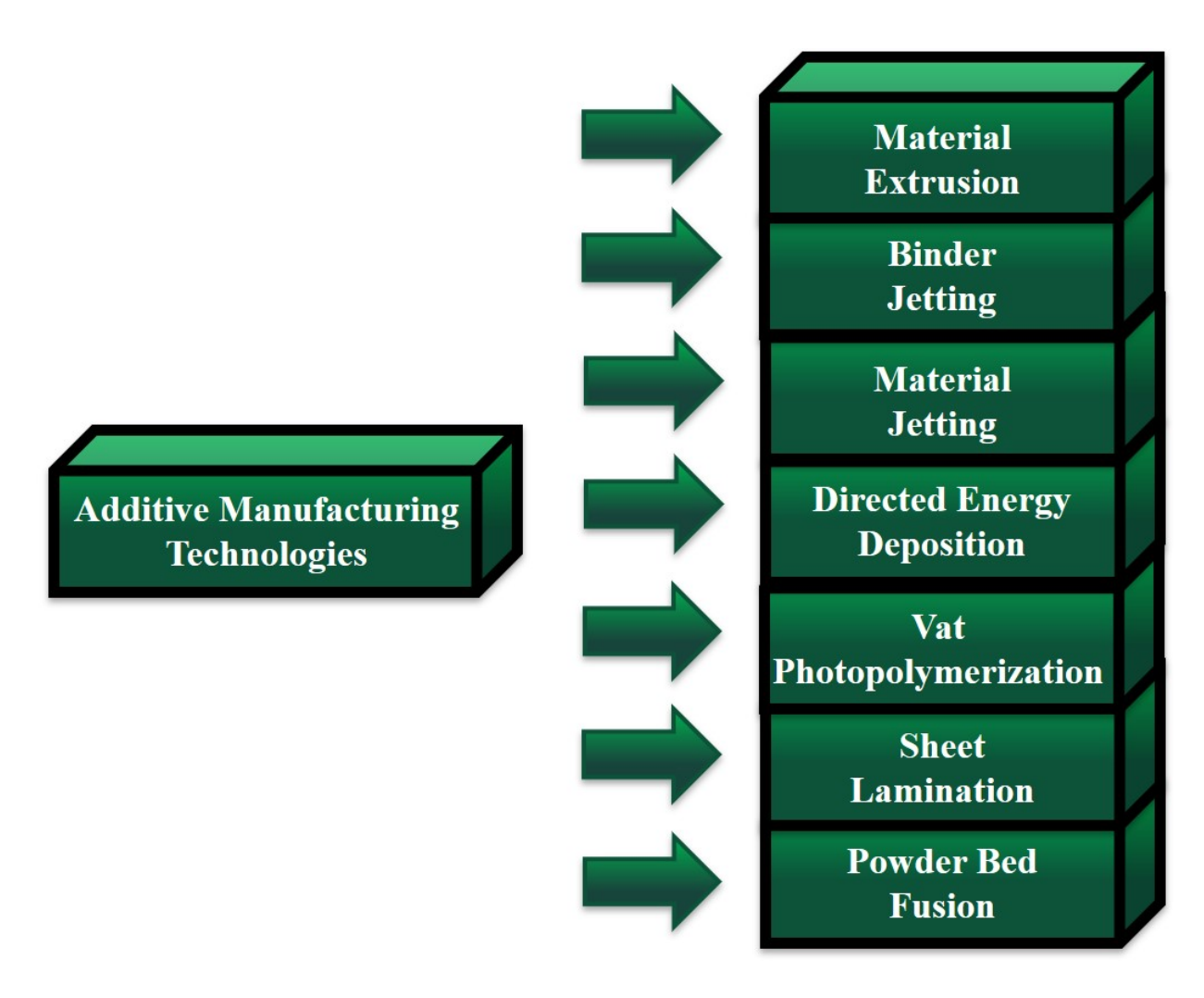


Figure 1.10: Seven categories of Additive Manufacturing (Standard Terminology for Additive Manufacturing Technologies F92792-12a).

Photopolymer jetting is also known as polyjet and multijet modeling. In Figure 1.11, shows the schematic of the overall printer for the photopolymer jetting process that uses an inkjet printhead containing a material (liquid photopolymer) for printing and is located above the build platform. The material is deposited onto the surface of the build platform followed by curing using the ultraviolet (UV) curing lamp which solidifies the liquid. This allows the material to be printed layer by layer to form a 3D structure. The supporting material, on the other hand, allows a steady support during the printing process and can be removed after the 3D structure is completed. The advantage of photopolymer jetting is that it can create a very precise model of the 3D structure as well as give a smooth layer on the surface. This is very beneficial towards fabricating RF components that require the surface to be smooth in order for the metal to adhere onto the structure.

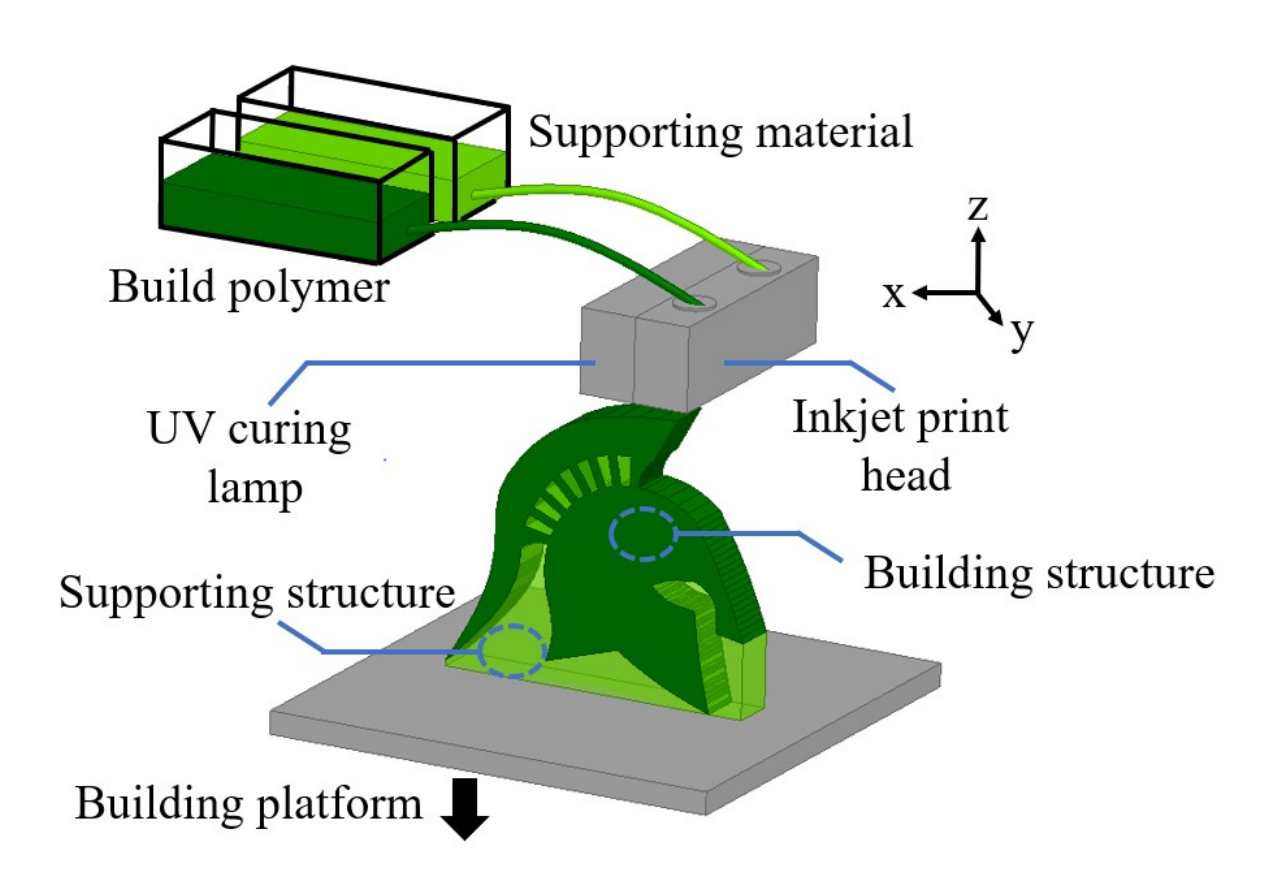


Figure 1.11: The schematic of photopolymer jetting 3D printer.

SLA is the other additive manufacturing process whose schematic is illustrated in Figure 1.12. In this printer, the build platform is immersed in a tank (transparent) which is filled with photosensitive resin. The movable UV laser beam (X-Y direction) selectively cures the photosensitive resin into a solid form. After each layer of curing, sweeper blade sweeps across the tank to create a smooth flat surface for the next resin layer. The build platform moves in the z-axis direction and the process is repeats until the desired 3D structure is completed. Finally, the finished 3D structure hangs upside down on the build platform so that the excess uncured resin drips back into the tank.

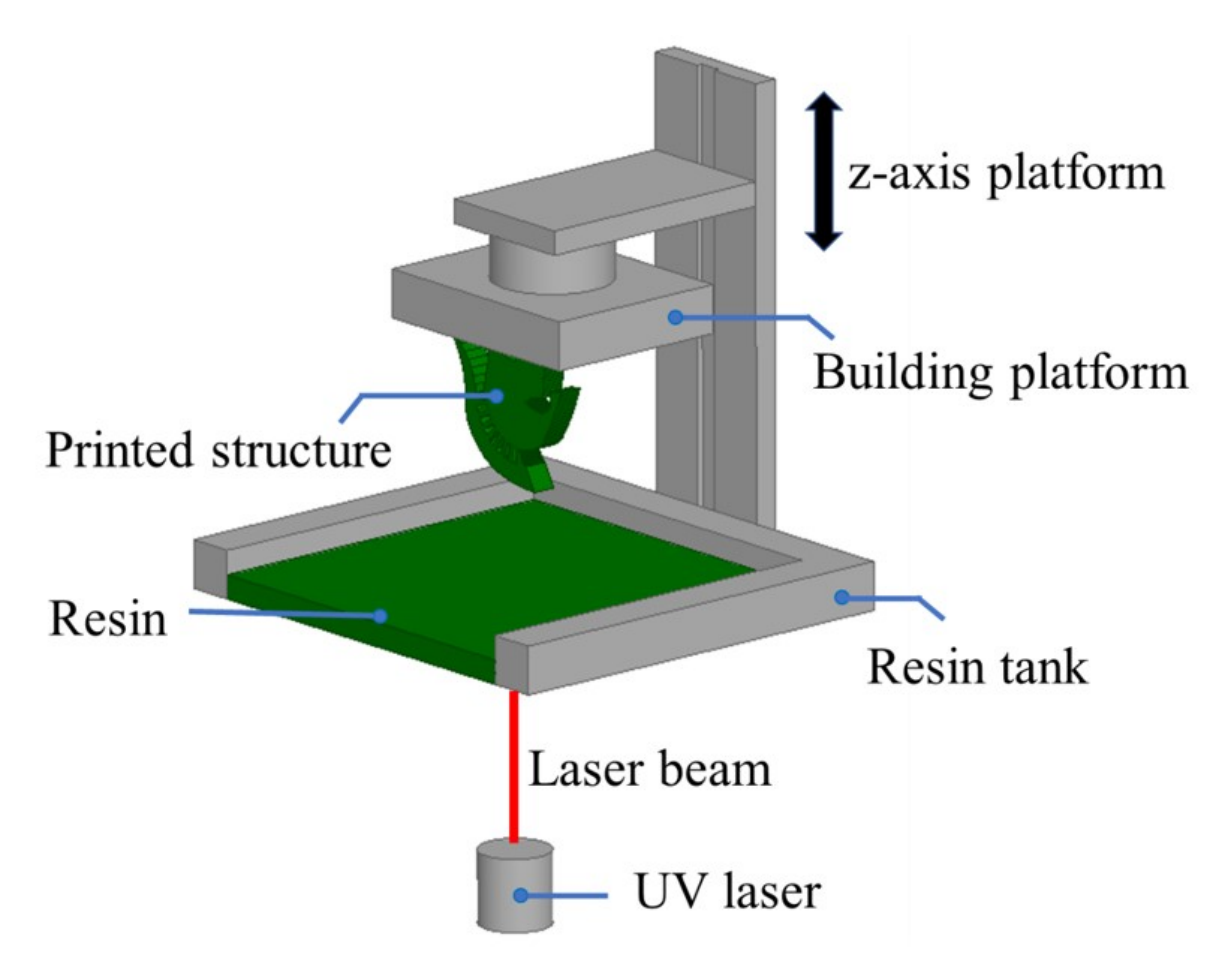


Figure 1.12: The schematic of SLA systems.

AM provides a clear advantage in term of manufacturing electronics due to the capability of printing non-flat or no-planar structures, allowing the structure to be printed in a 3D form in comparison to conventional manufacturing, which are usually in 2D form. Furthermore, mass customization can be achieved where individual needs of consumer can be catered to. Additionally, compared to the conventional manufacturing techniques such as subtractive or formative methods, AM generates lesser wastage in term of materials as well as energy consumption. AM also aids in avoiding hazardous wet etching chemicals during the manufacturing process. However, it still requires the use of isopropyl alcohol (IPA) in order to clean the supporting structure. One of the key advantages of AM is that structures can be printed in several pieces which simplifies the assembly process and avoids misalignment during the final assembly.

The goal of this dissertation is to advance the AM technology to fabricate a complete electronic system as shown in Figure 6.1. The envisioned system consists of a number of integrated RF and microwave components such as antennas, interconnects, MEMS based chips, shielding caps, flip chips, active and passive elements, etc. The ability of the 3D printer to print conductive and dielectric inks are used to realize a fully printed system. A number of new processes towards achieving the envisoned system is developed in this dissertation work such as selective metal patterning, embedding process for actives and passives, LEGO-like assembly of non-planar components with reduced form factor, and using loss less air as a substrate. The next section will summarize chapter by chapter contribution for the advancement of AM in fabricating RF and microwave components and systems.

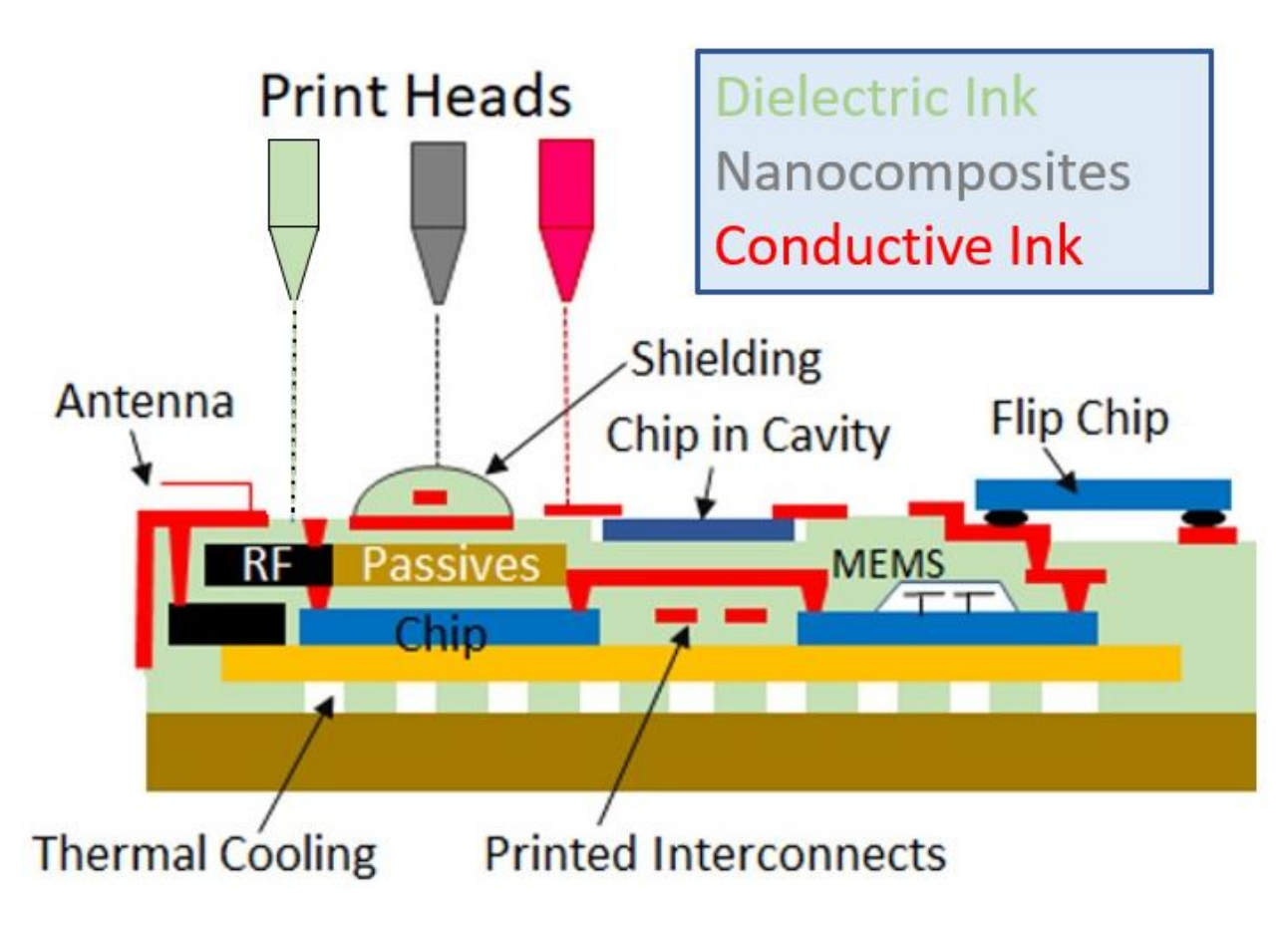


Figure 1.13: Envisioned fully 3D printed RF systems.

1.2 Summary of Dissertation Contributions

The main contributions of this dissertation are summarized below.

In Chapter 2, two different metal patterning process using AM were developed. To meet the challenge of patterning the conductive layers on a complex or a non-planar printed structures, two novel self-aligning patterning processes are demonstrated. First is a damascene-like mechanical polishing process, and the second is a lift-off process using a 3D printed lift-off mask layer. RF circuits such as microstrip transmission line, t-line resonator, circular ring resonator, and a patch antenna are designed and demonstrated. The developed processes allows the possibility of metal patterning on the plastic substrate similar to that of a conventional photolithography.

In Chapter 3, the advantage of AM to control printing along the third dimension (z-axis) is exploited to demonstrate non-planar RF structures with complex geometries. Various out-of-plane microwave structures such as transmission line, resonator, vertical mount microstrip patch antenna, elevated patch antenna, air-lifted antenna, and monopole based antenna are demonstrated. These antennas can be integrated directly on packaged chips or mounted vertically on high density electrical boards.

In Chapter 4, a LEGO-like assembly process is developed to allow air as a substrate material in order to limit loss of performance due to substrate losses. The air substrate is realized by printing the RF structures in two separate pieces and snapped together in a face to face manner using a LEGO-like process. Various RF structures such as low dispersion transmission line, T-line resonator, high-gain patch antenna, slot antenna, and cavity resonator are demonstrated.

In Chapter 5, fully 3D printed waveguides are realized using the LEGO-like assembly

process. The waveguide subsections are printed seperately and assembled using a LEGO-like process is after coating with metal. Complex geometry structure such as filters, slotted waveguide (leaky wave antenna), and multi-layer structure cavity-backed slotted array antenna are demonstrated. This process allowed manufacturing light weight waveguides for microwave applications.

In Chapter 6, three new AM approaches for embedding passive and active components for high-density RF packaging are developed. The approaches are: (i) face-up, (ii) face-down, and (iii) side-mount. The printer is stopped at pre-defined steps to embed the active components and the electrical connection is established by fabricating vias. An embedded diode based tunable t-line resonator, metamaterial-inspired tunable phase shifter, and a tunable patch antenna is demonstrated. This technique provides a heterogeneous integration with low parasitics associated at the interconnections.

In Chapter 7, two fully 3D printed harmonic RF systems utilizing the key features develop in the previous chapters is presented. The first system consists of two transceiver 3D printed Vivaldi antennas assembled together using the LEGO-like technique and a harmonic sensor tag. The sensor tag utilizes damascene-like mechanical polishing for metal patterning and a face-up embedding process for embedding the diode. The system is demonstrated as markers for buried pipe detection. The second system consists of an amplifier integrated with an air substrate based patch antenna using damascene-like metal patterning and LEGO-like assembly for demonstrating a RF front end system for compact 5G communication applications.

Chapter 2

Selective patterning process

2.1 Introduction

Increasingly, additive manufacturing (AM) is being explored as a means to simplify and decrease the cost of manufacturing electrical circuits and systems [17, 25, 26]. The cost of 3D printers and the materials used in them are continuing to decrease as the technology gains in popularity and utility. The possibility of avoiding complex machining or cleanroom fabrication is especially appealing to those working with radio frequency (RF) circuits and systems.

For realizing a RF circuit, pattering of conductive traces is necessary on the 3D printed substrate. In literature, much work has been done to explore AM techniques to produce 2D antenna structures by using conductive inks on paper [27, 28] and dielectrics [29, 30]. Unfortunately, there are limitations for the conductive inks commonly used, as silver-based conductive inks have a resistance roughly five to ten times greater than that of copper [31]. Silver paste also has a relatively poor conductivity and is therefore unsuitable for high-frequency applications. Also, silver paste is brittle, and cracks are formed over time, resulting in an increase in resistance. Additionally, much of the work demonstrating complex structures in general is done using silver-based inks and pastes for metallization, which is not well suited for high-frequency applications.

In this chapter, two novel metal pattering processes building upon AM for RF and mi-

crowave circuit applications incorporating metal patterning using copper on dielectric substrates is demonstrated. In the first proposed approach, a sacrificial shadow mask can be created similar to the work found in [32], where an SU-8 sacrificial mask is used for metal-lization of a polydimethylsiloxane surface. Here, a 3D printed sacrificial shadow mask layer is printed for direct metallization of the 3D printed dielectric substrate. After metallization, the mask layer is simply lifted off, leaving only the patterned area on the substrate.

In the second approach, a damascene-like process is proposed, where a trench or via is filled with copper, or some other metal similar to [33]. The process is realized for AM by 3D printing the designs slightly indented into its substrate, blanket metalizing the entire top, and then mechanically removing the copper from the raised layer. This leaves behind only the desired patterned structure. Unlike traditional damascene processing, the entire trench is not filled with copper; only a thin layer of copper is present in the trench floor and walls.

This chapter evaluates two different metal patterning processes for 3D printed RF circuits, the lift-off process and the damascene-like process for patterning copper. Using these techniques, traditional as well as geometrically complex RF passive circuits are demonstrated.

2.2 Fabrication

Two metal patterning processes are explored: a damascene-like process whereby the material outside of the trench region is mechanically removed, and a lift-off process with in situ deposition of a lift-off layer is done using 3D printing. The outline of both processes to fabricate a microstrip can be seen in Figure 2.1 and 2.2, where the damascene-like process and the lift-off process, respectively. As can be seen in the process outline, the processes are nearly identical. The key difference between them is the mechanism in which the excess metal from the metallization step is removed and how that final excess removal is accounted for in the initial design of the 3D printed structure.

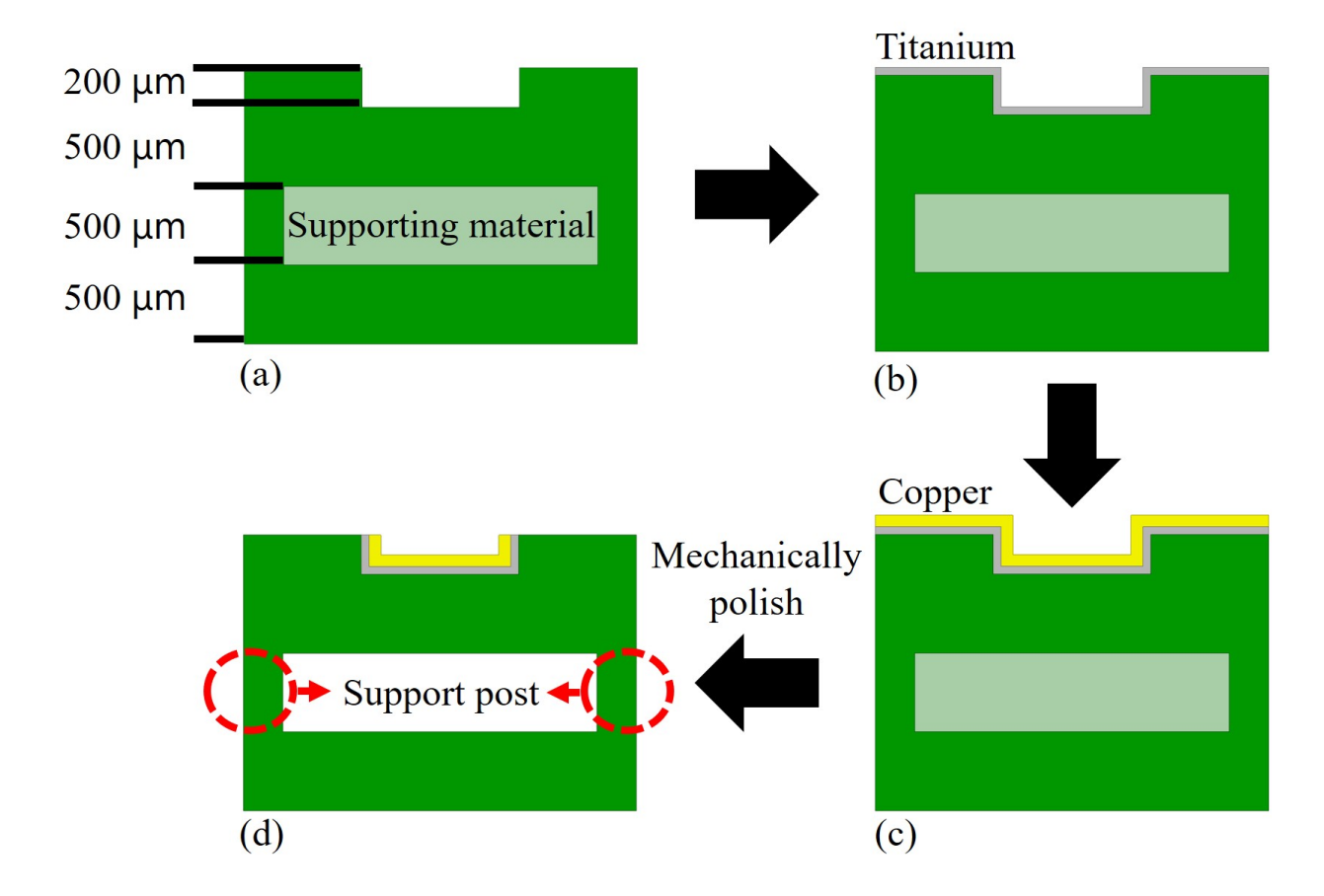


Figure 2.1: Process flow diagram illustrating the fabrication of a microstrip using the damascene-like process. (a) 3D printed structure, (b) Sputter 60 nm Titanium, (c) Sputter 0.5 μ m Copper and (d) removal of the supporting material.

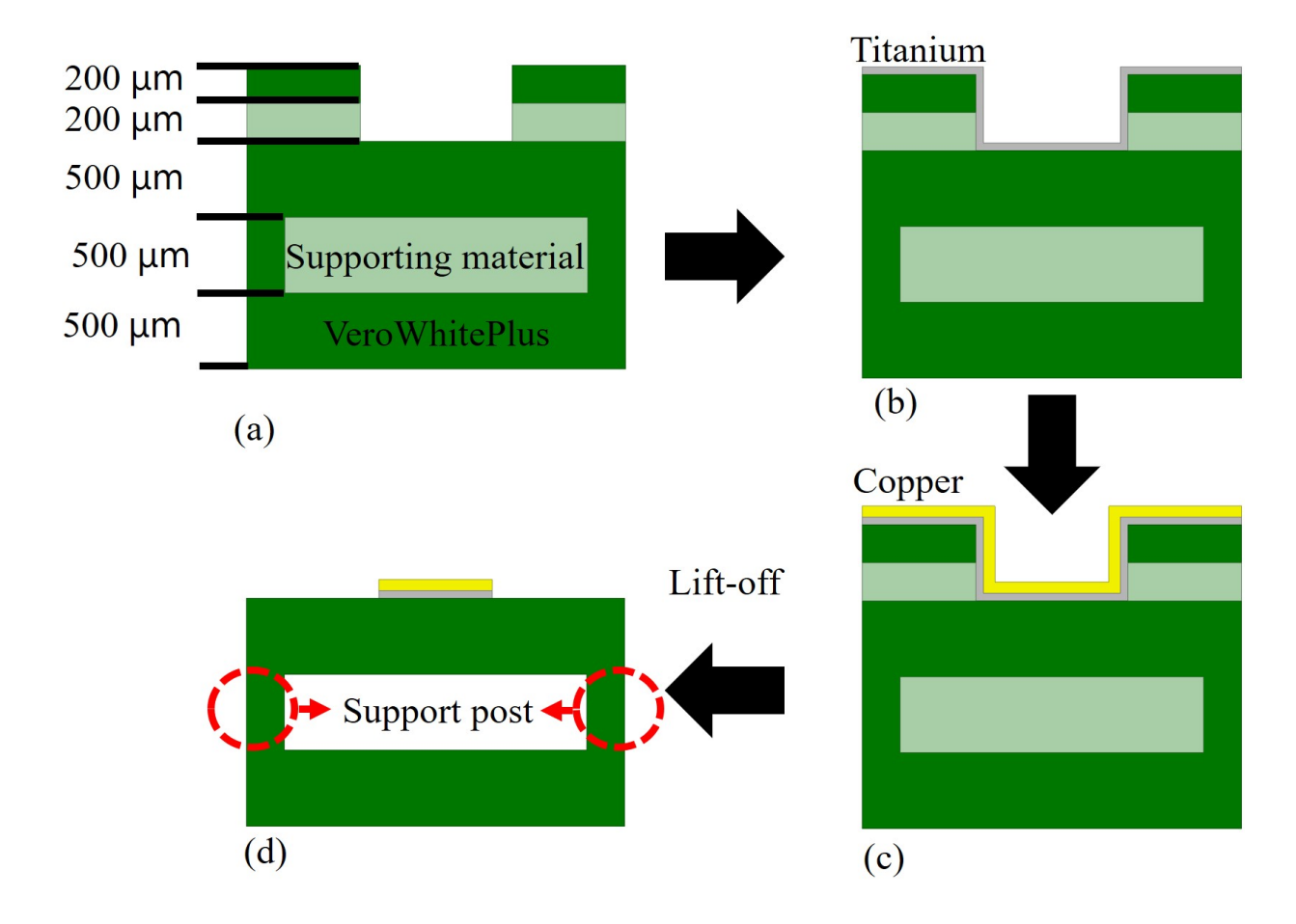


Figure 2.2: Process flow diagram illustrating the fabrication of a microstrip using in situ lift-off process. (a) 3D printed structure, (b) Sputter 60 nm Titanium, (c) Sputter 0.5 μ m Copper and (d) removal of the supporting material.

2.2.1 Damascene-like Process

The step-by-step illustration of the damascene-like process, to fabricate a microstrip with an air gap substrate is shown on in Figure 2.1. To create the trenched areas where metallization is desired, and account for the later need to mechanically remove excess copper, additional substrate material is added in the areas that are not to be patterned. This substrate height difference between where copper is desired and undesired allows for easy removal of the undesired copper by a chemical or mechanical process such as polishing using a fine-grit sandpaper. For this process, an additional substrate height of 200 μ m was used that protrudes on the side of the patterned metallization region.

After printing the substrate for the desired structure, with the additional substrate height where metal patterning is not desired, the entire structure is metalized using a Denton Vacuum Desktop Pro sputtering system. A 60 nm thick layer of Titanium (Ti) is deposited, which promotes adhesion between the dielectric material and the copper. Then, a 0.5 μ m layer of copper (Cu) is deposited.

After metallization, the unwanted copper is removed using mechanical polishing. Although a mechanical process was used here to remove the excess copper, a chemical process could also be employed. In the next step, the support material in the air gap layer is removed to create the final structure. Support material can be reliably removed by hand by either mechanically pushing it out with a thin pick or scraper or using pressurized water spray and can be further cleaned using a solution of $2\% \sim 3\%$ sodium hydroxide to soften the support material followed by an ultrasonic bath. In Figure 2.3, a close-up cross-sectional photograph of a cleaned sample is shown. A sample structure through this process can be seen in Figure 2.4, where a transmission line (T-line) resonator is shown directly after 3D

printing, metallization, and the mechanical removal of excess copper.

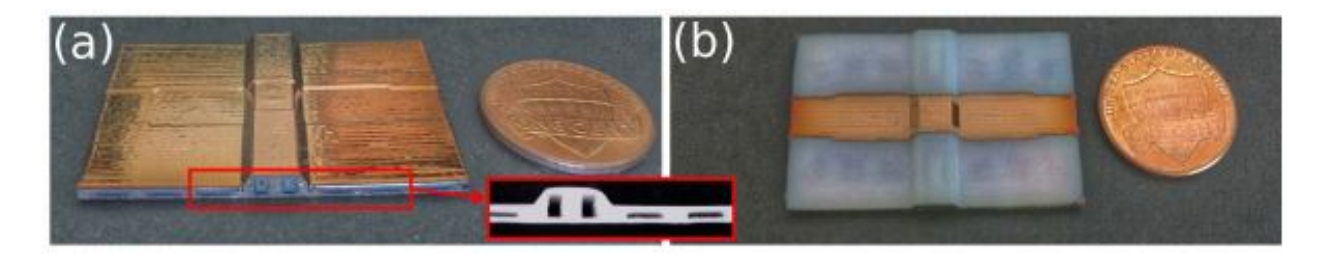


Figure 2.3: The cross-sectional image of a cleaned sample.



Figure 2.4: Sample structure after (a) 3D printing, (b) metallization, and (c) mechanical removal of the excess copper through the damascene-like process.

2.2.2 In Situ Lift-off Process

In addition to the damascene-like process, an in situ lift-off process for patterning metal to a 3D printed substrate is proposed. The step-by-step illustration of the in situ lift-off process, to fabricate a microstrip with an air gap substrate, is shown on in Figure 2.2. During the creation of the file representing the structure geometry to be sent to the 3D printer, a thin layer of VeroWhitePlus, a commercially available material from Stratasys, is added just above the substrate for the design. For the process used here, a 200 μ m-thick layer of VeroWhitePlus was added 200 μ m above the substrate. This added layer, similar to the damascene-like process, is only added where metallization is not desired. The added layer acts as a lift-off mask where, after metallization, the excess metal is removed by simply lifting the mask layer off the substrate as can be seen in Figure 2.5.

Similar to the damascene-like process, this approach includes printing of the initial structure, followed by sputtering a thin layer of Ti for adhesion with the following layer of Cu, and finally the desired metal patterning is realized by lifting off the in-situ mask layer. This lift-off process eliminates the need for alignment of the mask layer since the mask layer is deposited directly and in-situ. The layer is held in place by the thin layer of deposited support material, which is readily removed by chemical or mechanical cleaning.



Figure 2.5: In situ lift-off process is shown where a sacrificial layer is removed.

2.3 Process Demonstration

To demonstrate the capabilities of the damascene-like and in situ lift-off processes, various sample structures were designed, simulated, fabricated, and measured. All the designs are microstrip-based, including a microstrip line, resonators, patch antenna, and a cavity.

All designs were fabricated using both the damascene-like and in situ lift-off processes. The difference in performance of the devices made using both processes was negligible, and therefore only one set of measured results is shown for each device. The devices are coupled into using standard edge-mount SMA connectors that were adhered using silver paste. Silver paste was also used to provide a seal for the cavity around where the cavity bottom meets the lid on the top.

Measurements for the reflection and transmission coefficients were done using an Agilent N5227A PNA network analyzer, and the radiation pattern for the patch antenna was measured using a SATIMO StarLab near-field measurement system. The PNA was calibrated using a standard 3.5 mm calibration kit, and the StarLab with a manufacturer provided calibration horn antenna.

2.3.1 Microstrip Transmission Line

Microstrip lines are one of the most common types of interconnect for integrated circuit designs. To provide the most straightforward demonstration of the proposed process, a 10 mm-long 50 Ω line was fabricated, and its reflection and transmission coefficients were measured. As can be seen in Figure 2.6, low reflection and high transmission was observed in both the simulated and measured data. Simulation results for a 50 Ω line on a 1.5 mm substrate only composed of VeroWhitePlus were also included to show that reflection and

transmission coefficient performance is similar when the air gap substrate is not used.

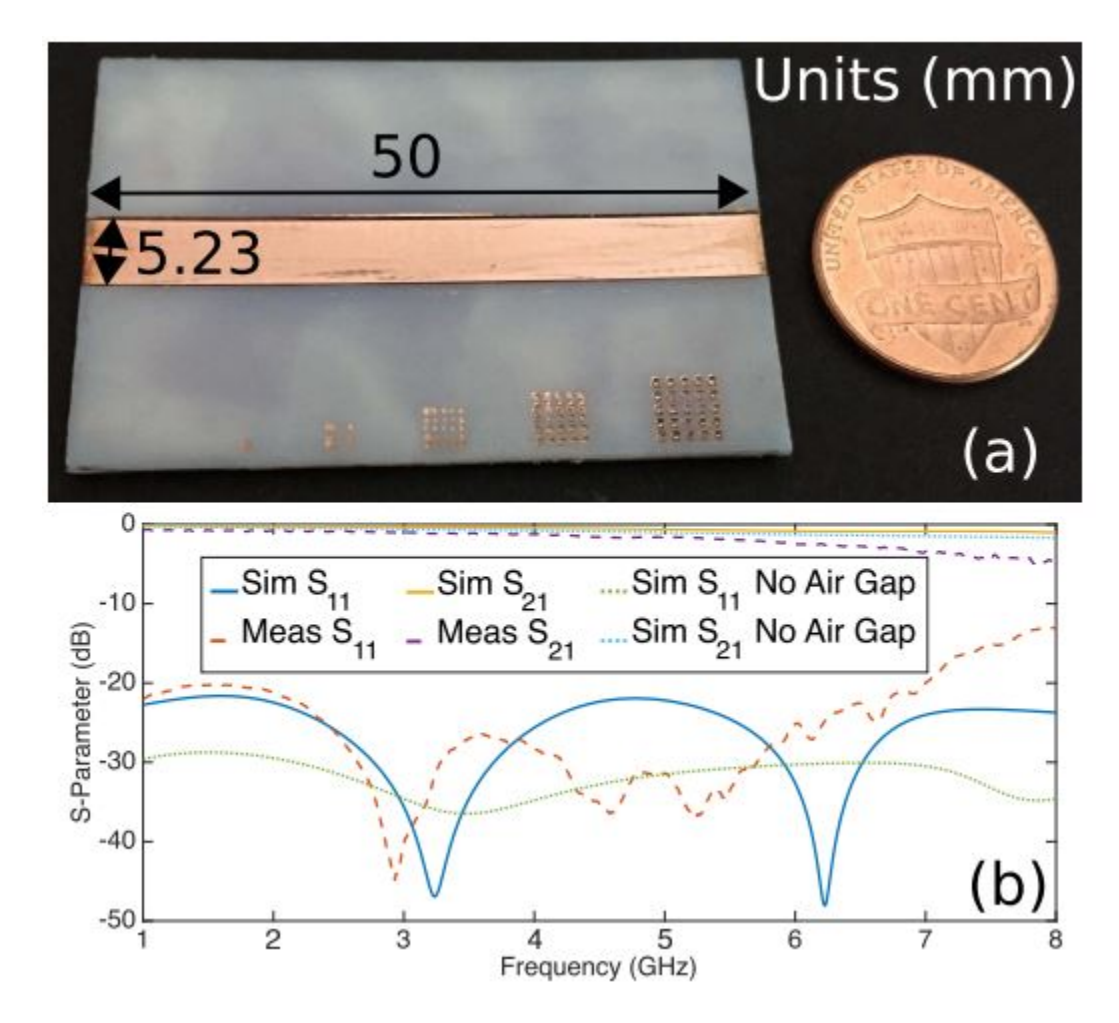


Figure 2.6: Microstrip T-line. (a) Final fabricated sample with dimensions and (b) Simulated and measured results.

2.3.2 T-Line and Circular Ring Resonator

Resonators are commonly used microwave elements in many active and passive circuits, such as filters, oscillators, amplifiers, and antennas. Resonator-based substrate characterization methods are most commonly employed to evaluate fabrication processes. The resonance frequency can be used to extract the dielectric properties of the substrate, and the Q-factor can be used to extract the loss tangent [34,35]. In this section, a few examples of resonators fabricated using the in-situ lift-off process are analyzed for their performance.

The microstrip-based T-line resonator is designed using an open circuited stub. The Q-factor of this T-line resonator is very low when compared to the circular or cavity resonator. This structure is chosen to demonstrate the fabrication of low-Q resonators using the lift-off technique. Figure 2.7, shows the schematic and dimensions of the simulated T-line resonator, the image of the fabricated T-line resonator, and the simulated and measured results. Overall good agreement is shown between simulation and measurement results.

Circular ring resonators are commonly used in the design of metamaterial-based circuits. To enhance the Q-factor, the circular ring resonator is designed to be edge coupled to the feeding microstrip line. The ring has a diameter of one wavelength, which determines the resonance frequency of the ring. The Q-factor of the ring resonator is tailored by changing the capacitive gap between the ring and the microstrip feed line. The structure is also fabricated using the lift-off process. Figure 2.8 shows the schematic and dimensions of the circular ring resonator, the image of the fabricated circular resonator, and the simulated and measured results. Overall, the simulation and measurement results agree on the resonators performance.

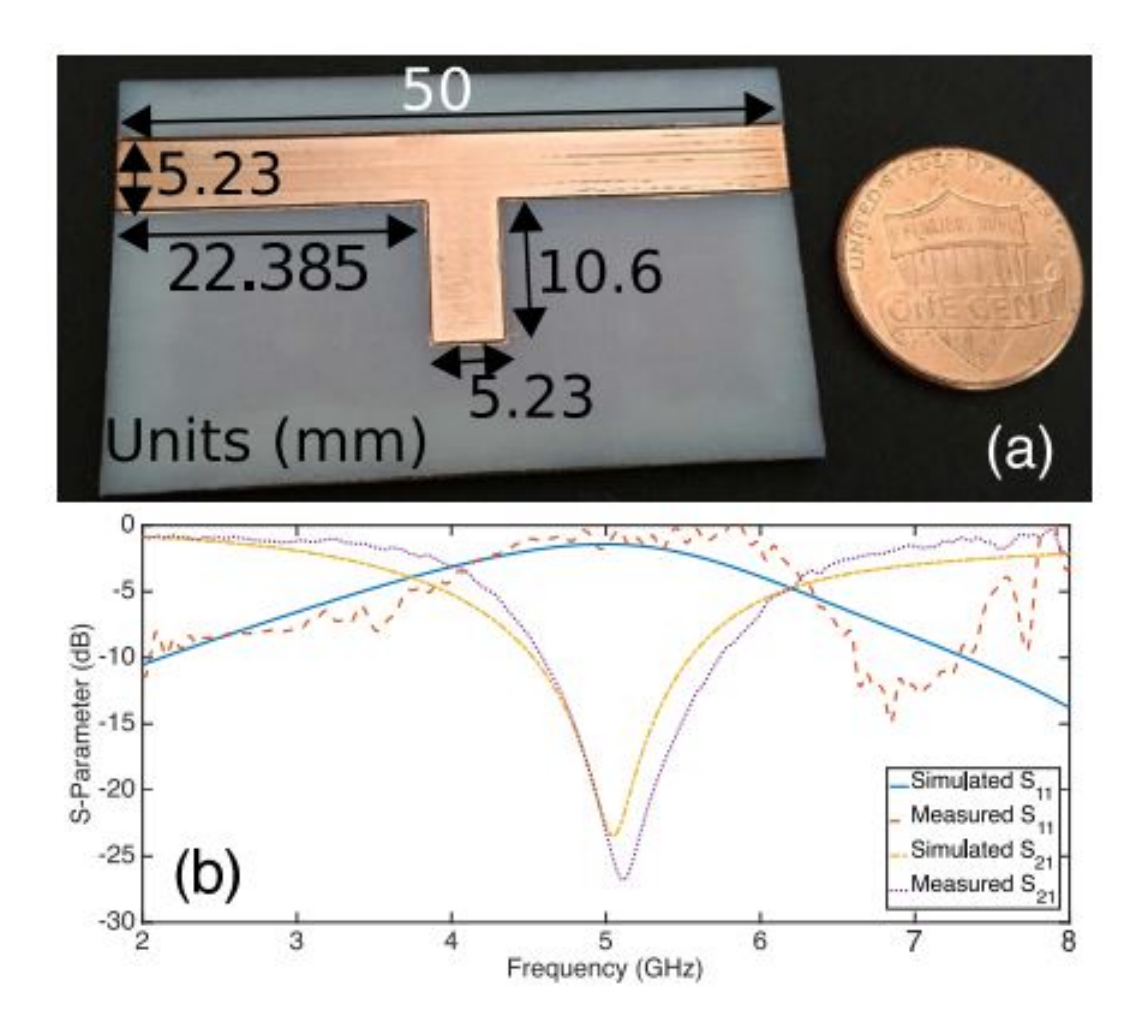


Figure 2.7: T-line resonator. (a) Final fabricated sample with dimensions, and (b) Simulated and measured results.

The circular ring resonator can also be used to extract the effective permittivity of the air gap substrate. Using the method from [34], which is outlined in the following, the permittivity of the proposed layered substrate was found to be 1.68. In the method used, c is the speed of light in a vacuum, and e_{eff} is a function of the ring radius, denoted by r_m , at the n^{th} resonant frequency, denoted by f_0 . Here, the first resonant frequency was used, which was observed at 3.03 GHz. The measured thickness of the substrate, h, was 1.25 mm, and the conductor thickness, t, was 0.5 μ m. Additionally, the strip width of the ring, ω , was 1.23 mm.

$$\omega_{eff} = \omega + \frac{1.25 \times t}{\pi} (1 + \ln(\frac{2h}{t})) \dots (1)$$

$$M = (1 + \frac{12 \times h}{\omega_{eff}})^{-0.5} \dots (2)$$

$$e_{eff} = (\frac{n \times c}{2\pi \times r_m \times f_0})^2 \dots (3)$$

$$e_r = \frac{2 \times e_{eff} + M - 1}{M + 1} \dots (4)$$

Using HFSS, the effective permittivity for air gap substrate at 3.03 GHz was found to be 1.75 using a $50-\Omega$ microstrip as the simulated model. This matches well with what was calculated from measurement. Additionally, the measured effective loss tangent can be estimated using the Q-factor by using the relationship that the loss tangent is the reciprocal of the Q-factor, the Q-factor being defined as the resonant frequency over the full width at half maximum. For this, the T-line resonator will be used instead of the circular ring

resonator as the circular ring resonator is strongly coupled and the wider bandwidth obscures the true loss tangent. Through simulation, the contributions from conductor and radiation losses can be estimated in order to calculate an estimate of only the dielectric loss tangent by simulating the same model and setting the dielectric loss tangent of VeroWhitePlus to zero. After removing the estimated contributions from conductor and radiation losses, the estimated dielectric loss tangent from the measured results is found to be 0.015. Using (1) for the substrate used in this chapter, one with 33% air, a dielectric loss tangent of 0.017

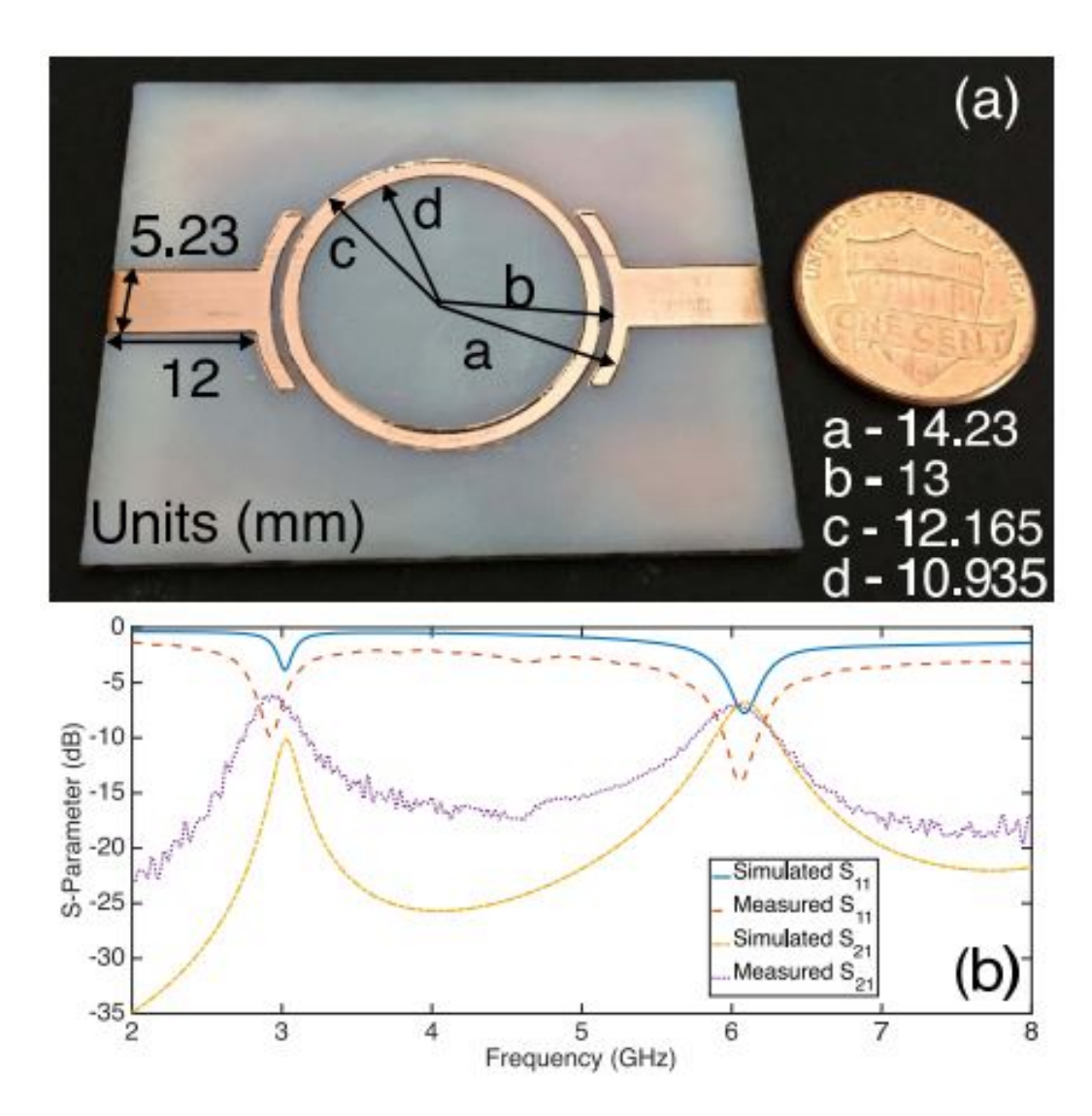


Figure 2.8: Circular ring resonator. (a) Final fabricated sample with dimensions, and (b) Simulated and measured results.

can be estimated, which matches well with the measured results. Although the amount of air in the substrate was limited due to practical reasons, it is indicated that a much lower effective loss tangent could be achieved if the amount of air in the substrate is increased.

2.3.3 Patch Antenna

The microstrip patch antenna has become one of the most used antennas in the field of communications. This is due to the simplicity in the design, light weight, low cost, low profile, and its ability to be easily integrated into different electronic devices. A simple rectangular patch antenna is designed, fabricated, and measured with an operational frequency near 4.72 GHz. The dimensions of the patch antenna, its final fabricated sample from the damascene-like process, and its simulated and measured results can be seen in Figure 2.9.

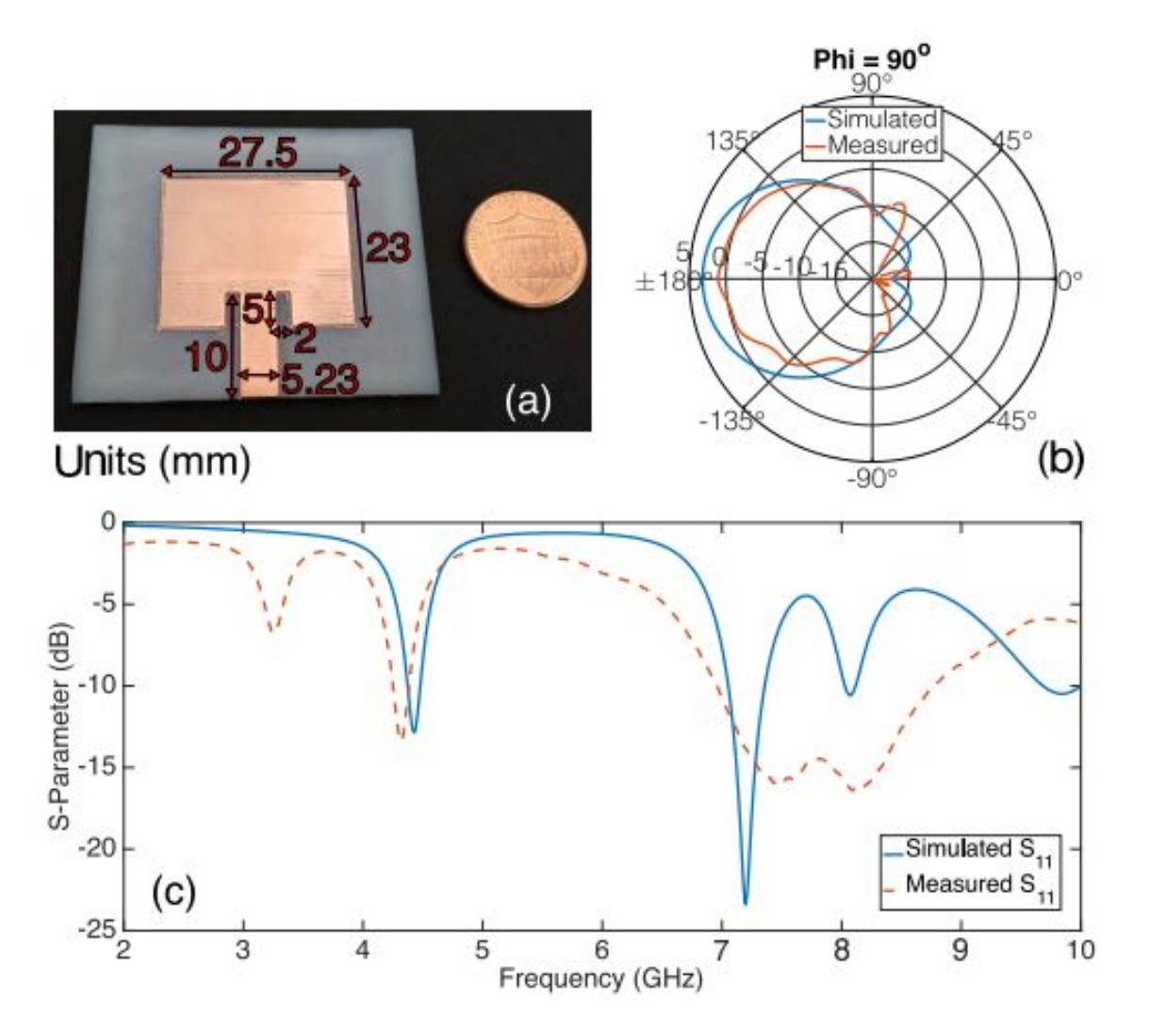


Figure 2.9: Patch antenna. (a) Final fabricated sample with dimensions and the simulated and measured results for the antennas, (b) Radiation pattern in the E-plane (dBi) and (c) Reflection coefficient.

The reflection coefficient matches well with the simulated result. The radiation patterns show a lower gain than expected by about 12 dB. As discussed in the previous section, around 12 dB can be attributed to surface roughness, although there were probably other factors contributing to the loss such as added resistance from the silver paste used for the connectors and a slightly thinner air gap than what was expected.

2.4 Discussion of Limitation and Possibilities

There are some limitations to the proposed processes when considering surface roughness, feature size limitations, minimum substrate thickness, and limitations regarding the support posts for the air gap substrate. The 3D printed structure inherently has 510 μ m of surface roughness depending on the final finish, which contributes to loss. Using this process and specific 3D printer, a minimum substrate thickness of 100 μ m was found due not to the minimum resolution of the printer, but to effects from mechanical handling of the parts. It was found that VeroWhitePlus layers of 0.5 mm in thickness were optimal for being thin while maintaining sufficient structural integrity to not bow or deform during the sputtering process. Finally, using this process, the support material is not perfectly removed and typically leaves behind around 50 μ m of residue. This does affect the effective dielectric constant, but is such a small percentage of the total substrate (around 4% for the designs presented here) that it has been considered negligible.

For the damascene-like process, the trench is not completely filled with metal, but rather is coated with a thin layer. To investigate any effects from this, HFSS was used to simulate a 50- Ω microstrip line on a 1.5 mm thick VeroWhitePlus substrate with the height of the additional sidewalls that create the trench varied. The sidewall height was simulated for values of 0 (no sidewall) to 300 μ m in 100 μ m increments. The metal was simulated as a finite conductivity boundary using copper as the material and a thickness of 0.5 μ m to realistically represent the devices made in this chapter.

In simulation, little to no difference was seen with respect to the reflection coefficient and the propagation loss or phase constant. Since the trench is not filled, the metalized sidewall acts as an extension of the microstrip line, thereby making it electrically wider and lowering the impedance. The results show that as the sidewall increases, it lowers the impedance. These results indicate that to reproduce designs accurately using the damascene-like process, this additional trace width should be accounted for by slightly shrinking the actual patterned designs.

There are fabrication possibilities present with this process that would be difficult, if not impossible, using traditional methods. One such example is of a non-planar microstrip, as seen in Figure 2.3. To create a non-planar substrate through methods like micromachining would be very difficult, and to pattern a non-planar substrate using traditional photolithography would be impossible. The proposed damascene-like and in-situ lift-off using 3D printing proposed here offer not just an alternative fabrication method, but a method to create structures that would otherwise be unrealizable. Using the proposed process, a raised microstrip such as the one shown could theoretically have no limit to the raised height. In reality, the height is limited by the capabilities of the 3D printer and metallization process used.

2.5 Conclusion

In this chapter, two metal patterning processes are demonstrated using 3D printing that allows patterning of metal layers on complex 3D structures, which would be difficult, if not impossible, using conventional lithography techniques. Sample devices including a microstrip, resonators, cavity, and patch antenna matched were designed, fabricated, metalized and measured with the results matching well with simulation.

Chapter 3

3D printed non-planar components

3.1 Introduction

In the previous chapter, two different metal patterning techniques were presented. In this chapter, utilizing the freedom on the third dimension (z-axis), 3D printing is employed for fabricating non-planar RF structures with smaller form factors. 3D printing has begun to play an important role, especially, in the development of custom packaging structures, components and interconnects. Increase in growth of small hand-held multifunctional wireless devices has limited the real estate available for system assembly. The need for high functional density in a small lattice space has been a motivation for researchers to provide an intelligent system in package (SiP) and system on package (SoP) solutions. These technologies integrate multiple electronics on the same and different layers in smaller lattice space. The evolution of integrated systems to 3D integrated systems with shrinking geometries and reduced footprint poses a significant challenge in multi-layer integration. The most common multi-level fabrication technique employs micromachining in which different levels are aligned using supporting structures [36,37]. The electrical continuity between different layers is established using interconnects or metal vias [38,39]. These multi-layer techniques are attractive since they offer a third degree of special freedom along the z-axis (out-of-plane), but have common limitations such as high misalignment error between the different layers, lower process compatibility between the layers and the support structures, complexity of vias or interconnects and thermal instability of the supporting structures [40,41].

3D printing is a boon for this technology as it reduces complexity in the integration of multilayers of electronics, in particular, high-gain antennas, such as patch or slot antennas which occupy a large area. The third degree of freedom along the vertical axis (z-axis) is particularly useful in confining structures within a small lattice space. The out-of-plane microwave structure is printed as a single piece eliminating the need for supports and hence reduces the errors due to misalignment. 3D printing also allows custom shaping of the fabricated components as per the needs of mounting an antenna in confined space. Figure 3.1 presents the application of 3D printing in designing a complex high-density packaging solution for a microwave system with an integrated out-of-plane patch antenna.

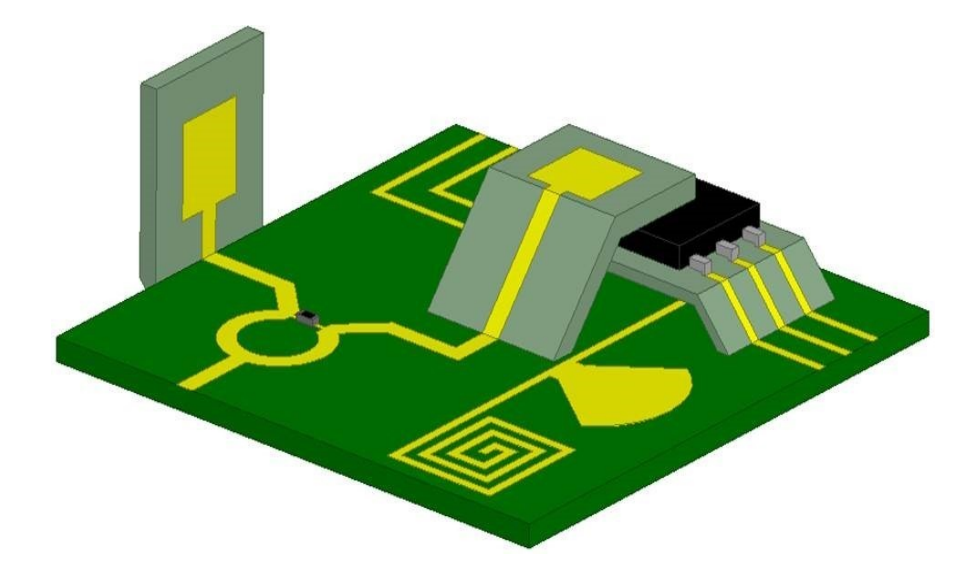


Figure 3.1: Packaging concept with 3D printed out-of-plane patch antenna

In this chapter, several out-of-plane microwave antennas are presented such as an elevated patch antenna (horizontal and vertical mount patch), air-gap patch antenna (regular patch and E-patch), monopole antenna (with and without a corner reflector) and Yagi-Uda antenna. A simple raised microstrip transmission line and a T-line resonator are also presented.

3.2 Design and Fabrication

All the devices are printed using a professional-grade commercially available 3D printer, an Object Connex350 utilizing the photopolymer resin VeroWhitePlus with dielectric constant ϵ_r of 2.8 and a loss tangent (tan δ) of 0.04 [42]. It uses a poly-jetting process for printing where the polymer is cured immediately by a UV lamp after being extruded at precise locations. The 3D printed plastic structures were metalized using sputtering followed by an electroplating process. All the designs and simulations presented in this chapter were performed using a commercial FEM solver, ANSYS HFSS[®].

The 3D printed structures were first cleaned using iso-propyl alcohol (IPA) and then cured under UV light, enabling smoother surface and better adhesion of the conductor layer to the plastic parts. The design of the structure is such that the regions where metal is required are trenched by 0.2 mm as shown in Figure 2.1. The added thickness of the non-metallized regions allows mechanically polishing off deposited blanket copper, similar to a simple damascene-like process [43]. Patterning of metal is a three-step process. First, a thin layer (60 nm) of titanium (Ti) followed by (500 nm) copper (Cu) is sputtered on the 3D printed structure. The Ti layer helps to enhance adhesion between Cu and the plastic. Second, a mechanical polishing process is used to remove the deposited copper from regions where metallization was not required. Finally, the sputtered metal layer is electroplated to approximately 5 μ m of Cu thickness.

3.3 Simulation and Measurement Results

3.3.1 Non-Planar Microstrip Line

Conventionally, microstrip lines are fabricated on a planar substrate. Non-planar microstrip lines are required for feeding out-of-plane antennas and hence presented first. The microstrip line has two bends, each with a bend angle of 45° . After metallization, standard SMA connectors are mounted on each side using conductive silver epoxy for probing. Figure 3.2 (a) shows the schematic of the non-planar microstrip line along with its dimensions. The fabricated microstrip line is shown in 3.2(b). The measured and simulated S-parameters are shown in Figure 3.3. It can be inferred from the graph that the measured and simulated result match closely and have lower transmission losses across 1-4 GHz. The measured data shows slightly higher transmission loss than simulated data beyond 4 GHz due to the higher resistance of the conductive silver epoxy ($\sim 0.0174~\Omega.\text{cm}$). Another possible contribution to the loss is surface roughness at the gradient sections.

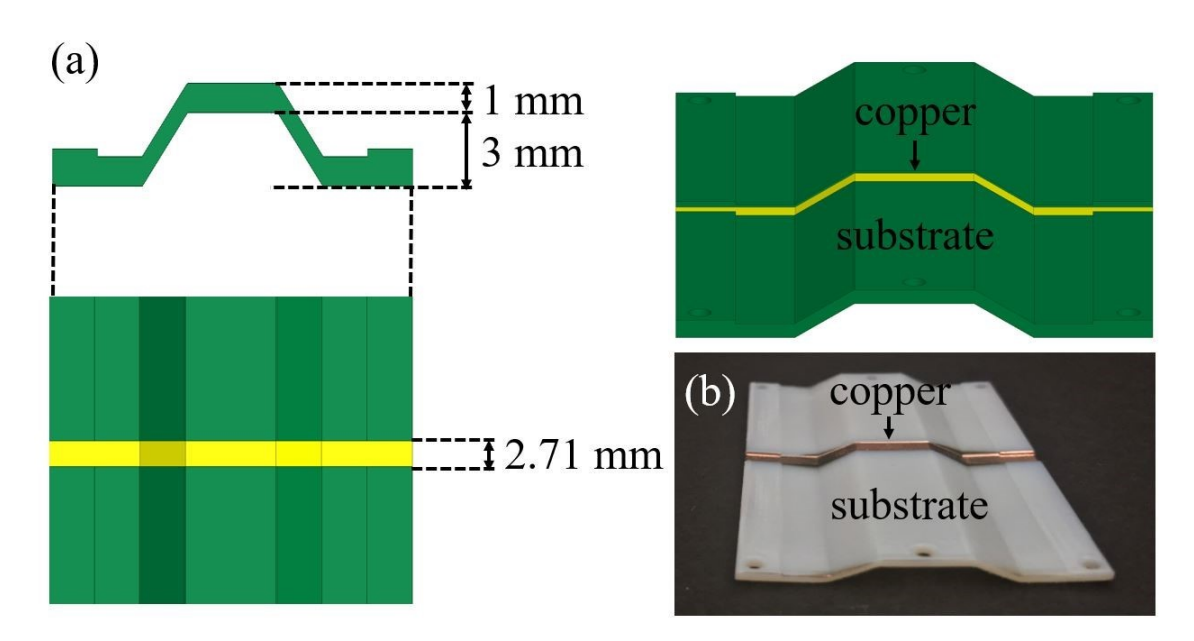


Figure 3.2: Non-planar microstrip transmission line: Schematic (top and side view) and fabricated structure.

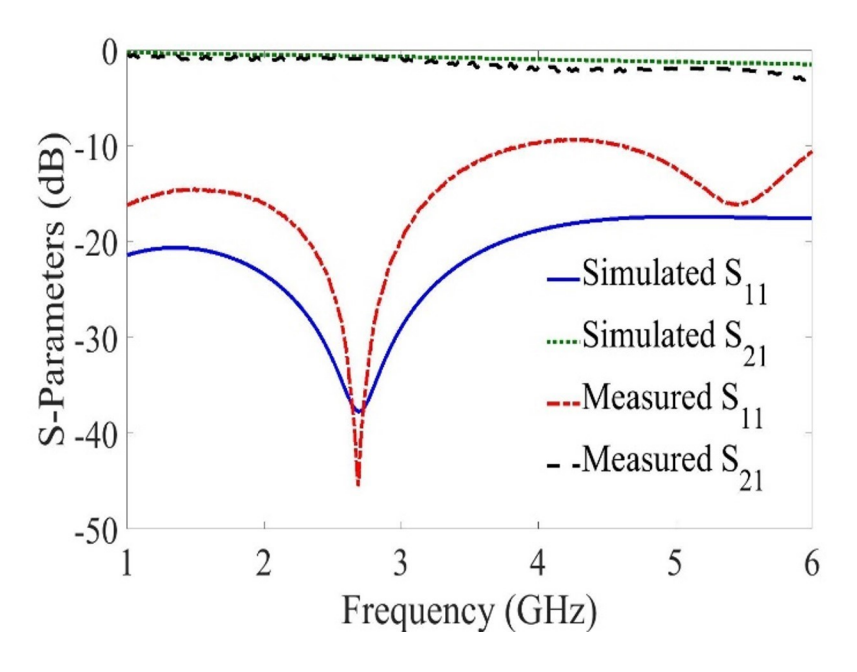


Figure 3.3: The simulated and measured reflection and transmission coefficient (S-parameters) of the non-planar microstrip line.

3.3.2 T-Line Resonator

Both planar and out-of-plane T-Line resonators are fabricated and characterized for performance comparison. The bend angle for the non-planar T-line is 45°. The T-line resonators are designed using an open circuited stub, and the dimensions used for both the T-lines are kept the same. Figure 3.4 (a) and (b) shows the dimensions and the image of the fabricated T-line resonator, planar and elevated, respectively. For these resonators, the simulated and measured results are in good agreement, see Figure 3.5 (a) and (b). The planar T-line resonator shows a resonance at 2.95 GHz with a maximum return loss of 29.5 dB and the out-of-plane design shows resonance at 2.92 GHz with a maximum return loss of 31 dB. It is clear from the results that the bend has a very minimal effect on the performance of the resonator over the measured frequency range.

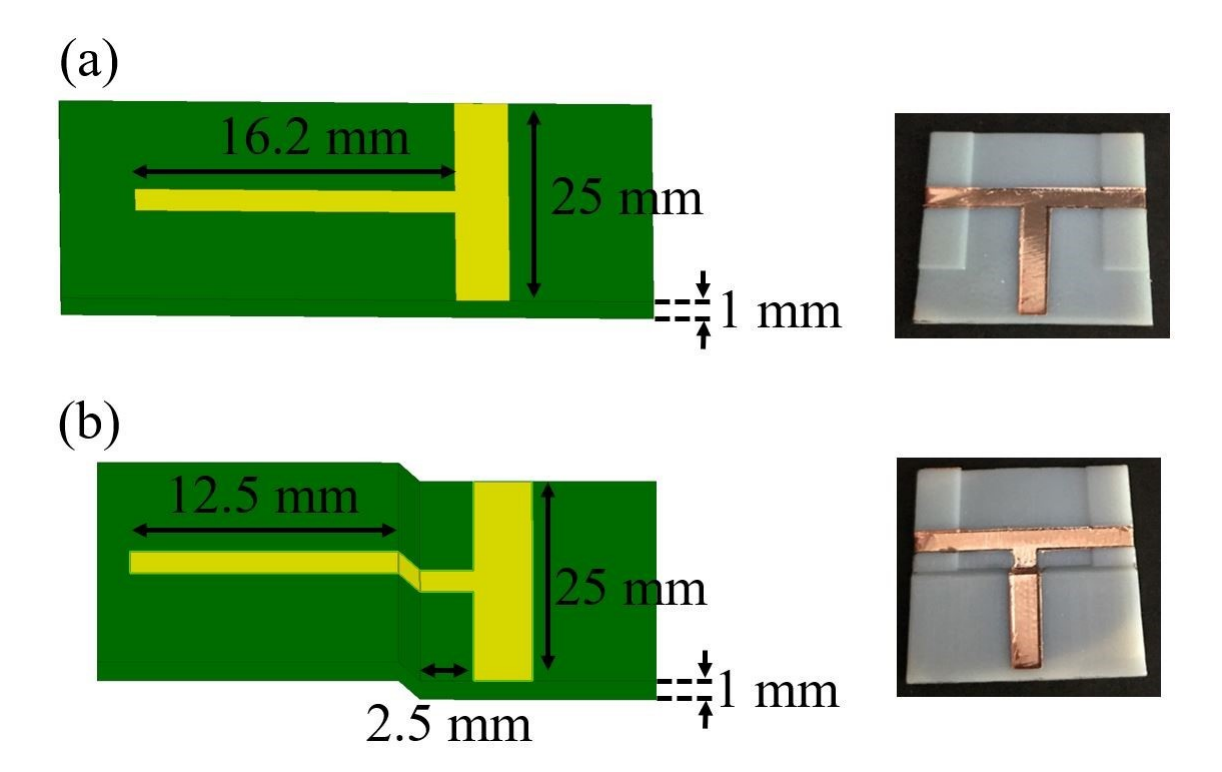


Figure 3.4: The simulated and measured reflection and transmission coefficient (S-parameters) of the non-planar microstrip line.

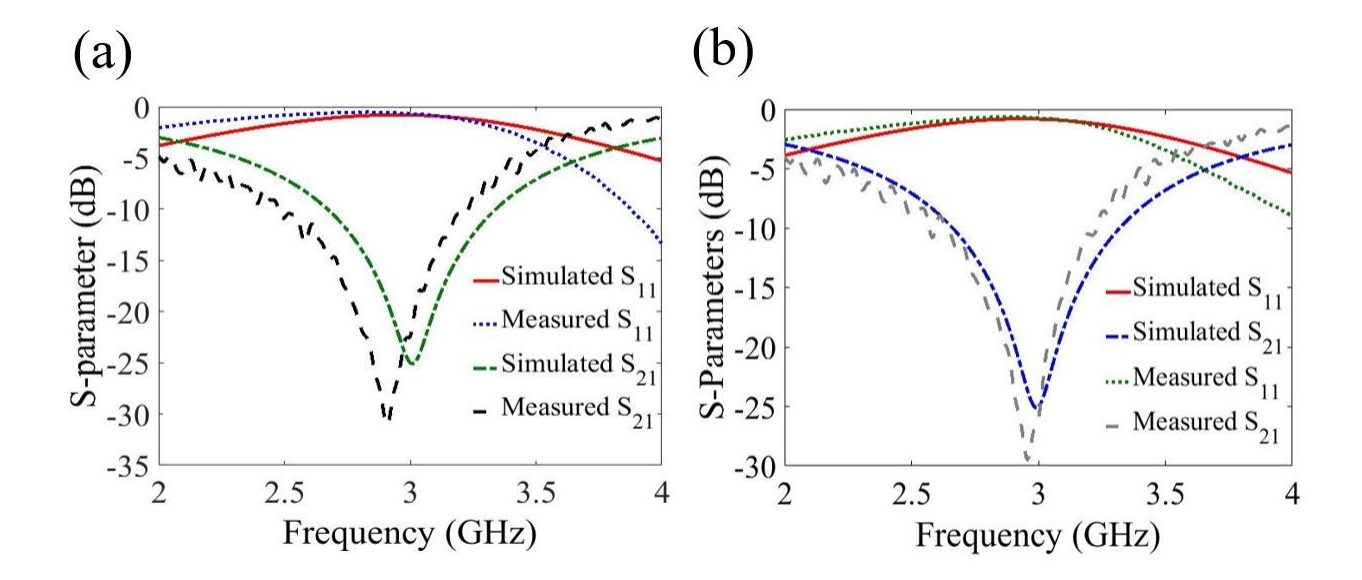


Figure 3.5: The simulated and measured reflection and transmission coefficient (S-parameters) of the non-planar microstrip line.

The effective dielectric constant of the substrate can be determined from the resonant frequency of the T-Line resonator by considering the length and width of the open-ended stub and a correction factor for the T-junction. An effective dielectric constant of 2.7 was determined using an approximate formula given in [44]. This value is close to the dielectric constant (2.8) of VeroWhitePlus (3D printed plastic) reported in the open literature.

3.3.3 Elevated Patch Antenna

Out-of-plane patch antennas are of special interest for inter- and intra-chip wireless interconnects for short-range communication [41]. They can be used to replace wire bonding or
flip-chip type bonding used to connect the RF circuit and off-chip antenna in the millimeterwave system. Performance of the on-chip planar antennas is limited due to poor excitation,
and substrate losses. In this section, 3D printed out-of-plane patch antennas (elevated patch
antenna) in two different configurations, horizontal mount and vertical mount are presented.

Figure 3.6(a) shows the schematic and dimensions for horizontal mount elevated patch antenna. The patch antenna is fed by a $50-\Omega$ microstrip line. The shape of the antenna was chosen to mimic the shape of a PCB compatible antenna that can be placed above a surface mount chip. The bend angle for the microstrip line feeding the antenna is designed to be 45° . Figure 3.6(b) shows the image of the fabricated antenna. The simulated and measured S_{11} results of the antenna is shown in Figure 3.7(a). The operational frequency of the patch is 5.38 GHz with a 10 dB bandwidth of 0.17 GHz. The slight mismatch in the measured and simulated results is due to design and fabrication tolerances. Figure 3.7(b) shows the simulated and measured radiation pattern for this antenna. The radiation pattern was measured using a SATIMO Starlab near-field measurement system. The measured gain of the horizontal mount elevated patch antenna at the resonance frequency is 2.82 dBi.

The second design configuration is the vertical mount elevated patch antenna. The antenna is fed out-of-plane with a 90° bend. Figure 3.8(a) shows the structure and its dimensions, and Figure 3.8(b) shows the fabricated structure after metallization. The simulated and measured reflection coefficients and radiation patterns are shown in Figure 3.9(a) and (b), respectively. The operating frequency of the antenna is centered at 5.39 GHz with

maximum return loss of 25 dB and a 10 dB bandwidth of 0.19 GHz. The measured gain of the vertical mount patch is 3.62 dBi at the center frequency. The measured and simulated reflection coefficient and radiation pattern are in good agreement with each other.

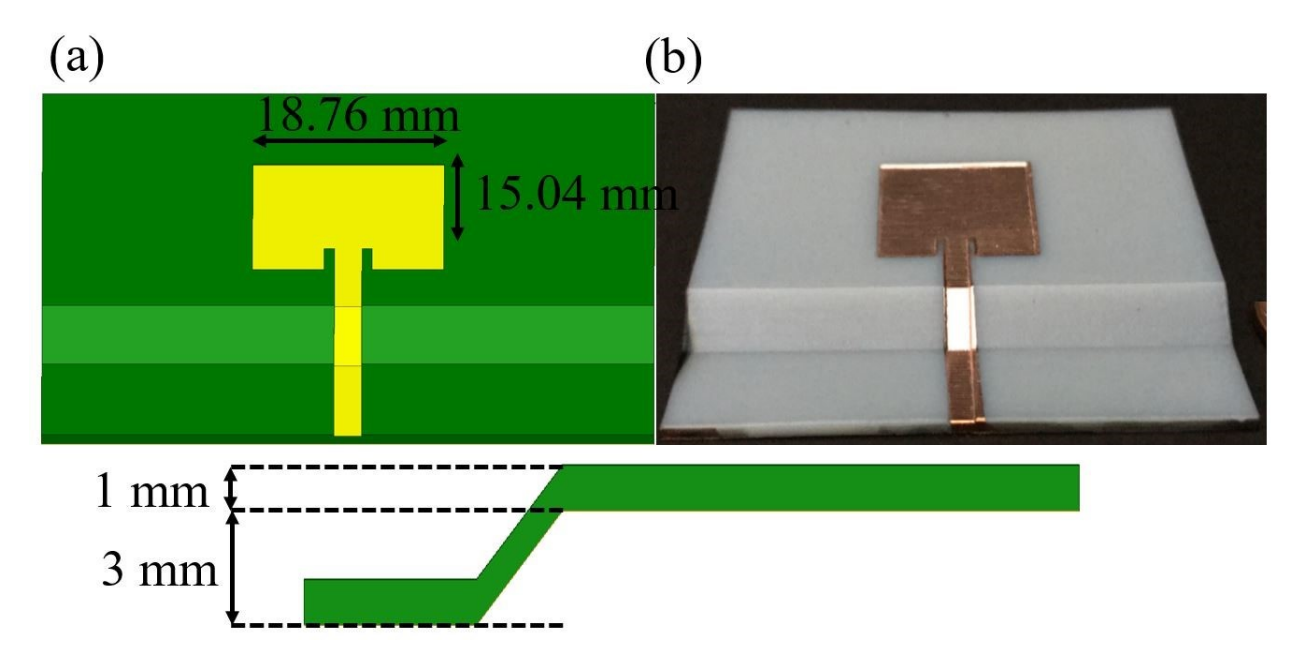


Figure 3.6: Horizontal mount elevated patch antenna (a) Schematic and the dimensions (b) 3D printed elevated patch antenna after metallization.

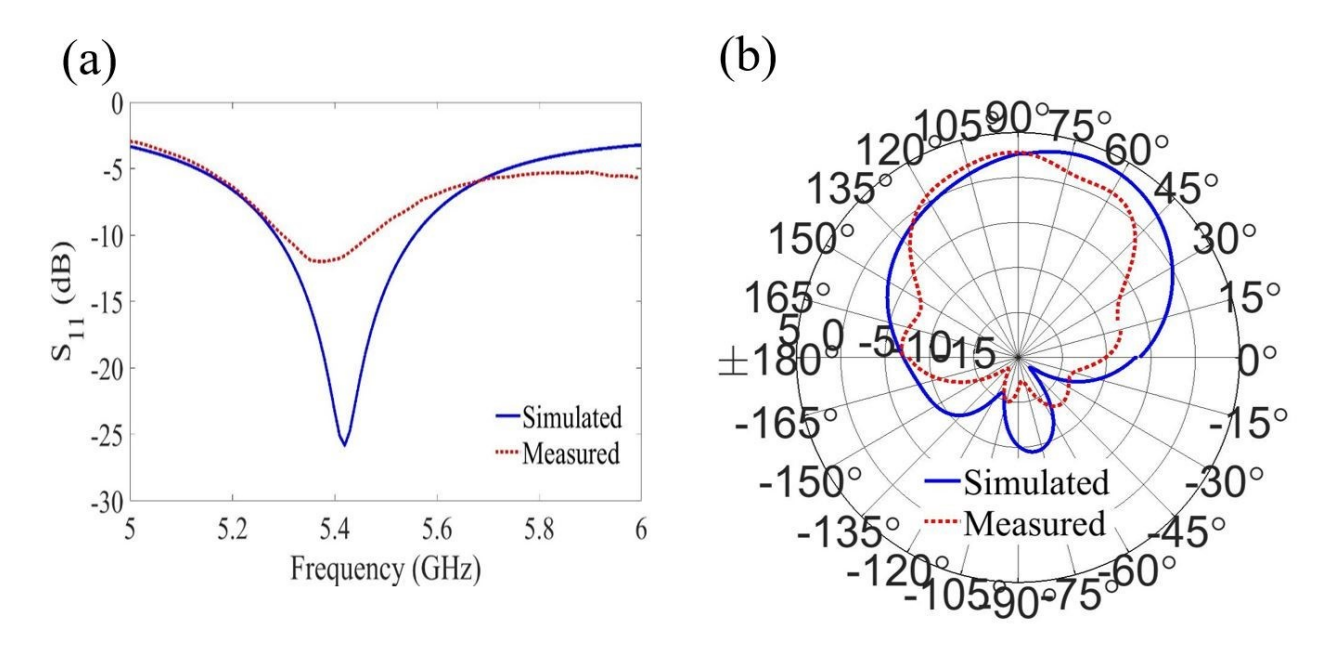


Figure 3.7: Simulated and measured results (a) S-parameters and (b) radiation pattern (dBi) in the E-plane of the horizontal mount elevated patch antenna.

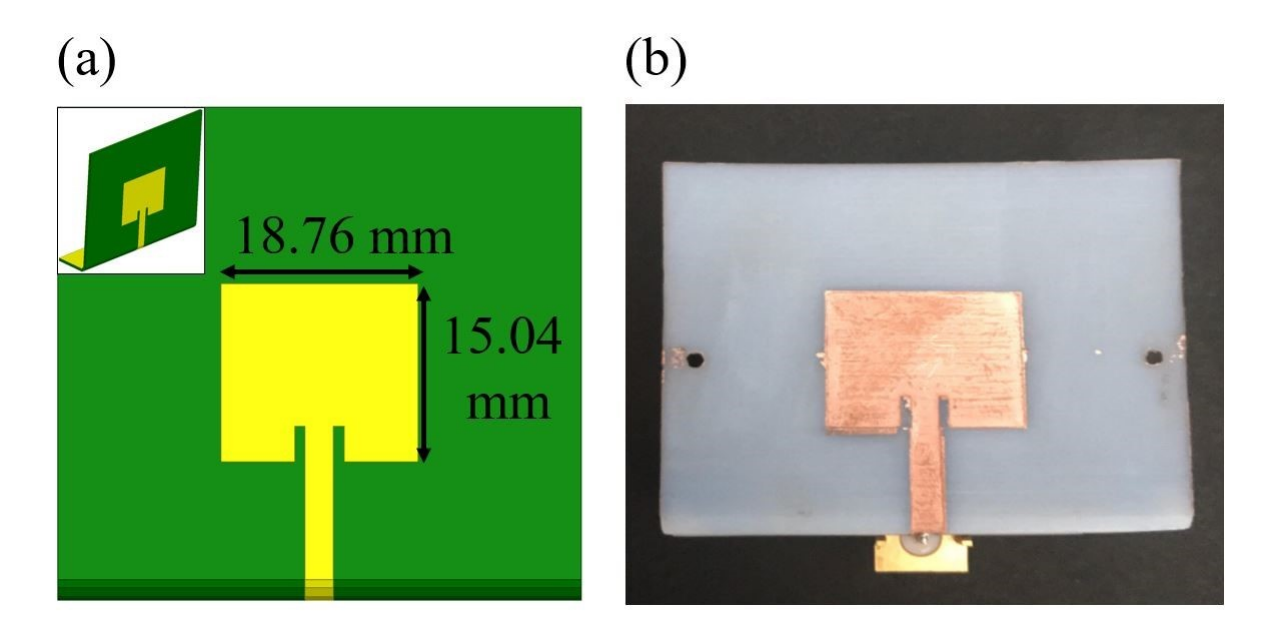


Figure 3.8: Vertical mount microstrip patch antenna (a) Schematic with dimensions, (b) image of the fabricated antenna with the SMA connector.

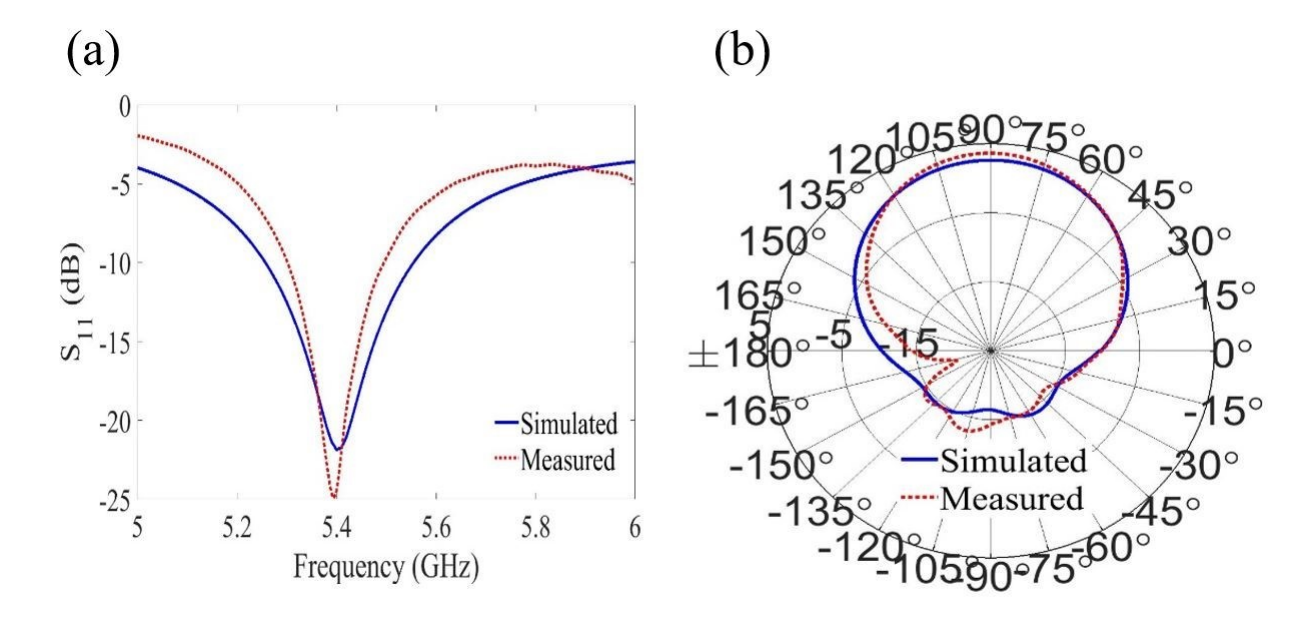


Figure 3.9: Vertical mount microstrip patch antenna, simulated and measured (a) reflection coefficient, and (b) radiation pattern.

3.3.4 Air Gap Patch Antenna

The use of an air cavity between the antenna and the ground plane improves bandwidth and radiation efficiency of the antenna. Two air-gap patch antenna designs are demonstrated using 3D printing and a LEGO-like assembly. First, a simple patch antenna is designed and characterized followed by a wide-band E-patch antenna with improved gain and bandwidth. In these designs, air gap is formed by printing the ground plane and the RF structure separately and assembled using a LEGO-like process using four support pillars. Supports and their complementing holes are printed on opposite sides and these two pieces are snapped together forming the final structure with the patch (metal) facing the ground plane. The schematic and the dimensions used in the design of a regular air-gap patch antenna are shown in Figure 3.10 (a) and the fabricated antenna is shown in Figure 3.10 (b). Also, the 3D printed structure can be integrated with conventional PCB designs as illustrated in Figure 3.10(c). In this design, the patch antenna is excited by a grounded coplanar waveguide and 3D printed feed pin. Figure 3.11 (a) and (b) shows the simulated and measured reflection coefficient and radiation pattern respectively. The measured results show that the resonance frequency is at 5.55 GHz with a maximum return loss (S₁₁) of 29.5 dB and 10 dB bandwidth of approximately 0.34 GHz. The mismatch between measured and simulated results is due to warping of the supporting material due to inherent substrate heating during the sputtering process. The warping leads to a change in the air gap of the antenna that in turn shifts the resonance frequency. The antenna shows a maximum measured gain of 4.19 dBi at 5.5 GHz.

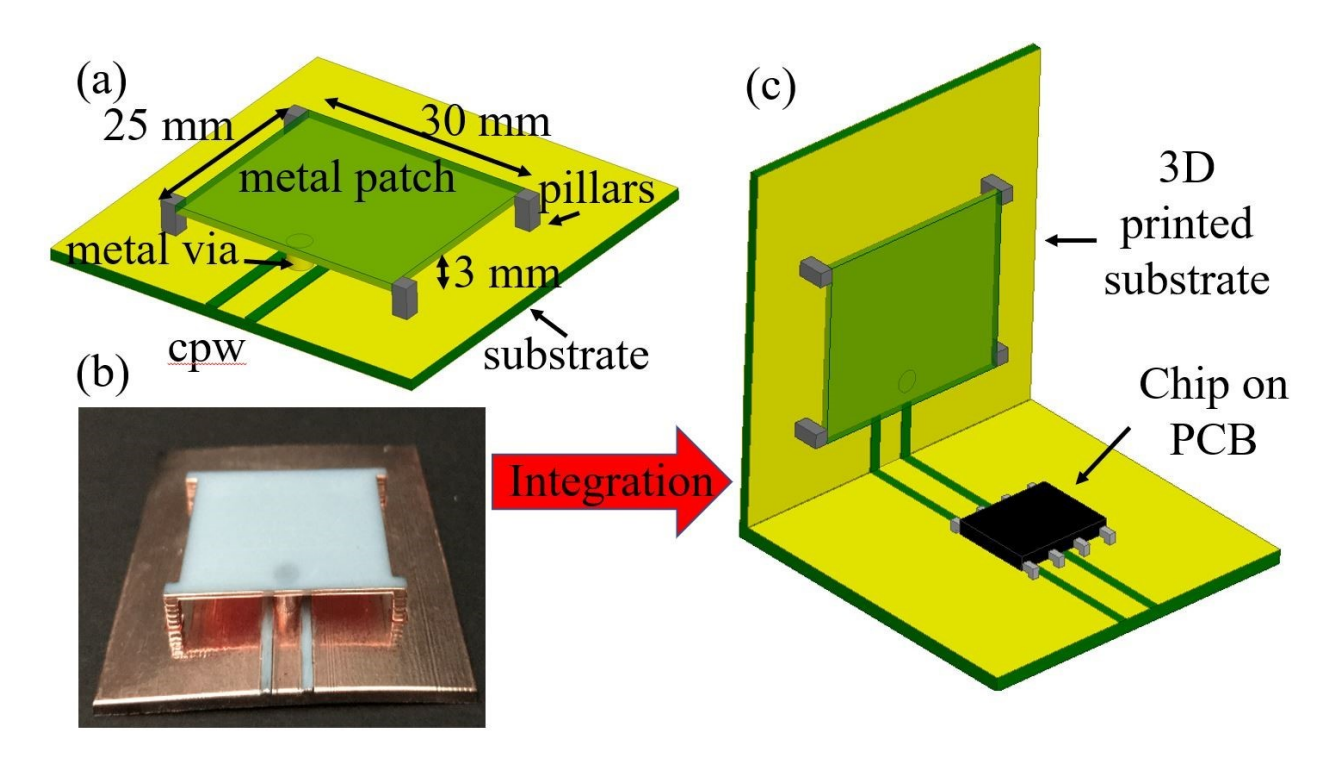


Figure 3.10: Air-gap patch antenna (a) Schematic of the patch antenna with dimensions, (b) Image of the fabricated patch and (c) illustration of the integration between 3D printed substrate structure and PCB.

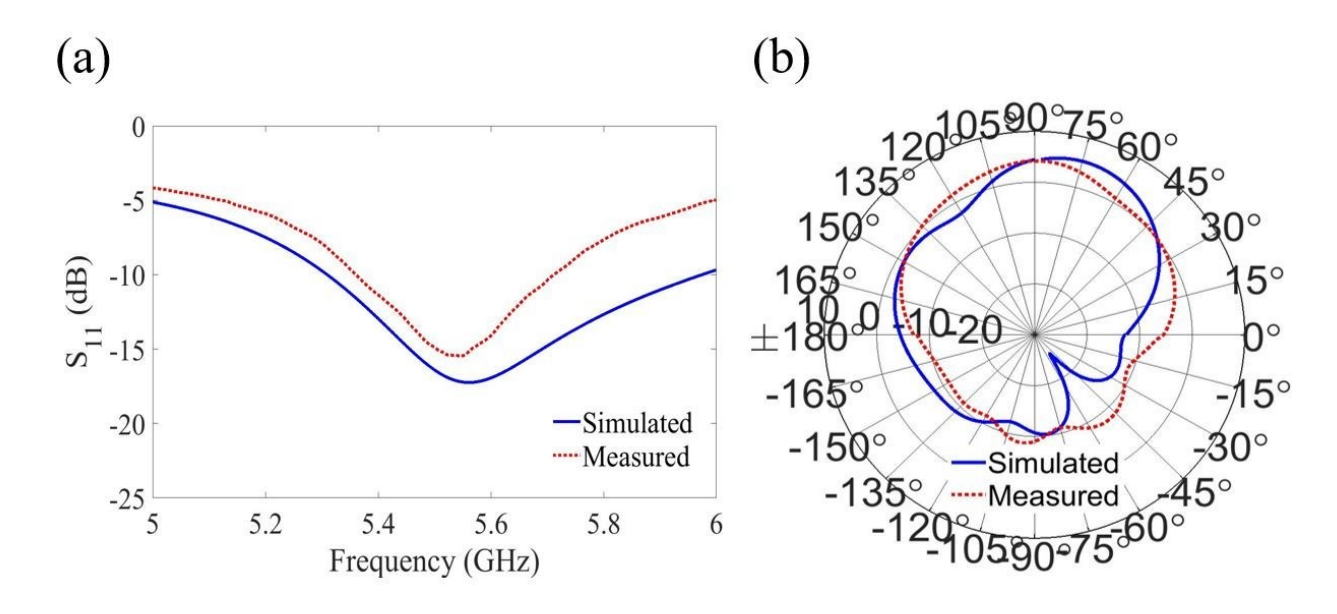


Figure 3.11: Air-gap patch antenna, simulated and measured (a) reflection coefficient and (b) radiation pattern.

3.3.5 E-Patch Antenna

E-patch antennas are commonly used for wideband applications. The resonance frequency and bandwidth of an E-patch antenna can be tailored by changing the length, width, and position of the slots [45, 46]. The slots dimensions, the substrate height, and the position of the excitation point position are optimized to achieve the desired characteristics. Two parallel slots are incorporated into the patch to enhance the bandwidth. The antenna is excited by a grounded coplanar waveguide and 3D printed feed pin and the slots are positioned symmetrically with respect to the feed point. Figure 3.12(a) shows the dimensions of the E-patch antenna and the image of the fabricated structure before and after metallization is shown in Figure 3.12(b). The simulated and measured reflection co-efficient and radiation pattern are shown in Figure 3.13(a) and (b) respectively.

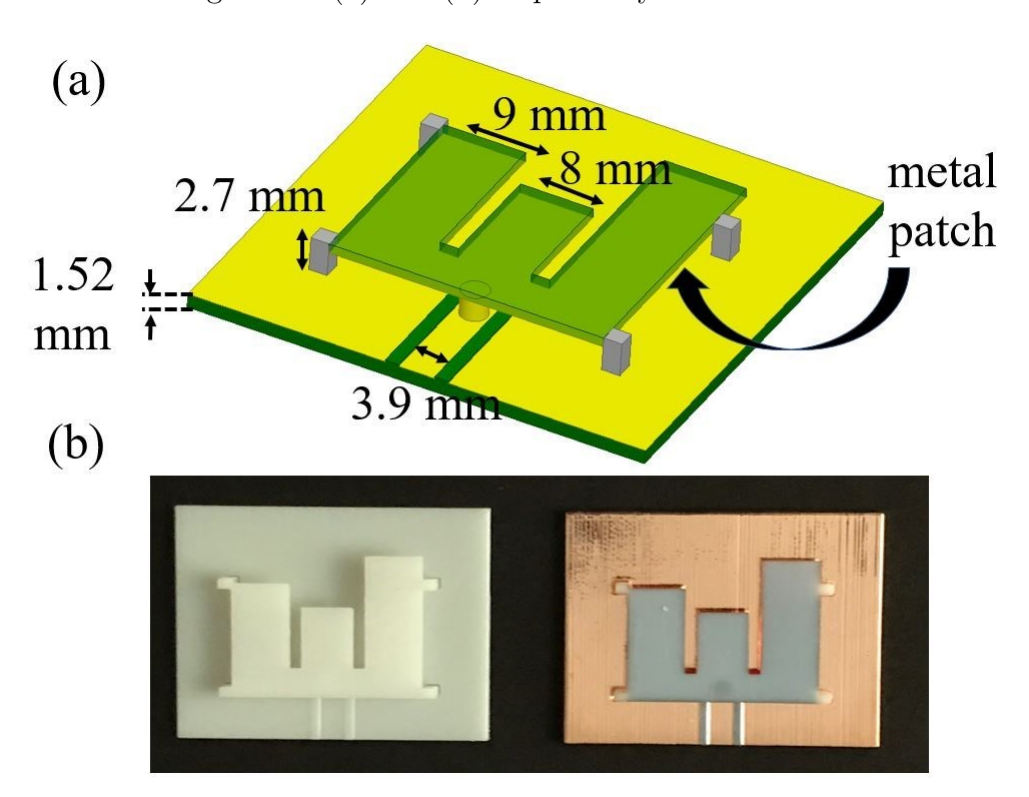


Figure 3.12: Air-gap E-patch antenna (a) Design and schematic with dimensions, (b) fabricated E- patch antenna (before and after metallization).

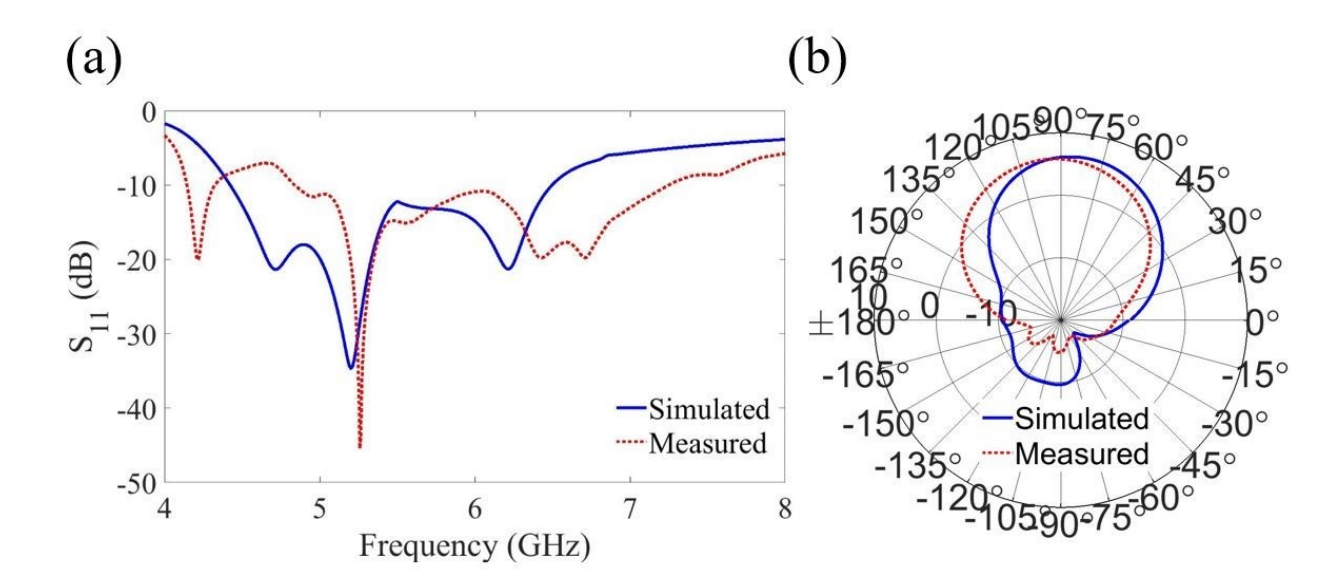


Figure 3.13: Air-gap E-patch antenna, simulated and measured (a) reflection coefficient, and (b) radiation pattern.

The E-shaped patch antenna has a 10 dB bandwidth of 4.9 GHz with a gain of 6 dBi. Mismatch in the simulated and measured results is due to similar reasons discussed earlier.

3.3.6 Monopole Based Antennas

In this section, a 3D printed monopole and Yagi-Uda antenna are demonstrated. A simple monopole antenna is designed and studied along with a corner reflector monopole. The design of the monopole antenna and its dimensions are shown in Figure 3.14(a). A vertical wire like structure of length 15 mm is used to achieve resonance at 4.8 GHz. The antenna is fed using a grounded coplanar line. Figure 3.14(b) shows the fabricated structure. The simulated and measured results for reflection coefficient and radiation pattern are shown in Figure 3.14 (c) and (d), respectively. The monopole operates at 4.8 GHz with a bandwidth of 1 GHz for a return loss of 10 dB or better. The antenna shows a maximum gain of 0.9 dBi at the resonance frequency. The drop in the gain and the uneven radiation pattern can be due to the surface roughness of the 3D printed substrate leading to an uneven deposition of metal around the monopole. Also, there are several pin holes along the metal coating of the pole leading to non-uniform current distribution on the surface of antenna which in turn affects the radiation pattern.

Next, a monopole antenna with corner cube reflector is presented. The gain of omnidirectional antennas (monopole and dipole) can be enhanced by reducing its radiation in other directions with the help of metal reflectors. Here, the performance of a vertical monopole antenna operating at 6 GHz is enhanced by using a corner reflector. Figure 3.15(a) shows the schematic of corner reflector monopole antenna and Figure 3.15(b) shows the fabricated antenna.

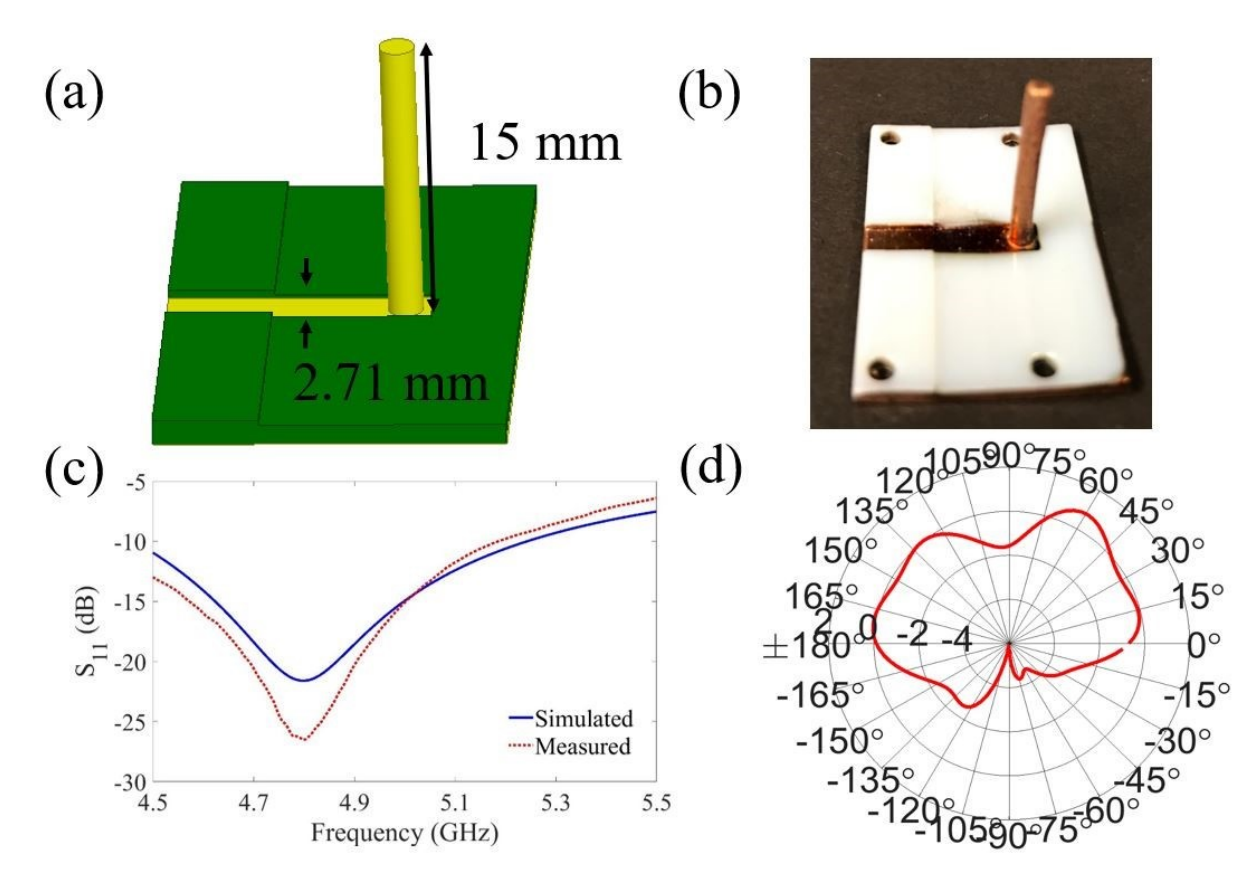


Figure 3.14: Monopole antenna (a) Design and schematic with dimensions, (b) fabricated monopole antenna, (c) simulated and measured reflection coefficient, and (d) measured radiation pattern.

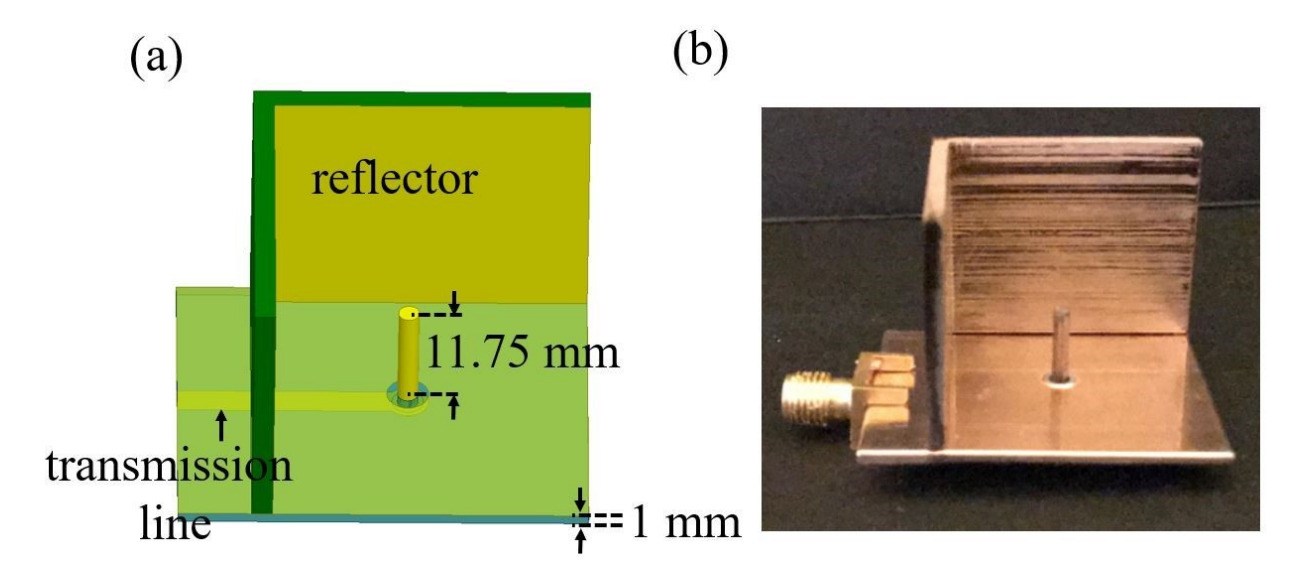


Figure 3.15: Monopole antenna with a reflector (a) Design and schematic with dimensions, (b) fabricated vertical monopole antenna with a reflector.

The simulated and measured results for the reflection coefficient and radiation pattern matches well as shown in Figure 3.16 (a) and (b), respectively. The resonance frequency of the antenna is at 6 GHz with 10 dB bandwidth of 0.61 GHz and it has a gain of 7.3 dBi. The monopole antenna with a corner reflector shows higher gain than a simple monopole antenna as expected. The radiation pattern confirms that the proposed antenna structure can be used as a directional radiator for direct communication between boards. In the future, using 3D printing, more complex design such as frequency dependent reflectors can be fabricated and can be used to achieve additional functionalities such as multiple frequency bands for better impedance matching and smaller front-to-back ratio [47].

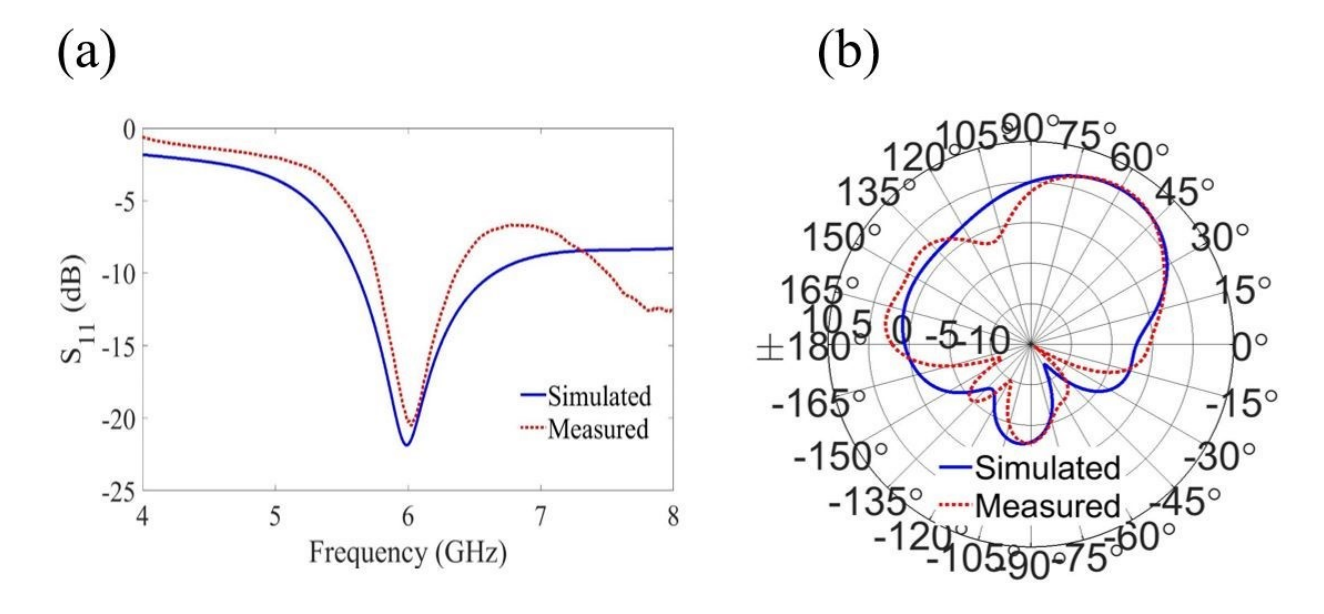


Figure 3.16: Monopole antenna with a reflector, simulated and measured (a) reflection coefficient and (b) radiation pattern in the E-plane direction.

Next, a 3D printed vertical Yagi-Uda antenna is presented. This antenna is one of the most popular end-fire antennas which can be used to achieve a medium gain with relatively low cross-polarization levels. A Yagi-Uda antenna consists of a driver element, a reflector and several directors as shown in Figure 3.17 (a). The driver element is directly fed by source while the other elements are parasitically coupled. Traditional Yagi-Uda antennas are built using several metal rods and are not well suited for integration. The major advantage of using 3D printing for fabricating Yagi-Uda antennas is that the directors of different height can readily be fabricated in comparison to a traditional micromachining process [40]. The antenna performances depend on individual elements heights and the spacing between adjacent elements, the design guidelines can be found in [40]. The coplanar waveguide (CPW) feed is connected to the driver element. The Yagi-Uda structure along with its dimensions and the image of the fabricated structure is shown in Figure 3.17 (a) and (b), respectively. The simulated and measured reflection coefficient and radiation pattern match well as shown in Figure 3.18 (a) and (b), respectively. The results show a gain of 6 dBi at 5 GHz which is comparable to Yagi-Uda presented in the literature using surface micromachining [36, 40].

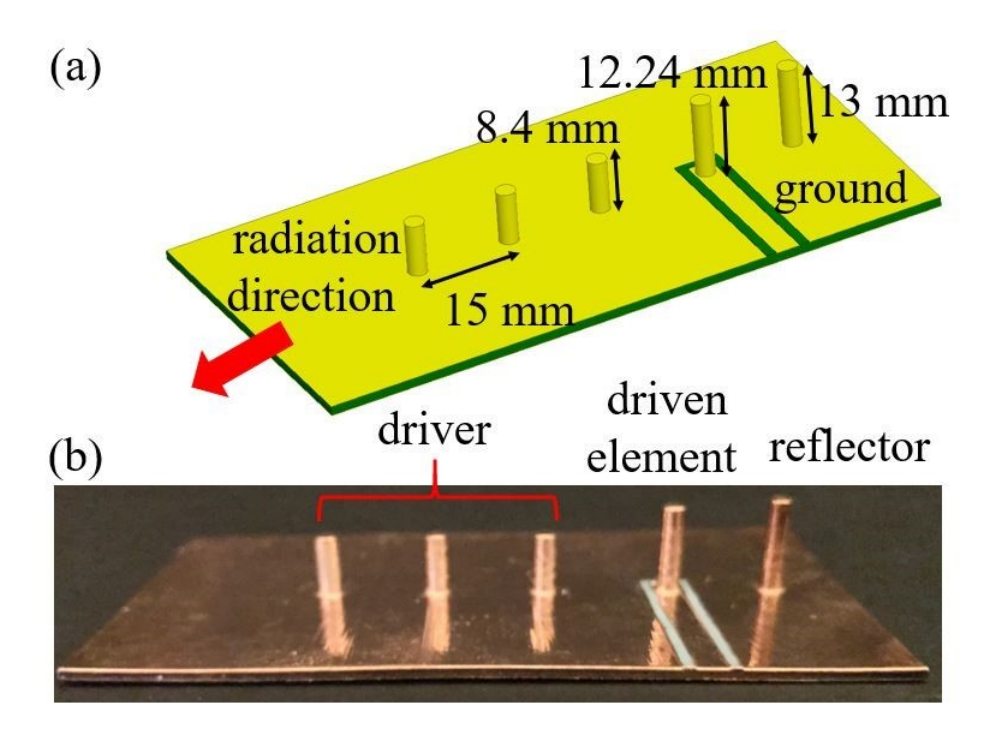


Figure 3.17: Vertical Yagi-Uda antenna (a) design and dimensions (b) image of the fabricated antenna.

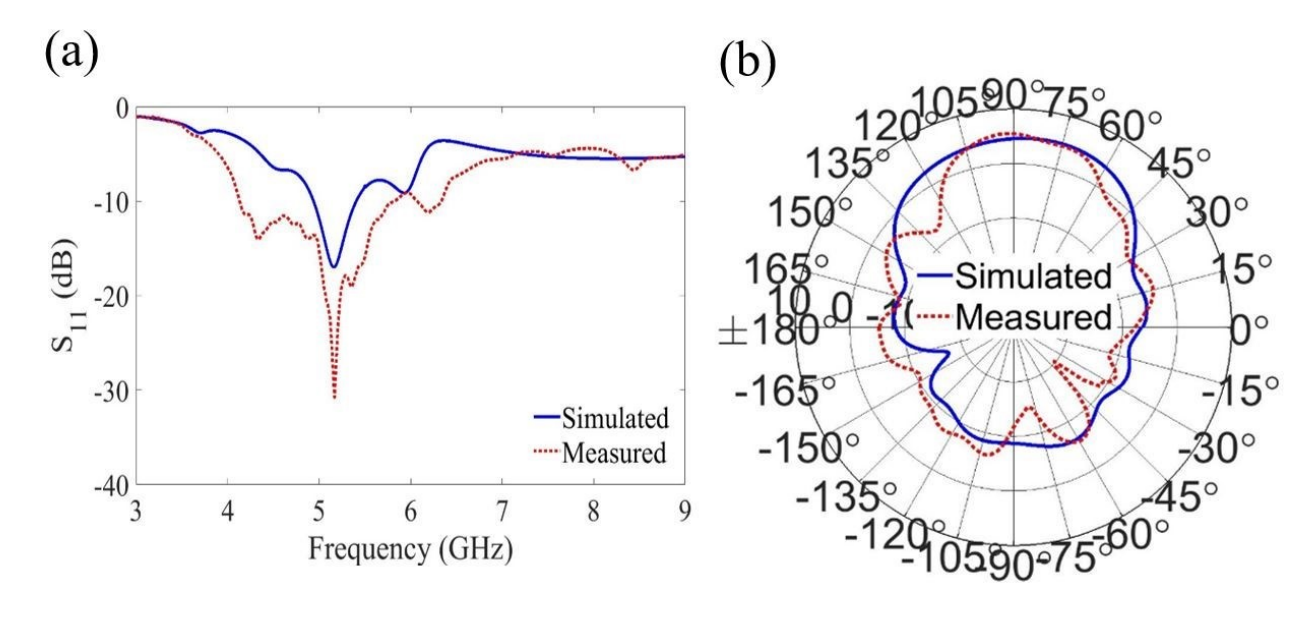


Figure 3.18: Vertical Yagi-Uda antenna, simulated and measured (a) reflection coefficient and, (b) radiation pattern (dBi).

3.4 Discussion

In this chapter, 3D printing is utilized to fabricate different out-of-plane antennas that offer environmental, cost and design benefits. However, there are still significant challenges for the use of these techniques at much higher frequencies. First and foremost, is the scarcity of availability of low loss dielectric materials for 3D printing. Dielectric loss plays a vital role in the performance of the microwave devices when used as a substrate. One way of eliminating loss is by using air as a substrate for fabricating microwave passive devices such as nonplanar E-patch or air-lifted patch demonstrated here, where the 3D printed polymer is used as the supporting structure. Another challenge for 3D printing high frequency components is the dimensional tolerance and surface roughness. Surface roughness is of major concern in 3D printing as it leads to rough deposition of the metal called the scallop effect leading to higher losses. Techniques such as mechanical polishing, chemical polishing, can be used to improve surface quality of 3D printed structures. Here, IPA dipped wipes were used to smoothen the surface down to $<5 \mu m$. The particle size of the polymer determines the dimensional tolerance and surface roughness of the printed product and with advancements in developing better polymers for printing, the printed structures with higher dimensional tolerance and improved surface roughness can be expected in future. Also, with further advances in surface treatment film technologies quality of 3D printed structures will further improve from tolerance, surface roughness, and metal adhesion. Overall, 3D printing can be effectively be utilized in designing complex multi-level designs such as SiP or SoP with ease and good structural integrity.

3.5 Conclusion

The out-of-plane technique enables overcoming challenges of incorporating RF components in limited real-estate on a packaging substrate. The design, fabrication, and characterization of several non-planar antenna designs such as an elevated patch antenna (horizontal and vertical mount patch antenna, broadband air-gap (air cavity) patch antenna, monopole antenna (with and without corner cube reflector), and a Yagi-Uda antenna are presented. In the future, these antennas can be utilized to provide inter and intra-chip wireless interconnects for short-range communication that is compatible with SiP and SoP or other high density packaging technologies. Overall, 3D printing provides a new paradigm shift in the integration of RF components in high density packaging environments.

Chapter 4

3D printed low loss air substrates

4.1 Introduction

The previous chapter demonstrated the capability of fabricating non-planar structures using 3D printing. A major limiting factor in 3D printing of high-frequency circuits fabrication is the scarcity of lowloss dielectric materials for printing. This chapter address in eliminating the drawback through the use of air as the substrate material [48] for fabricating different RF components. In general, an air substrate is an ideal candidate and is desired for many applications such as high-gain and high-bandwidth antennas and low-loss high-performance transmission lines. It is impossible to fabricate metal layer directly on air, hence a number of methods have been proposed in the literature to emulate air substrate. One such method is to print the device directly on materials with very low dielectric constant (ϵ_r) such as foam; another method is to use a lower ϵ_r substrate with air gaps (hollow) to reduce the effective ϵ_r . Over the last two decades, various μ -wave circuits such as microstrip transmission lines [49–51] patch antennas [52–57] and filters [58, 59] are implemented on partial and complete hollow substrates using complex micromachining and microassembly techniques. Micromachining technologies can include bulk or surface machining of silicon (Si), dielectrics, and photosensitive polymers. The most commonly used Si micromachining involves various technological challenges such as realization of holes or vias (hundreds of micrometer deep) and the removal of Si for air-filled cavity by wet or dry etching. Another alternative for fabricating such complex structures is the use of micromolding technique (injection molding and hot embossing), followed by metallization [60]. However, the cost of the mold can be expensive and there are practical limitations on achieving the required geometry of the 3D structure. 3D printing can be adopted as an alternate technique to fabricate hollow structures or substrates with air gaps.

Several key RF components such as low-dispersion microstrip transmission line, T-line resonator, patch antenna, slot antenna, and cavity resonator are demonstrated in this chapter. The structures are printed on separate layers (top layer and ground plane) along with spacers and snapped together using a LEGO-like process. The metal layers are designed to face each other with an air gap between them. Here, the 3D printed plastic layers are only used for mechanical support. The effect of the thickness of the support material on RF performance was also investigated. The key advantages of the fabrication process of this chapter include: 1) use of low loss air substrate; 2) ability to fabricate multilayer structure; 3) easy fabrication of complex non-planar geometries; and 4) low-temperature process.

4.2 Analysis

To demonstrate the advantage of using air substrate for RF circuit design, simulations were carried out for a 50 Ω microstrip transmission line and a patch antenna. The first set of simulations was carried out to demonstrate that air is an ideal substrate for the design of low-loss transmission lines. All the simulations presented here were performed using a commercial finite element method solver, ANSYS High Frequency Structural Simulator (HFSS). Figure 4.1 shows the simulated propagation loss as a function of dielectric loss (loss tangent, tan δ) for a microstrip line (50 Ω) designed for substrates with different ϵ_r values and at a fixed frequency of 5 GHz. In these simulations, the substrate height was fixed at 2 mm while the width was adjusted to maintain 50 Ω impedance for different ϵ_r values. The desired performance was optimized for maximum transmitted signal in order to get the best possible results. It can be seen from Figure 4.1 that materials having lower dielectric constant and lower loss tangent provide the desired low propagation loss for fixed substrate height. From these results, it can be seen that air ($\epsilon_r = 1$) is an ideal substrate for low-loss transmission line design.

The height of air gap also affects the performance of microstrip-based circuits. Figure 4.2 shows the simulated propagation loss for a 50 Ω transmission line as a function of frequency for lossless air substrate ($\epsilon_r = 1$ and $\tan \delta = 0$) with different substrate thickness (h). Results clearly show that propagation loss decreases as the substrate thickness increases. However, above a thickness of 3 mm, the drop in propagation loss is not significant. In addition, the loss increases with frequency as expected.

Simulations were also carried out to demonstrate the advantage of using air substrate for the design of a patch antenna. The gain of the antenna was analyzed at 5 GHz as a

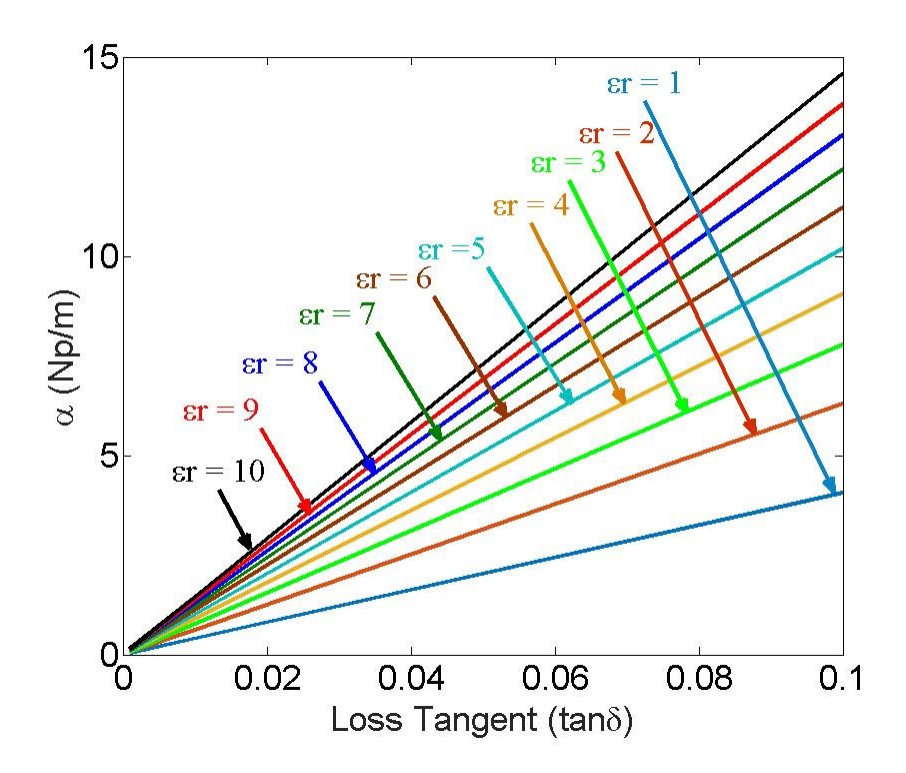


Figure 4.1: Propagation loss of a 50 Ω transmission line as a function of loss tangent (tan δ) for substrates with different dielectric constant (ϵ_r) values.

function of substrate with different ϵ_r values ($\epsilon_r = 110$), fixed thickness (h = 2 mm), and loss tangent (tan $\delta = 0$). The dimensions of the patch were optimized, using HFSS, to achieve maximum possible gain for each ϵ_r value. Figure 4.3 shows the antenna gain as a function of the dielectric constant (ϵ_r). The results clearly show that gain can be improved by lowering ϵ_r for a fixed thickness. Hence, an air substrate is an ideal solution for high-gain antenna designs. The gain of an antenna also depends on the thickness of the substrate, and thicker air gap substrate can be used to achieve ever higher gain.

The next set of simulations was carried out to study the effect of 3D printed support material on the performance of RF circuits. Here, 3D printed VeroWhitePlus is utilized as the support material to fabricate different RF structures. It has a dielectric constant of 2.8 and loss tangent of 0.04 [61]. Prior to assembly, the structures are 3D printed and

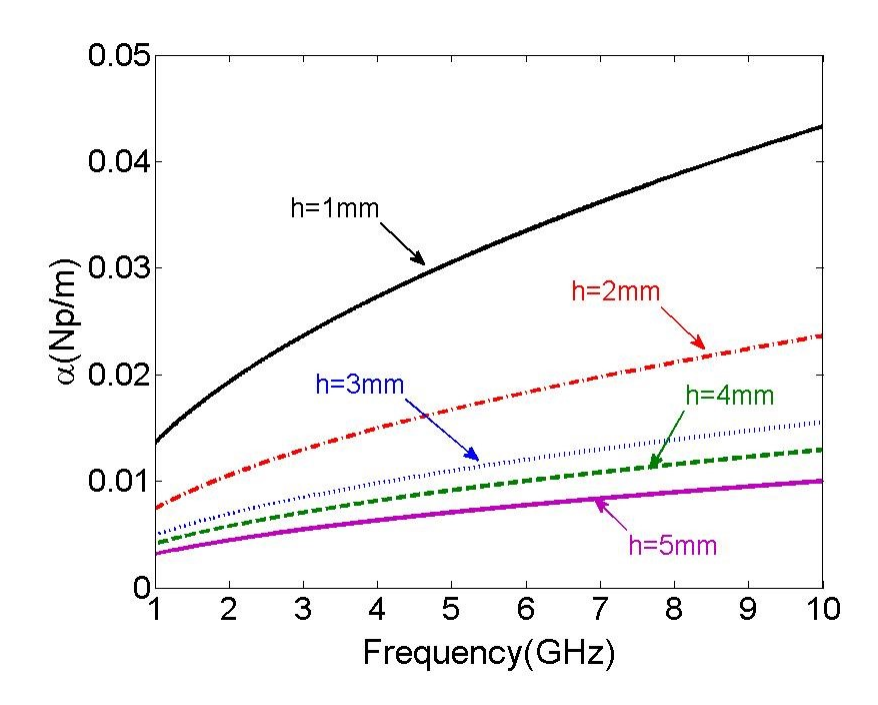


Figure 4.2: Propagation loss of a 50 Ω transmission line as a function of frequency for different heights (h) and fixed $\epsilon_r = 1$ and tan $\delta = 0$ of the air substrate.

metalized as separate layers [see Figure 4.4 (a) and (b)]. To achieve self-alignment and assembly, holes and supporting pillars (spacers) are built along the edges of the top and bottom layers, respectively. These two layers are snapped together with copper-coated sides facing each other as shown in Figure 4.4(c). The pillars help to maintain air spacing between the two layers and also to interlock the pieces. During operation, for microstrip structures, the propagating signal is largely concentrated between the two metal layers in the air region, and a small fraction of signal may propagate in the 3D printed mechanical support region.

In order to study the effect of support material on RF performance, simulations were carried out for a 50 Ω microstrip transmission line deposited on support structure with different thicknesses. Figure 4.5 shows the propagation loss (α) for different thickness of the 3D printed support material (VeroWhitePlus) over a frequency range of 110 GHz. The air substrate thickness (air gap) was fixed at 2 mm, while width of the microstrip line was

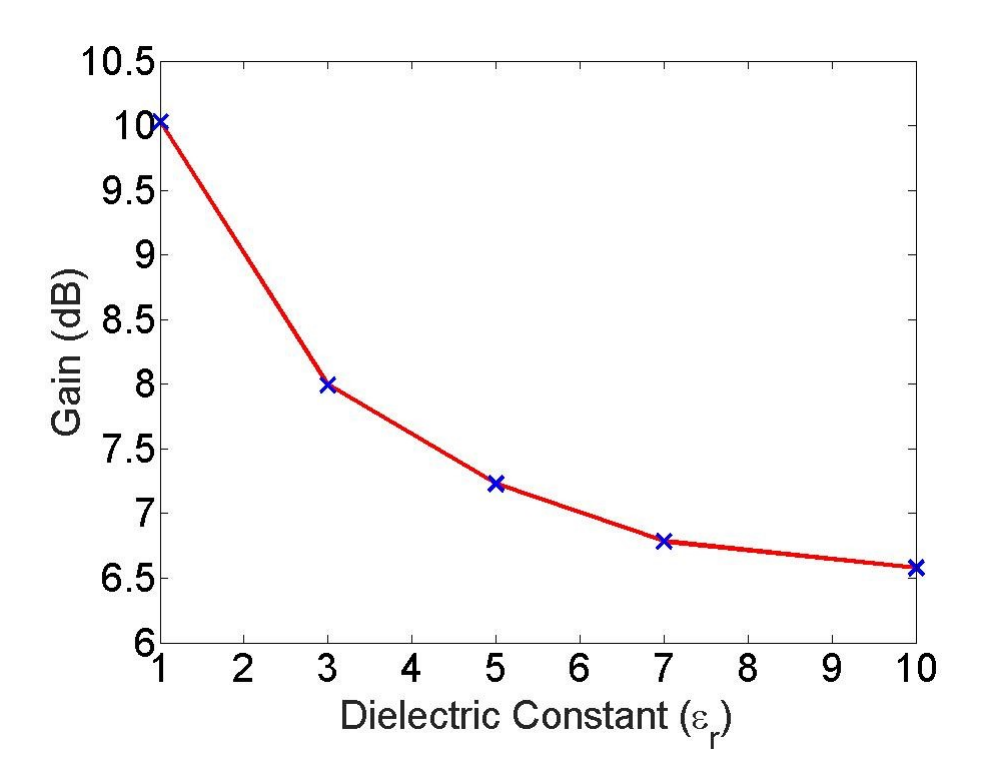


Figure 4.3: Simulation results for gain of a patch antenna as a function of substrate dielectric constant (ϵ_r) for fixed substrate height (2mm) and loss tangent (tan δ =0).

modified to maintain 50 Ω characteristic impedance. The result clearly shows that thin support material has negligible effect on the propagation loss of the microstrip transmission line. However, the support layer must be mechanically sturdy, and hence a support layer with thickness of 2 mm is selected for all structures of this chapter. As a comparison, 2-mm-thick support material having $\tan\delta$ of 0.01 provides approximately $10\times$ less propagation loss (Np/m) as compared to VeroWhitePlus ($\tan\delta=0.04$). 3D print compatible lowloss material may be available in the future, and thus the loss can further be reduced using such materials for the support region.

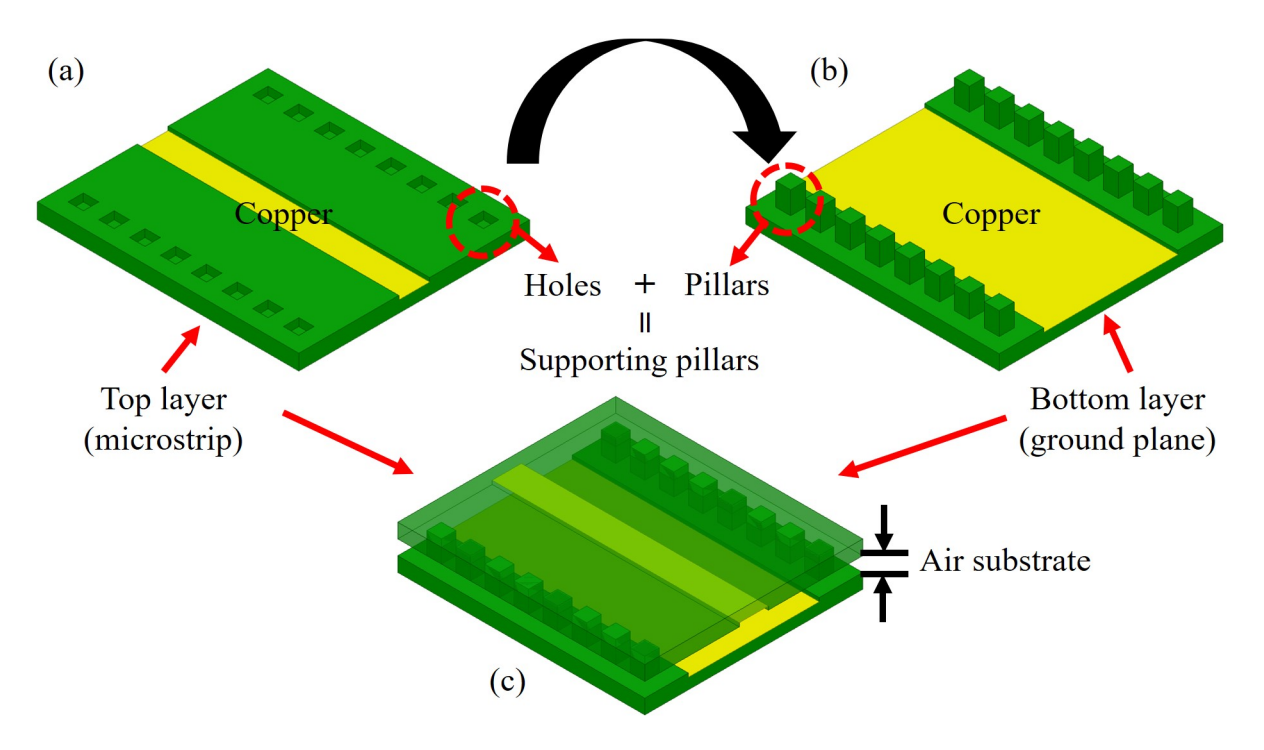


Figure 4.4: Schematic of the cross-sectional view of proposed fabrication and LEGO-like assembly technique (a) top layer (b) bottom layer along with support pillars and (c) assembly of the two layers to achieve an air substrate.

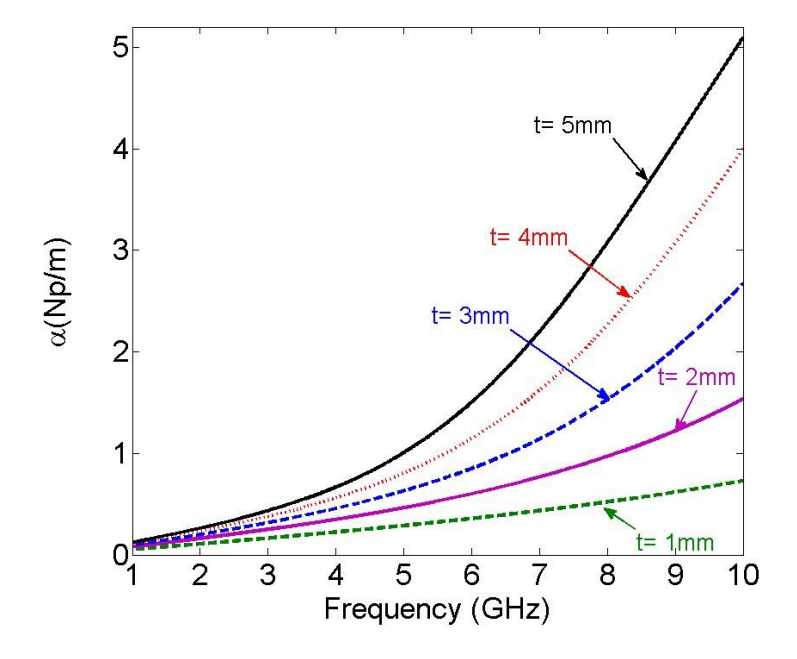


Figure 4.5: Propagation loss of a 50 Ω transmission line as a function of frequency for different thickness of the 3D printed support material.

4.3 Fabrication

A step-by-step fabrication process for RF structures on air substrate is outlined in Figure 4.6. The Left side of the figure shows the fabrication steps for the top layer, and the right side shows the steps for the bottom ground layer. These two layers are snapped together as shown in Figure 4.6(d). All of the RF components are printed using a professional-grade commercially available 3D printer (Objet Connex350) utilizing a photopolymer resin called VeroWhitePlus. Figure 4.6 also shows example of 3D printed patch antenna structure. The structures were metallized using sputtering followed by electroplating. For patterning of conductive layers on non-planar printed structures, a simple damascene-like process is used [43].

After printing, the structures were first cleaned using isopropyl alcohol and completely cured under blanket UV light. Longer exposure under UV light ensures that the material is completely cured, which helps minimize warpage during metal sputter deposition. In the printed parts, trenches are designed where metal pattern is needed. Trenches with 0.2 mm depth are formed as shown in Figure 4.6(a). Titanium/copper (Ti/Cu) with thickness of 60/500 nm is sputter deposited. Here, Ti layer is used to enhance adhesion between Cu and VeroWhitePlus. After metallization, the structures are mechanically polished to remove excess metal film outside the trench regions similar to a damascene process. The thickness of the metal is further increased (to $56 \mu m$) using Cu electroplating. SMA connectors [Figure 4.6(c)] are then attached using silver paste (resistivity $0.017 \Omega.cm$) between the microstrip line and the 3D printed edge holder. This edge holder is coated with metal on all sides, and this directly connects to the ground plane on the second piece when assembled. Assembly of the two pieces is shown in Figure 4.6(d). Silver epoxy is layered on the edge holder before

assembly. Air spacing of 2 mm is present between the metal layers. This thickness was chosen based on the geometry of the edge-mount SMA connectors.

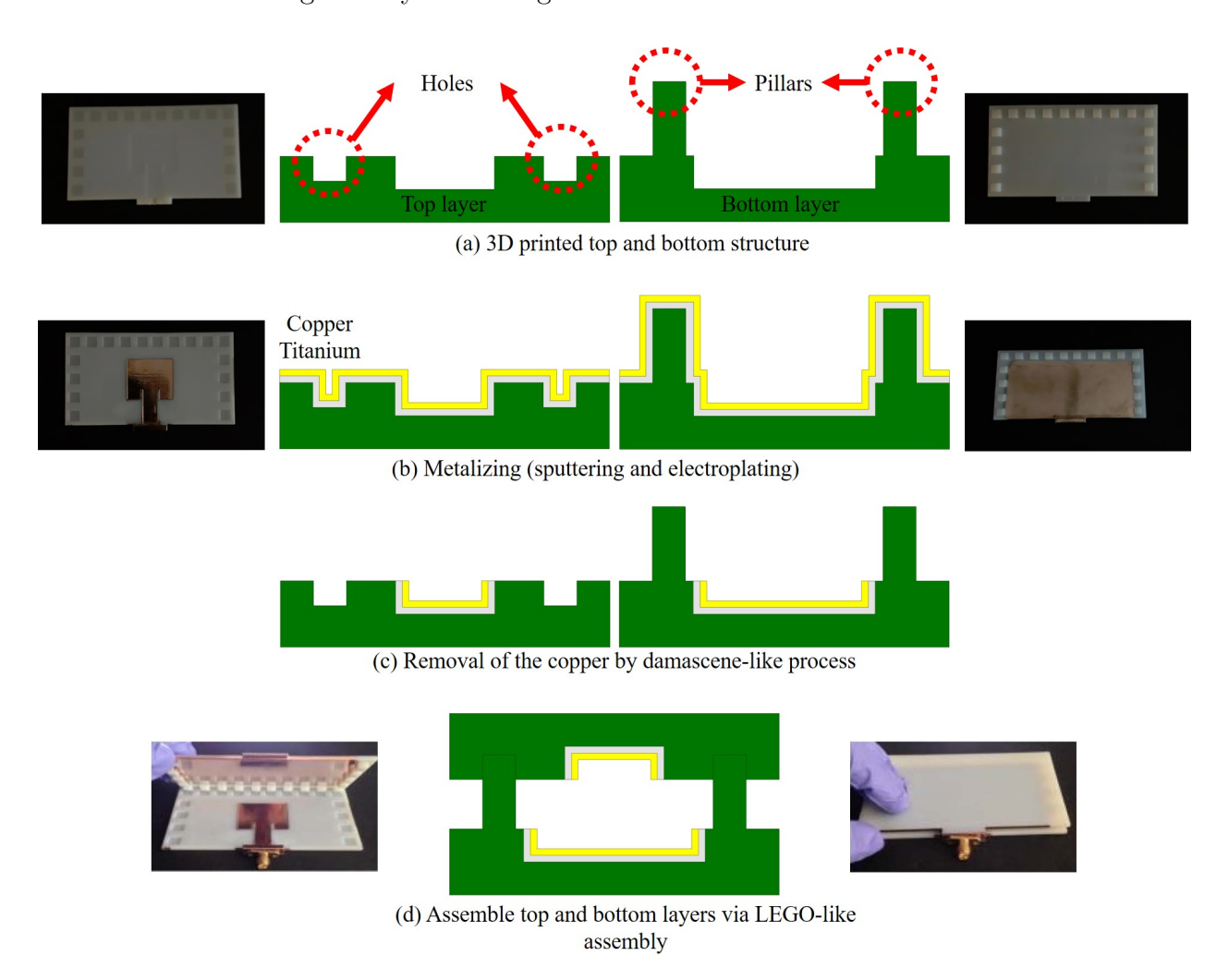


Figure 4.6: Damascene-like fabrication process and LEGO-like assembly for air-based substrate microwave devices using 3D printing.

4.4 Microstrip Line and T-Line Resonator

A 50 Ω microstrip line was fabricated using the process outlined in Figure 4.6. Figure 4.7(a) shows the fabricated structure (top layer and ground plane) before assembly. Figure 4.7(b) shows a good match between simulated and measured S-parameters over a frequency range of 15 GHz. Overall, low reflection and high transmission are seen in both the simulated and measured data. The microstrip line shows measured loss of 0.17 dB/cm at 4 GHz, and it is slightly higher than the simulated loss. This deviation is due to resistive losses from the silver paste used to attach the SMA connectors. Further difference can be attributed to reduction in air gap due to slight warping of the VeroWhitePlus layers that occurred during metal sputter deposition. These differences are not included in the simulation.

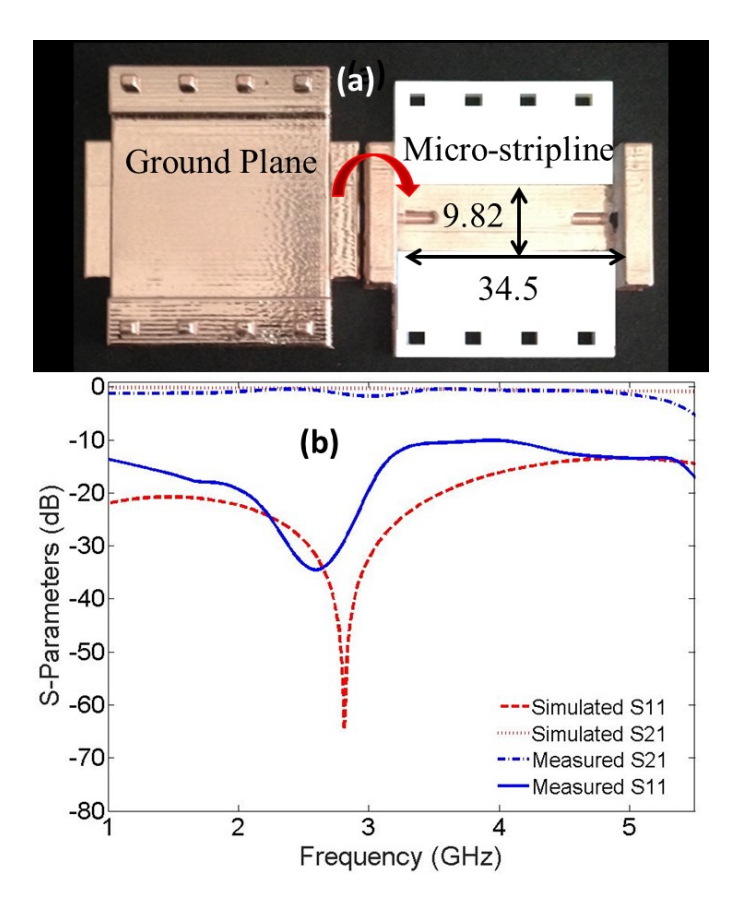


Figure 4.7: Microstrip transmission line: (a) Fabricated structure before assembly with dimensions (in mm) and (b) simulated and measured S-parameters.

Next, a T-line resonator is designed, fabricated, and characterized. The microstrip-based T-Line resonator is designed using an opened stub. Figure 4.8(a) shows the fabricated structure before assembly. The simulated and measured results are in good agreement as shown in Figure 4.8(b). It shows a resonance at 5.25 GHz with a maximum return loss of 20 dB. The measured results of the T-line are also used to demonstrate that the effective dielectric constant of the substrate is approximate~ 1. The effective dielectric constant can be determined from the resonant frequency of the T-line resonator by taking into account the length and width of the open-ended stub and a correction factor for the T-junction. Ignoring the open-end effects, an approximate formula for calculating the effective dielectric constant is given as follows and can be found in [31]:

$$\epsilon_{eff} = \left(\frac{n \times c}{4f_r(l + \frac{\omega}{2} - t_{eff})^2}\right)^2 \dots (5)$$

where n is the order of resonance, c is the speed of light, f_r is the resonance frequency, l is the length of the open stub, w is the width of the feedlines, and t_{eff} is the correction factor for the T-junction. The correction factor can be calculated using the following formula:

$$t_{eff} = \omega \times (0.5 - (0.05 + 0.7e^{-1.6} + 0.25(\frac{f_n}{f_1})^2))\dots(6)$$

where f_n is the nth-order resonance frequency and w is the width of the microstrip line. Using (5), (6), and the dimensions of stub as given in Fig. 8(a), the effective dielectric constant for the air gap is estimated to be 1.01. This value is close to the dielectric constant of air. This is slightly above the air dielectric constant and is due to field penetrating the support material.

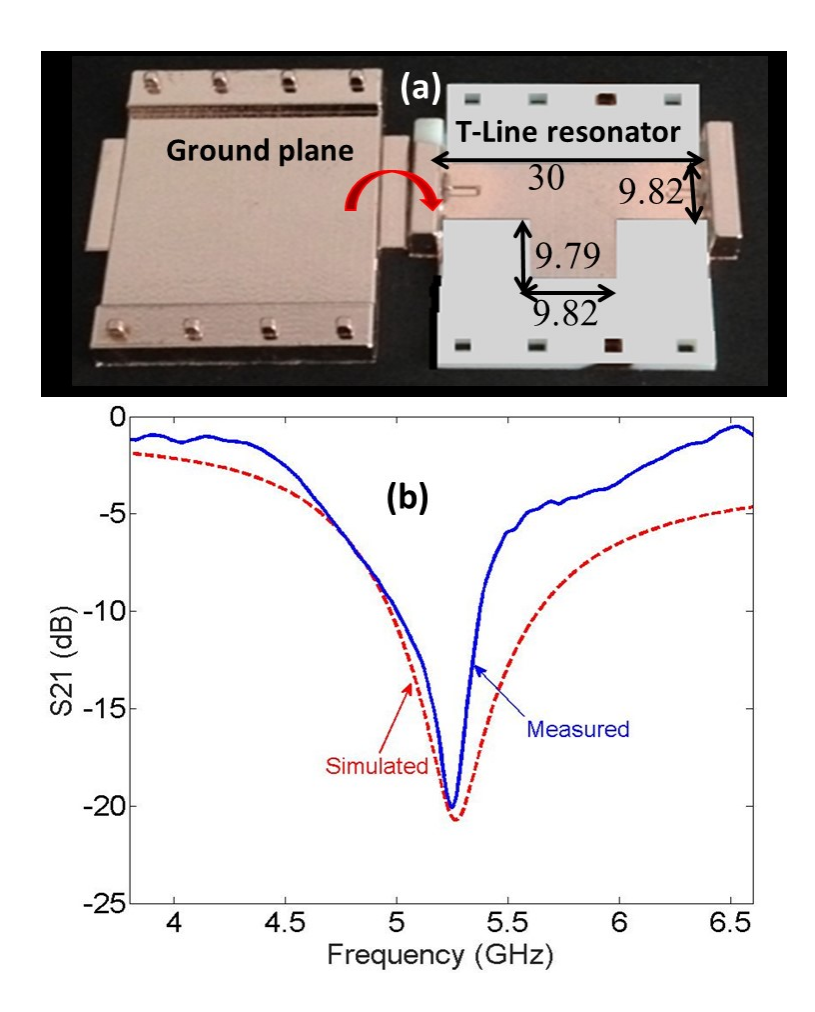


Figure 4.8: T-line resonator: (a) Fabricated structure before assembly with dimensions (in mm) and (b) simulated and measured transmission coefficient.

4.5 Patch Antenna

Antennas with two different RF feed techniques, microstrip transmission line inset feed and direct coaxial feed, are designed and fabricated. The air gap (air substrate height) is fixed at 2 mm for the patch antenna design to accommodate SMA connector. Figure 4.9 shows the schematic of the patch antenna with inset feed, final assembled structure, and its simulated and measured results. The RF characterization of the antennas was carried out using a network analyzer and SATIMO Starlab near-field radiation pattern measurement system. The measurement setup was calibrated using manufacturer-provided standard antennas before measuring the radiation pattern of the fabricated device. The measured reflection coefficient (S₁₁ [Figure 4.9(c)] matches well with the simulated results. Measured results show a resonance at 4.89 GHz with maximum return loss of 13 dB. The antenna shows wider bandwidth as a result of air substrate. The 10 dB return-loss bandwidth of the patch was determined to be 0.12 GHz from the measured results. The peak gain of the antenna is approximately 6 dBi seen in Fig. 4.9(d).

The difference between the measured return loss and simulated results can be attributed to the surface roughness, added series resistance from the silver paste, and a slightly thinner air gap due to warping as a result of exposure to heat during the metallization process and due to stress in plated copper.

Next, the patch antenna with coaxial feed is simulated, fabricated, and measured. Figure 4.10 shows the fabricated patch antenna on air substrate with coaxial feed with the dimensions used for design, and its simulated and measured results. Measured results show resonance at 4.49 GHz with maximum return loss of 20 dB. The measured 10-dB bandwidth and the gain are 0.20 GHz and 7.25 dBi, respectively.

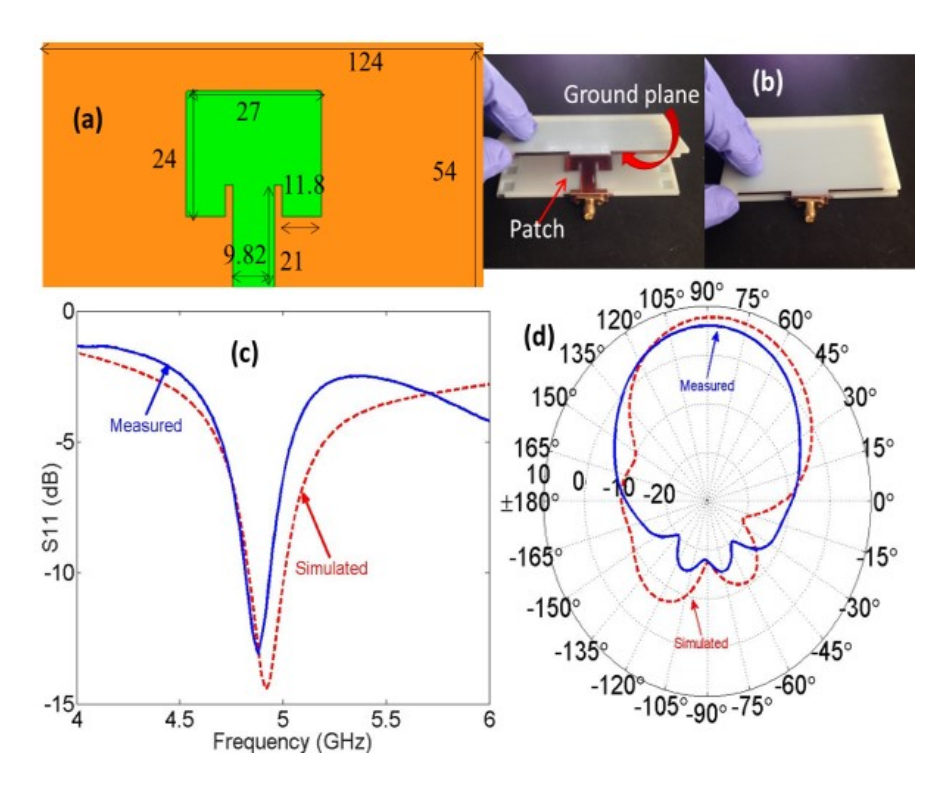


Figure 4.9: Patch antenna with SMA feed: (a) Dimension of patch antenna (in mm) (b) fabricated patch antenna, simulated and measured (c) reflection coefficient, and (d) radiation pattern.

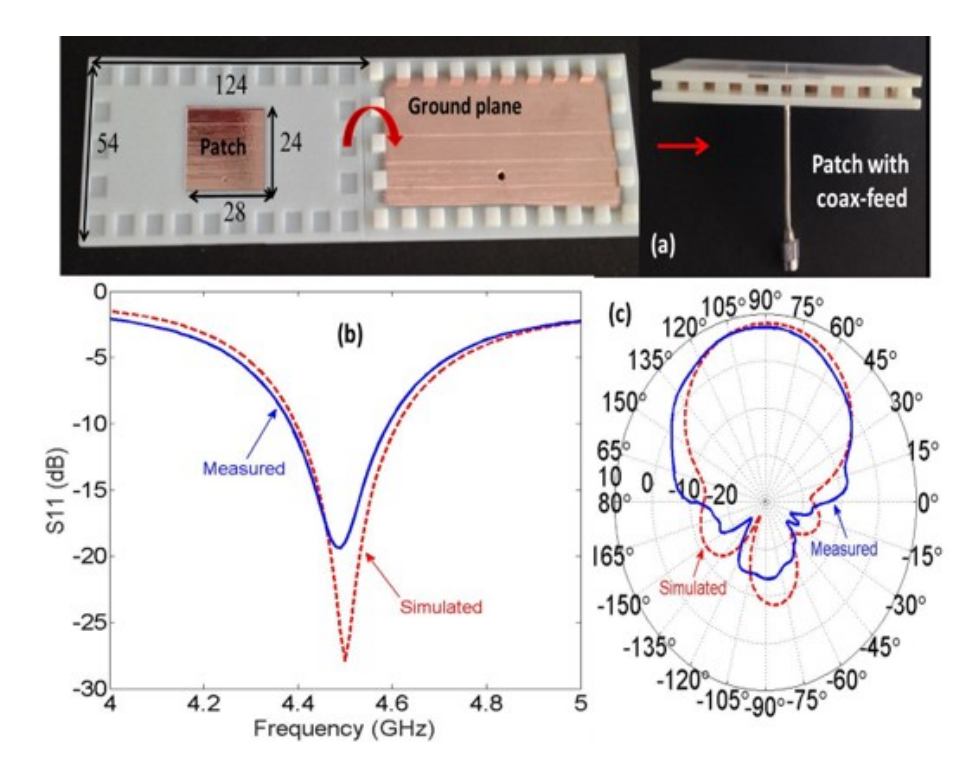


Figure 4.10: Patch antenna with coaxial feed: (a) fabricated patch antenna with dimensions (in mm), simulated and measured (b) reflection coefficient, and (c) radiation pattern.

4.6 Slot Antenna

Slot antennas are of interest in μ -wave and millimeterwave applications due to their planar nature, moderate gain, and relatively easy integration with active devices. A simple slot antenna fabricated using 3D printing is presented. Unlike the structures discussed above, the slot antenna does not require a ground plane, and thus a single metal layer is needed. The slot region of the antenna avoids the use of lossy dielectric and, using 3D printing, the slot can be made arbitrarily thick in comparison to conventional planar structures. The schematic of the slot antenna design along with its dimensions is shown in Figure 4.11(a). Figure 4.11(b) shows the printed antenna after metallization and assembly of coaxial cable. The simulated and measured reflection coefficient and radiation pattern match well as shown in Fig. 4.11(c) and (d), respectively. The antenna shows a resonance at 2.5 GHz and 10-dB bandwidth of 0.98 GHz with a peak gain of 2.72 dBi. The air-filled slot antenna performs better than a dielectric filled slot antenna due to reduction in substrate loss.

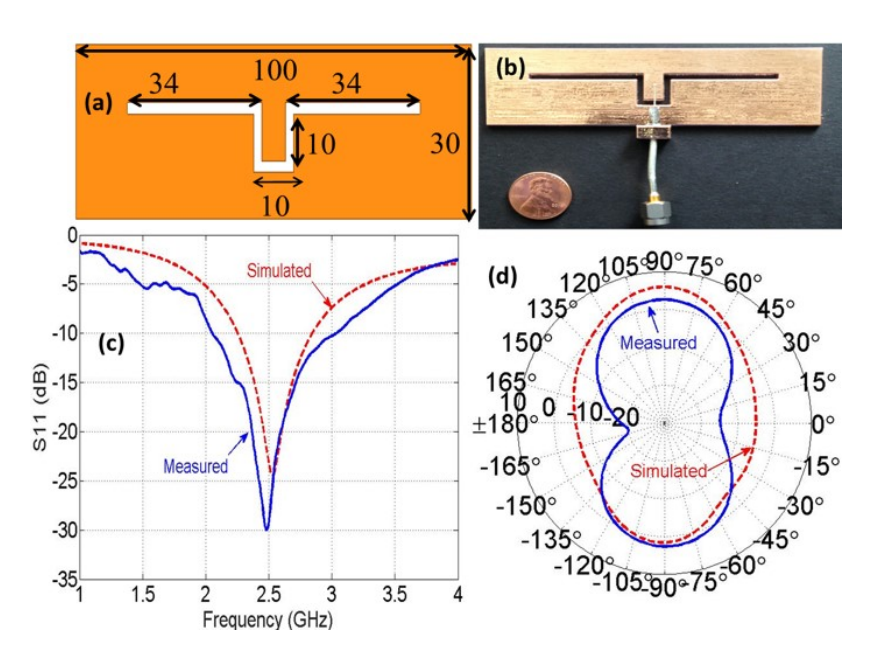


Figure 4.11: Slot antenna: (a) schematic for slot antenna with dimensions (in mm) ,(b) Image of the fabricated antenna, and the simulated and measured results (c) reflection efficient and, (d) radiation pattern.

4.7 Cavity Resonator

An S-band, multilayered, slot-coupled rectangular cavity filled with air is realized using 3D printing. The geometry of the multilayered cavity is shown in Figure 4.12. The geometry consists of two identical cavities, i.e., top (I) and bottom (III) having length 50 mm, width 50 mm, and height 1.72 mm. The cavities are stacked on top of each other and share a common center plane in the middle (II) with a thickness of 2 mm. Two identical rectangular slots cut through the center plane (II), enabling coupling between the top and the bottom cavities. A 50 Ω microstrip line (length = 5 mm, width = 8.41 mm) extends out from the opposite side on both the top (I) and the bottom (III) cavities to excite and probe the cavities. Similarly, the center plane (II) is extended out on both sides (length 5 mm, width 20 mm) to attach the SMA connectors using silver paste. The resonance frequency of the multilayered cavity depends on dimensions of the cavity and coupling between the top and bottom cavity, which depends on the size and appropriate position of the slot in the center plane. The position and size of the slot is optimized using HFSS simulations to get maximum coupling. The simulated results in Figure 4.13 show the resonant frequency at 2.5 and 3.6 GHz, and measured results show the peaks are at 2.47 and 3.3 GHz. The mismatch in the results is due to the following reasons.

- 1) The VeroWhitePlus support material along the cavity walls contribute toward a higher effective dielectric constant (>1), and hence frequency peak shifts to the left.
- 2) Reduced air gap due to warping of center plane (II) during metallization, which is needed to be metallized on both sides.
 - 3) Lossy conductive silver paste on the connectors that affect coupling to the cavity.

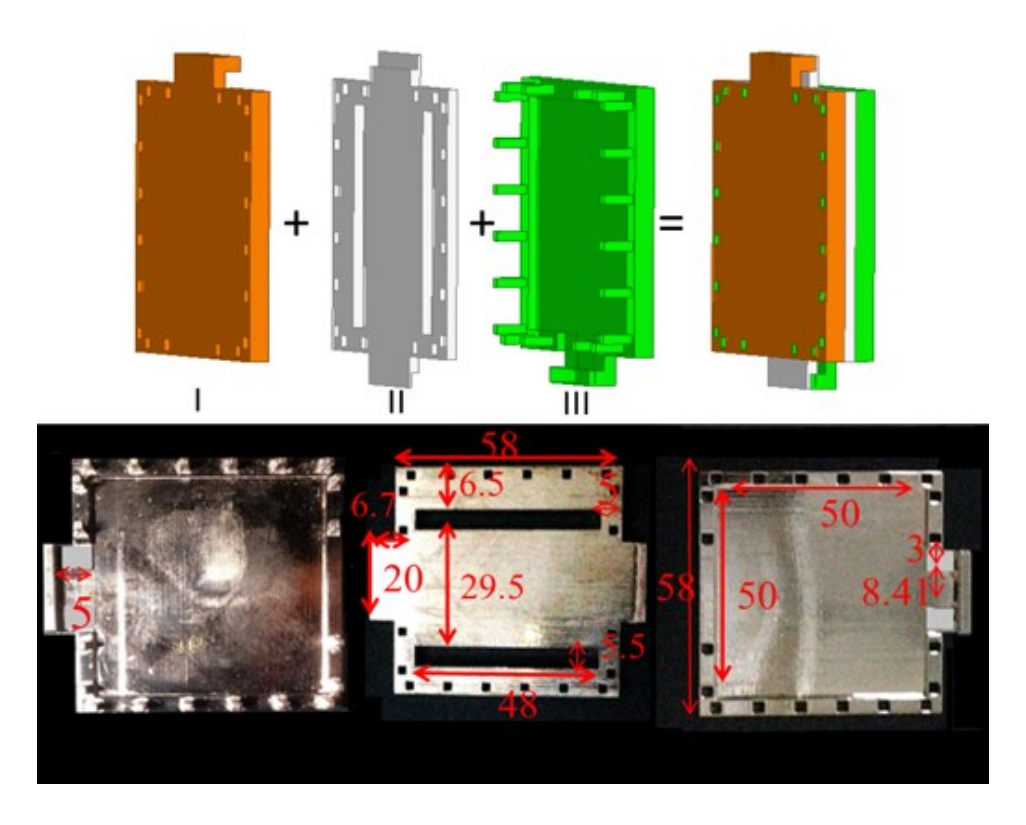


Figure 4.12: Schematic for multilayer cavity resonator structure and fabricated layers before assembly (Dimensions in mm).

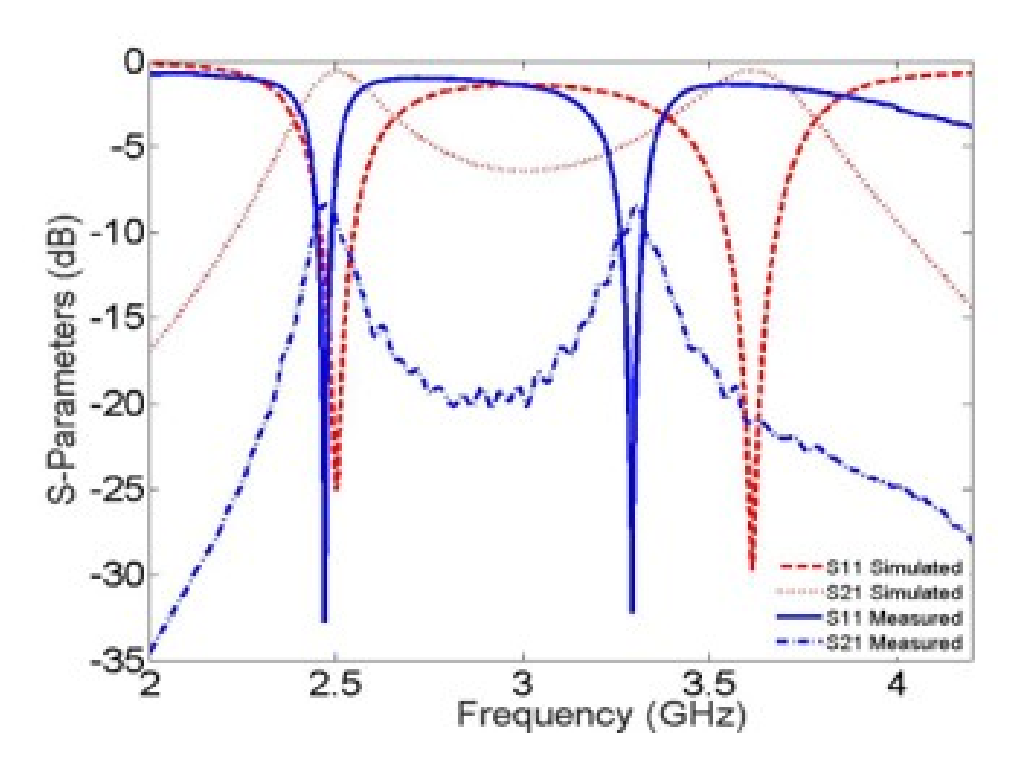


Figure 4.13: Simulated and measured S-parameters (reflection and transmission) of cavity resonator.

4.8 Challenges and Limitations

The fabrication technique presented in this chapter for RF and μ -wave circuits on air substrates offers environmental, cost, and design benefits. However, there are still significant challenges for use of these techniques at much higher frequencies. Some of those challenges are losses due to lower conductivity of silver paste, surface roughness of 3D printed material that is approximately 5 μ m, and warping of the 3D printed polymer during the metallization process. Here, silver paste is used to connect the SMA connectors as high-temperature soldering cannot be used with plastic material. Silver paste is relatively lossy and adds about 25 Ω of series resistance to the structure. Another reason for shift in measured results in comparison to simulation is due to the variation in air gap due to slight warping or bowing of the VeroWhitePlus support structure from heat generated during sputter deposition of metals and due to stress induced during electroplating. Low-temperature metallization process with reduced stress is necessary to avoid warpage. The high-frequency operation of devices fabricated using this process is also hindered by surface roughness of the 3D printed structure. Improvement in 3D printed surfaces is necessary to adopt printed structures for the design of millimeter and terahertz circuits.

4.9 Conclusion

3D printing is used to demonstrate RF circuits on air substrates. To demonstrate the benefit of 3D printing using air as a substrate, including analysis is performed showing that air substrates significantly lower the propagation loss for transmission lines and improve the gain of patch antennas. Low transmission loss is achieved when the propagating signal in a T-line is confined in the air region. The fabricated microstrip line shows a measured loss of 0.17 dB/cm at 4 GHz.

Three antenna designs fabricated using 3D printing are demonstrated. By creating an air gap between the radiating patches and the ground plane, the gain of the devices has been improved significantly over conventional microstrip patch antennas. The best performing patch antenna (coaxial fed) shows peak gain of 7.64 dBi (at 4.49 GHz) and 0.2 GHz bandwidth. The air-filled slot antenna performs better than a dielectric-filled slot antenna. It has a bandwidth of 0.98 GHz with a peak gain of 2.72 dBi. A three-metal-layer air cavity resonator is also demonstrated using 3D printing. Overall, the proposed process shows an approach to design low-loss air substrate using 3D printing. This allows for the design of novel circuits and also provides an avenue to overcome the challenge of the lack of availability of low-loss 3D dielectric materials.

Chapter 5

3D Printed Light-Weight components

5.1 Introduction

In the previous chapter, the advantages of using air as a subtrate is demonstrated by following a LEGO-like approach in fabricating RF components. Using the leverage on creating air substrates, this chapter focuses on the ability of 3D printing to fabricate light weight components such as waveguides which are traditional heavy. Lightweight and low-cost microwave components are required for space-borne and satellite communications, automotive and hand-held systems [62, 63]. The waveguides are chosen as example RF structure for demonstrating the light weight aspect of 3D pritning. Waveguides are broadly used for a variety of low-loss components such as filters, resonators, attenuators, and antennas. Hollow metallic waveguides are preferred over other waveguides due to their low-loss, high power handling capability, and improved isolation between neighboring structures [64]. In spite of these advantages, metallic waveguides are expensive to manufacture, and also due to the use of solid metal these waveguides are heavy. Metal waveguide structures are typically fabricated using techniques such as metal plate soldering, electroforming, dip-brazing and electronic discharge machining [65, 66]. 3D plastic printing with a LEGO-like assembly and subsequent metallization have been utilized to achieve a smoother surface with lighter weight [67, 68].

This chapter presents the fabrication of metal coated 3D printed plastic waveguides and

its utility in the design of X-band passive components such as filters, antennas, and antenna arrays. To achieve good metal coating, each of the passive components is bisected and printed in separate pieces, metalized and then assembled using a LEGO-like technique as the fabrication allows multi-level waveguide integration. All of the components here are printed using a professional-grade commercially available 3D printer (Objet Connex350) utilizing a photopolymer resin called VeroWhitePlus. Both clear and white colored resins were utilized here in the fabrication of waveguides. All the structures were blanked metalized, and all the design and simulations were validated using a commercially available FEM simulation tool, ANSYS HFSS (High Frequency Structural Simulator).

5.2 Fabrication

The waveguide structures are printed in two separate layers as shown in Figure 5.1. Lego-like support pillars and holes are printed to allow the two layers to snap together with each other for proper alignment. After print, the structures are first cleaned using iso-propyl alcohol (IPA) placed in an ultrasonic bath, and they are subsequently cured under UV light. Blanket metallization of 3D printed structures is carried out using a two-step process. First, a seed layer of Titanium/Copper (Ti/Cu: 100nm/500nm) is blanket sputter deposited on all sides. The Ti layer acts as an adhesive layer between the Cu and the plastic. Second, a thick layer ($\sim 5 \mu$ m) of Cu is electroplated. The structures are then assembled together as depicted in Figure 5.1(c). The measured surface roughness of the inner walls is approximately $\sim 5 \mu$ m. Figure 5.1(d) shows an example 3D printed waveguide structure after metal coating. A thin layer of highly conductive silver paste was used to permanently join the pieces together.

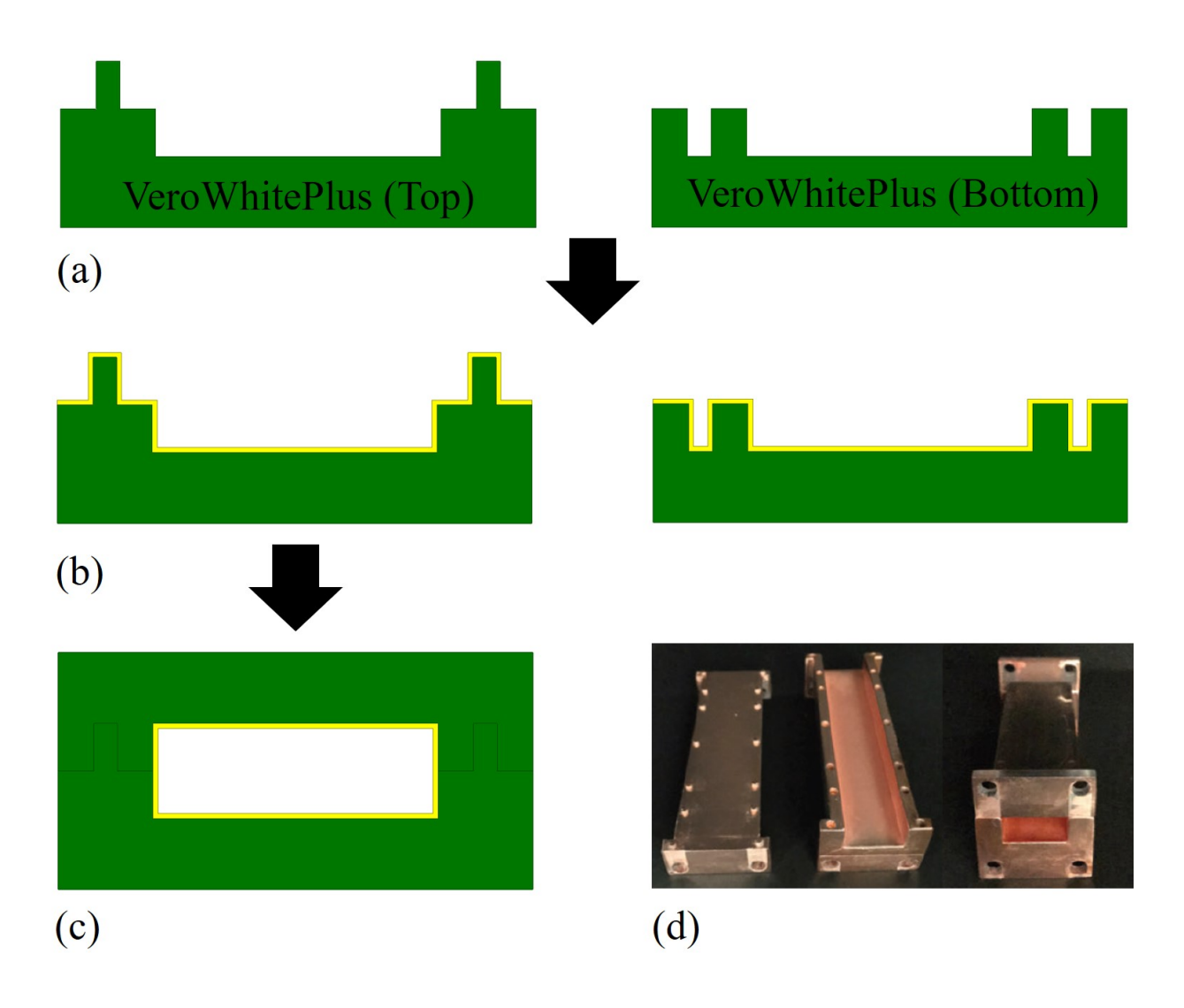


Figure 5.1: (a) 3D printed plastic parts, (b) parts are blanket metalized, (c) the parts are snapped together, (d) shown is an example waveguide after metallization.

5.3 Simulation and Measurement Results

5.3.1 X- and K-band Rectangular Waveguides

Rectangular waveguides are commonly used for low-loss high power handling applications. The cut-off frequency depends on the dimensions of the inner hollow region. For the X-band (8 - 12 GHz) design, the dimension used are: width (a) = 22.86 mm, height (b) = 10.16 mm and length = 100 mm as shown in Figure 5.2. For the K-band (18 - 27 GHz) design, the dimension used are: width (a) = 10.67 mm, height (b) = 4.32 mm and length = 50 mm. The printed waveguides, before metallization, are shown in Figure 5.3. The X-band waveguide after metallization is shown in Figure 5.1(d). For the measurements, these 3D printed straight sections were attached to broadband waveguide adapters at each end. Using vector network analyzer, VNA (N5227A), the S-parameters of these waveguides were measured over 5 13 GHz frequency range.

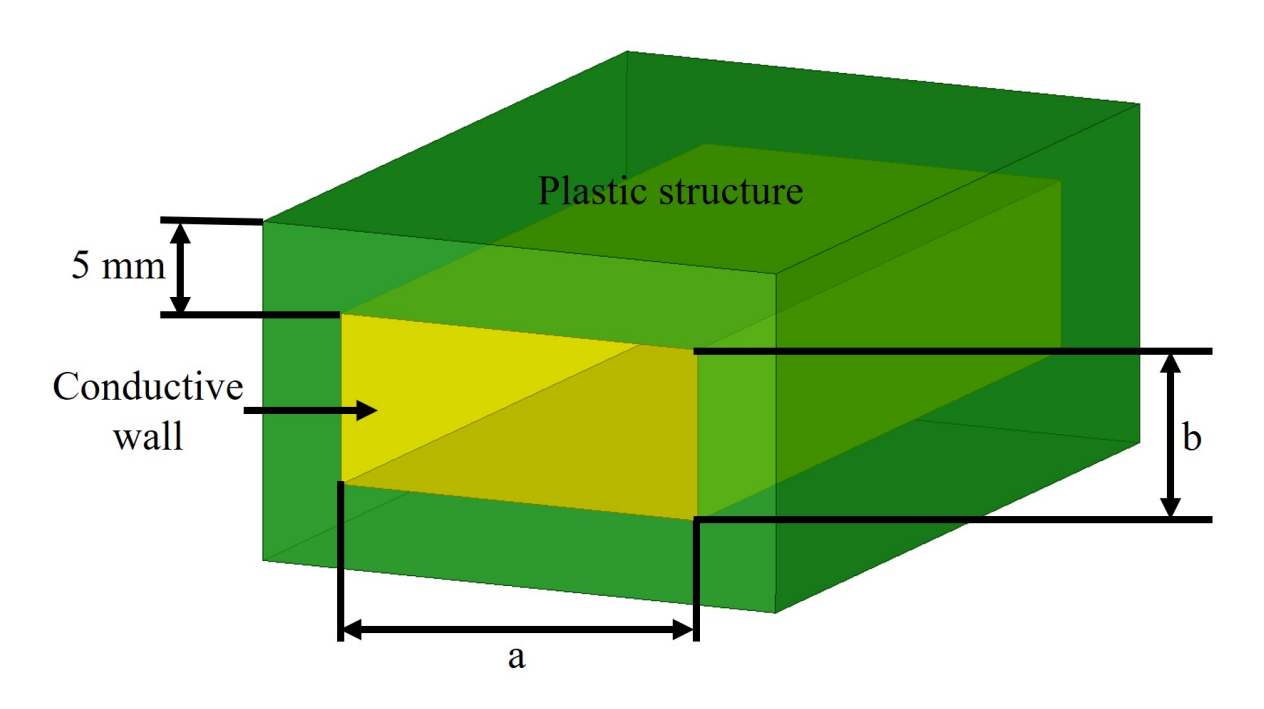


Figure 5.2: The dimension of the waveguide.

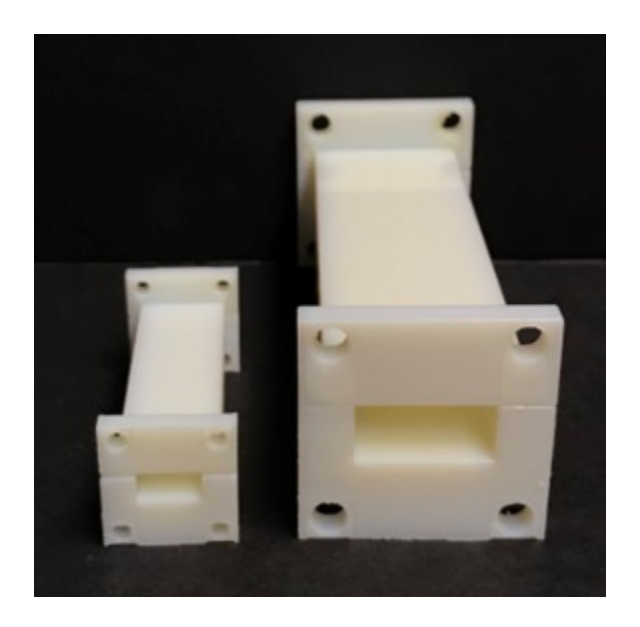


Figure 5.3: The pre-metallization 3D printed waveguide for K-band and X-band.

Figure 5.4 shows the simulated and measured S-parameters for the X-band waveguide. Overall, the simulation and measurement results match closely. The discrepancy can be attributed to surface roughness, fabrication tolerances of the printer ($\sim \pm 25~\mu m$), and the potential air gap between the two pieces when snapped together due to small warpage along the length. Furthermore, there is a slight misalignment between the coupler and the waveguide which leads to an impedance mismatch. Figure 5.5 shows the measured and simulated S-parameters of the K-band waveguide in which the simulation and measured results match closely. The discrepancy here also is largely due to surface roughness and misalignment between the coupler and the waveguide. However, in both waveguide designs, the loss is less than 0.1 dB/cm which shows the promising applicability of these printed components.

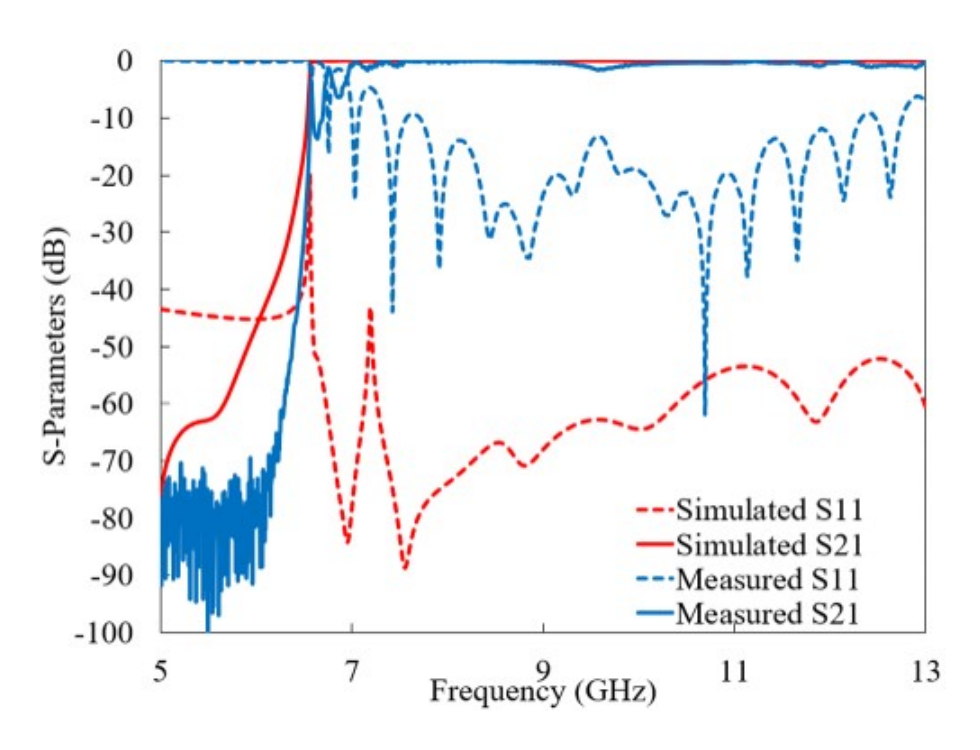


Figure 5.4: Simulated and measured S-parameters of the X-band waveguide (length = 100 mm).

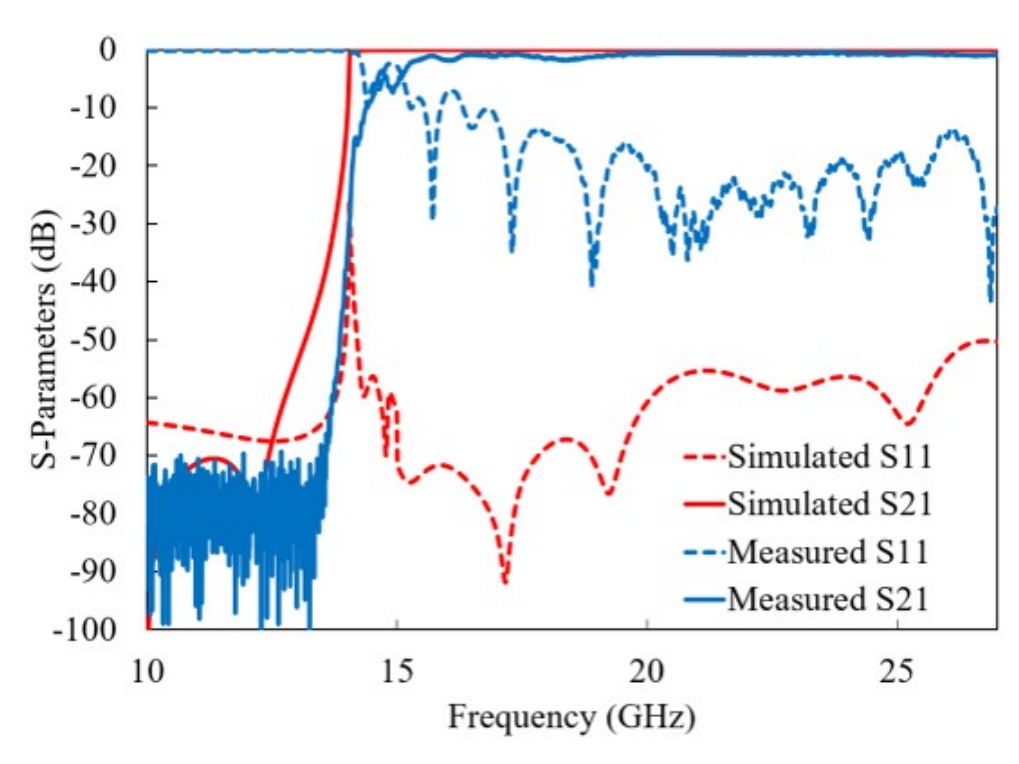


Figure 5.5: Simulated and measured S-parameters of the K-band waveguide (length = 50 mm).

5.3.2 Rectangular Waveguide Iris Filter

Waveguide filters are an essential part of a microwave system such as communication where a selective frequency band can be allowed (bandpass, low pass or high pass) or blocked (bandstop). One of the popular rectangular waveguide based filter is the iris filter [69]. It consists of multiple metal partitions in the waveguide to form capacitive and inductive regions (high and low impedance regions). Figure 5.6 shows the schematic of an iris filters along with the dimensions used in the design. The 3D printed iris filter before and after metallization is shown in Figure 5.7 (a) and (b), respectively. Simulated and measured results of the iris filter are shown in Figure 5.8, and the results match closely. The slight discrepancy of the results can be accounted due to the print resolution as well as the surface roughness that cause the extra loss in the measurement. A slight shift in the resonance frequency can be attributed to the fabrication tolerances of slots. In addition, for this structure, there is a slight misalignment between the input port and the waveguide coupler which leads to a higher transmission loss, and it can be seen in the measured S₂₂ results.

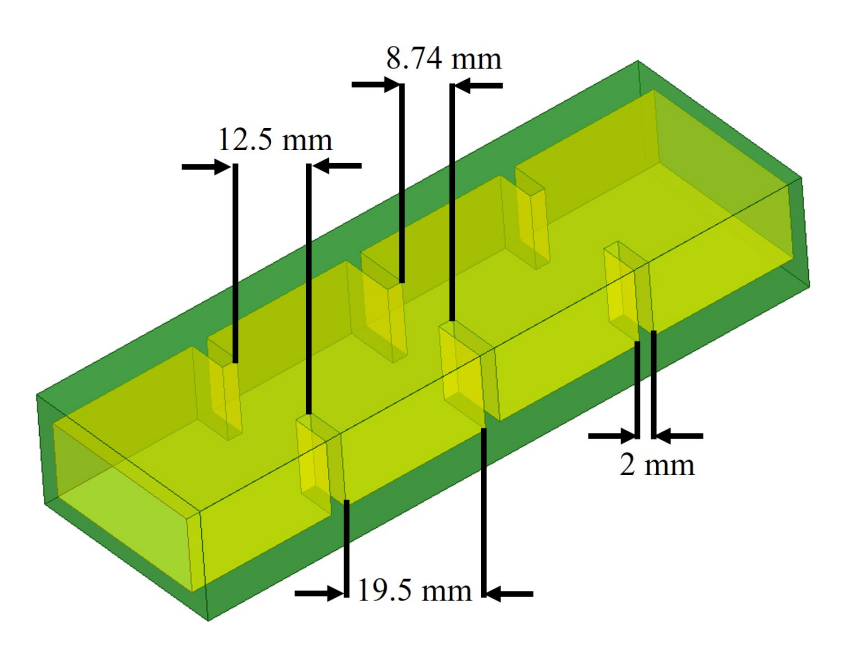


Figure 5.6: Schematic of an iris filter.

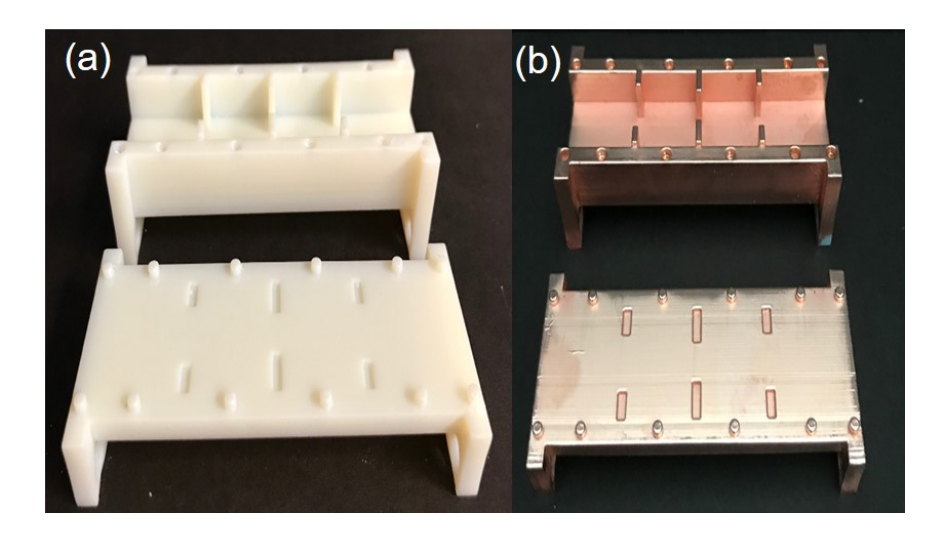


Figure 5.7: Sections of the fabricated iris filter (a) before and (b) after metal coating.

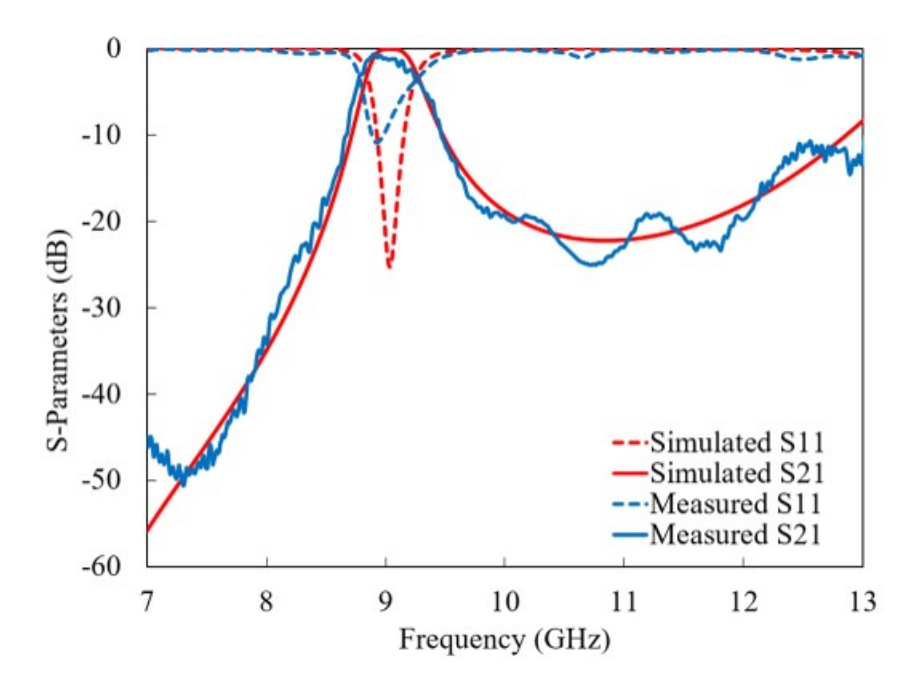


Figure 5.8: Simulated and measured results of the waveguide iris filter.

5.3.3 Leaky Waveguide Antenna

Leaky wave antennas are simple to design and implement as compared to antenna arrays for high gain designs. There are several technologies that can be used to design a leaky wave antenna (e.g., microstrip, substrate integrated waveguides, etc.). Among these, the rectangular waveguide with a slit along the structure, see Figure 5.9, is attractive due to the low-loss nature. In this leaky waveguide design, the slit length, height, and depth were designed to achieve high gain at 9 GHz. Figure 5.10 shows the measured and simulated return loss of the antenna, which shows a wideband operation. The slight discrepancy in these results is due to similar reasons discussed earlier. Figure 5.11 shows the simulated and measured radiation pattern at 8.8 GHz. The measured gain is approximately 10 dBi. The radiation patterns were measured using Satimo StarLab-18 near-field antenna measurement system. The results show that the simulated and measured results match closely. It also demonstrates that slit dimensions, that are critical in a leaky wave antenna design, can be fabricated with high precision using 3D printing.

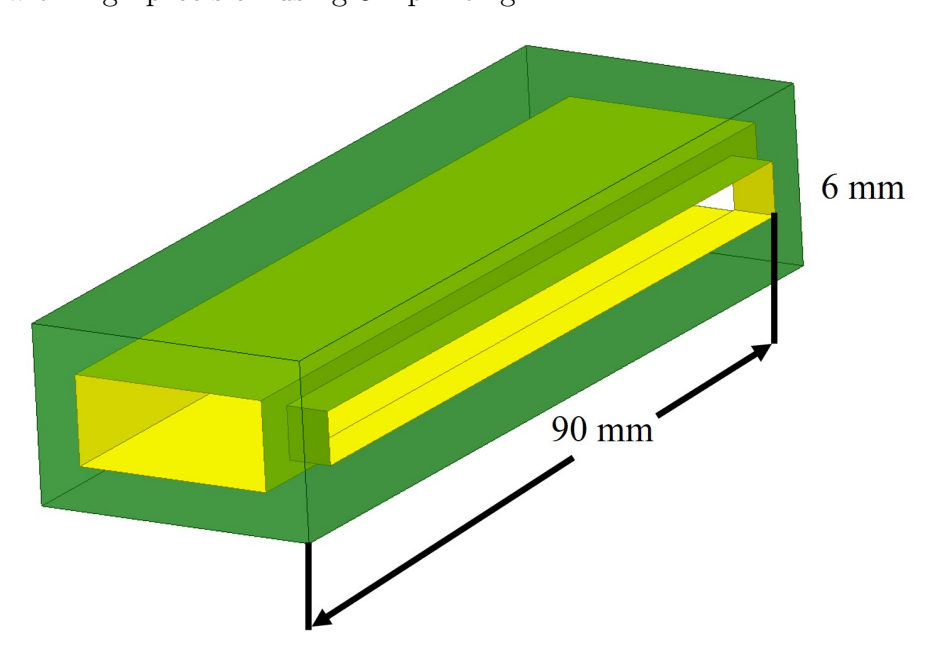


Figure 5.9: X-band leaky waveguide antenna design.

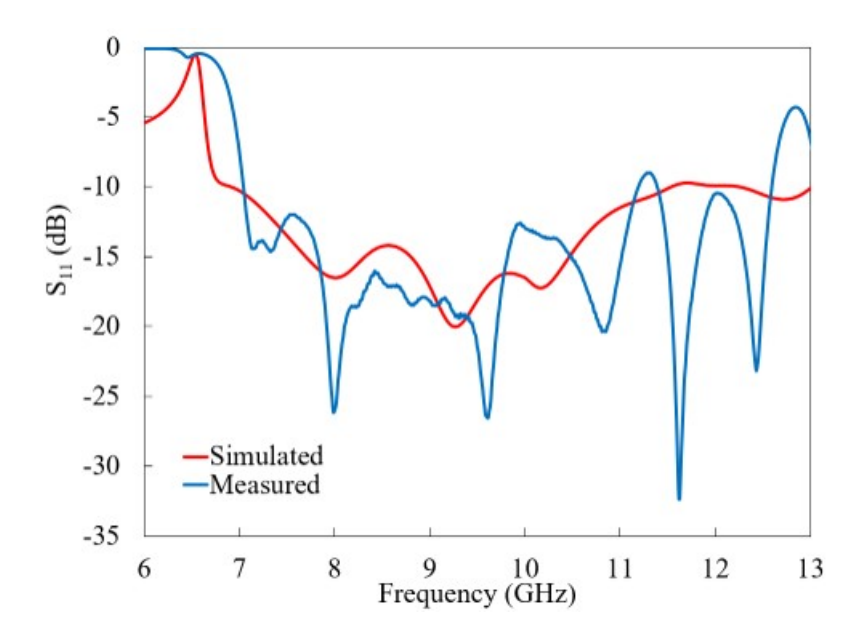


Figure 5.10: The simulated and measured reflection coefficient of the leaky waveguide antenna.

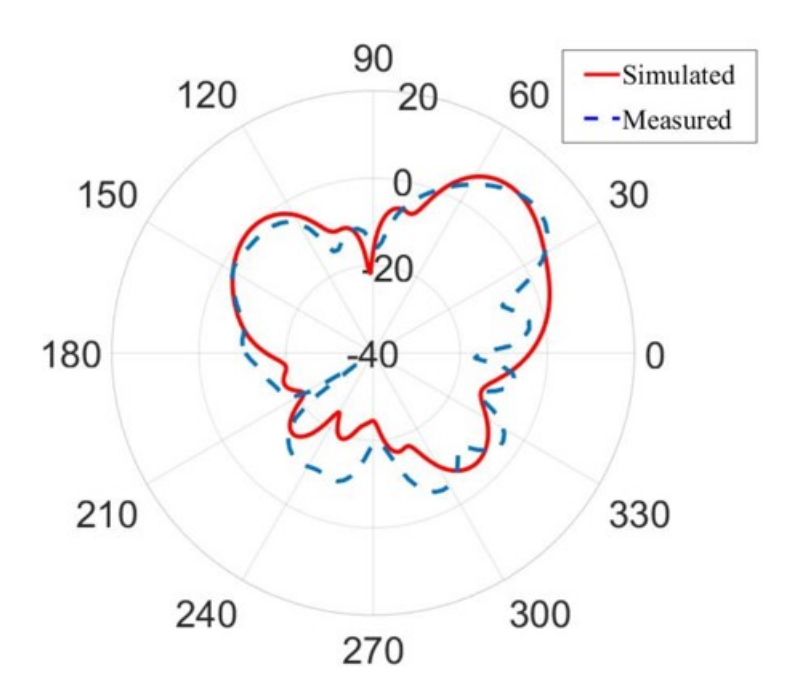


Figure 5.11: Measured and simulated radiation pattern in the H-plane of the leaky waveguide antenna at $8.8~\mathrm{GHz}$.

5.3.4 Cavity-Backed Slotted Antenna Array

To further demonstrate the possibility of fabricating complex antenna structures through 3D printing, a cavity-backed slotted antenna array was designed and fabricated. Figure 5.12 shows the cross-sectional view of the 2x4 slotted array based on the design presented in ref. [70]. Figure 5.13 shows the key printed components before and after assembly. The measured and simulated S_{11} are shown in Figure 5.14. Figure 5.15 shows the measured gain as a function of frequency, it shows that high gain over a wide band can be attained using this design. Also shown in the inset of Figure 5.15 are the simulated and measured radiation patterns at 7.5 and 8.7 GHz, these results match closely.

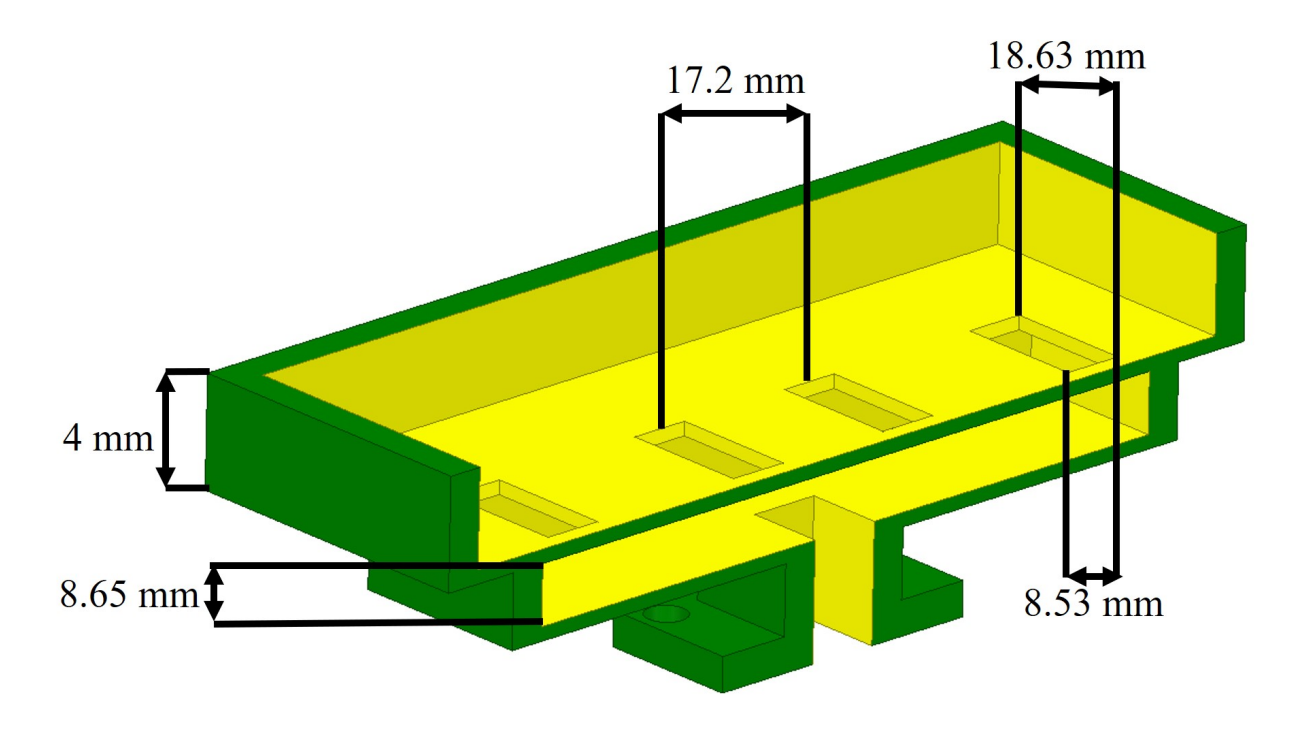


Figure 5.12: The cross-sectional view of the cavity back slotted antenna array.

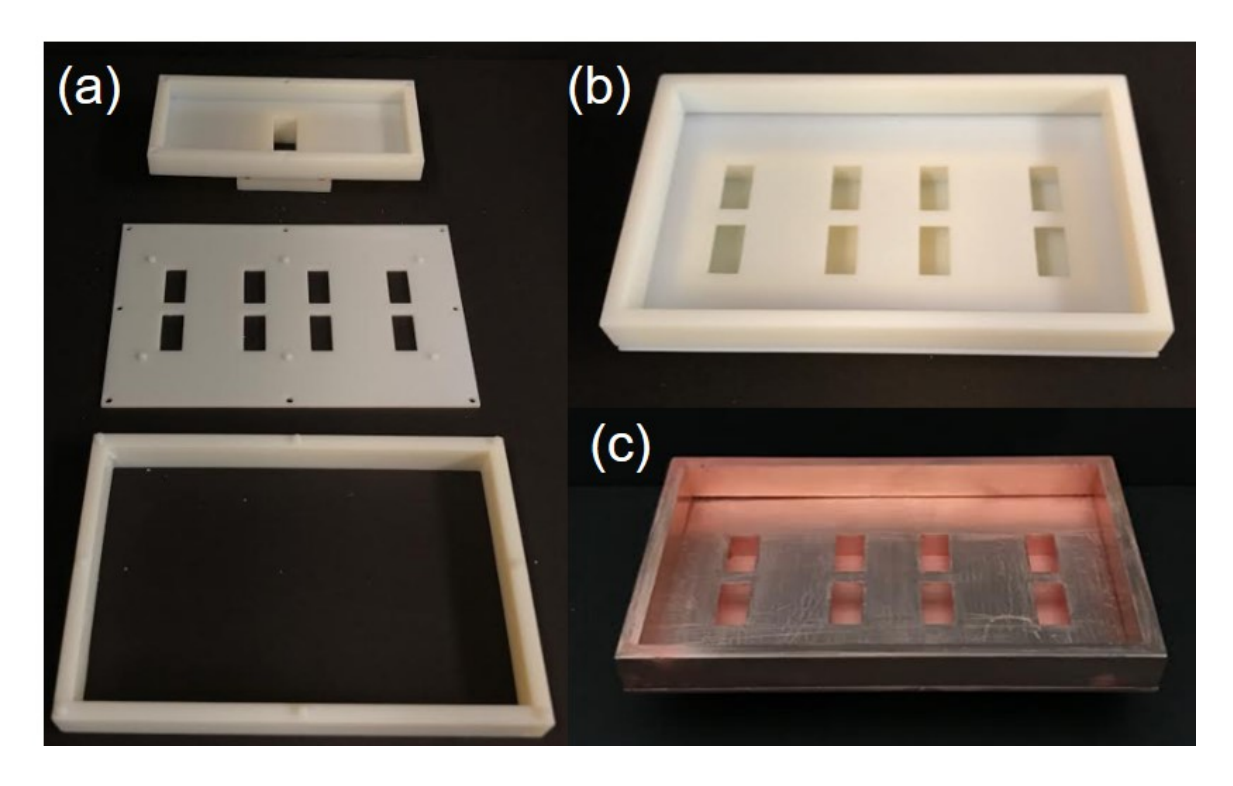


Figure 5.13: The 3D printed structure of the cavity-backed slotted antenna (a) before and (b) after assembly, and (c) assembled after metal coating.

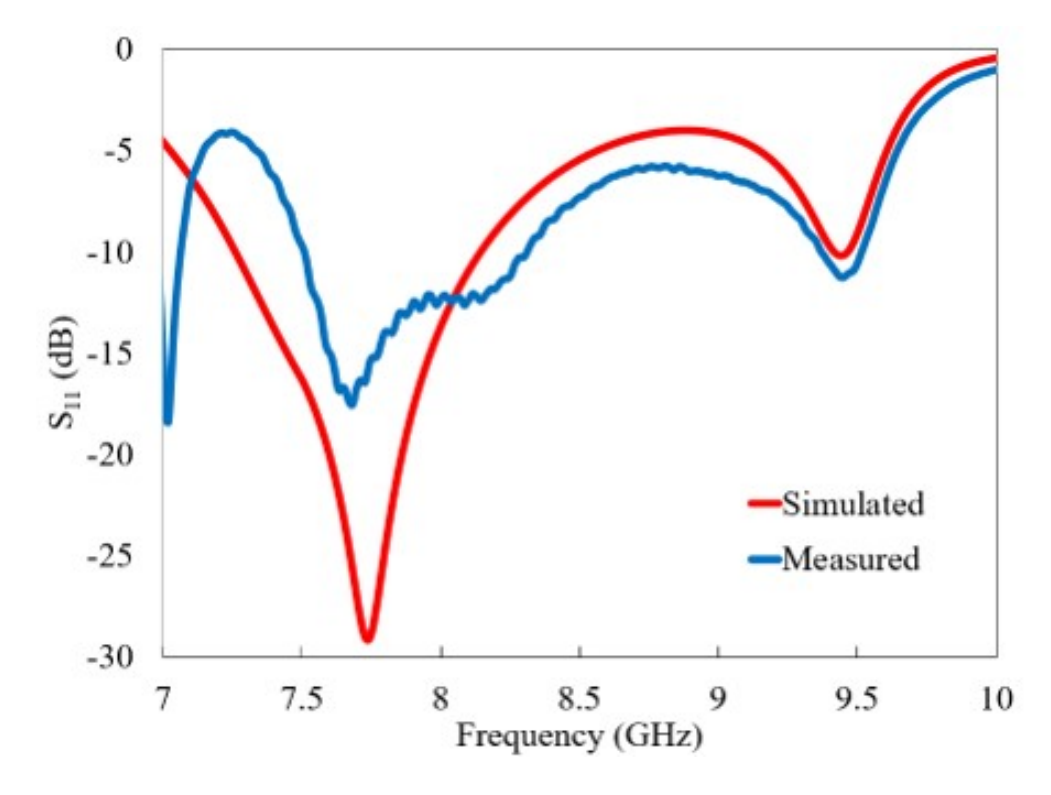


Figure 5.14: Simulated and measured S_{11} of the cavity-backed slotted antenna array.

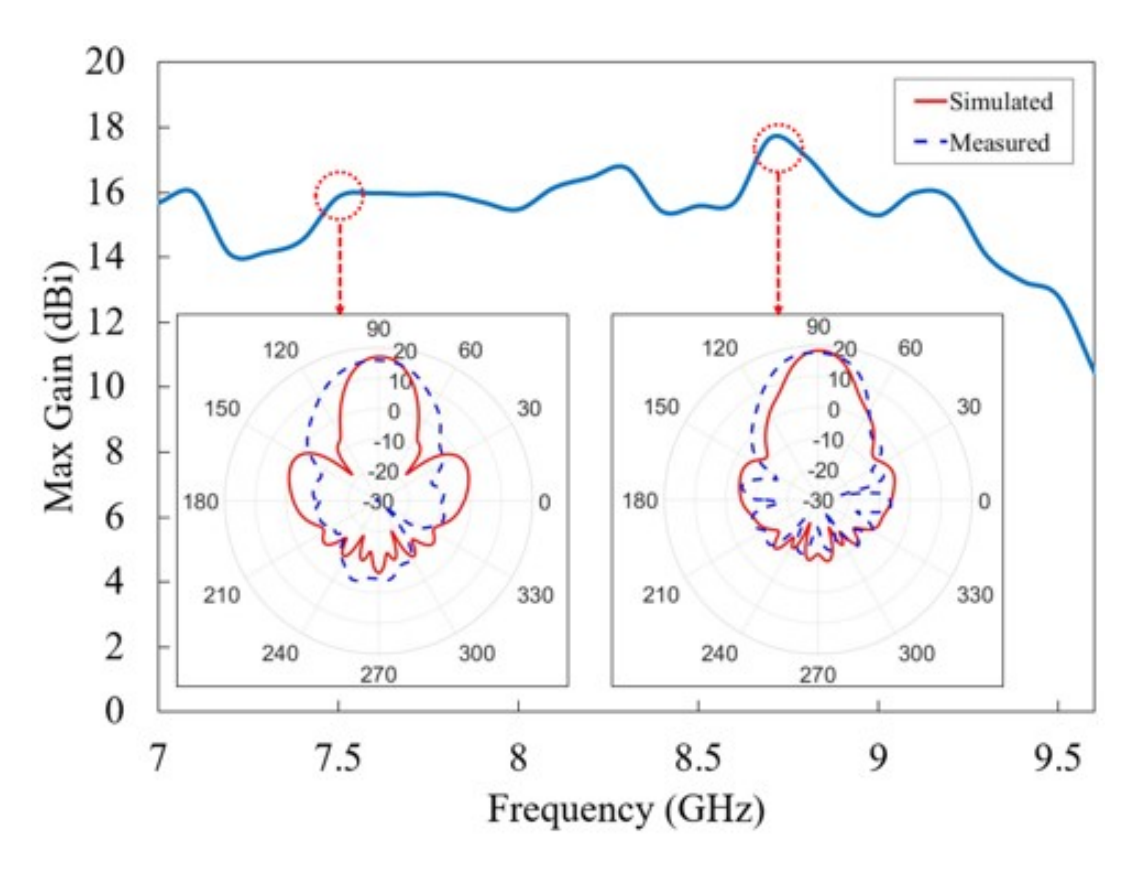


Figure 5.15: Measured gain of the slotted array. The inset shows the simulated and measured radiation patterns at $7.5~\mathrm{GHz}$ and $8.7~\mathrm{GHz}$, respectively.

5.4 Conclusion

Several 3D printed rectangular waveguide based light weight passive components are demonstrated in this chapter. The results of the rectangular waveguides show that low-loss X-band and K-band light-weight plastic waveguides are possible. The iris filter demonstrates that 3D printing allows the fabrication of low-loss filters having similar performance to the conventional metallic structures. Overall, this chapter demonstrates that high frequency, low-loss, light-weight waveguide based passive structures can readily be fabricated using 3D plastic printing followed by metal coating. In particular, 3D printing reduces the time between design and prototyping and, a single tabletop tool can be used to fabricate complex structures.

Chapter 6

Embedding process for passive and active components

6.1 Introduction

In the preceding chapters, 3D printing is demonstrated as a best candidate for fabricating RF components and circuits. In order to realize a fully 3D printed system, three novel processes for embedding active and passive components are presented in this chapter. Emerging wireless applications such as smart home /city [71], wireless body area networks [72], requires integration of a diversity of technologies, such as analog/RF circuits, sensors, digital CMOS circuits, antennas, polymers, new materials, packaging and interconnections. In addition, future compact hand-held wireless systems requires highly-integrated packaging schemes with smaller footprint and reduced parasitics to realize miniaturized functional modules for efficient operation at microwave and mm-wave frequencies [73]. Embedding of semiconductor chips as integral part of the substrate is a promising packaging technology offering advantages such as miniaturization, superior electrical performance due to shorter interconnects, and an inherent self packaging approach. In literature, embedded devices are manufactured by conventional micro-machining, laser drilling, laser-based direct wiring, stereolithographic, and thermal embedding techniques [74–76]. However, the biggest challenge with these techniques is misalignment between different layers during lamination, need for intermediate layers and complex fabrication steps. In addition, these technologies present shape limitations, material compatibility issues, significant cost impact [77], and have to be defined at the beginning of the device design to fit within the whole assembly process. Therefore, its very hard to achieve customization i.e., embedding chips with different sizes, shapes and heights using the conventional fabrication processes. An approach that allows seamless integration of passive and active components together while avoiding fabrication complexity is needed to meet the next generation of packaging challenges. Packaging schemes which allow shorter and impedance-matched interconnects between the substrate and the chip are required to maintain signal integrity.

Embedding process based on the AM have much relaxed design rules in comparison to its conventional counterparts, and the process allows embedding of components in a free formable substrate. AM based embedding process can be used to advance SiP solutions, which not only includes active and passive components but also includes antennas, sensors, and actuators, which cannot be integrated readily using conventional embedding techniques. Moreover, AM based approaches can simplify this complicated embedding process by merging the steps of embedding and encapsulation onto its substrate, in addition to off the shelf encapsulation and packaging.

This chapter presents an approach which allows embedding of active elements as integral part of the substrate or structure using additive manufacturing as a tool to fabricate high functional density packaging systems. Figure 6.1 shows the proposed concept towards a fully 3D printed (polymer and conductive printing) RF package. Different active and passive RF components, MEMS, lens, antennas are integrated within different layers and connected electrically through vias and interconnect. Approaches such as flip-chip, chip-in-cavity as well as face-up assembly techniques can be used in a single package fabrication.

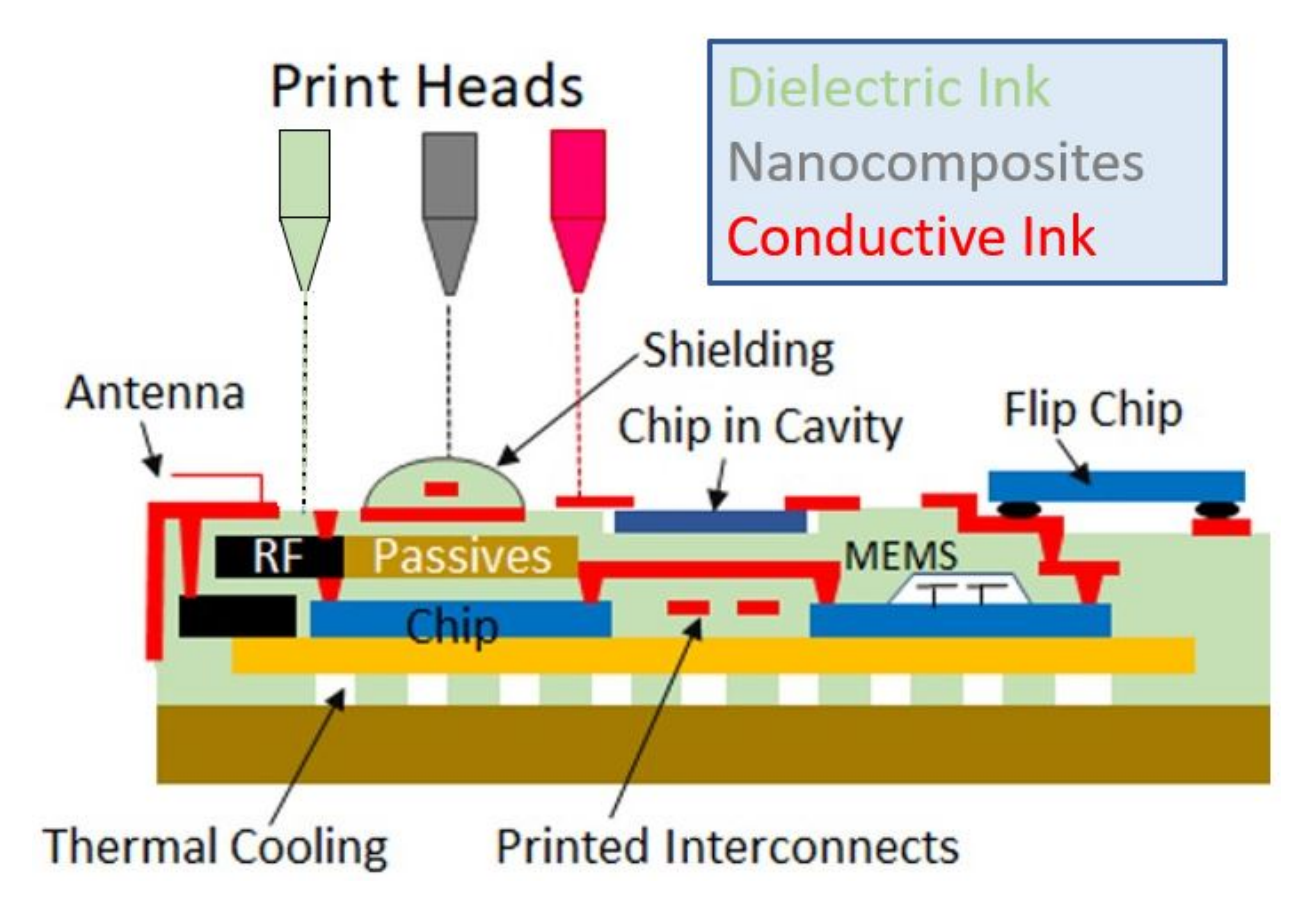


Figure 6.1: Envisioned fully 3D printed RF systems.

3D printed technology is utilized for embedding pre-packaged chips (size 1.7 mm x 0.9 mm and height 0.7 mm mold compound) into different microwave circuits. The ability to print any size and shape provides the solution for fabricating high-performance components critical to size-sensitive applications like those in the wireless and hand-held device markets where component density is increasing dramatically. The precise edge definition and repeatability of the 3D printing process are particularly relevant to high-frequency requirements. Various tunable RF circuits such as a T-line resonator, metamaterial-inspired phase shifter, and a patch antenna are designed and demonstrated. Three different fabrication processes for embedding are proposed and demonstrated.

6.2 Analysis

To demonstrate the benefits of the proposed embedded actives using 3D printing process over the traditional wire bonding techniques, simulations were carried out using the commercially available simulation tool ANYSYS High Frequency Structure Simulator (HFSS®). Vias and pads were also included in the simulations. Figure 6.2(a) and Figure 6.2(b) shows the schematic cross-section view of each structure used in the simulation. A 50 Ω microstrip transmission line structure connected to a diode is used here as a test structure. Air (1.52) mm) is chosen as the substrate material to directly show the impact of different techniques (embedded vs. wire bonding) by eliminating the influence of the substrate material losses. The embedded structure has via connecting to both pads of the diode, and the wire bonding structure has two wires connecting to the diode pads. Simulation is done with one diode connected (i.e., single via connected). Figure 6.2 shows the S-parameters of the microstrip connecting to a diode using embedded and conventional wire bonding structures. Both structures show good transmission signal, S_{21} , at low frequencies. However above 7 GHz, the S_{21} of the wire bonding structure decreases while the embedded active structure still maintains good transmission characteristics. The wire-bond has an insertion loss of 2.1 dB at 7 GHz, while the embedded structure shows 0.76 dB at the same frequency. The difference in S_{21} between the two approaches indicates the associated parasitics (resistance, inductance and capacitance) in the wire bonding method that cannot be neglected at high frequencies. In contrast, the embedded structure has considerably low-parasitics, and leads to the realization of high cutoff frequency circuits and systems.

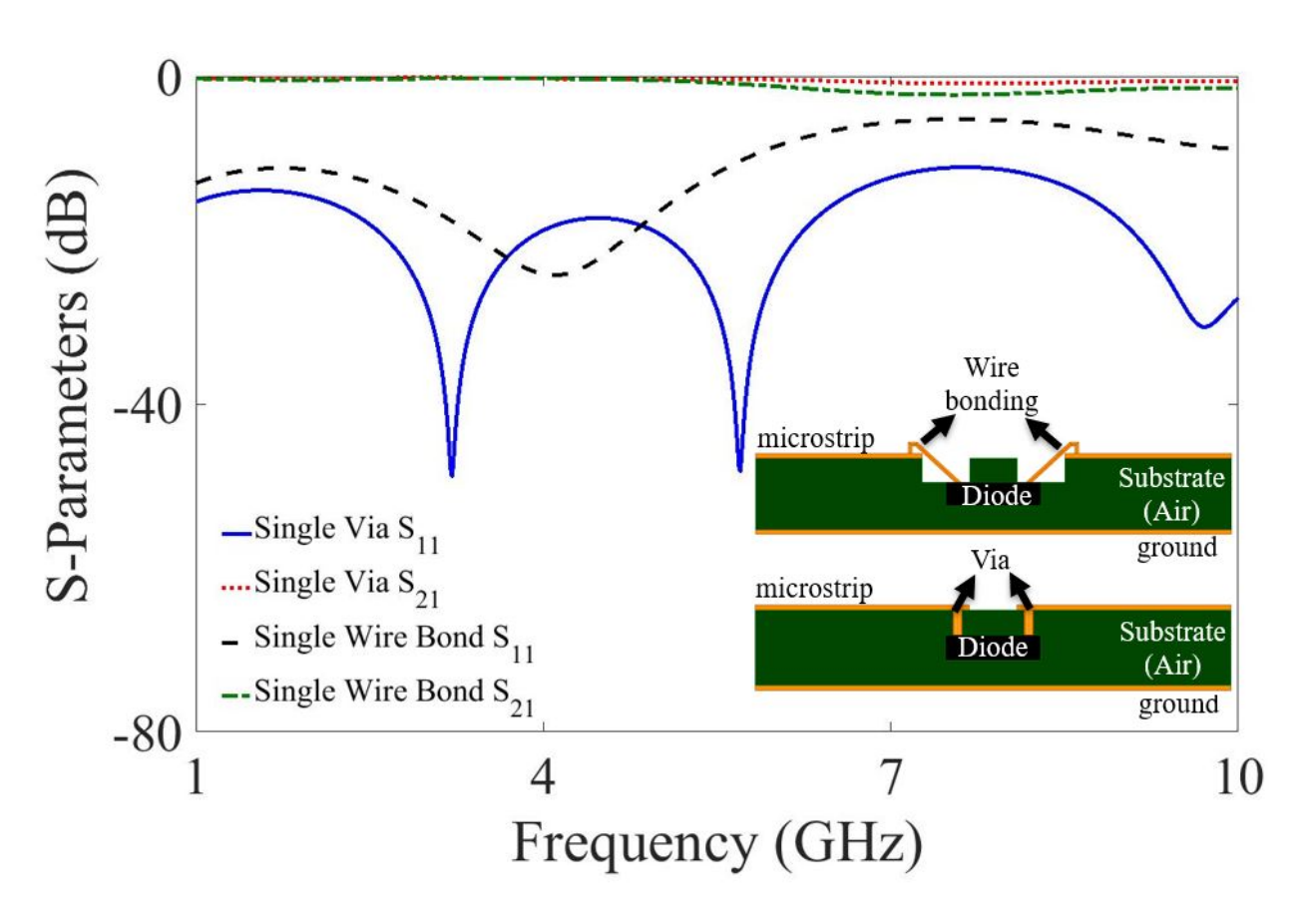


Figure 6.2: The comparison of S-parameters of simulated for (a) embedded active structure using via, and (b) embedded active structure using wire bonding.

6.3 Material characterization

The components that are presented demonstrating the embedding techniques are fabricated using Formlabs photosensitive high-temperature acrylic polymer whose electrical properties are not reported in open literature. The material is first characterized in the frequency band of interest before designing the RF circuits. The transmission/reflection method proposed by Nicholson-Ross-Weir (NRW) is used to extract the dielectric constant and loss tangent of the cured photopolymer [78,79]. Samples were characterized in both the F-band (4.9 to 7.05) GHz) and the X-band (8.2 to 12.5 GHz) using waveguides from Maury Microwave and the Agilent technologies ENA series Network Analyzer (E5071C). The calibration was done at the ends of the waveguides using manufacturer provided SOL (short, open, load) calibration kit. Samples were printed slightly larger than the waveguide dimension and mechanically polished to fit the waveguide as tight as possible. The width of the sample for the F-band was 5.23 mm, and that of the X-band was 6.73 mm. The samples were inserted into the waveguide and the 2-port S-parameters were measured. All measurements were performed 5 times and the data was averaged out 64 times. The data was analyzed using MATLAB by shifting the calibration plane and de-embedding the data to either side of the sample. Figure 6.3 shows the measured dielectric constant and loss tangent for the acrylic photopolymer.

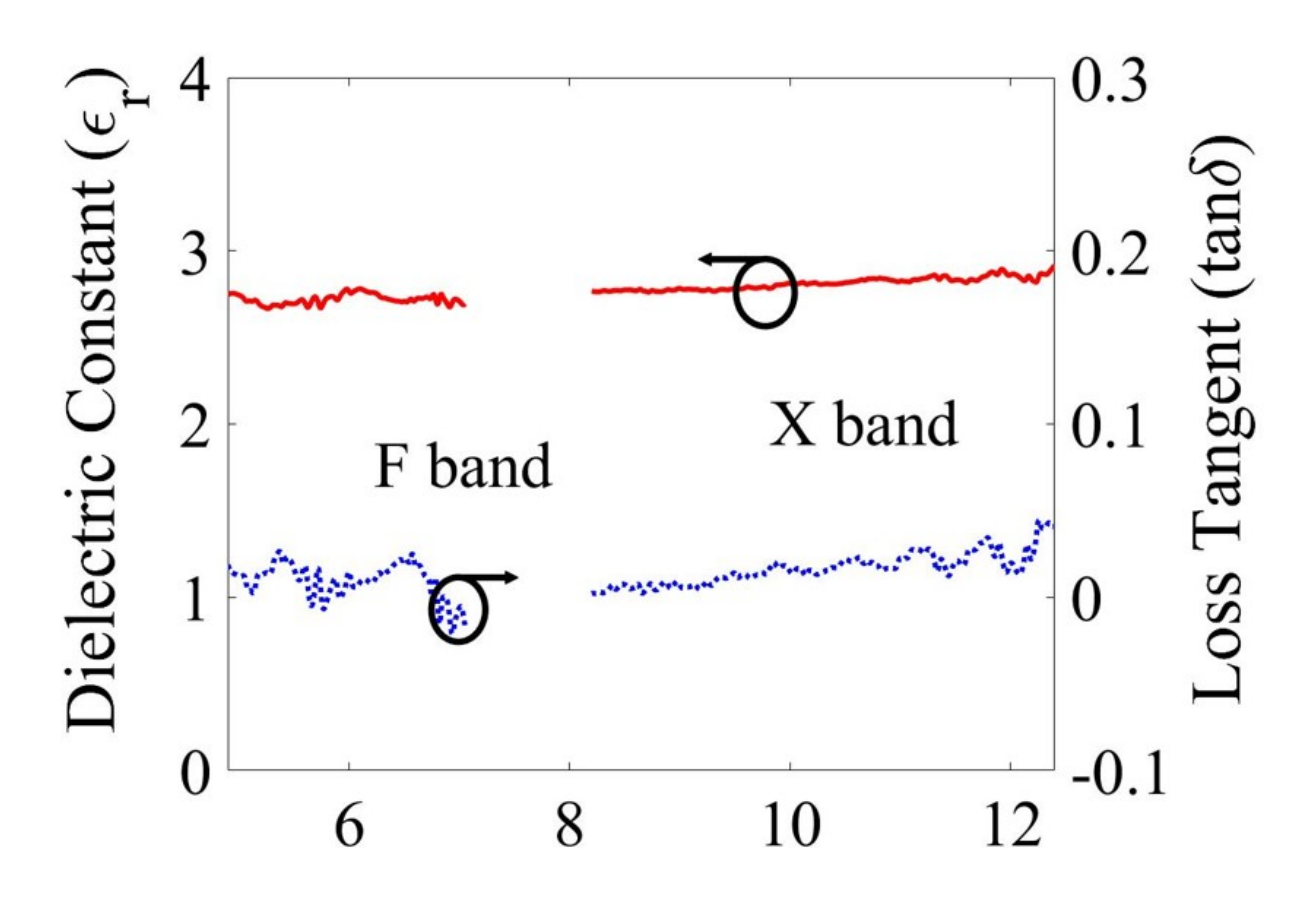


Figure 6.3: Measured dielectric constant and loss tangent of the acrylic photo polymer.

6.4 Fabrication Process

Commercially available Formlabs 3D printer was used in fabricating the circuits. It is based on the stereolithography (SLA) technique which uses a laser to locally cross link the liquid resin into a hardened structure using a process called photopolymerization, as shown in Figure 6.4. The 3D printing process can print high aspect ratio structures which are needed to create vias and suitable base structures (pockets) for embedding of chips with different thicknesses with tight tolerance. A print resolution of approximately 100 μ m in the X-Y plane and 25 μ m in the Z-plane can be readily printed. The machine can be temporarily halted during printing which allows for insertion of chips in the pockets before continuing to print the follow on layers. The platform holding the samples can readily be removed during these temporary halts and the remounting process has a tolerance of less than 25 μ m in the X-Y plane. Dimensions of the individual chips were measured prior to printing the base structure in order to achieve a good fit in the pocket while mounting. The dimensions of the pocket were made larger by 100 μ m on all sides relative to the chip size for ease of mounting. The size accuracy is essential for embedding process to avoid any gap between the diode and cavity side walls which can lead to further misalignment of via and the pad. Forming high accuracy vias using wet-etching process is very difficult, hence most conventional techniques uses laser drilling, plasma etching or micro-machining to build cavities. Therefore 3D printing provides a better solution with less material waste and less number of fabrication tools.

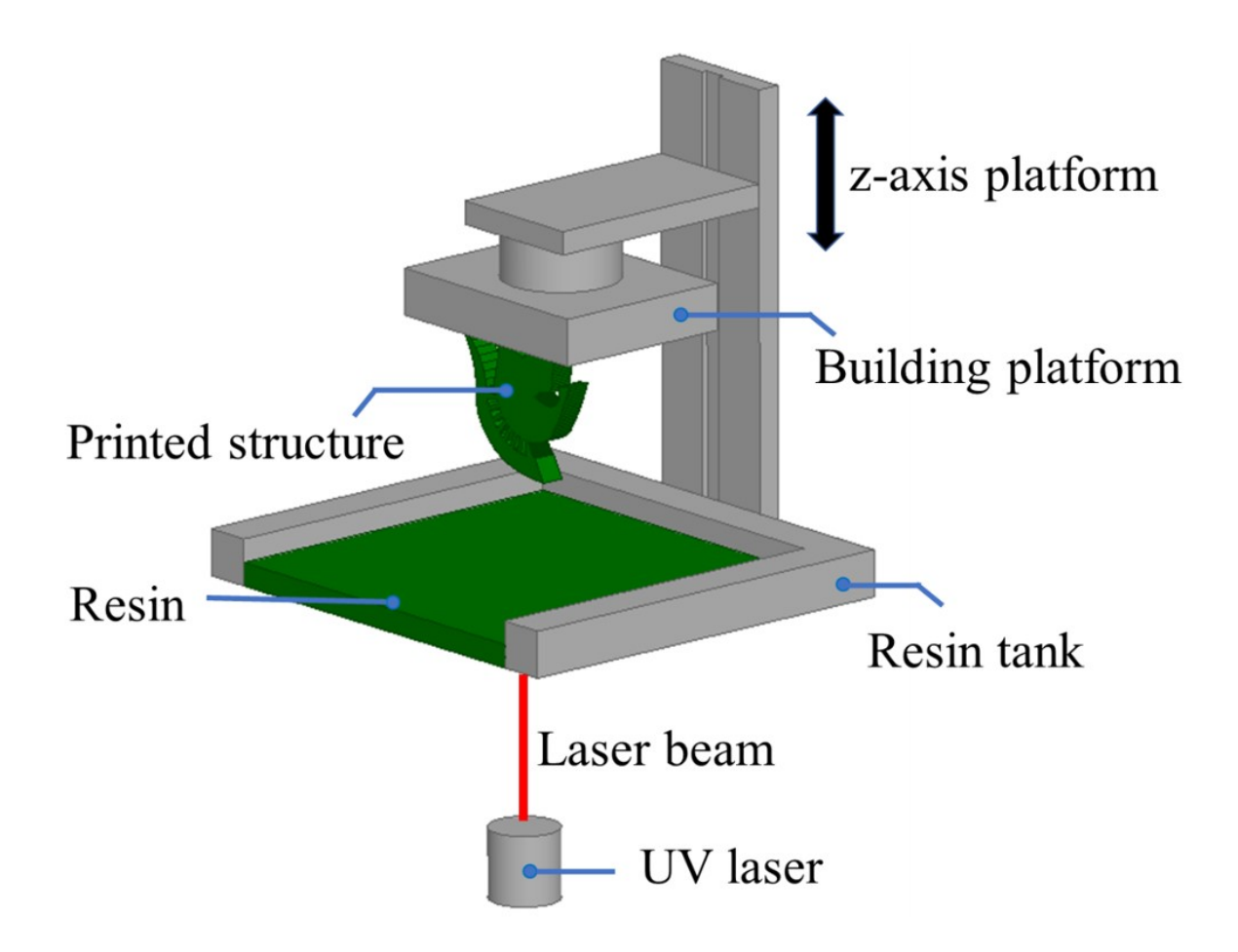


Figure 6.4: Schematic of the Formlabs 3D printer.

Figure 6.5 shows three different embedding techniques, face-up, face-down, and side-mount, for mounting of active devices. To demonstrate these techniques in a single structure, a cube (dice) is 3D printed, and Schottky diodes (BAT 15-03W) with dimensions 1.7 mm x 0.9 mm and thickness of 0.7 mm are embedded on all six faces of the cube during the print process. On the top face of the cube, the chip is embedded using face-up approach, in the bottom face, face-down approach is used and in the rest four sides of the cube, side-mount approach is used. The vias (0.45 mm x 0.3 mm) are printed with 60^{0} slope so that the sidewalls can easily be coated during blanket metallization. The process involves three critical steps. The first step of any embedding process (face up, face down or side mount)

is printing of the base (support) substrate or the carrier structure. Base substrate with a predetermined layer thickness (approximately 1.2 mm) is 3D printed with chip pocket or cavity matching precisely to the specific chip to be embedded. Next, the chip is placed in the pocket and layers are further printed on top to encapsulate the chip. The printed structures are cleaned using isopropyl alcohol (IPA) and nitrogen gas (N₂) to remove excess resin from the vias and chip pocket. It is followed by photopolymer curing for 10 minutes using a UV lamp. Longer post printing exposure lead to warpage and were avoided. For the face-up chip assembly, the chip is embedded into the 3D model with the contact pins facing upwards as shown in Figure 6.5(a). In the face down fabrication technique, the chip is embedded with contact pins facing downwards as shown in Figure 6.5(b). Similar to the face-up process, the printer is paused at a predetermined layer, and the chip is placed into the pocket. For the side mount technique, the chip with extended pins is embedded with the pins facing upwards as shown in Figure 6.5(c). To form metal patterned structures, a thin metal seed layer (Titanium/Copper:Ti/Cu:500nm/5000nm) is first blanket sputter deposited on the printed parts followed by Cu electroplating to achieve a total thickness of approximately 5-6 μ m of Cu. The metal layer is patterned using a damascene-like process. Figure 7 shows the printed cube, before and after metallization, with diodes embedded on all six sides. All diodes showed similar behavior and demonstrates a versatile process to embed active in 3D printed structures, and the process is repeatable.

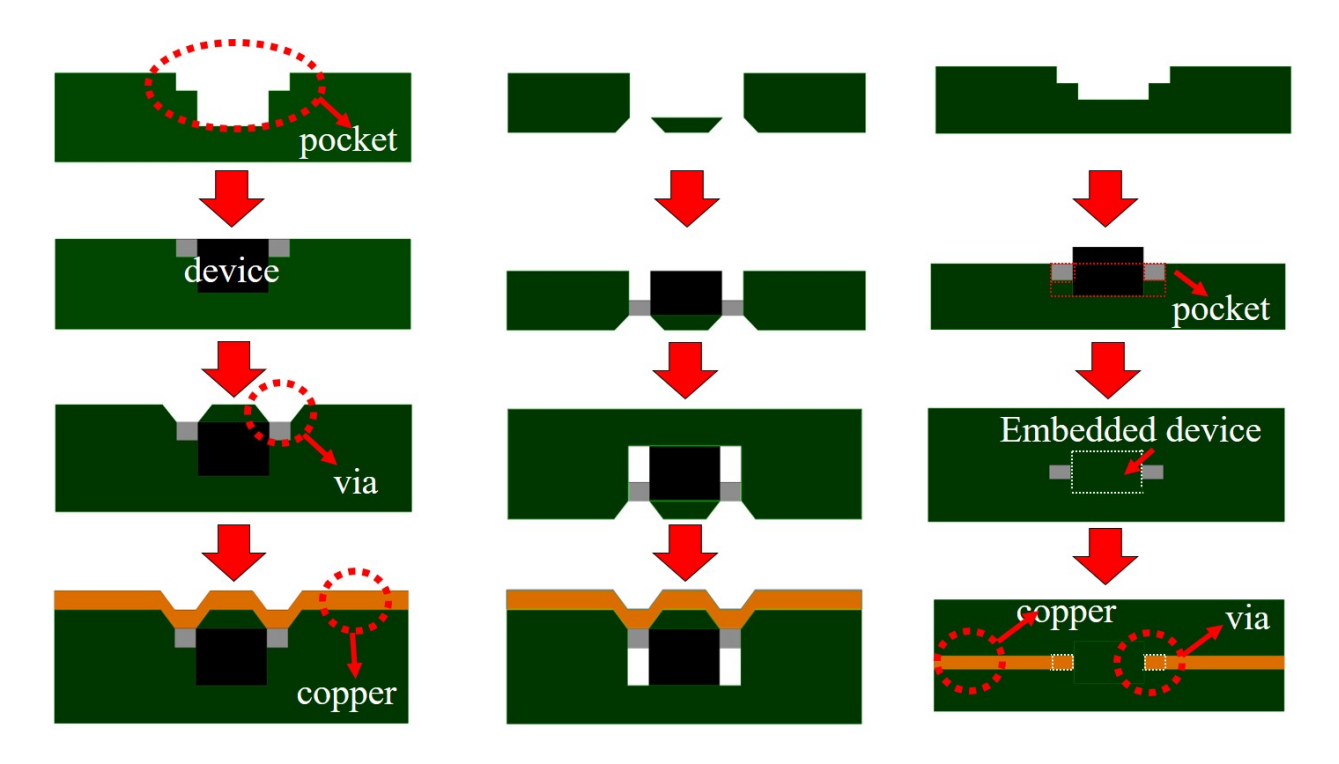


Figure 6.5: Fabrication steps for 3D printing of different embedding schemes: (a) Face-up (b) Face-down, and (c) Side-mount.

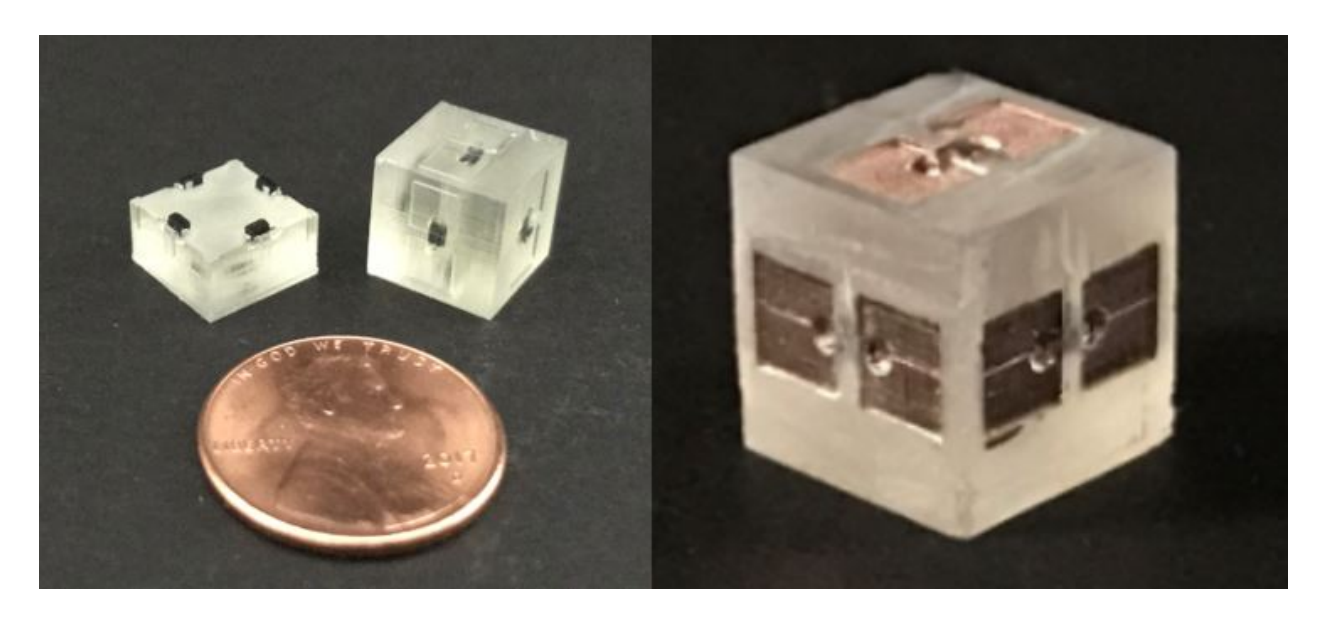


Figure 6.6: Measured I-V characteristics of the Schottky diode embedded in the cube structure.

6.5 Measurement and Results

RF components such as the T-line resonator, metamaterial-inspired phase shifter, and a tunable patch antenna were designed and fabricated to demonstrate the capabilities of the 3D printer in embedding active components within the 3D printed plastic structure. First, DC measurements of a diode were carried out after multiple thermal cycles to demonstrate reliability of the structure.

6.5.1 Thermal cycling

The material used in traditional embedding processing has to meet the thermo-mechanical properties for low warpage and should avoid profound die shift after the embedding and metallization process. Therefore, it is essential that the polymer material used for 3D printing should have a low coefficient of thermal expansion (CTE), and the material should withstand high post process temperature (e.g., soldering). In this work, edge mount SMA connectors are soldered to allow characterization of the RF circuits. To demonstrate and quantify the thermal performance of this embedded chip package and to verify the feasibility of this packaging scheme, thermal cycling measurements were conducted. The thermal loading started at room temperature with the upper-temperature range of +90°C. The ramp-up time to reach maximum temperature of 90°C is 10 min, followed by a dwell time of 10 minutes, and a ramp down time of 10 min. The device was assumed stress-free at 25°C. Each thermal cycle was performed for 30 minutes, and 20 such cycles were carried out. The embedded chip used in this process is a Schottky diode (BAT 15-03W), and the I-V characteristics of the diode were measured before and after thermal cycling. Figure 6.7 shows the I-V curves for the diodes before thermal cycling and after 5, 10, 15, and 20 thermal cycles. It is clear

from the figure that there is minimal or no change in the performance of the diode, which indicates proper interconnection reliability.

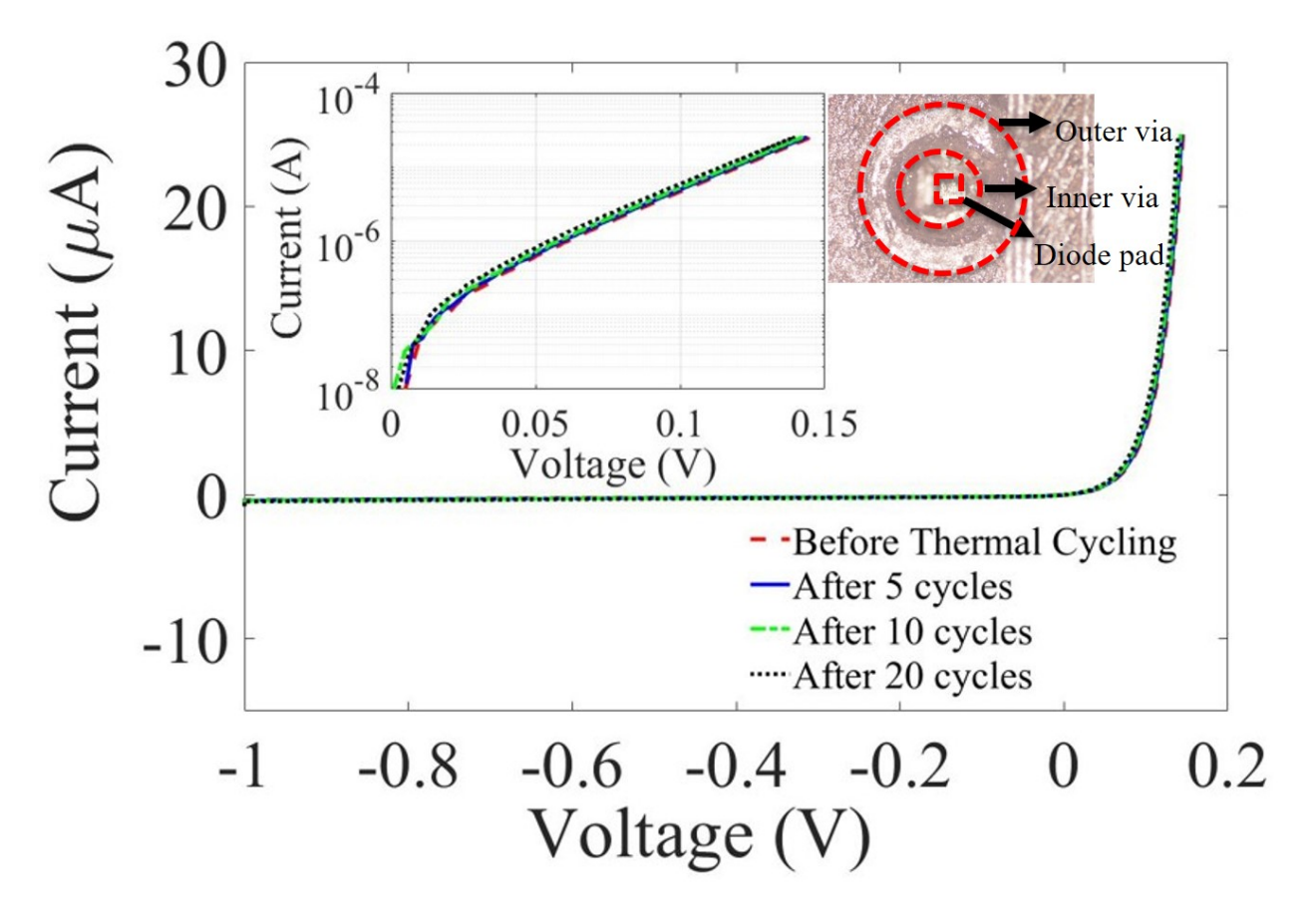


Figure 6.7: Measured I-V characteristics of the Schottky diode embedded in the 3D printed package after multiple thermal cycles, the inset shows log I vs V and the optical image of vias after 20 thermal cycles (90°C).

6.5.2 T-Line Resonator

A T-line resonator is commonly used in the design of filters and in impedance matching circuits. The resonance frequency of the T-line resonator can be tuned by loading the stub with a capacitive element. Here, a varactor diode (Skyworks 1430) is integrated in series to the shorted stub and the position is optimized to achieve maximal tuning. The circuit is biased by applying a voltage using a RF bias tee. The effective capacitance of the circuit changes for different biasing conditions thereby shifting the resonance frequency of the resonator. Figure 6.8 shows the design of the T-line resonator along with its dimensions as well as the fabricated structure with edge-mount connectors. Figure 6.9 and Figure 6.10 shows the change in phase and change in the resonance frequency under different biasing conditions of the varactor diode. The T-line resonator at zero bias shows a resonance at 5.25 GHz with maximum return loss of 17 dB. With a bias of 5, 10, and 15 V the resonance frequency shifts to 5.75, 6, and 6.15 GHz, respectively. Experimental results demonstrate that a high tuning range can be achieved for the resonator with a lower variation of the DC biasing voltage with a minimum or no effect on the return loss.

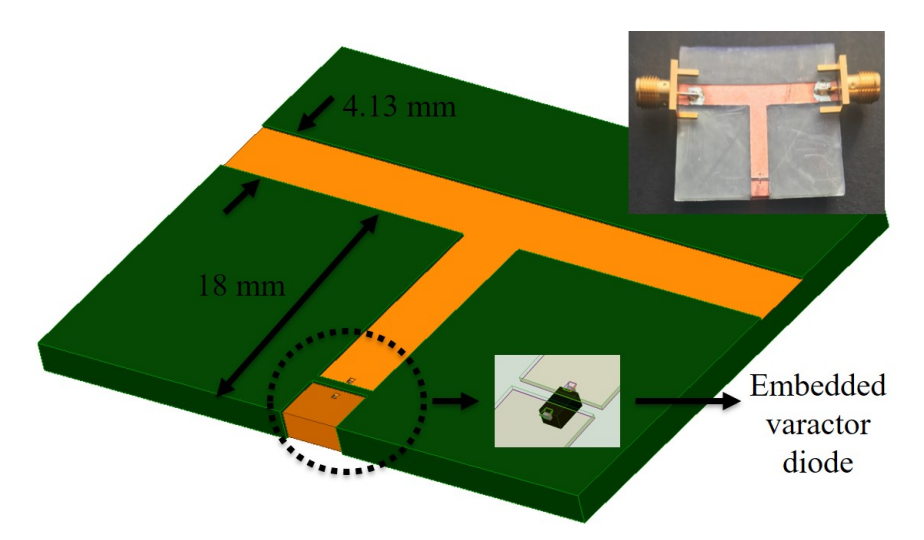


Figure 6.8: Design of the T-line resonator structure along with the dimension used, inset shows the 3D printed resonator with the embedded varactor diode.

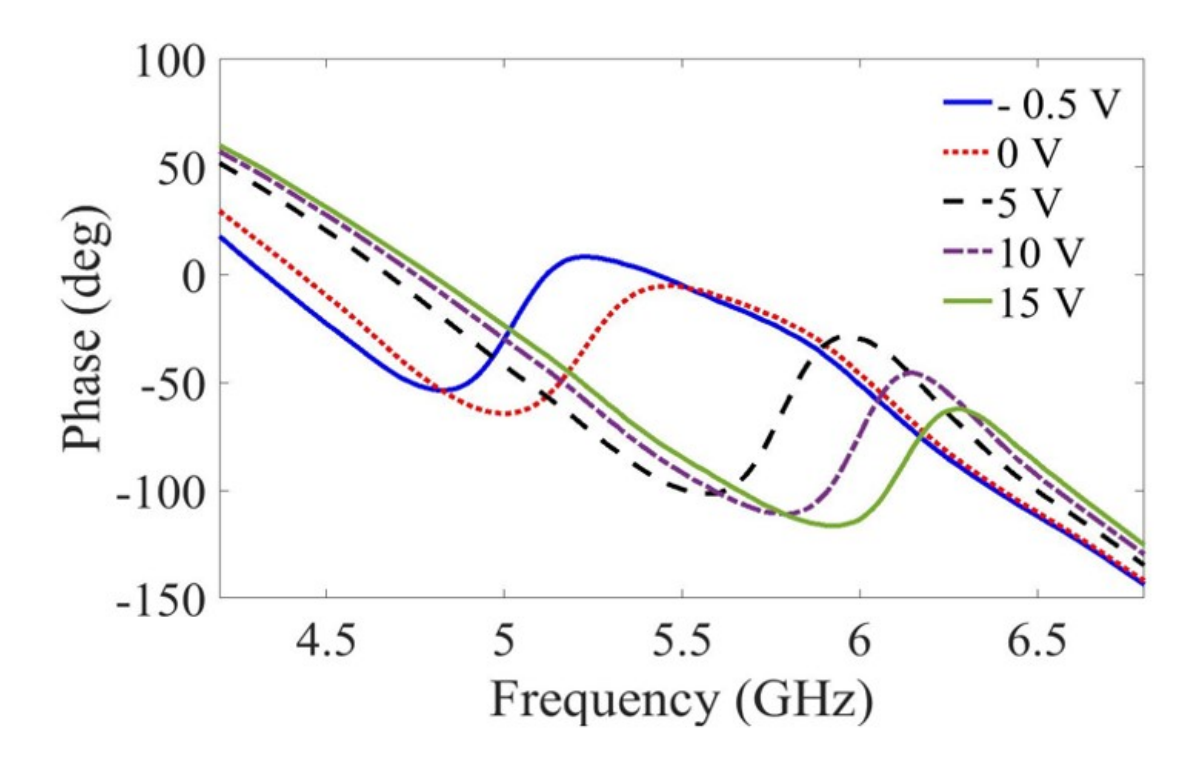


Figure 6.9: Measured results showing change in phase of the T-Line resonator under different varactor diode bias conditions.

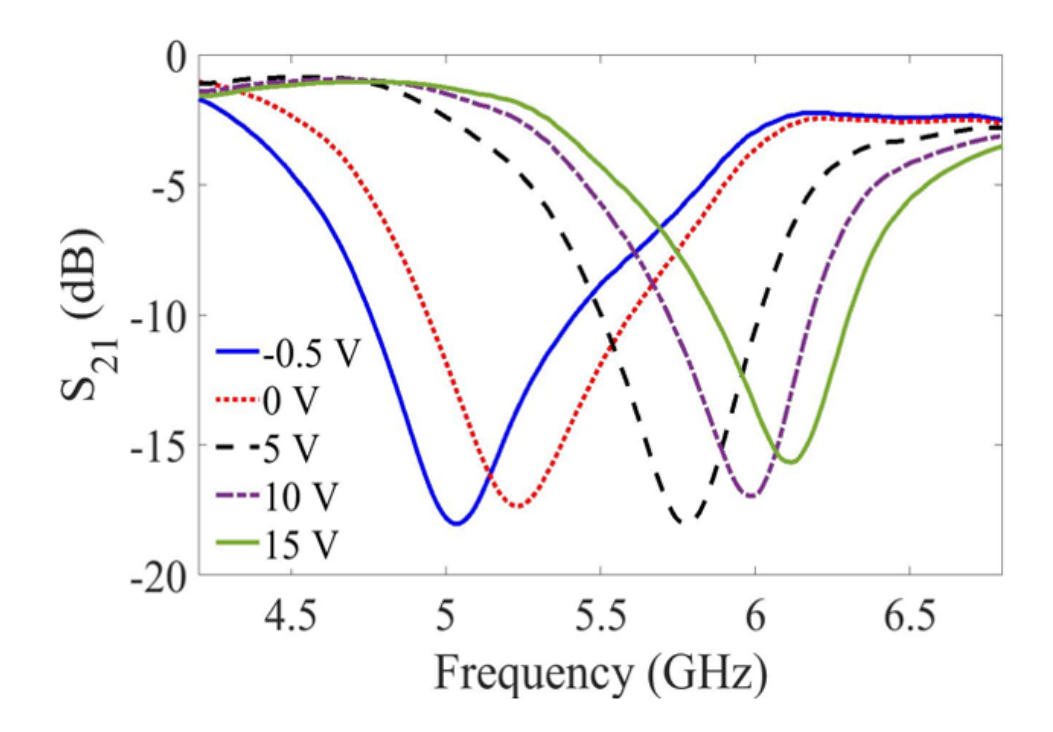


Figure 6.10: Measured results showing change in resonance frequency of the T-Line resonator under different varactor diode bias conditions.

6.5.3 Metamaterial-Inspired Phase Shifter

Phase shifters play an important role in phased-array antenna systems, phase-modulation communication systems, and emerging adaptive antenna systems for broadband 5G wireless mobile communications. Phase shifters are required for beam steering in antenna arrays and for avoiding signal degradation due to multipath propagation [80, 81]. The phase shifters should be compact and low cost to enable commercial applications. Phase shifters are miniaturized using metamaterial inspired designs. Metamaterial-inspired structures provide unique propagation characteristics that can be readily tailored by modifying the physical structure and can be easily fabricated. Split ring resonators are commonly used as metamaterial unit cells. Here, two ring resonators are capacitive coupled to each other and are incorporated as part of a microstrip transmission line to design a compact phase shifter. A diode is embedded in the gap of the transmission line to which square split rings are coupled. The design along with the dimensions of the metamaterial based phase shifter is shown in Figure 6.11 as well as the 3D printed circuit after metallization. The measured frequency responses of the relative phase shift, and insertion loss of the circuit with different biasing voltages are shown in Figure 6.12 and 6.13, respectively. The results clearly show that the phase can readily be tuned electronically using embedded varactor diodes.

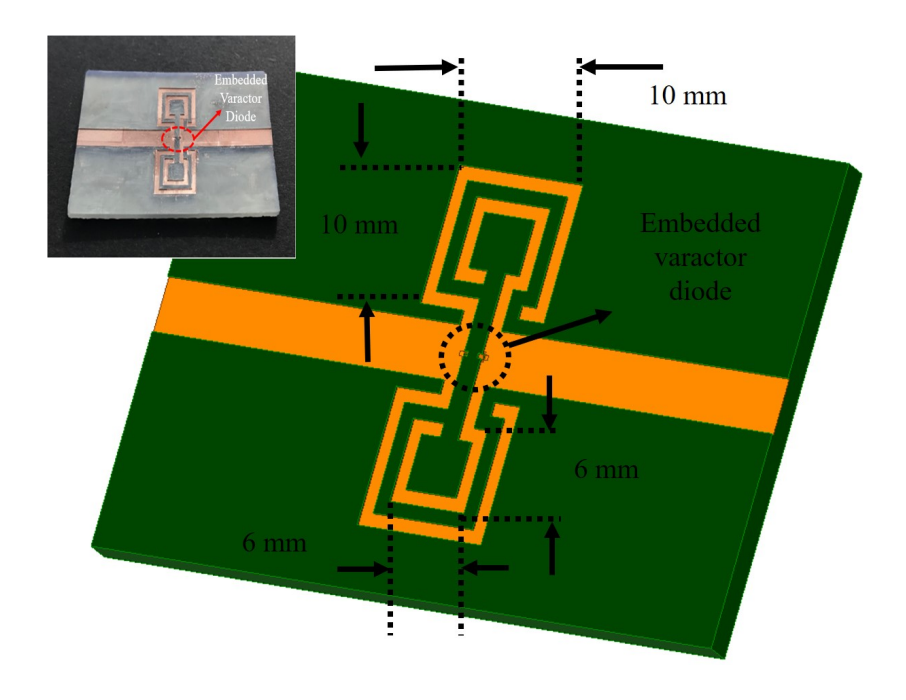


Figure 6.11: Schematic of the metamaterial-inspired phase shift along with the dimension used, the inset shows the 3D printed phase shifter with embedded varactor diodes.

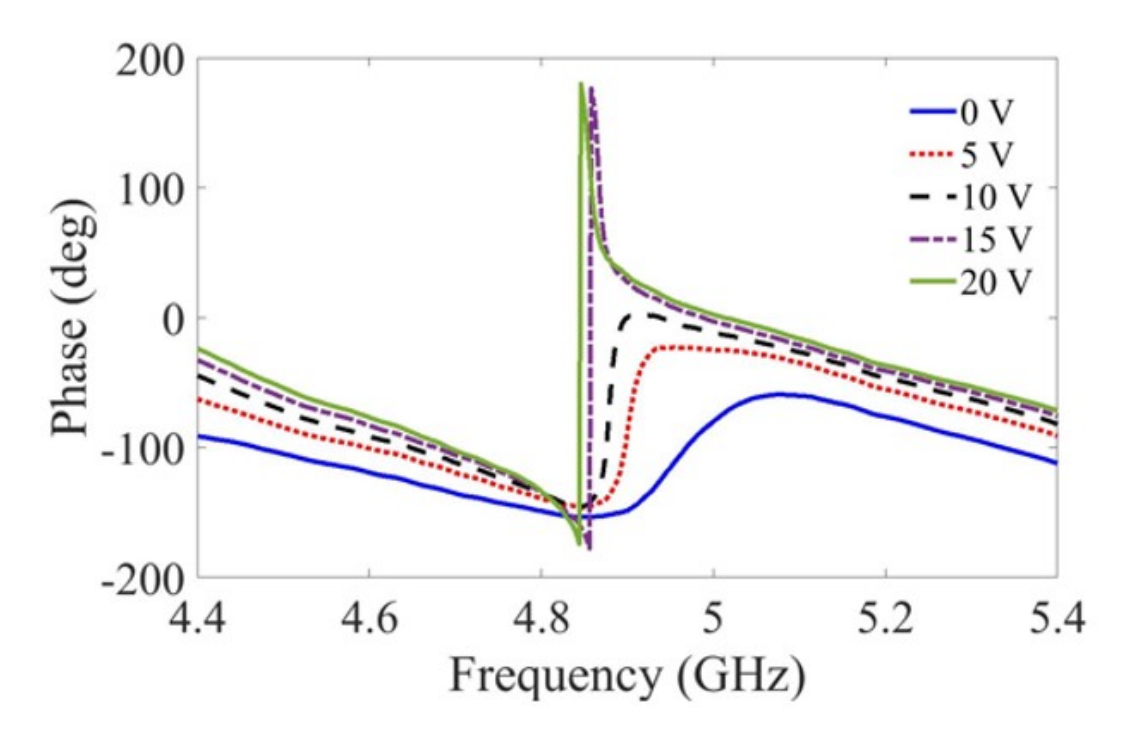


Figure 6.12: Measured results showing change in phase of phase shifter with change in biasing voltage.

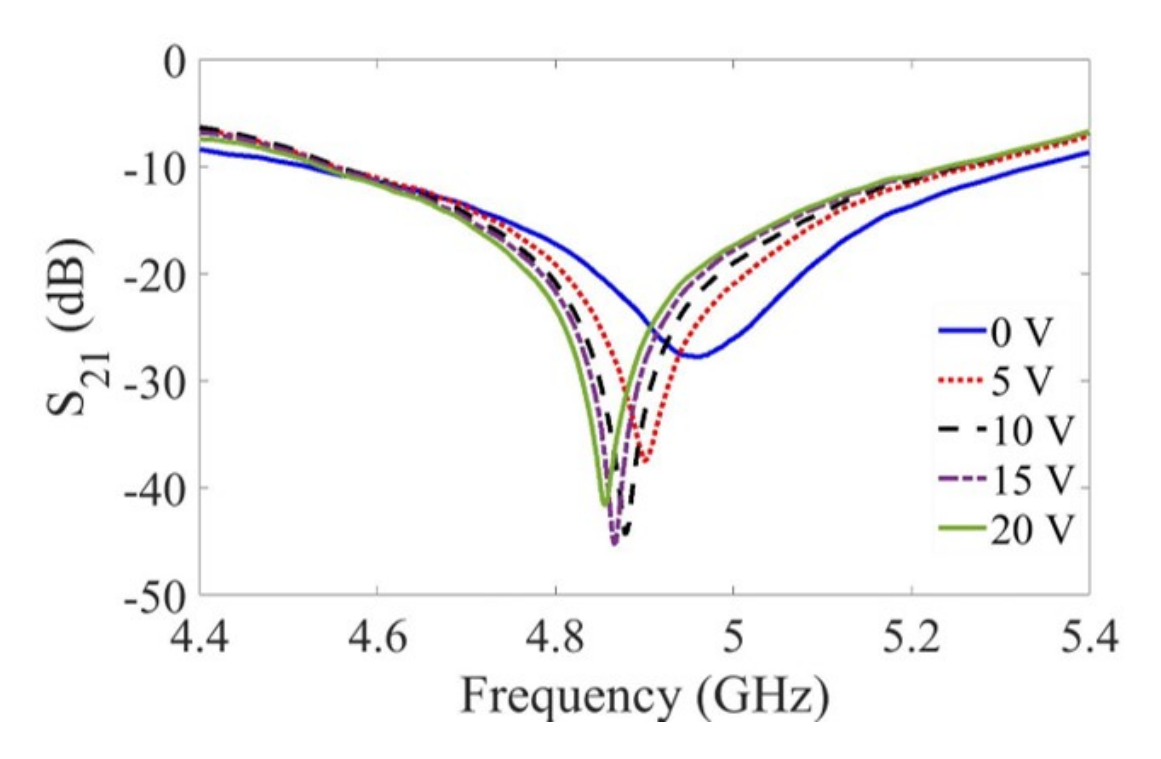


Figure 6.13: Measured results for change in resonance frequency of phase shifter due to the change in biasing voltage.

6.5.4 Tunable Patch Antenna

A patch antenna is a commonly used microwave device due to its simple design and ease of integration on planar structures. Tunable patch antennas with the potential of reconfigurable frequency, radiation pattern and polarization is increasingly popular in the modern wireless communication and radar applications [82,83]. In this work, the frequency tunable microstrip patch antenna with embedded varactor diode is presented. Figure 6.14 shows the schematic of the tunable patch along with its dimensions. By changing the applied DC bias on the varactor, the loading capacitance can be tuned and hence there is a shift in resonant frequency of the microstrip patch antenna. To accommodate varactor diodes for tuning, a slit in the patch was introduced where the diodes are placed across the gap. The inductive pads are included to allow DC biasing with minimal impedance loading. A narrow line with high inductance is used to attach the pads to the antenna for RF isolation. The effective capacitance of the patch changes under different biasing conditions which in turn shifts the resonance frequency. The simulation and measurement results are shown in Figure 6.15. Figure 6.16 shows a change in the resonance frequency from 6.35 to 6.7 GHz under different biasing conditions. This tunable antenna shows that the resonance frequency can be changed without changing the physical dimension of the structure. The measured return loss, S_{11} , of the antenna is less than -10 dB within the tuning range. The simulated and measured gain at zero bias is shown in Figure 6.17, and the gain of antenna at 6.4 GHz is 5.48 dBi.

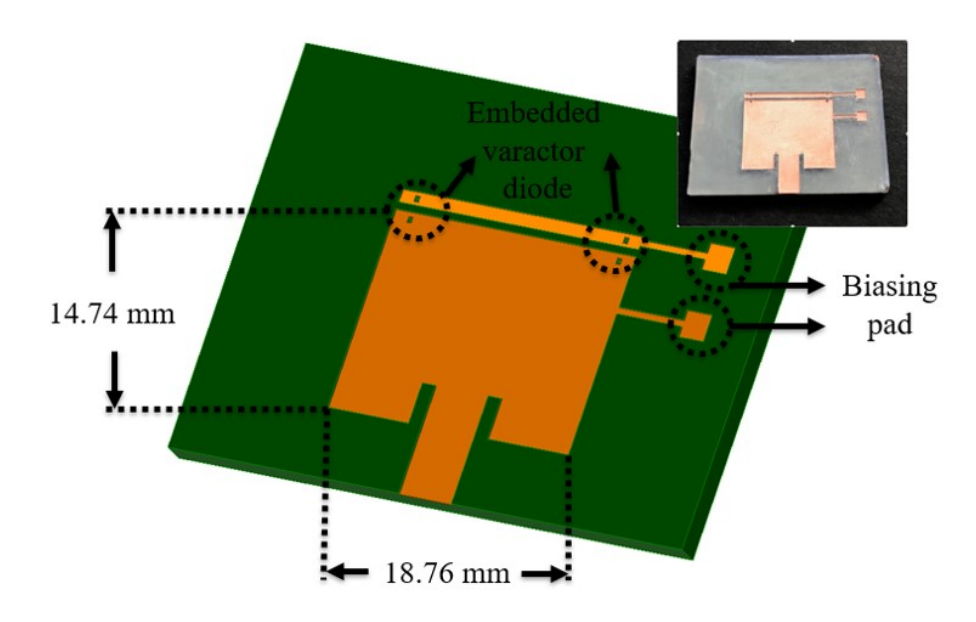


Figure 6.14: Schematic and dimensions for the tunable antenna design, and the inset shows the fabricated patch antenna.

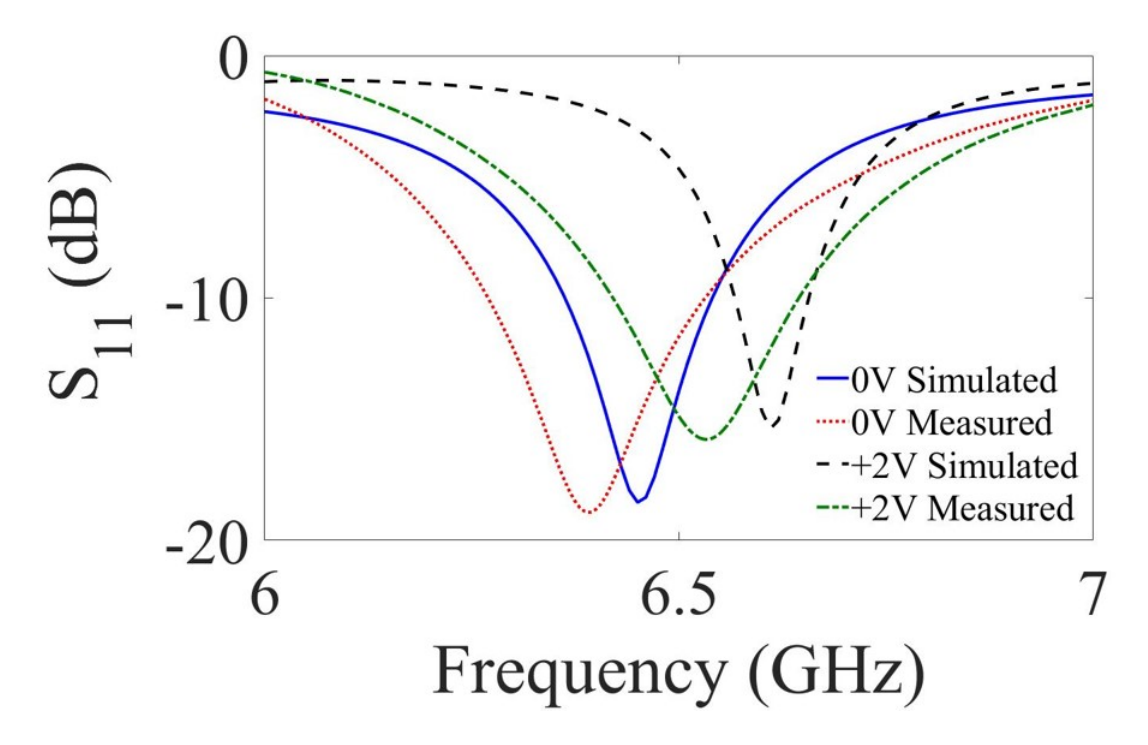


Figure 6.15: The comparison between simulation and measurement result for the tunable patch under different bias condition.

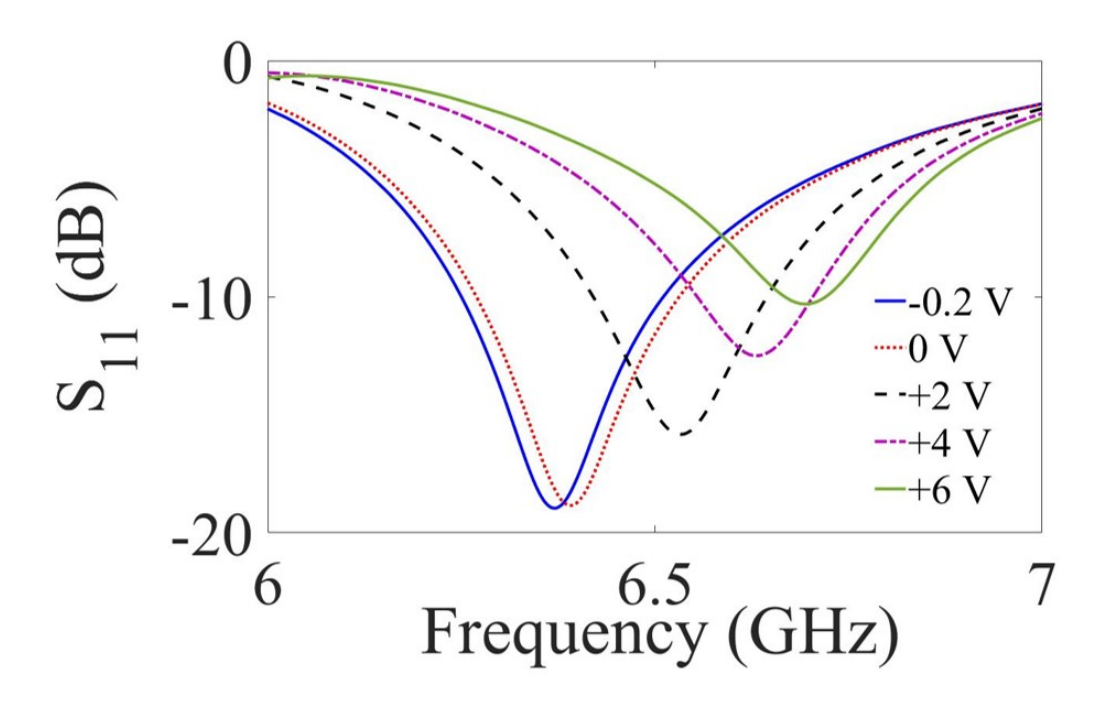


Figure 6.16: Measured results for tunable patch antenna showing change in operating frequency under different voltage bias conditions.

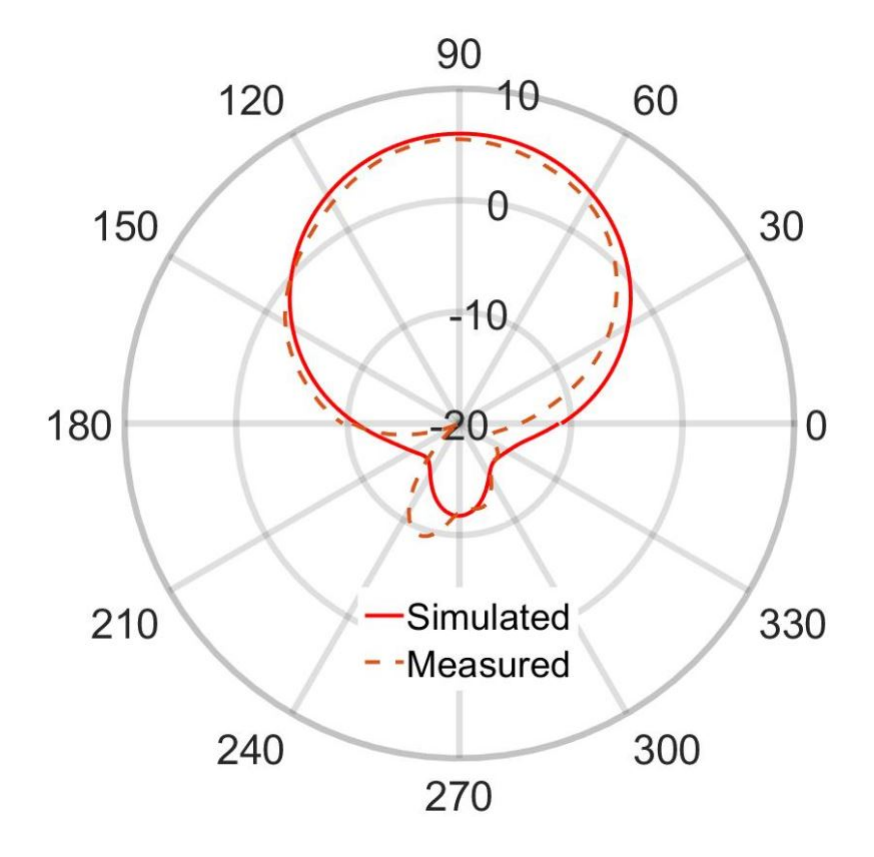


Figure 6.17: Simulated and measured radiation pattern for the tunable patch antenna at 6.4 GHz with the gain of 5.9 dBi and 5.48 dBi respectively at zero bias.

6.5.5 Discussions

In this chapter, it is demonstrated how active surface mount components can be embedded in RF circuits/devices/packages using AM. Despite all the benefits of AM embedded process discussed earlier, there are still significant challenges to the use of these techniques at much higher frequencies (mm-wave). Some of those challenges are surface roughness of 3D printed material, warpage due to prolonged post-printing UV exposure, residue in the cavity/vias, compensation for components dimensional tolerance and the high dielectric loss of printed material as listed in Table 1. One of the significant challenges in AM is the surface roughness of the 3D printed substrate. Mechanical polishing of the 3D printed surface before metallization can be used to reduce the roughness but it is still significantly large for components working at the mm-wave range. Optimizing the post-printing UV exposure time is also very critical as extended exposure leads to substrate warpage. In this work, 10 minutes post-exposure was chosen after careful experimentation and optimization. The performance of 3D printed embedded structures depends a lot on the connection; thus it is essential that the 3D printed vias/cavities are residue free. Here, the cavity is cleaned using Isopropyl alcohol while continuously blowing with dry Nitrogen gas. Printing vias to make electrical connection to the active component is an additional challenge. In this chapter, vias are printed with slanting edges to allow easier deposition of the metal into holes and subsequently the pins of the components. Another challenge for embedding SMT components is to compensate for a dimensional tolerance of the component such as legs, packaging, and height into the cavity. Also, the thickness of each printed layer should be pre-estimated to stop the 3D printer to place components accurately. Beyond the material loss of the polymer, another critical factor that affects the performance of microwave devices

Table 6.1: Tangent Loss for Different 3D Printable Polymers

| Printable Polymers | Frequency | Loss tangent (tan | Reference |
|-----------------------|------------------|-------------------|-----------|
| | | δ) | |
| PLA | 1.7 GHz - 4 GHz | 0.0395 | [84] |
| | | | |
| ABS | 0.1 GHz - 10 GHz | 0.06-0.0151 | [48] |
| | | | |
| NinjaFlex 100% | 2.4 GHz | 0.06 | [85] |
| | | | |
| Verowhite | 1.5 GHz | 0.0285 | [86] |
| | | | |
| Formlab high tempera- | 4 GHz - 12 GHz | 0.02 | This work |
| ture epoxy | | | |

is the SMA connectors and parasitic associated with soldering. Using less solder material and the choice of connectors allows improvement in the performance of the devices. The embedded microwave components presented in this chapter is a first step in realizing a fully printed RF system as shown in Figure 6.1. Further characterization of features such as surface roughness, feasible cavity sizes, and shape, printing on existing substrates or conformal forms enabling the fabrication of RF devices into existing systems need to be explored. In the future, low loss substrate materials and new printing technology with improved resolution that may take the fabrication to micro, or nano level are envisioned. To achieve fully 3D printed systems and to integrate bare-die components, a combination of different printing technologies such as 3D polymer printing (stereolithography) and inkjet printing (metallic traces/interconnections) may be required to allow a dynamic range of resolutions with added functionalities. The integration of RF electronics with additive manufacturing will require continuous development of materials, printers, and processes.

6.6 Conclusion

This work demonstrated simple, low-cost approach for embedding active devices using AM for the fabrication of compact RF circuits. Tunable circuits such as a T-line resonator, metamaterial-inspired phase shifter, and patch antenna were presented, demonstrating the capability of the proposed fabrication technique. It can be concluded from the DC, thermal and RF characterization of the devices that the 3D printed embedded fabrication process is reliable and can be used in the design and fabrication of RF and microwave components and opens up a significant opportunity to design systems with high functional density. The use of AM allows device design with a customizable packaging process where packaging can be adapted for different component even on the same device with high precision and without any misalignment. The use of embedding process effectively reduces the circuit length, improves the electrical performance and thermal properties and allows miniaturized and high-density electronic packaging. With further advances in print technology, this process can be adopted in embedding of bare dies in a 3D configuration which will lead to significant circuit miniaturization. Also, this process provides a complete packaging solution for future circuits and systems.

Chapter 7

3D Printed Electronic System

7.1 Introduction

In this chapter, two different 3D printed systems are presented that encompasses the various fabrication processes developed in the previous chapters. The goal of this dissertation is to show a pathway towards designing and fabricating complete systems using 3D printing processes utilizing the advantages of AM in terms of rapid prototyping of complex geometries with ease. Using the metal patterning process developed in Chapter 2 and air as substrate in Chapter 5, LEGO-like assembly developed in chapters 3, and 4, and embedding devices developed in Chapter 6, two fully 3D printed systems are presented in this chapter. In the first part, an example application of 3D printed harmonic system with transceiver antennas and a sensor tag is presented for underground pipeline localization and detection. Second part of the chapter presents a compact 3D printed RF front-end system for 5G communication applications.

7.2 3D Printed harmonic system

The proposed 3D printed harmonic system is aimed at providing location information of buried objects such as pipelines. Since the pipelines are fabricated from plastics, the sensor tag can be easily embedded into the pipe while manufacturing as the entire pipeline along with the tag can be fabricated using 3D printing as shown in Figure 7.1.

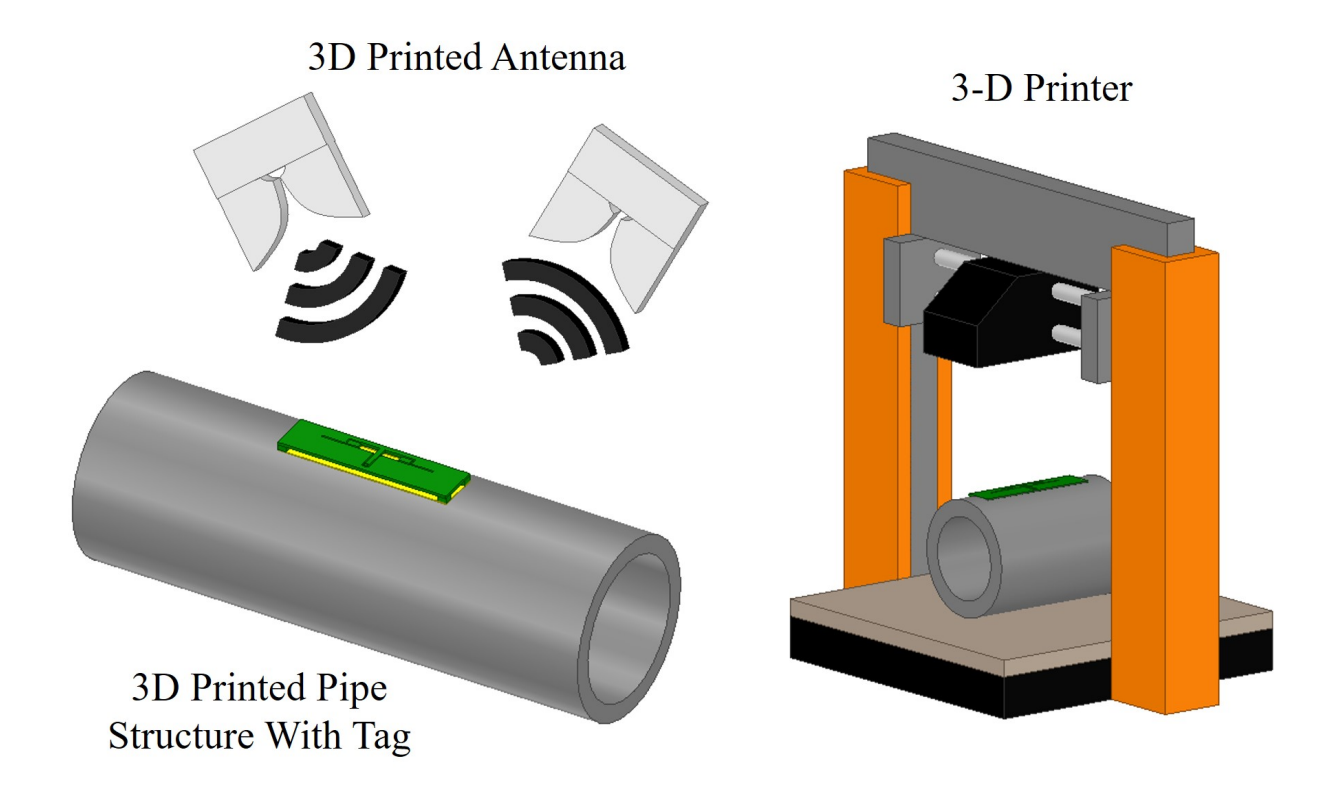


Figure 7.1: 3D Printed Harmonic RF System

The 3D printed harmonic system consists transceiver Vivaldi antennas that are fabricated using non-planar structures and LEGO-like assembly technique. The sensor tag consists of dual slot coupled antennas fabricated using air as substrate and damascene-like metal patterning operating at the fundamental frequency of 2.55 GHz and the second harmonic frequency of 5.1 GHz. A BAT 15-03W diode is coupled to the antennas for generating harmonics by embedding into the slots using 3D embedding face-up technique. The antennas are linearly polarized and the polarization is used for mapping the location of the buried pipelines.

7.2.1 Design and Fabrication

The harmonic sensing system consists of two components, (i) transmitting and receiving antennas, and (ii) the harmonic sensor tag. The components are printed using a commercial Formlabs Form 2 3D printer that uses a stereolithography process in which a high temperature epoxy material is printed layer by layer and cured using ultra violet (UV) light. The components are printed in parts and are fit together using a LEGO-like process. The printed parts are metallized using a two-step process, first a 60 nm of titanium (Ti) is sputter deposited followed by 500 nm of copper (Cu). Ti is used as an intermediate layer to aid in adhesion of copper to the printed plastic. Second, 5-6 μ m of Cu is plated using electroplating to increase the thickness of the metal layer. The metallized plastic parts are clamped together in a LEGO-like fashion as explained in chapter 3 and 5.

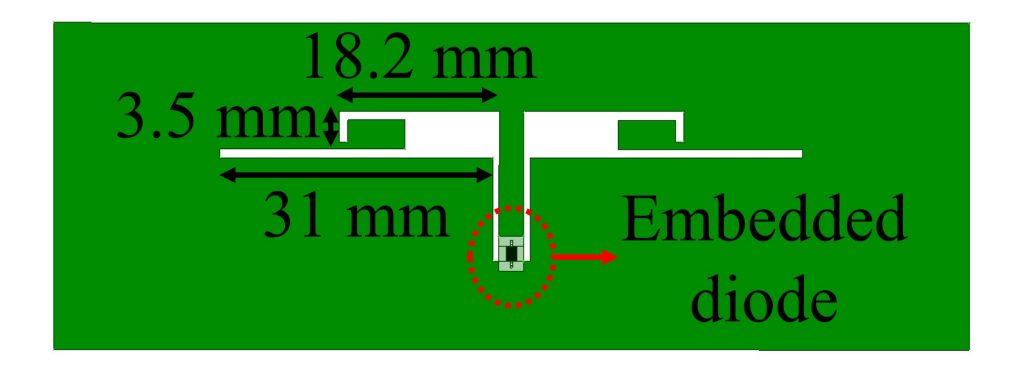


Figure 7.2: Schematic of the harmonic tag with dimensions.

The harmonic sensor tag consists of a slot coupled dual band antenna and a diode for generating the harmonics. The slot antenna is designed to operate at two frequency bands, f_0 and $2f_0$. The diode is embedded in the antenna such that the slot is impedance matched to the diode to achieve maximum efficiency of the harmonic power conversion. The design and optimization of the tag is performed using High Frequency Structural Simulator (HFSS[®]).

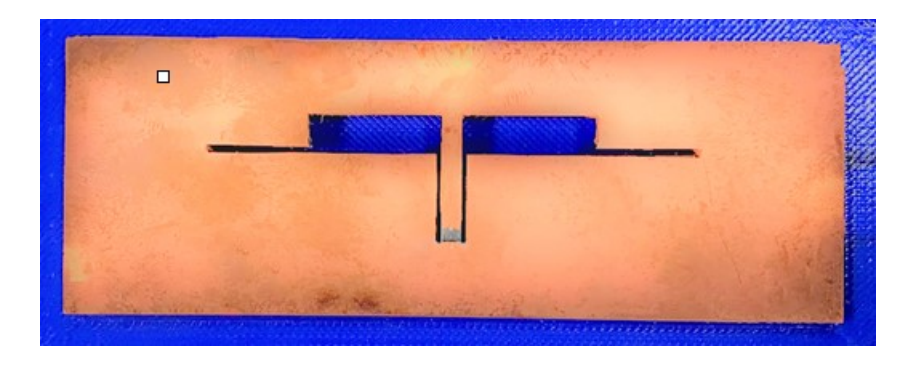


Figure 7.3: Image of fabricated tag.

The schematic with dimensions of the fabricated tag is shown in Figure 7.2 and its image is shown in Figure 7.3.

Here, the transmitting antenna is designed to operate at the fundamental frequency (f_0) , 2.55 GHz, and the receiver antenna at the second harmonic frequency $(2f_0)$, 5.1 GHz. A wide band Vivaldi antenna design is chosen for both the antennas and are based on the design guidelines outlined in our previous work in [87]. Coaxial cables are silver pasted to probe both the antennas. The transmitting antenna is connected to an RF source for transmitting the query signal at 2.55 GHz and the receiving antenna is connected to a spectrum analyzer to read the reflected signal at 5.1 GHz. The dimension and image of the metallized 3D printed transmitter/receiver antenna are shown in Figure 7.4 and 7.5, respectively.

The diode is embedded into the antenna structure using a face-up embedding process developed in our previous work chapter 6. In this process, a cavity is printed first on the base structure for placing the active component. The printer is stopped at a pre-defined step and the diode is manually placed with the legs facing up. The printing is continued and the structure is completed with vias for providing electrical connectivity to the diode. The tag is metallized with Ti/Cu and electroplated with Cu to achieve a solder-free embedding of an active element within the printed plastic as shown in Figure 7.6.

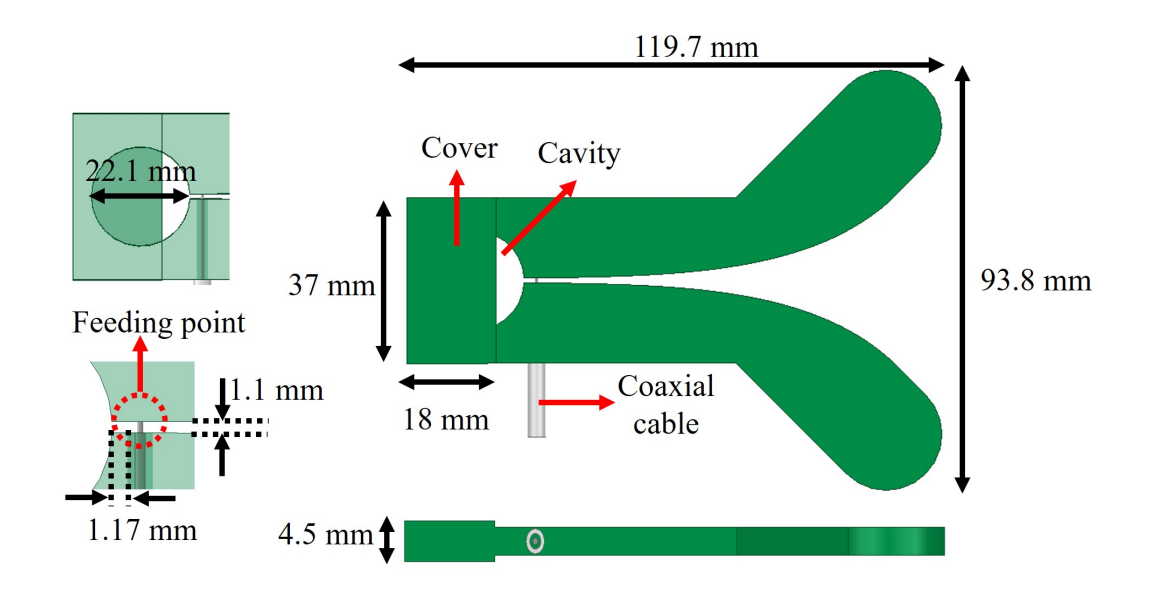


Figure 7.4: Geometry and dimensions of Vivaldi.



Figure 7.5: Schematic of the harmonic tag with dimensions.

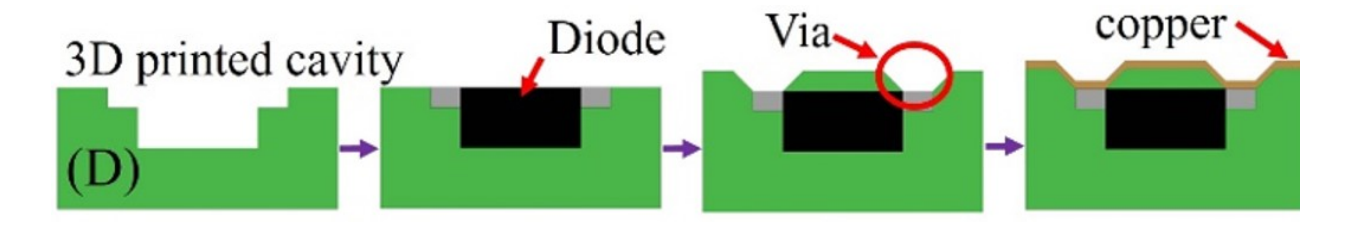


Figure 7.6: Face-up solder-free embedding process of the diode using 3D printing.

7.2.2 Measurement and Results

The performance of the printed sensor tag along with the printed transceiver antennas is demonstrated by performing four different experiments. The performance of the printed harmonic sensor tag is enhanced by an addition of a reflector behind the tag. The back reflector is fixed 1 cm behind the tag for all the experiments. The first experiment is performed to determine the efficiency of the doubler and to determine the best operating fundamental frequency. The second experiment is performed to show the relationship between the read range and the received power at the chosen fundamental frequency. The third experiment shows the capability of tag as markers for location detection under the soil. The fourth experiment shows the relationship between angular position of the tag and the received power for determining the direction of the pipeline. All the experiments are repeated four times and the values averaged out.

7.2.2.1 Frequency versus received power

The harmonic sensor tag is wide band in nature and it is necessary to determine the best operating frequency of the tag. For this purpose, the harmonic tag is placed at a fixed distance (read range) of 30 cm (~ 1 foot) from the transmitter and receiver antennas and the received power at the second harmonic frequency (2f₀) as a function of input fundamental frequency (f₀) with a fixed input power (P_{in}) of 13 dBm is plotted. Figure 7.7. shows the harmonic sensor tag performs the best at the fundamental frequency of 2.55 GHz with a received power of -53 dBm.

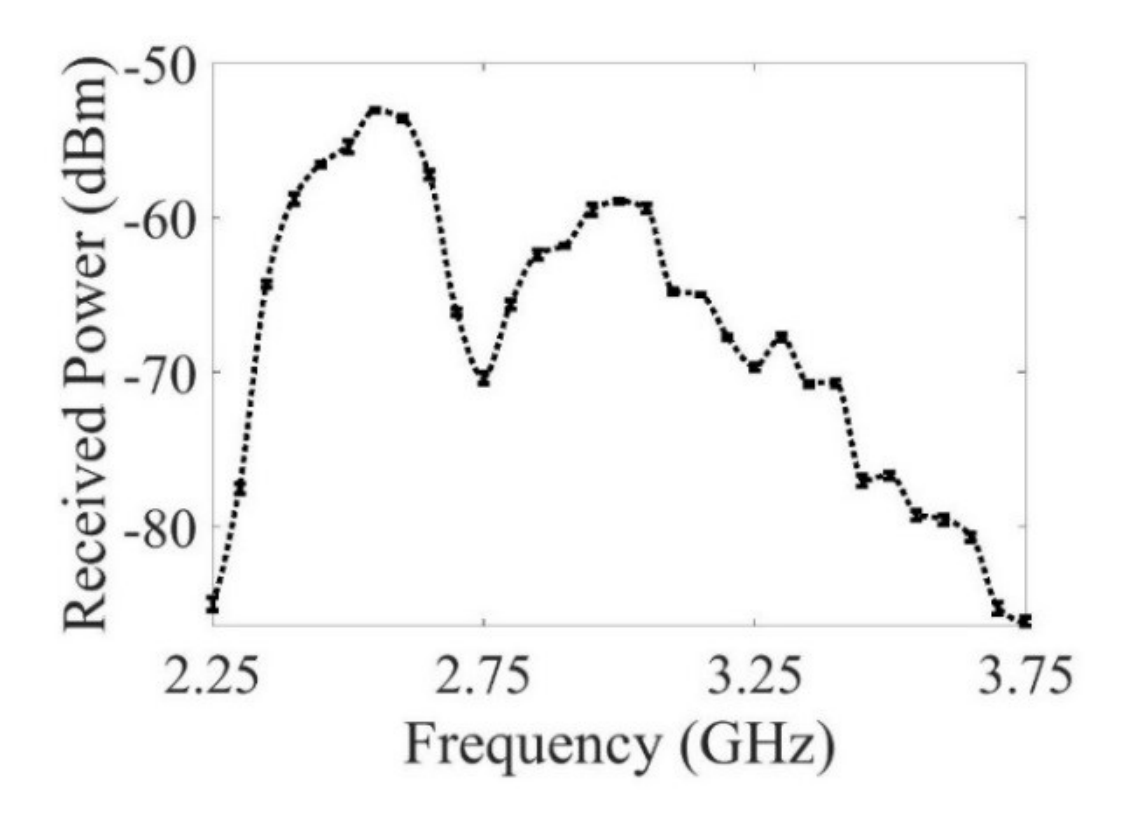


Figure 7.7: Received power at second harmonic frequency $(2f_0)$ as a function of fundamental frequency (f_0) with a fixed Pin and read range

7.2.2.2 Read range versus received power

The fundamental frequency (f_0) is fixed at 2.55 GHz for all the follow on experiments. The second experiment demonstrates the enhanced read range of the harmonic sensor tag. The position of the tag is fixed along x-y coordinates and the received power is plotted as function of height (z-coordinate). The input power is fixed at +13 dBm and the bandwidth of the spectrum analyzer is fixed at 1 kHz. The noise floor at this frequency for the proposed setup is approximately -95 dBm. Figure 7.8. shows the relationship between the read range and the received power and it can be seen that with the read range at two and half feet, the received power is still well above the noise floor. The received power can further be increased by improving the conversion efficiency of the tag or by increasing the input power.

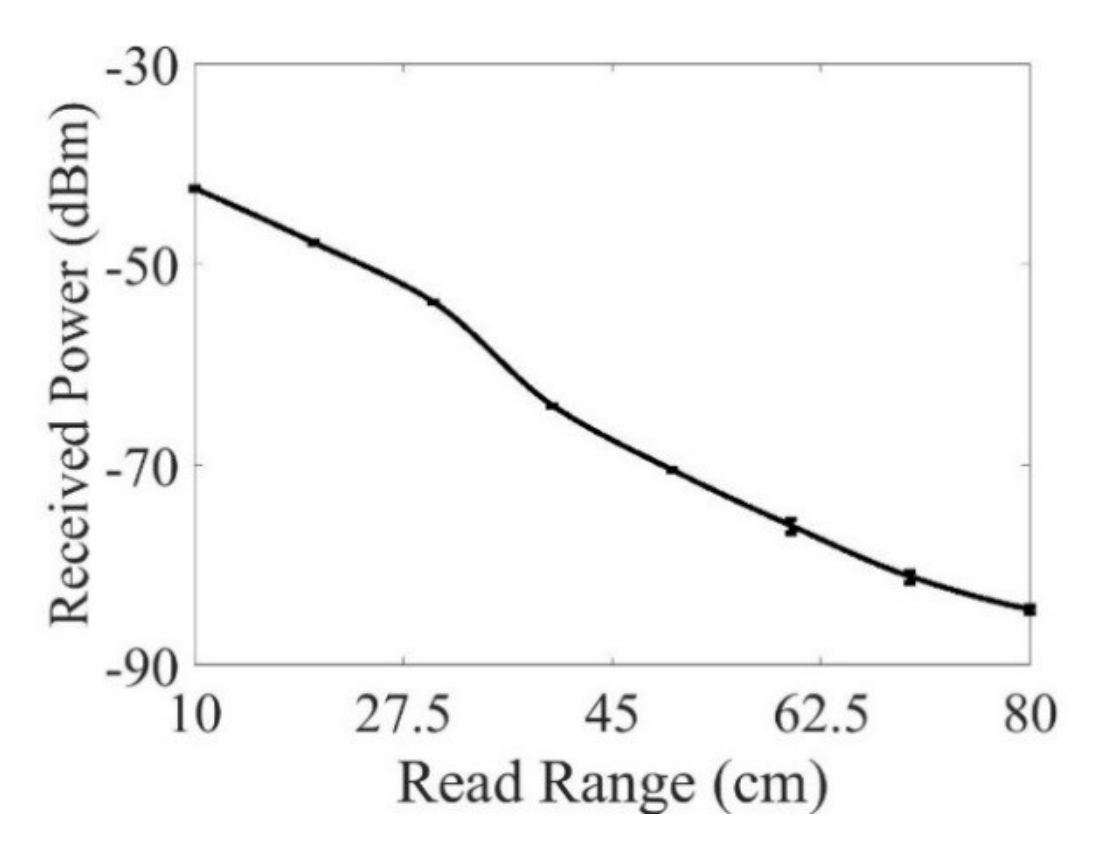


Figure 7.8: Received power at second harmonic frequency ($2f_0 = 5.1 \text{ GHz}$) as a function of read range with a fixed input power of +13 dBm.

7.2.2.3 Position versus received power

The third experiment demonstrates the capability of the designed tag as location markers for buried pipes. For this purpose, the read range of the tag is fixed at 30 cm and input power at +13 dBm. A 2D grid of 100 points within an area of 900 cm² is chosen and the received power is measured as a function of the location of the tag at each point on the grid. The center of the grid is chosen as (0,0) and each point is 3 cm apart in x as well as y direction. The center of the tag is placed at each grid point and the received power over the grid is plotted as shown in Figure 7.9. This plot shows the detection capability of the 3D printed harmonic sensor as a location marker.

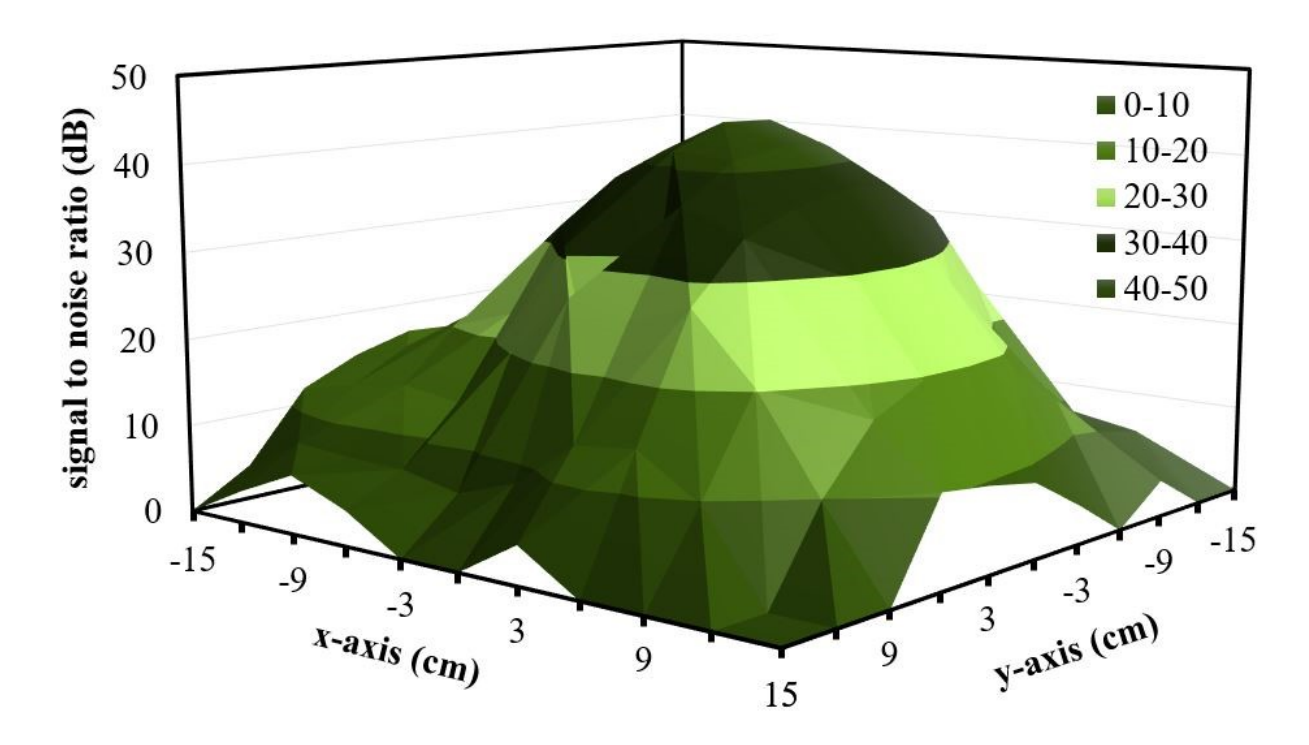


Figure 7.9: Received power, using noise floor as reference at second harmonic frequency $(2f_0)$, as a function of tag location (x, y) with a fixed Pin of +13 dBm and a read range of 30 cm.

7.2.2.4 Angle versus received power

The designed harmonic tag is capable of determining not just the location of the tag under the ground but also the direction of the buried pipe by exploiting the polarization of the antenna. The slot antenna is linearly polarized and the polarization is used as a marker for determining the direction of the buried pipe. For this purpose, the read range of the tag is fixed at 30 cm, input power at +13 dBm, and the fundamental frequency at 2.55 GHz. The tag is placed at the center of the grid and rotated 180 degrees in steps of 5 degrees. The received power is plotted as a function of angle and is shown in Figure 7.10.

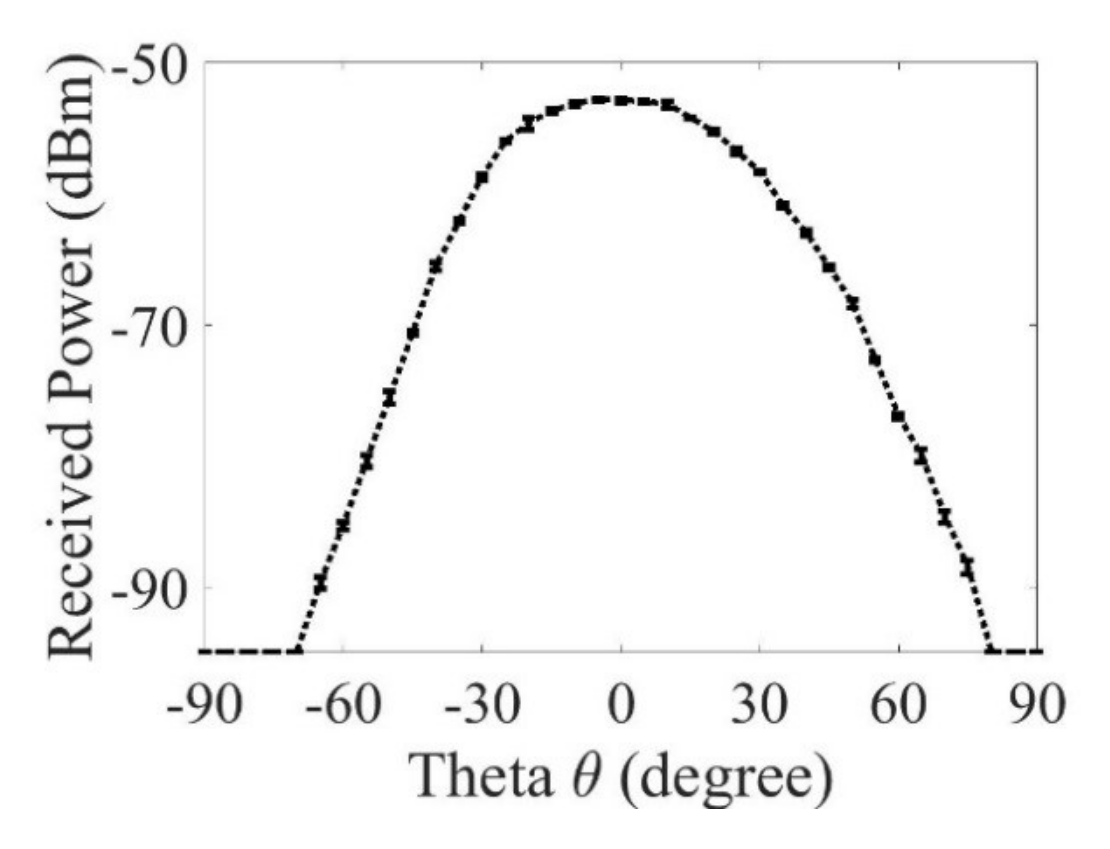


Figure 7.10: Received power at the second harmonic frequency $(2f_0)$ as a function of tag angle theta with a fixed P_{in} of +13 dBm and a fixed read range of 30 cm.

7.2.2.5 Depth versus received power

The above experiments shows that the designed tag can be applied as markers for both direction and location of objects underground. In order to demonstrate the application of the tag for pipeline location and detection, the harmonic sensor tag was buried under the soil at two different depths and the received power is measured. Time domain reflectometry (TDR) can be used to measure the time difference between the transmitted signal and the received harmonic signal. Utilizing the high SNR and TDR data, the depth of the pipe can be estimated. All purpose sand is used for burying the tag for the experiments. Table 2 lists the received power of the tag for different depths buried in soil.

Table 7.1: Received power at the second harmonic frequency $(2f_0)$ for different tag depth under the soil

| th (cm) | Received power at 2f ₀ (dBm) |
|---------|---|
| | -66.95 |
| | |
| | -75.75 |
| | |

7.2.3 Discussion - Harmonic Sensing System

The 3D printed passive harmonic sensing system provides a low cost approach for detecting buried plastic pipes with improved clutter rejection and higher signal to noise ratio. Employing 3D printing to realize the harmonic sensing system is attractive due to the ease of rapid prototyping of complex geometries. Although 3D printing allows customized prototyping, it has few challenges associated with it such as non-availability of low loss print materials, low conductive lossy silver paste for mounting the coaxial cable onto the Vivaldi antennas, controlled curing process to prevent warping, and surface roughness of the printed plastic. In future, advancement in 3D printing with the development of new low loss high temperature compatible materials providing smoother surfaces will improve the efficiency of the system. The current depth detection capability of the sensor is approximately 20 cm. This can be increased by increasing the gain of the transceiver antennas, and by increasing the input power of the query signal. The read range can also be increased by performing energy harvesting at the tag element to enhance conversion efficiency. A suitable lower frequency can be chosen for the tag operation by performing the power budget analysis under different soil attenuation conditions. The tag can be placed inside a plastic enclosure to prevent direct loading of the dynamic soil environment such as moisture. Although, the designed system is capable of detecting the buried tag, further analysis is required in terms of soil moisture content and other effects associated with the soil environment. In order to precisely locate the tag, along with a raster scan of SNR, a beam scanning can also be incorporated as part of the interrogator at each point along the scan. The receiver antenna can be rotated and the received SNR can be measured as a function of beam angle (ϕ). The read range of the tag can be estimated using a modified Friis transmission equation as shown in Eq. 7.

$$P_{R_{int}}(\phi) = \left(\frac{P_{T_{int}}G_{t_{int}}(\phi)G_{r_{tag}}\lambda_{f_0}^2}{(4\pi d)^2}\right)\eta\left(\frac{G_{t_{tag}}G_{r_{int}}(\phi)\lambda_{2f_0}^2}{(4\pi d)^2}\right)$$
(7)

where, $P_{R_{int}}$, $P_{T_{int}}$ are the received and transmitted power of the interrogator, $G_{T_{int}}$, $G_{T_{tag}}$ are the gain of the fundamental and second harmonic tag antennas, are the gain of the fundamental and second harmonic interrogator antennas, d is the read range, η is the conversion efficiency of the harmonic doubler, Λ_{f_0} , Λ_{2f_0} , are the wavelengths at the fundamental and second harmonic frequency, respectively, and ϕ is the beam angle. The received power (SNR) at the interrogator and the gain of the interrogator antenna depends on the beam angle (ϕ). Overall, a battery-free harmonic approach with a long life time allows real-time monitoring of plastic objects buried underground without any excavation or periodic maintenance.

This chapter presents a simple to implement 3D printed harmonic system for buried assets localization and detection. The harmonic system consists of fully 3D printed transceiver antennas and a harmonic sensor tag embedded with a non-linear element. The advances in 3D printing allowed a solder-free embedding technique of the diode into the printed antenna substrate. The harmonic nature of the tag provides higher signal to noise ratio with improved clutter rejection capability. The polarization extinction ratio of the tag is used for detecting the direction of the pipe along with the location. The designed system is capable of detecting the tag buried at a depth of 20 cm from the surface. In the future, fully 3D printed plastic

pipes with directly embedded harmonic sensor tags are envisioned that provides a real-time and an economical mapping of the labyrinth of underground buried pipelines in an urban infrastructure.

7.3 3D Printed Substrates for the Design of Compact RF Systems.

3D printing allows rapid customization of complex structures due to the inherent freedom to print in all directions. With the advancement in printing technology, multi-material printing are employed to realize cost-effective packaging solutions [88]. Typically, sensitive Rf components are shielded using metallic enclosures to prevent signal interference. By employing 3D printing, customized enclosure can be fabricated with air substrate based components on the surface of the enclosures for further miniaturization of the packaged system. Using a combination of AM strategies, 3D printing can be used as an alternative fabrication technique for realizing high-density electronics packaging. Figure 7.11 shows an example of the envisioned fully 3D printed customizable packaging enclosure with multiple components such as an air substrate based antenna and many active and passive devices for 5G applications.

The proposed RF back end module consists of an amplifier sub-module with surface mounted integrated chip along with the associated passive components (inductos, capacitors) and an air substrate based patch antenna sub-module fabricated using 3D printing.

7.3.1 Design and Fabrication

The performance of the individual sub-modules are analyzed first followed by the integrated module. All the components are printed using a commercially available 3D- printer (Object Connex350) that uses a photopolymer resin VeroWhitePlus[®] with dielectric constnt $(\epsilon_r \approx 2.8)$ and loss tangent $(\tan \delta \approx 0.04)$ [89]. The 3D printed structures are metallized first with a blanket sputtering of a thin seed layer of Titanium (Ti - 500 nm) and Copper (Cu -

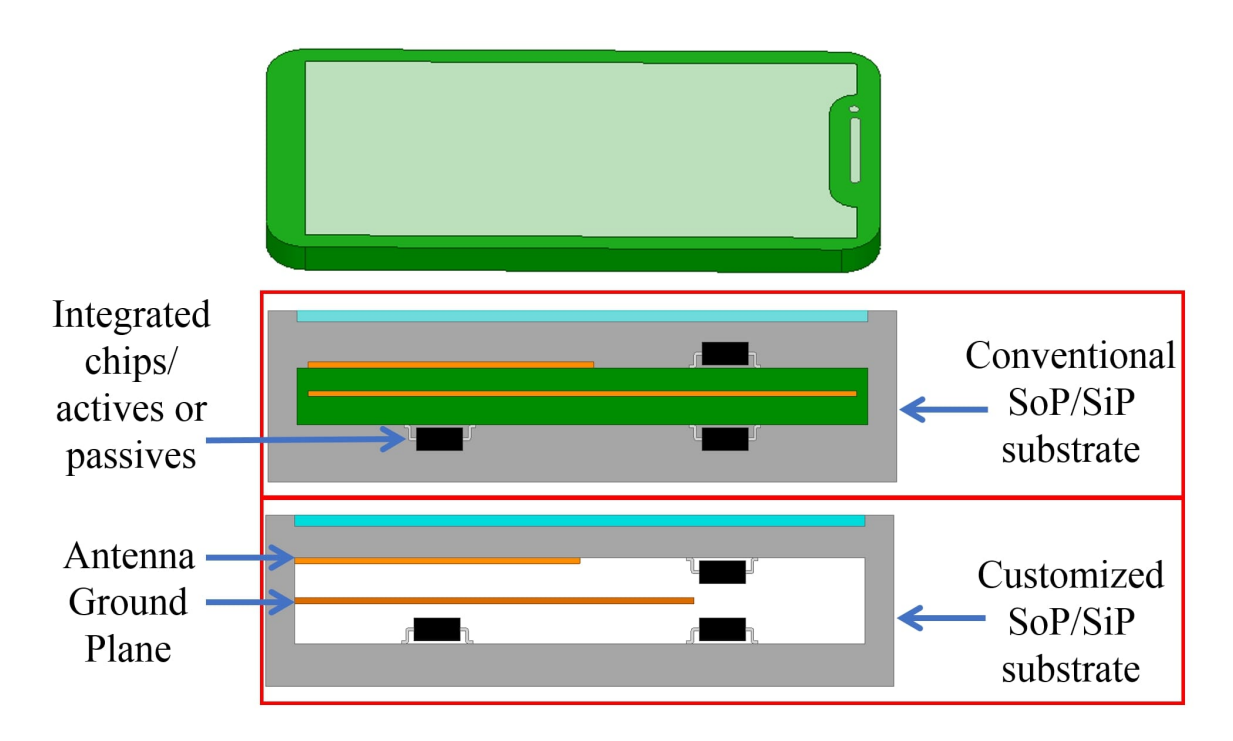


Figure 7.11: An example of the envisioned 3D printed electronic packaging with customizable substrate for 5G applications.

5000 nm) followed by electroplating of Cu to achieve an additional Cu thickness of 5-6 μ m. The metal layer is patterned using a damascene-like process as explained in [43]. The areas on the structure where metal is to be retained are printed 200 μ m lower than the rest and the unwanted metal on the elevated areas is removed using a mechanical polishing process.

Figure 7.12 shows the flow of a damascene-like process.

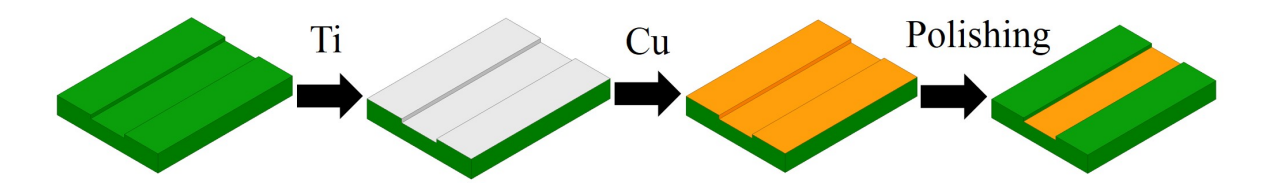


Figure 7.12: Patterning conductive traces on 3D printed substrate using a damascene-like process.

7.3.1.1 Air-Substrate based Patch Antenna

A simple patch antenna operating at 5.4 GHz is chosen for integrating with an amplifier to demonstrate the RF module. The antenna uses air as a substrate and is connected to the amplifier circuitry using a conductive post. The post is connected to the top and bottom layers using conductive silver paste. 3D printing allows fabricating using air as a substrate by printing the antenna in two separate parts (top and bottom layers) with support pillars on one side and corresponding holes on the other side. The two pieces are snapped together using a LEGO-like assembly process. Figure 7.13 shows an example schematic of the LEGO-like assembly process.

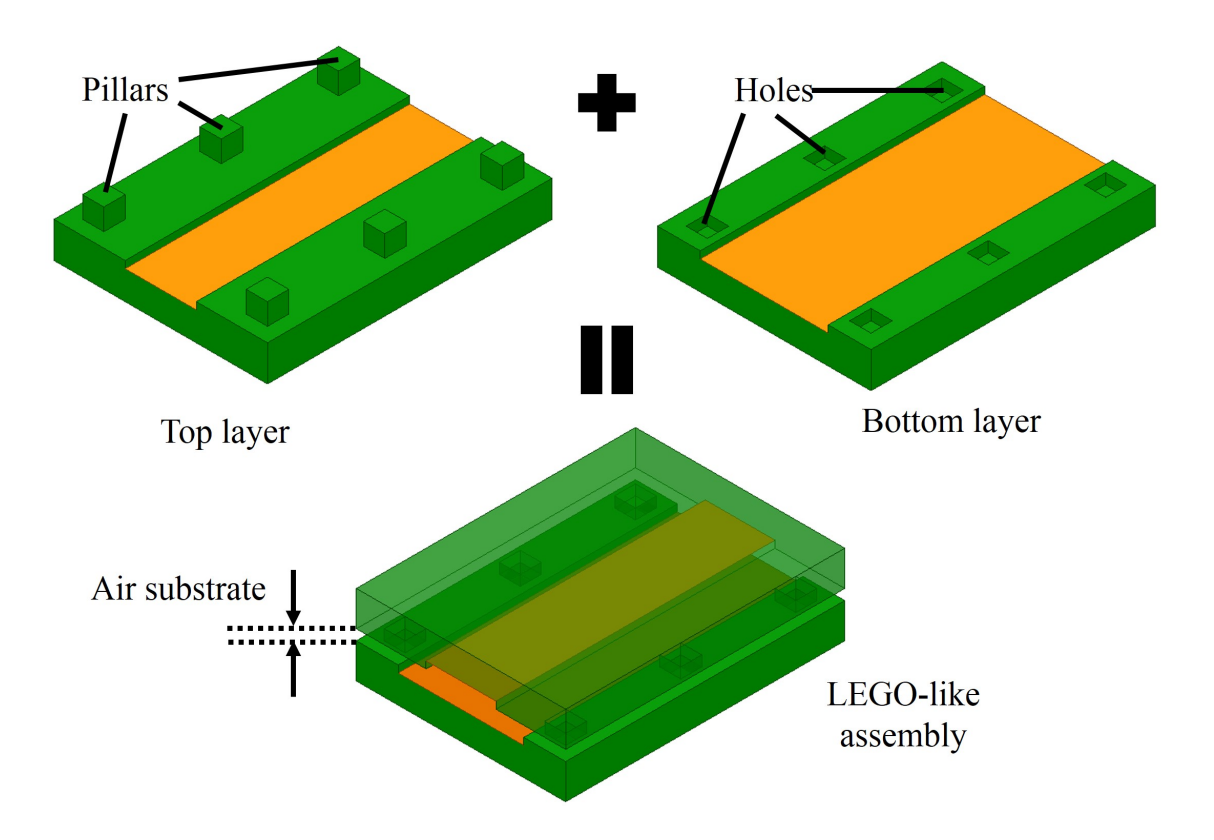


Figure 7.13: An example of LEGO-like assembly process for air substrate based circuits.

Figure 7.14A shows the schematic of the air substrate based patch antenna along with the dimensions. Figures 7.14B and C shows the image of the structure before and after metallization and Figure 7.14D shows the image after assembly.

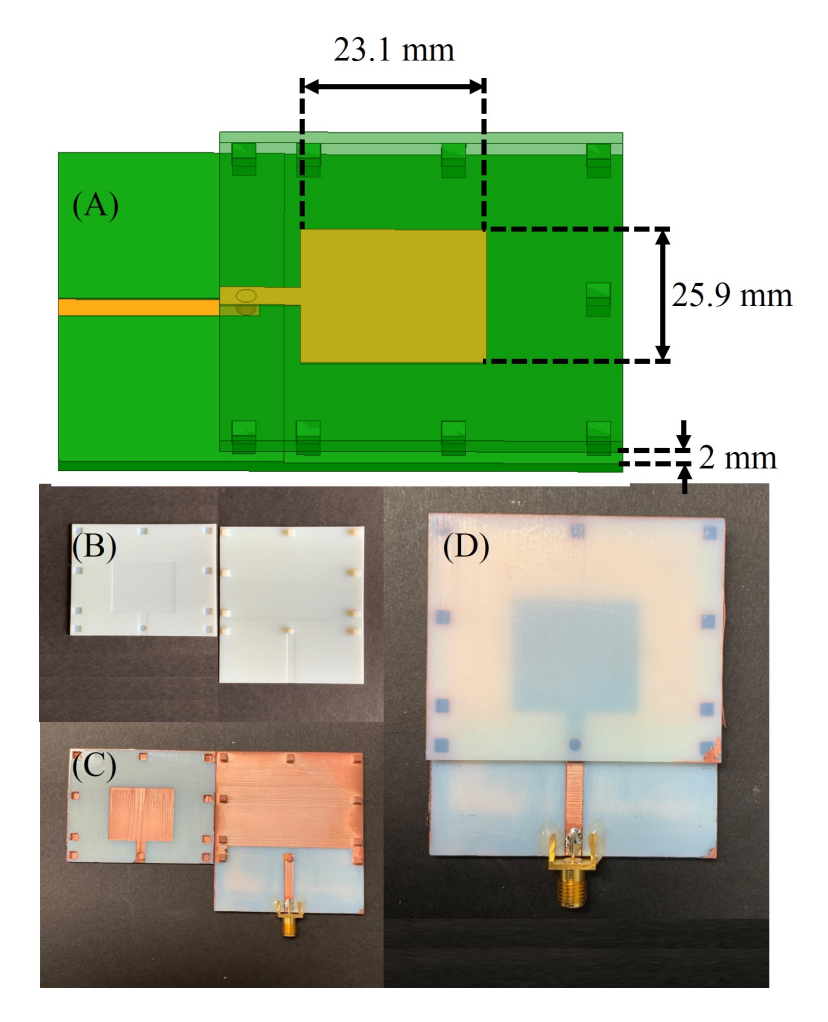
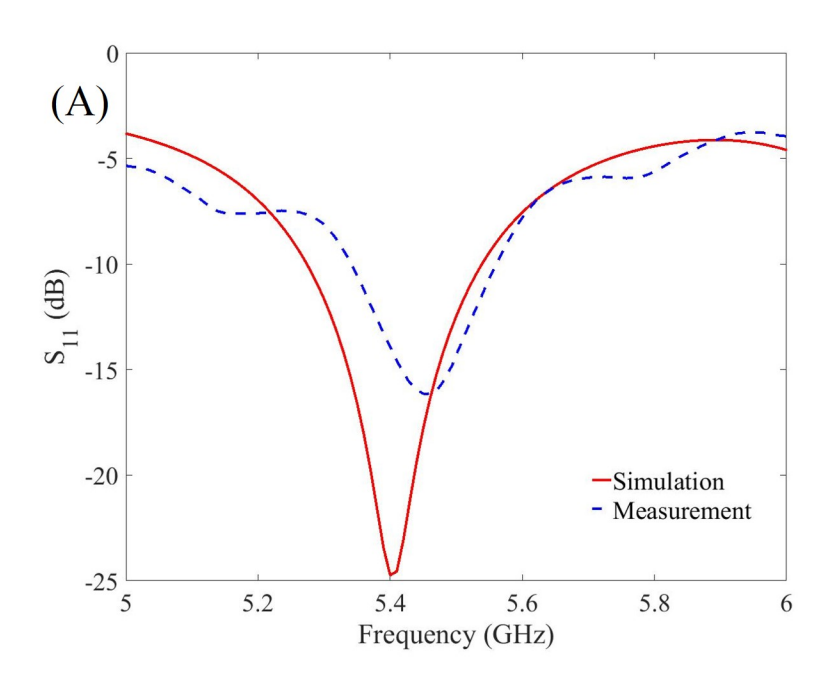


Figure 7.14: 3D printed air substrate based patch antenna (A) Schematic with dimensions, (B) and (C) structure before and after metallization, respectively, and (D) image after LEGO-like assembly.

Figure 7.15 shows the simulated and measured reflection co-efficients and the radiation patterns. The simulated and measured results matches closely and the slight mismatch is due to the loss associated with slight reduction in air gap due to warping of the substrate during the sputtering process as well as the poor conductivity of the silver paste. The fabricated patch operates at 5.4 GHz with a gain of 6.04 dBi.



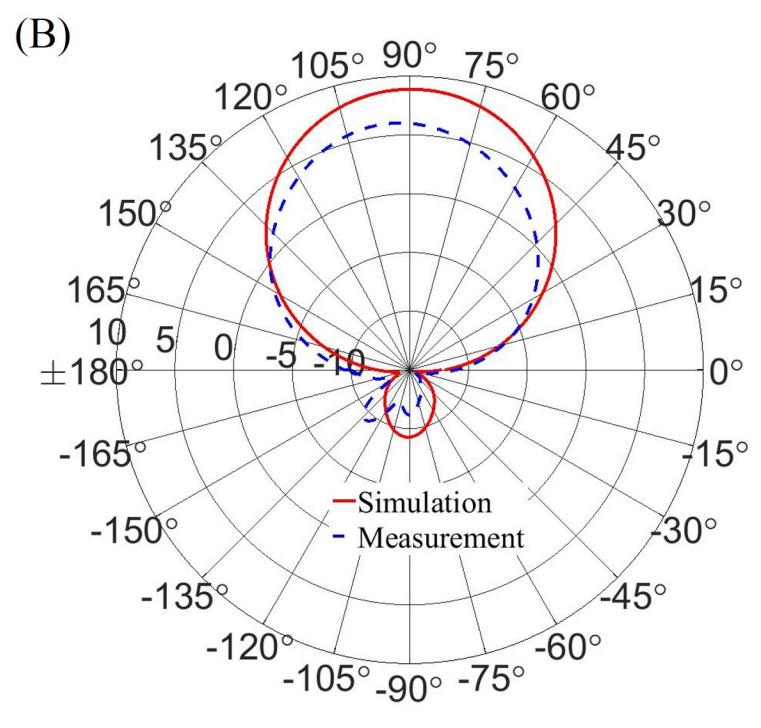


Figure 7.15: Simulated and measured results for (A) reflection coefficients (B) radiation patterns of the air substrate based patch antenna.

7.3.1.2 Amplifier Module

The amplifier is designed next using a commercially available surface mount wide band amplifier chip from Mini Circuits(GVA-84+). Figure 7.16A shows the basic amplifier circuit design consisting of a bias circuit with an inductor at the input and DC blocking capacitors at both the input and the output of the amplifier. Figure 7.16B shows the schematic of the amplifier circuit in a 3D printed configuration.

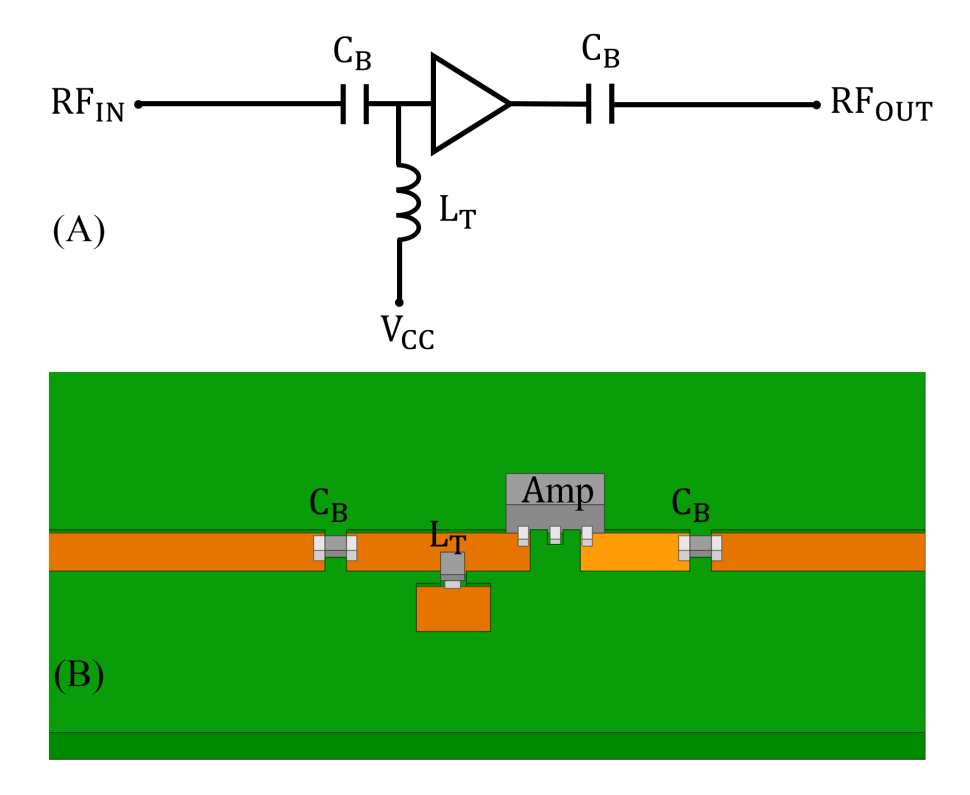


Figure 7.16: Schematic of the (A) amplifier circuit with lumped components, and (B) 3D printed configuration.

In order to validate the design, two different amplifier circuits are simulated using Agilent's Advanced Design System (ADS). For the first circuit, the amplifier is terminated using a matched 50 Ω , and for the second circuit, the matched termination is replaced by the Sparameters of the designed patch antenna. FEM solver High Frequency Structural Simulator (HFSS[®]) is used to design and simulate the S-parameters of the patch antenna. Figure 7.17

shows the simulated reflection coefficients at the input port of the amplifier circuit for both the terminations. It can be seen from the Figure 7.17 that the chosen amplifier shows a good performance over 5-6 GHz band when terminated by a matched load and when terminated by the patch, the amplifier's band of operation is restricted to that of the antenna's operational bandwidth. Figure 7.18 shows the image of the 3D printed amplifier.

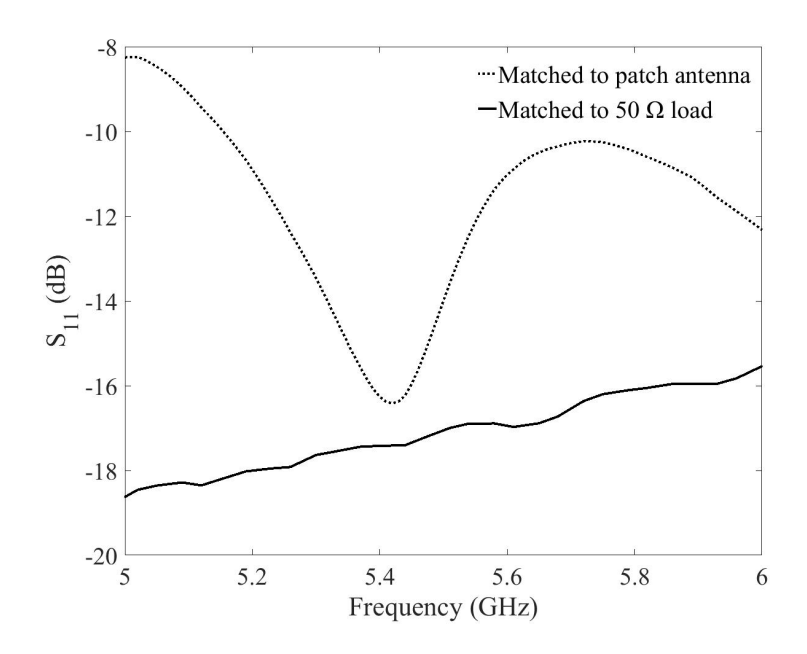


Figure 7.17: Simulation results for analyzing amplifier performance.

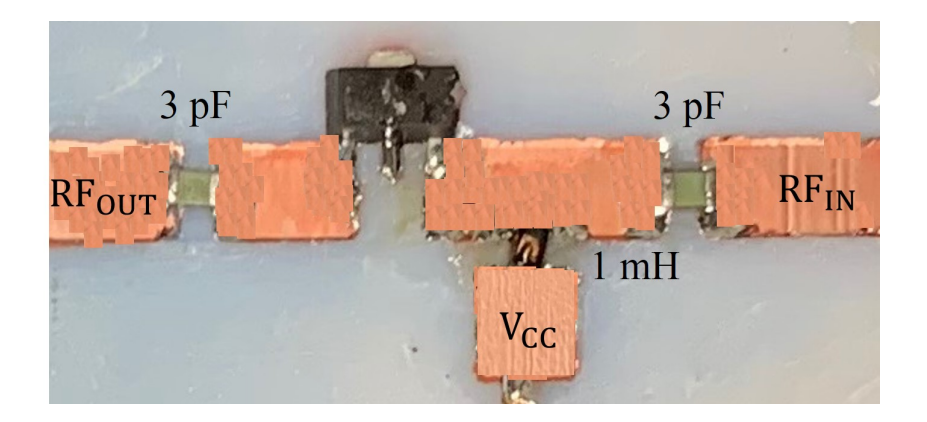


Figure 7.18: Image of the fabricated 3D printed amplifier.

7.3.1.3 Integrated RF Module

The amplifier and the air substrate based patch antenna are combined together forming a single RF module. Figure 7.19A shows the schematic of the module, Figure 7.19B and C shows the fabricated structure before and after metallization. Figure 7.19D shows the assembled module. Here, the power received by the patch antenna is amplified and measured on a spectrum analyzer.

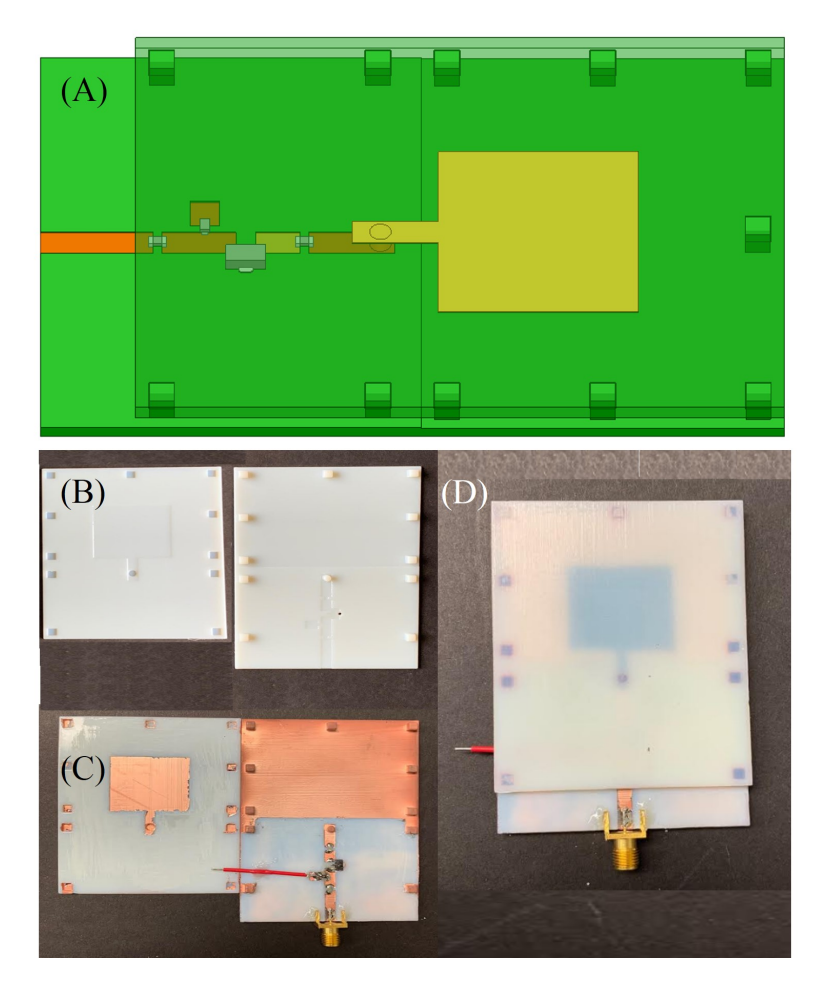


Figure 7.19: 3D printed integrated RF module: schematic (A), structure before and after metallization (B) and (C), respectively, and , (D) integrated module after the assembly process.

7.3.2 Results

Two sets of experiments are performed to evaluate the performance of the RF module. The experiments are performed in the anechoic chamber where the transmitter antenna is placed at a distance of 118 inches from the receiver module. For both the experiments, a commercial wide band Vivaldi antenna is used as a transmitter connected to an RF source. The device under test is connected to a DC source for biasing, and a spectrum analyzer for measuring the data. Figure 7.20 shows the measurement setup.

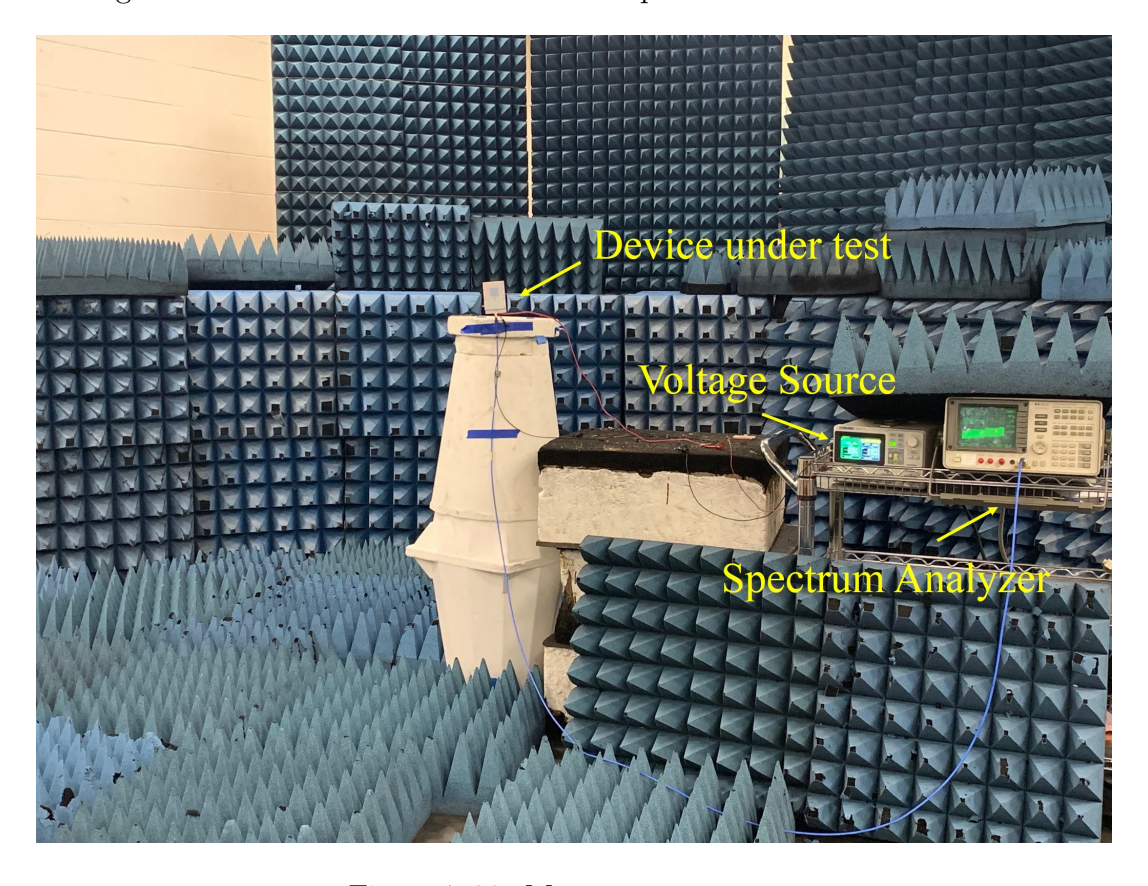


Figure 7.20: Measurement setup.

The first set of experiments is performed to analyze the effect of integrating an amplifier with the air substrate based patch antenna as a function of frequency with a fixed input power of 5.5 dBm. For the measurements, first, an air substrate based patch antenna without the amplifier is connected and the received power is measured. Second, the integrated module,

which includes the antenna and the amplifier is connected and received power is measured as a function of frequency with a fixed bias voltage of 4.6 V. Figure 7.21 shows the measured results for the first set of experiments.

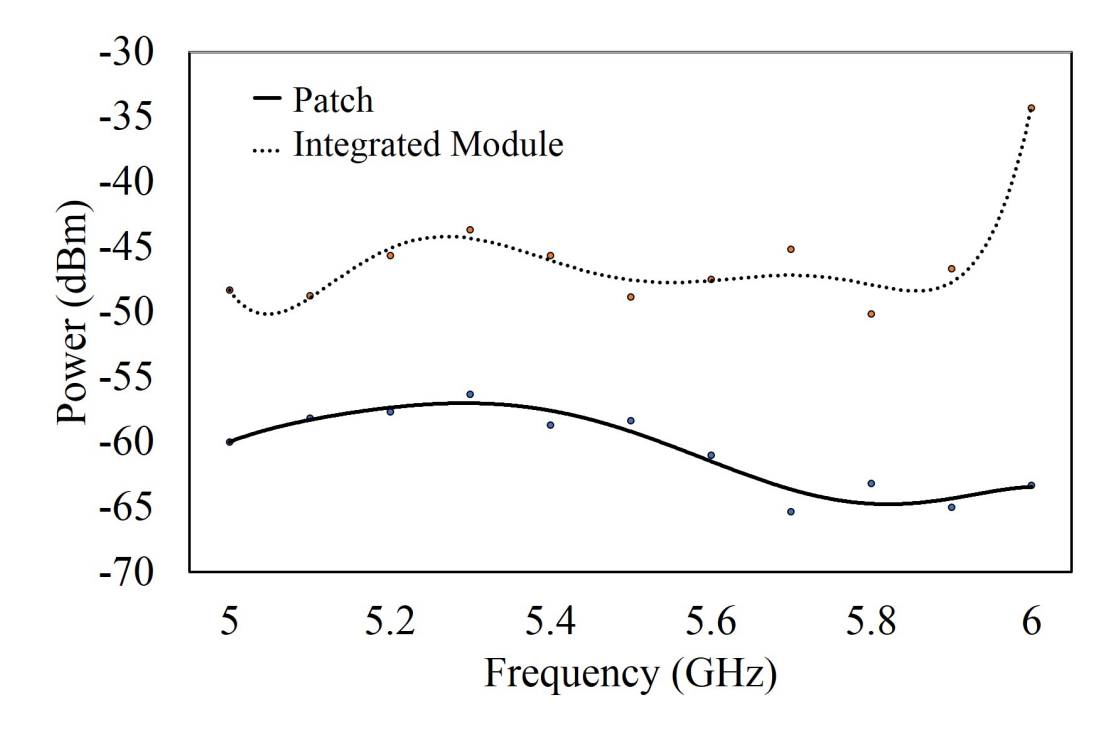


Figure 7.21: Measured received power as a function of input frequency.

As expected, the amplifier improves the signal strength in comparison to the direct received signal from the patch. The integrated module provides a good gain at the resonance frequency of the patch antenna (5.4 GHz). The second set of experiments is performed to analyze the effect of bias voltage on the received signal. The input frequency and signal power are fixed at 5.4 GHz and 5.5 dBm, respectively, and the received signal is measured as a function of bias voltage. Figure 7.22 shows the measured gain using a spectrum analyzer as a function of bias voltage. The amplifier performs the best beyond 4 V as seen from Figure 7.22. A combination of the two experiments helps in quantifying the performance of the integrated RF module showcasing the ability of 3D printing to fabricate a compact RF module for 5G and other applications.

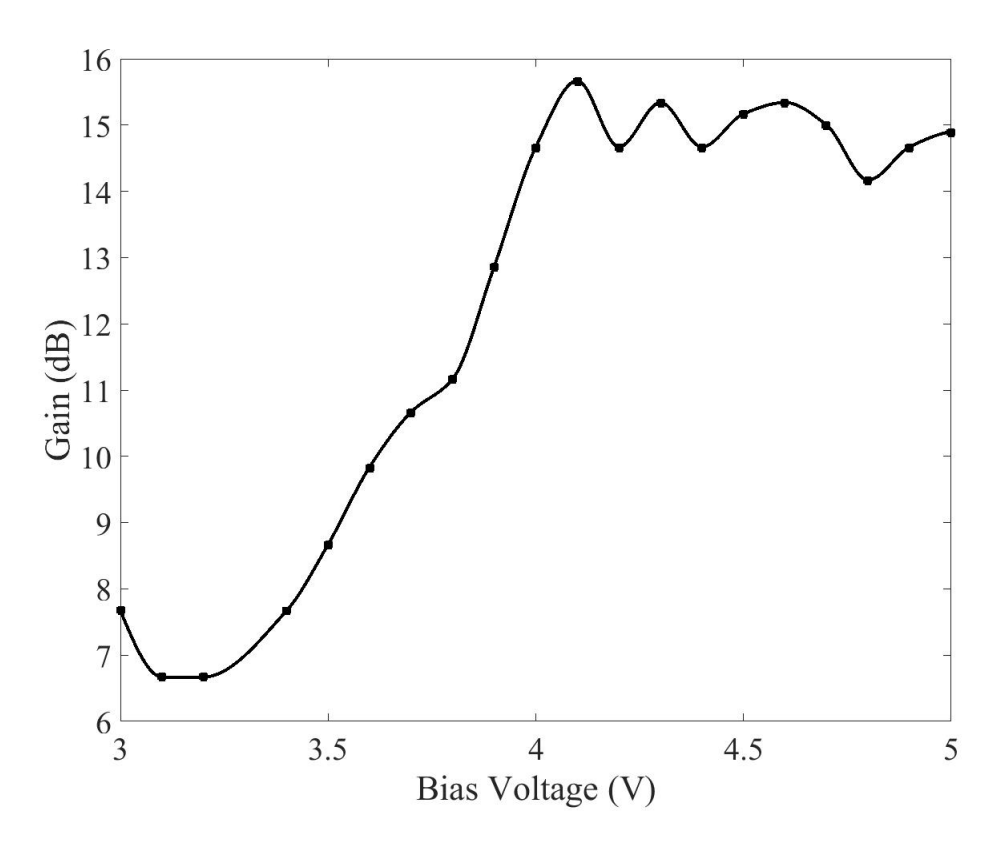


Figure 7.22: Measured gain as a function of bias voltage.

7.3.3 Discussion- 3D Printed Substrates for the Design of Compact RF Systems.

In this paper, a 3D printed RF system for 5G communication application is presented in which multiple components can be incorporated onto a custom printed plastic substrate. The vertical stacking of components allows reduction in the overall form factor of the system leading to a simpler SiP or SoP solution for realizing compact system designs. Although 3D printing is beneficial in realizing multi-layer structures, there are still some challenges associated using these techniques such as surface roughness, warpage due to heating, parasitics associated with soldering the SMT components, and the high dielectric loss associated with the photopolymer VeroWhitePlus. For reducing surface roughness, mechanical polishing

can be incorporated as an intermediate step before metallization. Warpage during sputtering process can be reduced by using a high temperature print polymer. Another critical factor that effects the performance of the RF circuits is the parasitics associated due to soldering on the surface mount components onto the 3D printed plastic. This can be reduced by introducing solder-free embedding techniques where different active and passive components can be incorporated as part of the substrate with corresponding vias for maintaining electrical connection. The effect of the dielectric loss associated with the 3D printed substrate can be reduced by utilizing LEGO-like assembly technique and by using air as a substrate over the whole structure. For a practical purpose, realizing fully 3D printed SoP/SiP solutions requires a combination of multiple printing techniques capable of printing metals, dielectrics, and nano-particles as well as advancement in print resolution, developing low loss print polymers, and automated assembly techniques.

7.4 Conclusion

In this chapter, two different 3D printed systems are presented that encompasses the various fabrication processes developed in the previous chapters. In the first part, an example application of 3D printed harmonic system with transceiver antennas and a sensor tag is presented for underground pipeline localization and detection. Second part of the chapter presents a 3D Printed Substrates for the design of compact RF systems for 5G communication applications. These techniques opens up the possibility of utilizing additive manufacturing as a possible candidate for manufacturing high-density and multi-functionality RF systems.

Chapter 8

Conclusions

In this dissertation, a number of techniques have been presented that advances AM technology for printing RF circuits and components. The advantages of AM for fabricating complex geometries in a rapid manner is exploited in developing these new fabrication techniques that allow seamless integration of multiple layers with ease. These techniques provide a pathway to achieve the envisioned 3D printed system as shown in Figure 6.1.

In chapter 2, two new processes for selectively patterning metals is presented, the damascene-like process and the lift-off process. The first technique introduces trenches in regions where metal trace is required and the rest of the regions are elevated to be mechanically polished after metallization process. The second technique introduces a shadow mask printed over the substrate to prevent metal from being deposited onto the unwanted regions. Once the metallization is completed, the shadow mask is removed and the patterned structure is realized.

In Chapter 3, the metal pattering processes developed in Chapter 2 is used on non-planar structures to realize different RF components. Utilizing the freedom on the z-axis, different non-planar structures are printed with reduced form factor for various SiP and SoP applications.

In Chapter 4, the losses associated with 3D printed materials are eliminated by introducing air as a substrate using a LEGO-like assembly process. The RF components are printed in two pieces with support pillars and corresponding holes and are selectively patterned using

the techniques developed in Chapter 2. The two pieces are snapped together to realize the final structure.

In Chapter 5, the light-weight nature of the 3D printed RF components is showcased by fabricating different waveguide structures. Using the combination of non-planar geometries and LEGO-like assembly approach, a number of guided wave structures are presented.

In Chapter 6, three new processes for embedding passive and active components into the 3D printed substrates is presented, face-up, face-down, and side-mount. The printer is stopped at pre-defined steps and the components are placed into cavities manually and the printing is continued. Vias are printed for providing electrical connection between the different embedded components. The technique is showcased by printing a cube with diodes embedded on all six faces along with the thermal characterization.

In Chapter 7, a fully 3D printed harmonic system and an RF front end system are presented utilizing the techniques developed in all the previous chapters. For the harmonic system, two non-planar transceiver antennas are fabricated using LEGO-like assembly process. A harmonic sensor tag with a dual slot antenna coupled to an embedded diode is fabricated using damascene-like metal patterning, face-up embedding and air-substrate based slot. The sensor system demonstrates the capability of 3D printing of complex geometry based structures in a customized and an economical way. For the front-end system, an amplifier sub-module and an air-substrate based antenna sub-module are integrated using 3D printing techniques such as damascene-like metal patterning and LEGO-like assembly.

In summary, the processes developed in this dissertation is the first step in advancing the AM technology to fabricate complex fully 3D printed RF systems with multiple functionalities.

8.1 Future Work

In future, a combination of metal printing such as inkjet along with dielectric printing such as SLA can be integrated in a single printer to print both metal and dielectrics simultaneously. The new process will allow solder free interconnections among various components on the 3D printed plastic substrate. A method for dispensing nano composites integrated with the printer allows fabrication of novel bio electronic devices. It can also be used for printing different shielding covers over the RF components. Employing high resolution printers allows embedding of bare dies which will be a giant leap in realizing miniaturized circuits using 3D printing. Another aspect of development lies in the automation of processes of the low cost printer similar to a PCB manufacturing machine where computer aided techniques such as robotic arms can be integrated for easier embedding of multiple components making the printing process fully automated.

8.1.1 3D Printing in Biomedical Applications:

The availability of bio-compatible print polymers has allowed printing of wearable bioelectronics such as mouth guards to prosthetic arms. The ability to model and customize the implants based on the individual needs is a boon for providing immediate assistance to the people in need. Moreover, the development of high rigid and mechanically stable printed polymers allows them to be used as implant structures from tooth to bones. The ability to print flexible polymers which can be coated with a bio-compatible material can be used for providing customized wearable body sensors such as heart rate monitor, pH sensor, sweat sensor, etc. Using embedding techniques developed in this dissertation allows packaging of electronics inside bio-compatible polymers making them an ideal choice for wearable technologies.

8.1.2 3D Printing in Aerospace Applications:

The ability of the AM to generate light weight components with good mechanical stability is a boon for the aerospace industry. Currently, researchers are exploring few methods are 3D printing in real-time in space. Once these methods are established, the 3D printer in the space station can be used to fabricate components in real-time allowing maintenance and repair work performed quickly. Furthermore, 3D printing can be used to print edible substances in space as food for astronauts. The light-weight manufacturing LEGO-like techniques introduced in this dissertation is ideal for space printing applications.

8.1.3 3D Printing in Transportation Applications:

The number of utilities are exponentially growing in recent years. Most of these utilities such as electric cables, transmission cables, water, sewer etc are channeled using pipelines from one place to another. Currently, the traditional heavy metallic pipelines are being replaced by light-weight and mechanically stable plastic pipelines. 3D printing technology allows printing of pipelines directly enabling a cheaper means of fabrication process. Furthermore, using the embedding techniques developed in this dissertation, sensors can be easily extruded into the pipelines for multiple purposes such as leakage detection, location marking, etc. A similar application has been demonstrated in the last chapter of this dissertation.

8.1.4 3D Printing in Smart Agriculture Applications:

Sustainable agriculture using smart techniques have become an area of recent interest due to the anticipated increase in global food shortage. 3D printing can be applied to fabricate low cost smart sensors for quality control of agricultural products. Embedding sensors into the 3D printed substrate using the techniques developed in this thesis can aid in developing new low cost multi-use sensing techniques. For example, monitoring soil pH or moisture content using 3D printed electrodes coated with pH or moisture sensitive films. 3D printing can also be used for different microfluidic sensing applications for quality control of liquid food such as milk.

APPENDICES

APPENDIX A

Sputtering Process

Procedure:

- 1. Pump the air out of the chamber.
- (a) Open the Nitrogen gas, turn on ThermoFlex 1400, Vacuum and Rate/Thickness Monitor.
- (b) Open up the chamber, push the Shutter 1 button on the screen to open the shutter of the Titanium gun.
- (c) After the check is complete, place the sample that needs to be sputtered at the center of the chuck. Close the chamber and put the lock on.
- (d) Go the screen view, select Auto pump/vent, push the Auto pump button to pump the air out the chamber.
- (e) After about 1 hour or when the displayed pressure on the screen becomes stable.
 - 2. Sputter the Titanium on the sample (600 A thick).
- (a) Calculate the thickness of the Ti layer. For example, normally 600 A (Anystrom) thick of Ti needs to be sputtered, which is equal to 60 nm thick. However, the thickness displayed on the monitor is half of the actual thickness, which means 300 A thick should be showed on the monitor in this case.

- (b) Open the Airgas and the valve. Turn on the power supply that sits in between the vacuum and the monitor. Go to the Rate/Thickness monitor, press Program, choose Film 1 which correspond to Ti sputtering configuration. Then push Next several times to the end of the setup, and press Program again.
- (c) In screen view, select DC sputter control—DC1—DC Ignition. Make sure the 125 w power correctly displayed on the power supply. Do not press shutter 1, because we need to burn off the Ti target till it looks light blue. Zero the time on the monitor
- (d) When the Ti becomes light blue. Return to the screen, select shutter 1 to open the shutter of the Ti gun. Zero the time again.

3. Sputter the Copper on the sample (1000 A thick).

- (a) Press shutter 1 to close the Ti gun. And select DC2—DC Ignition to heat up the copper target. Again, do not press shutter 2 now. Program Film 2 as in the previous step.
- (b) Allow the copper target to be heated up for 30 seconds, then press shutter 2 to start sputter the copper on the sample. Zero the time.
- (c) The actual thickness of the copper is the same as the thickness showed on the monitor.

 If 10 k A thick of copper needs to be sputtered, when the monitor shows 10k A thick, the sputtering process should be stopped by pressing the shutter 2 to close the copper gun.

4. Auto vent the chamber.

(a) Go to the Screen, select Auto pump/vent—Auto vent. When it is done, the lock of the chamber will fall. Then take out the sample by wearing the gloves.

(b) Change the transparent glass cover, turn off all the power supply and shut off the air gas and the Nitrogen.



Figure A.1: Denton Vacuum Desktop Pro

APPENDIX B

Electroplating Process

Procedure:

- (1) Set up the copper plating tank (2 gal)
- (2) Add 3 lbs of copper crystals followed by 1.5 liters of copper sulphate and 140 ml Sulfuric Acid.
- (3) The rest of the tank is filled with distilled water.
- (4) Attach a copper plate and connect it to a power supply with a constant voltage of 5 V.

 The current varies from 0.25 A 0.75 A depending on the size of the part to be plated.
- (5) Hang the part to be plated inside the bath with the support of copper clips or wires for approximately 15-30 minutes depending on the thickness of the plated copper.

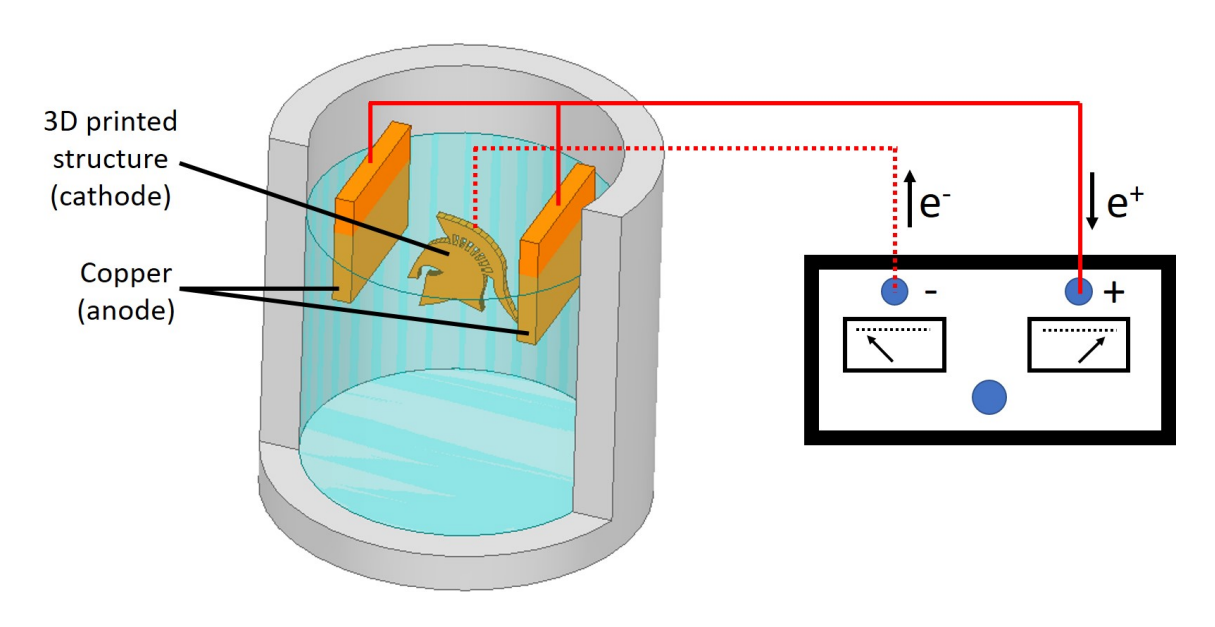


Figure B.1: Illustration of electroplating.

BIBLIOGRAPHY

BIBLIOGRAPHY

- [1] C. Tryon, B. Pobiner, and R. Kauffman, "Archaeology and human evolution," *Evolution: Education and Outreach*, vol. 3, no. 3, p. 377, 2010.
- [2] T. Thomas, "Animal power production: mechanisms for linking animals to machines. 7p," in *Animal traction for agricultural development. Proceedings of workshop held*, 1988, pp. 7–12.
- [3] S. Kumar, A. Nassehi, S. T. Newman, R. D. Allen, and M. K. Tiwari, "Process control in CNC manufacturing for discrete components: A STEP-NC compliant framework," *Robotics and Computer-Integrated Manufacturing*, vol. 23, no. 6, pp. 667–676, 2007.
- [4] H. Oktem, T. Erzurumlu, and I. Uzman, "Application of Taguchi optimization technique in determining plastic injection molding process parameters for a thin-shell part," *Materials & design*, vol. 28, no. 4, pp. 1271–1278, 2007.
- [5] W. E. Frazier, "Metal additive manufacturing: a review," Journal of Materials Engineering and Performance, vol. 23, no. 6, pp. 1917–1928, 2014.
- [6] P. Barker, "Behold the world's first 3D-printed car," Nov 2016. [Online]. Available: https://www.redbull.com/us-en/local-motors-strati-is-the-worlds-first-3D-printed-car
- [7] U. Klammert, U. Gbureck, E. Vorndran, J. Rödiger, P. Meyer-Marcotty, and A. C. Kübler, "3D powder printed calcium phosphate implants for reconstruction of cranial and maxillofacial defects," *Journal of Cranio-Maxillofacial Surgery*, vol. 38, no. 8, pp. 565–570, 2010.
- [8] S. V. Murphy and A. Atala, "3D bioprinting of tissues and organs," *Nature biotechnology*, vol. 32, no. 8, p. 773, 2014.
- [9] L. Hockaday, K. Kang, N. Colangelo, P. Cheung, B. Duan, E. Malone, J. Wu, L. Girardi, L. Bonassar, H. Lipson *et al.*, "Rapid 3D printing of anatomically accurate and mechanically heterogeneous aortic valve hydrogel scaffolds," *Biofabrication*, vol. 4, no. 3, p. 035005, 2012.
- [10] S. Franssila, Introduction to microfabrication. John Wiley & Sons, 2010.
- [11] E. R. Brown, "RF-MEMS switches for reconfigurable integrated circuits," *IEEE Transactions on microwave theory and techniques*, vol. 46, no. 11, pp. 1868–1880, 1998.

- [12] H. Becker and C. Gärtner, "Polymer microfabrication methods for microfluidic analytical applications," *ELECTROPHORESIS: An International Journal*, vol. 21, no. 1, pp. 12–26, 2000.
- [13] A. Guiseppi-Elie, N. F. Sheppard Jr, S. Brahim, and D. Narinesingh, "Enzyme microgels in packed-bed bioreactors with downstream amperometric detection using microfabricated interdigitated microsensor electrode arrays," *Biotechnology and bioengineering*, vol. 75, no. 4, pp. 475–484, 2001.
- [14] Z. Xu, Y. Zhang, P. Li, and C. Gao, "Strong, conductive, lightweight, neat graphene aerogel fibers with aligned pores," *Acs Nano*, vol. 6, no. 8, pp. 7103–7113, 2012.
- [15] C. I. Calle and R. B. Kaner, "Graphene-based ultra-light batteries for aircraft," 2014.
- [16] P. Garrou, C. Bower, and P. Ramm, Handbook of 3D Integration, Volume 1:Technology and Applications of 3D Integrated Circuits. John Wiley & Sons, 2011.
- [17] E. Macdonald, R. Salas, D. Espalin, M. Perez, E. Aguilera, D. Muse, and R. B. Wicker, "3D printing for the rapid prototyping of structural electronics," *IEEE access*, vol. 2, pp. 234–242, 2014.
- [18] L. J. Hornbeck, "Digital light processing for high-brightness high-resolution applications," in *Projection Displays III*, vol. 3013. International Society for Optics and Photonics, 1997, pp. 27–41.
- [19] Q. Jia and D. Gu, "Selective laser melting additive manufacturing of inconel 718 superalloy parts: Densification, microstructure and properties," *Journal of Alloys and Compounds*, vol. 585, pp. 713–721, 2014.
- [20] S.-H. Ahn, M. Montero, D. Odell, S. Roundy, and P. K. Wright, "Anisotropic material properties of fused deposition modeling ABS," *Rapid prototyping journal*, vol. 8, no. 4, pp. 248–257, 2002.
- [21] K. Taminger and R. A. Hafley, "Electron beam freeform fabrication: a rapid metal deposition process," 2003.
- [22] S. Meteyer, X. Xu, N. Perry, and Y. F. Zhao, "Energy and material flow analysis of binder-jetting additive manufacturing processes," *Procedia CIRP*, vol. 15, pp. 19–25, 2014.
- [23] R. Singh, "Process capability study of polyjet printing for plastic components," *Journal of mechanical science and technology*, vol. 25, no. 4, pp. 1011–1015, 2011.

- [24] J.-P. Kruth, M.-C. Leu, and T. Nakagawa, "Progress in additive manufacturing and rapid prototyping," *Cirp Annals*, vol. 47, no. 2, pp. 525–540, 1998.
- [25] D. Espalin, D. W. Muse, E. MacDonald, and R. B. Wicker, "3D printing multifunctionality: structures with electronics," *The International Journal of Advanced Manufacturing Technology*, vol. 72, no. 5-8, pp. 963–978, 2014.
- [26] A. Joe Lopes, E. MacDonald, and R. B. Wicker, "Integrating stereolithography and direct print technologies for 3D structural electronics fabrication," *Rapid Prototyping Journal*, vol. 18, no. 2, pp. 129–143, 2012.
- [27] G. Orecchini, F. Alimenti, V. Palazzari, A. Rida, M. Tentzeris, and L. Roselli, "Design and fabrication of ultra-low cost radio frequency identification antennas and tags exploiting paper substrates and inkjet printing technology," *IET microwaves, antennas & propagation*, vol. 5, no. 8, pp. 993–1001, 2011.
- [28] A. Rida, L. Yang, R. Vyas, and M. M. Tentzeris, "Conductive inkjet-printed antennas on flexible low-cost paper-based substrates for RFID and WSN applications," *IEEE Antennas and Propagation Magazine*, vol. 51, no. 3, 2009.
- [29] M. Ahmadloo and P. Mousavi, "A novel integrated dielectric-and-conductive ink 3D printing technique for fabrication of microwave devices," in *Microwave Symposium Digest (IMS)*, 2013 IEEE MTT-S International. IEEE, 2013, pp. 1–3.
- [30] G. McKerricher, D. Titterington, and A. Shamim, "A fully inkjet-printed 3-D honeycomb-inspired patch antenna," *IEEE antennas and wireless propagation letters*, vol. 15, pp. 544–547, 2016.
- [31] B.-O. Choi, C. H. Kim, and D. S. Kim, "Manufacturing ultra-high-frequency radio frequency identification tag antennas by multilayer printings," *Proceedings of the Institution of Mechanical Engineers, Part C: Journal of Mechanical Engineering Science*, vol. 224, no. 1, pp. 149–156, 2010.
- [32] J. N. Patel, B. Kaminska, B. L. Gray, and B. D. Gates, "A sacrificial SU-8 mask for direct metallization on PDMS," *Journal of Micromechanics and Microengineering*, vol. 19, no. 11, p. 115014, 2009.
- [33] P. C. Andricacos, C. Uzoh, J. O. Dukovic, J. Horkans, and H. Deligianni, "Damascene copper electroplating for chip interconnections," *IBM Journal of Research and Development*, vol. 42, no. 5, pp. 567–574, 1998.

- [34] L. Yang, A. Rida, R. Vyas, and M. M. Tentzeris, "RFID tag and RF structures on a paper substrate using inkjet-printing technology," *IEEE Transactions on Microwave Theory and Techniques*, vol. 55, no. 12, pp. 2894–2901, 2007.
- [35] R. Bahr, T. Le, M. M. Tentzeris, S. Moscato, M. Pasian, M. Bozzi, and L. Perregrini, "RF characterization of 3D printed flexible materials-ninjaflex filaments," in *Microwave Conference (EuMC)*, 2015 European. IEEE, 2015, pp. 742–745.
- [36] R. Willmot, D. Kim, and D. Peroulis, "A Yagi- Uda array of high-efficiency wire-bond antennas for on-chip radio applications," *IEEE Transactions on Microwave Theory and Techniques*, vol. 57, no. 12, pp. 3315–3321, 2009.
- [37] J.-G. Kim, H. S. Lee, H.-S. Lee, J.-B. Yoon, and S. Hong, "60-ghz CPW-fed post-supported patch antenna using micromachining technology," *IEEE Microwave and Wireless Components Letters*, vol. 15, no. 10, pp. 635–637, 2005.
- [38] S. Beer and T. Zwick, "122 GHz antenna-integration in a plastic package based on a flip chip interconnect," in *Microwave Workshop Series on Millimeter Wave Integration Technologies (IMWS)*, 2011 IEEE MTT-S International. IEEE, 2011, pp. 37–40.
- [39] Y. Zhang, M. Sun, K. Chua, L. Wai, and D. Liu, "Integration of slot antenna in LTCC package for 60 GHz radios," *Electronics Letters*, vol. 44, no. 5, pp. 330–331, 2008.
- [40] B. Pan, G. DeJean, J. Papapolymerou, M. Tentzeris, Y. Yoon, and M. Allen, "High performance system-on-package integrated Yagi-Uda antennas for W-band applications and mm-wave ultra-wideband data links," in *Electronic Components and Technology Conference*, 2006. Proceedings. 56th. IEEE, 2006, pp. 6–pp.
- [41] A. Shamim, K. N. Salama, E. Soliman, and S. Sedky, "On-chip antenna: Practical design and characterization considerations," in *Antenna Technology and Applied Electromagnetics & the American Electromagnetics Conference (ANTEM-AMEREM)*, 2010 14th International Symposium on. IEEE, 2010, pp. 1–4.
- [42] M. I. M. Ghazali, J. A. Byford, S. Karuppuswami, A. Kaur, J. Lennon, and P. Chahal, "3D printed out-of-plane antennas for use on high density boards," in *Electronic Components and Technology Conference (ECTC)*, 2017 IEEE 67th. IEEE, 2017, pp. 1835–1842.
- [43] J. A. Byford, M. I. M. Ghazali, S. Karuppuswami, B. L. Wright, and P. Chahal, "Demonstration of RF and microwave passive circuits through 3-D printing and selective metalization," *IEEE Transactions on Components, Packaging and Manufacturing Technology*, vol. 7, no. 3, pp. 463–471, 2017.

- [44] M. I. M. Ghazali, S. Karuppuswami, A. Kaur, and P. Chahal, "3-D printed air substrates for the design and fabrication of RF components," *IEEE Transactions on Components*, *Packaging and Manufacturing Technology*, vol. 7, no. 6, pp. 982–989, 2017.
- [45] M. I. M. Ghazali, E. Gutierrez, J. C. Myers, A. Kaur, B. Wright, and P. Chahal, "Affordable 3D printed microwave antennas," in *Electronic Components and Technology Conference (ECTC)*, 2015 IEEE 65th. IEEE, 2015, pp. 240–246.
- [46] S. Karuppuswami, A. Kaur, M. I. M. Ghazali, and P. Chahal, "RFID compatible sensor tags for remote liquid sample interrogation," in *Electronic Components and Technology Conference (ECTC)*, 2016 IEEE 66th. IEEE, 2016, pp. 2401–2407.
- [47] A. Chatterjee and S. K. Parui, "Performance enhancement of a dual-band monopole antenna by using a frequency-selective surface-based corner reflector," *IEEE Transactions on Antennas and Propagation*, vol. 64, no. 6, pp. 2165–2171, 2016.
- [48] P. I. Deffenbaugh, R. C. Rumpf, and K. H. Church, "Broadband microwave frequency characterization of 3-D printed materials," *IEEE Transactions on Components, Packaging and Manufacturing Technology*, vol. 3, no. 12, pp. 2147–2155, 2013.
- [49] I. Llamas-Garro and A. Corona-Chavez, "Micromachined transmission lines for millimeter-wave applications," in *Electronics, Communications and Computers*, 2006. CONIELECOMP 2006. 16th International Conference on. IEEE, 2006, pp. 15–15.
- [50] T. J. Spencer, P. J. Joseph, T. H. Kim, M. Swaminathan, and P. A. Kohl, "Air-gap transmission lines on organic substrates for low-loss interconnects," *IEEE Transactions* on Microwave Theory and Techniques, vol. 55, no. 9, pp. 1919–1925, 2007.
- [51] T. J. Spencer, R. Saha, J. Chen, R. Bashirullah, and P. A. Kohl, "Air cavity transmission lines for off-chip interconnects characterized to 40 GHz," *IEEE Transactions on Components, Packaging and Manufacturing Technology*, vol. 2, no. 3, pp. 367–374, 2012.
- [52] B. Pan, Y.-K. Yoon, G. E. Ponchak, M. G. Allen, J. Papapolymerou, and M. M. Tentzeris, "Analysis and characterization of a high-performance ka-band surface micromachined elevated patch antenna," *IEEE Antennas and Wireless Propagation Letters*, vol. 5, no. 1, pp. 511–514, 2006.
- [53] G. P. Gauthier, J.-P. Raskin, L. P. Katehi, and G. M. Rebeiz, "A 94-GHz aperture-coupled micromachined microstrip antenna," *IEEE Transactions on Antennas and Propagation*, vol. 47, no. 12, pp. 1761–1766, 1999.

- [54] R. Al-Dahleh, C. Shafai, and L. Shafai, "Frequency-agile microstrip patch antenna using a reconfigurable mems ground plane," *Microwave and optical technology letters*, vol. 43, no. 1, pp. 64–67, 2004.
- [55] S. Pavuluri, C. Wang, and A. Sangster, "A high-performance aperture-coupled patch antenna supported by a micromachined polymer ring," *IEEE Antennas and Wireless Propagation Letters*, vol. 7, pp. 283–286, 2008.
- [56] S. K. Pavuluri, C. Wang, and A. J. Sangster, "High efficiency wideband aperture-coupled stacked patch antennas assembled using millimeter thick micromachined polymer structures," *IEEE Transactions on Antennas and Propagation*, vol. 58, no. 11, pp. 3616–3621, 2010.
- [57] S. Targonski, R. Waterhouse, and D. Pozar, "Design of wide-band aperture-stacked patch microstrip antennas," *IEEE Transactions on Antennas and Propagation*, vol. 46, no. 9, pp. 1245–1251, 1998.
- [58] L. Harle and L. P. Katehi, "A vertically integrated micromachined filter," *IEEE transactions on microwave theory and techniques*, vol. 50, no. 9, pp. 2063–2068, 2002.
- [59] —, "A silicon micromachined four-pole linear phase filter," *IEEE transactions on microwave theory and techniques*, vol. 52, no. 6, pp. 1598–1607, 2004.
- [60] F. Sammoura, Y.-C. Su, Y. Cai, C.-Y. Chi, B. Elamaran, L. Lin, and J.-C. Chiao, "Plastic 95-GHz rectangular waveguides by micro molding technologies," Sensors and Actuators A: Physical, vol. 127, no. 2, pp. 270–275, 2006.
- [61] K. Y. Park, N. Wiwatcharagoses, and P. Chahal, "Wafer-level integration of microlens for THz focal plane array application," in *Electronic Components and Technology Conference (ECTC)*, 2013 IEEE 63rd. IEEE, 2013, pp. 1912–1919.
- [62] C. Kudsia, R. Cameron, and W.-C. Tang, "Innovations in microwave filters and multiplexing networks for communications satellite systems," *IEEE Transactions on Microwave Theory and Techniques*, vol. 40, no. 6, pp. 1133–1149, 1992.
- [63] A. Barnes, A. Boetti, L. Marchand, and J. Hopkins, "An overview of microwave component requirements for future space applications," in *Gallium Arsenide and Other Semiconductor Application Symposium*, 2005. EGAAS 2005. European. IEEE, 2005, pp. 5–12.
- [64] D. M. Pozar, Microwave engineering. John Wiley & Sons, 2009.

- [65] J. Gundersen and E. Wollack, "Millimeter wave corrugated platelet feeds," in *Journal of Physics: Conf. Ser*, vol. 155, 2009, p. 012005.
- [66] G. P. Le Sage, "3D printed waveguide slot array antennas," *IEEE Access*, vol. 4, pp. 1258–1265, 2016.
- [67] E. G. Geterud, P. Bergmark, and J. Yang, "Lightweight waveguide and antenna components using plating on plastics," in *Antennas and Propagation (EuCAP)*, 2013 7th European Conference on. IEEE, 2013, pp. 1812–1815.
- [68] M. DAuria, W. J. Otter, J. Hazell, B. T. Gillatt, C. Long-Collins, N. M. Ridler, and S. Lucyszyn, "3-D printed metal-pipe rectangular waveguides," *IEEE Transactions on Components, Packaging and Manufacturing Technology*, vol. 5, no. 9, pp. 1339–1349, 2015.
- [69] S. Choocadee and S. Akatimagool, "The simulation, design and implementation of band-pass filters in rectangular waveguides," *Electrical and Electronic Engineering*, vol. 2, no. 3, pp. 152–157, 2012.
- [70] B. Lee, F. J. Harackiewicz, B. Jung, and M.-J. Park, "Cavity-backed slot antenna array for the repeater system of a satellite digital multimedia broadcasting service," *IEEE Antennas and Wireless Propagation Letters*, vol. 4, no. 1, pp. 389–392, 2005.
- [71] T. D. Mendes, R. Godina, E. M. Rodrigues, J. C. Matias, and J. P. Catalão, "Smart home communication technologies and applications: Wireless protocol assessment for home area network resources," *Energies*, vol. 8, no. 7, pp. 7279–7311, 2015.
- [72] R. Negra, I. Jemili, and A. Belghith, "Wireless body area networks: Applications and technologies," *Procedia Computer Science*, vol. 83, pp. 1274–1281, 2016.
- [73] W. Hong, "Solving the 5G mobile antenna puzzle: Assessing future directions for the 5G mobile antenna paradigm shift," *IEEE Microwave Magazine*, vol. 18, no. 7, pp. 86–102, 2017.
- [74] A. Piqué, S. Mathews, B. Pratap, R. Auyeung, B. Karns, and S. Lakeou, "Embedding electronic circuits by laser direct-write," *Microelectronic engineering*, vol. 83, no. 11-12, pp. 2527–2533, 2006.
- [75] A. Kujala, R. Tuominen, and J. Kivilahti, "Solderless interconnection and packaging technique for embedded active components," in *Electronic Components and Technology Conference*, 1999. 1999 Proceedings. 49th. IEEE, 1999, pp. 155–159.

- [76] A. Joe Lopes, E. MacDonald, and R. B. Wicker, "Integrating stereolithography and direct print technologies for 3D structural electronics fabrication," *Rapid Prototyping Journal*, vol. 18, no. 2, pp. 129–143, 2012.
- [77] A. Romig Jr, P. Dressendorfer, and D. Palmer, "High performance microsystem packaging: A perspective," *Microelectronics Reliability*, vol. 37, no. 10-11, pp. 1771–1781, 1997.
- [78] A. Nicolson and G. Ross, "Measurement of the intrinsic properties of materials by time-domain techniques," *IEEE Trans. Instrum. Meas*, vol. 19, no. 4, pp. 377–382, 1970.
- [79] W. B. Weir, "Automatic measurement of complex dielectric constant and permeability at microwave frequencies," *Proceedings of the IEEE*, vol. 62, no. 1, pp. 33–36, 1974.
- [80] G. S. Shiroma, R. Y. Miyamoto, and W. A. Shiroma, "A full-duplex dual-frequency self-steering array using phase detection and phase shifting," *IEEE transactions on microwave theory and techniques*, vol. 54, no. 1, pp. 128–134, 2006.
- [81] M. Tsuji, T. Nishikawa, K. Wakino, and T. Kitazawa, "Bi-directionally fed phased-array antenna downsized with variable impedance phase shifter for ISM band," *IEEE transactions on microwave theory and techniques*, vol. 54, no. 7, pp. 2962–2969, 2006.
- [82] Y. Sung, "Reconfigurable patch antenna for polarization diversity," *IEEE Transactions on antennas and propagation*, vol. 56, no. 9, pp. 3053–3054, 2008.
- [83] J. Ou Yang, "A novel radiation pattern and frequency reconfigurable microstrip antenna on a thin substrate for wide-band and wide-angle scanning application," *Progress In Electromagnetics Research*, vol. 4, pp. 167–172, 2008.
- [84] J. Bjorgaard, M. Hoyack, E. Huber, M. Mirzaee, Y.-H. Chang, and S. Noghanian, "Design and fabrication of antennas using 3D printing," *Progress In Electromagnetics Research*, vol. 84, pp. 119–134, 2018.
- [85] S. Moscato, R. Bahr, T. Le, M. Pasian, M. Bozzi, L. Perregrini, and M. M. Tentzeris, "Infill dependent 3D-printed material based on ninjaflex filament for antenna applications," *IEEE Antennas and Wireless Propagation Letters*, vol. 15, no. 1, pp. 1506–1509, 2016.
- [86] R. L. Dumene, P. Kennedy, C. B. Williams, D. Sweeney, and G. Earle, "Creating embedded radiofrequency structures using polyjet material jetting," in *International Solid Freeform Fabrication Symposium*, 2015.

- [87] M. I. M. Ghazali, K. Y. Park, J. A. Byford, J. Papapolymerou, and P. Chahal, "3D printed metalized-polymer UWB high-gain Vivaldi antennas," in *Microwave Symposium* (IMS), 2016 IEEE MTT-S International. IEEE, 2016, pp. 1–4.
- [88] N. Arnal, T. Ketterl, Y. Vega, J. Stratton, C. Perkowski, P. Deffenbaugh, K. Church, and T. Weller, "3D multi-layer additive manufacturing of a 2.45 GHz RF front end," in 2015 IEEE MTT-s International Microwave Symposium. IEEE, 2015, pp. 1–4.
- [89] M. I. M. Ghazali, S. Karuppuswami, A. Kaur, and P. Chahal, "3-D printed air substrates for the design and fabrication of RF components," *IEEE Transactions on Components, Packaging and Manufacturing Technology*, vol. 7, no. 6, pp. 982–989, 2017.